Physico-chemical study of calcite colloidal suspensions : from macroscopic rheology to microscopic interaction

Teresa Liberto

N° d'ordre NNT : 2018LYSE1140

THÈSE DE DOCTORAT DE L'UNIVERSITÉ DE LYON

opérée au sein de

l'Université Claude Bernard Lyon 1

École Doctorale ED52

Physique et Astrophysique de Lyon

Spécialité de doctorat : Physique

Soutenue publiquement le 19/09/2018, par :

Teresa Liberto

Physico-chemical study of calcite colloidal suspensions: from macroscopic rheology to microscopic interaction

---

Devant le jury composé de :

Coussot Philippe, Directeur de Recherche IFSTTAR,	Rapporteur
Pochard Isabelle, Mâitre de Conférences, Université de Franche-Comté	Rapporteure
Ramos Laurence, Directrice de Recherche CNRS, Université de Montpellier	Examinatrice
Schoelkopf Joachim, Responsable industriel, Omya	Examinateur
Vanel Loïc, Professeur, Université Claude Bernard Lyon 1	Examinateur
Colombani Jean, Professeur, Université Claude Bernard Lyon 1	Directeur de thèse
Barentin Catherine, Professeur, Université Claude Bernard Lyon 1	Co-directrice de thèse
Le Merrer Marie, Chargée de recherche CNRS, Institut Lumière Matière	Co-directrice
Bellotto Maurizio, Responsable industriel, Politecnico di Milano	Invité

Acknowledgments

Writing the acknowledgments means that it is time to sum up this long, wonderful and winding journey. When I started my PhD, I changed country, language, department and research subject. The thesis made me discover both my limits and my strengths in a different way than in the past. For the first time I felt completely responsible for a project and also for the coordination of different ideas coming from my four supervisors. The initial enthusiasm was not enough to pass away all the complexities that I found, mainly due to my background far away from physics. Thank to all the people I met on my way, I have learned another science language and I have discovered what making research means.

All this process would not have been possible without my supervisors Catherine Barentin, Maurizio Bellotto, Jean Colombani and Marie Le Merrer. I owe my deepest gratitude to Catherine for guiding me in the rheological and physical world, always with a smile and a word of support. I'm grateful to Maurizio to follow the project despite the distance and to share the enormous expertise in the construction field. I am deeply thank to Jean for selecting and believing in me and to create and support a team around my project. I would like to thank Marie to fill with energy and smart ideas all our endless meetings, becoming a chemistry lover. Few lines cannot express what we have done together.

I want to express my gratitude to the members of my dissertation committee: Philippe Coussot, Isabelle Pochard, Laurence Ramos, Joachim Schoelkopf, Loïc Vanel for reviewing my thesis but also for the questions which stimulated me to widen my research from various perspectives.

During my PhD I had the opportunity to collaborate with: Sebastien Manneville, Brice Saint-Michel and Vincent Dolique (ENS Lyon), Anna Costa and Davide Gardini (ISTEC of Faenza), Agnès Piednoir and Nicolas Blanchard (ILM Lyon). Thank you for your important contribution to my research.

My sincere thank also goes to all the members of my European project NanoHeal for the amazing time spent together all around the world. Without our stimulating discussions, your insightful comments and encouragements, it would not have been possible to conduct this research. In particular, a special thank to: Nico Bovet, Tue Hassenkam, Susan Stipp (KU Group) and Kristina Durkic (Dynea group) who provided me the opportunity to join their team during my secondments, and who gave access to the laboratory and research facilities. Another special thank to all the ESRs, I discovered beautiful people and met new friends.

I would like to thank all the members of the Institut Lumière Matière in the liquids and interfaces and biophysics groups for welcoming me, helping and supporting me during all these three years.

I would especially like to thank all my old friends which despite the distance were always with me, and also the new ones which recreated a second family to lean on.

Last but not the least, I would like to thank with all my heart my family: my parents, my sisters, my brothers in law, my nephew and my nieces. Thank you for supporting my life and especially throughout these three years of thesis. You are the most greatest treasure!

Physico-chemical study of calcite colloidal suspensions: from macroscopic rheology to microscopic interaction

Calcite (calcium carbonate) is an extremely widespread material that can be found naturally in rocks (i.e. marble, limestone) and is employed in many industrial fields such as paper filling, pharmaceutical, art or construction. Understanding the mechanical properties of calcite suspensions is a first step to improve the workability of the paste as well as the final properties of solid mineral materials. Macroscopic characterization of calcite suspensions via rheological measurements are linked to microscopic interactions, via DLVO analysis. Our calcite pastes are weakly attractive systems showing a typical colloidal gel behavior and characterized by an elastic shear modulus and a critical strain. The elastic domain of pure calcite suspensions is characterized for a wide range of volume concentrations. The deformation at the end of linearity exhibits a minimum versus concentration, a major prediction of colloidal gel theory, never verified so far. The interaction forces between particles are tuned by addition of simple ionic species. Rheological measurements are analyzed through DLVO calculations, obtained by chemical speciations and ζ potential measurements on dense suspensions. Addition of calcium hydroxide improves initially the workability of the paste, enhancing the reactivity when in contact with CO_2. The role of interaction forces is also evaluated with flow measurements. The addition of sodium hydroxide increases strongly the attraction between particles, inducing shear bands at the macroscopic scale. This correlation is well known for emulsions but never verified so far for colloidal gels.

Keywords: Rheology, calcite, colloidal-gel, DLVO interaction.

Étude des propriétés de suspensions colloïdales de calcite de l'échelle macroscopique à l'échelle microscopique.

La calcite (carbonate de calcium) est un matériau extrêmement répandu dans les roches telles que le marbre et comme constituant dans des domaines variés (bâtiment, pharmacie, papier, art). La compréhension des propriétés mécaniques des suspensions de calcite constitue une étape importante pour améliorer à la fois leur maniabilité ainsi que les propriétés finales du matériau fabriqué. Cette étude relie les propriétés rhéologiques (élasticité, écoulement) de ces suspensions à leurs interactions microscopiques. Les interactions attractives entre particules de calcite confèrent aux pâtes les propriétés de gels colloïdaux caractérisés par un module élastique et une déformation critique, et ce pour une large gamme de concentrations. L'étude de ces grandeurs en fonction de la concentration a permis de mettre en évidence pour la première fois l'existence de deux régimes de déformation (liens forts et faibles) prédits théoriquement et de caractériser la dimension fractale. L'étude des interactions a été réalisée grâce à la mesure du potentiel Zeta des pâtes, du pH et au calcul de la longueur de Debye résultant de la force ionique. L'ajout d'additifs tels que la chaux ou la soude modifie les interactions. La chaux réduit fortement l'élasticité initiale des pâtes, facilitant leur maniabilité et renforçant la réactivité de la pâte en présence de CO_2. L'ajout de soude augmente fortement l'attraction entre les particules ce qui se traduit à l'échelle macroscopique par l'existence de bandes de cisaillement. Cette manifestation de l'attraction entre colloïdes à l'échelle macroscopique avait été observée dans des émulsions concentrés mais encore jamais dans les gels colloïdaux.

Mots clefs : rhéologie, calcite, gel de colloïdes, interaction DLVO.

Résumé

Les matériaux cimentaires, naturels et artificiels, jouent un rôle de premier plan dans notre vie de tous les jours. Le succès du béton à ciment, par exemple, tient à la grande disponibilité de ses matières premières telles que le calcaire, l'argile, le sable et le gravier, à sa facilité de mise en œuvre et à ses excellentes propriétés mécaniques. Le ciment le plus courant est le ciment Portland ordinaire (OPC). Malheureusement, sa production contribue à hauteur de 5% aux émissions de CO_2 anthropogéniques, principalement émises lors de la fabrication du ciment à partie du calcaire (calcination), qui dégage une demi-tonne de CO_2 par tonne de ciment produite. La réabsorption du CO_2 est un processus très lent, qui prend des centaines à des milliers d'années. Pour cette raison, on assiste depuis une dizaine d'années au développement de la recherche de bétons "verts", ou "à bas CO_2", aux propriétés chimiques et mécaniques nouvelles. À côté des ciments à bas CO_2, la recherche sur le ciment couvre aussi les champs de la santé, par exemple avec les ciments bio-compatibles, la construction et la préservation du patrimoine, avec les ciments à bas carbonate par exemple, ou l'industrie pétrolière et gazière, à la recherche de l'optimisation de l'extraction, ou de solution de stockage du CO_2.

Le fort impact potentiel de ces nouveaux matériaux sur notre environnement, nos monuments et nos bâtiments, a conduit à la formation d'un European Training Network, financé par la commission européenne, appelé Nanoheal. Ce groupe multidisciplinaire composé de 6 entreprises européennes et 6 universités, travaillant de concert, couvre : la physique, la chimie, les sciences de la terre, la science des matériaux, le génie civil et le génie pétrolier.

Encadrant 15 doctorants, ce programme cherche à comprendre les propriétés mécaniques de la chaux, des roches carbonatées, du carbonate biogénique et des suspensions de calcite, étudiant plus particulièrement leur durabilité, leurs mécanismes de croissance en nano-confinement, et leurs propriétés de cicatrisation. L'effet de molécules organiques simples est également étudié à toutes les échelles, de l'échelle atomique à l'échelle macroscopique, pour modifier les forces d'interaction de surface et piloter ainsi les propriétés macroscopiques. Le but à long terme du projet est d'acquérir la connaissance nécessaire pour comprendre et améliorer le comportement de systèmes aussi divers que les roches réservoirs de gaz et pétrole, les ciment osseux biocompatibles, et les matériaux de construction. Les applications des travaux du réseau couvrent donc autant le domaine biomédical, que la recherche environnementale, la construction et la conservation du patrimoine.

Dans ce contexte, le principal objectif de ma thèse est de comprendre l'effet des interactions à l'échelle colloïdale sur les propriétés de suspensions, liant ainsi les mécanismes microscopiques et macroscopiques. Nous avons choisi la calcite comme système modèle et nous avons étudié ses propriétés viscoélastiques à l'aide de mesures rhéologiques, à la fois à faibles amplitudes d'oscillation et en écoulement. Nous avons étudié une large gamme de concentrations en calcite, ainsi que l'effet d'additifs inorganiques.

Dans un premier temps, nous avons d'abord vérifié la pureté de la poudre par cryoXPS. Nous avons ensuite observé la taille et la forme des particules par microscopie optique, électronique et atomique. La

taille moyenne des particules est 70 nm. Les particules présentent des facettes atomiques, conformément à leur structure rhomboédrique.

Les suspensions de calcite pure sont obtenues par dispersion de la poudre dans l'eau desionisée. Les additifs sont ajoutés directement dans la solution avant mélange avec la poudre. Nos suspensions présentent un comportement typique de gel colloïdal à toutes les concentrations que nous avons étudiées (entre 5 et 30% volumique). Les études à faible amplitude d'oscillation montrent clairement un régime élastique, caractérisé par un module élastique G' et une déformation critique γ_{cr}, au-delà de laquelle la suspension se comporte plastiquement.

Nous avons dans un premier temps étudié les propriétés viscoélastiques de suspensions de calcite pure, considérées comme notre système de référence. Nous avons d'abord réalisé des mesures dans le régime linéaire de déformation à l'aide d'un rhéomètre couplé à un dispositif de spectroscopie d'onde diffusive (DWS), technique optique de diffusion multiple de la lumière, qui a permis de confirmer l'absence d'artefacts (glissement aux parois, bande de cisaillement) dans notre cellule de mesure. En augmentant progressivement la fraction volumique de solide, nous avons mis en évidence pour G' et γ_{cr} l'existence de deux lois d'échelle: G' change d'exposant positif, alors que γ_{cr} passe par un minimum. Ce comportement non-monotone de la limite élastique en déformation peut être interprété dans le cadre du modèle standard d'élasticité fractal des suspensions colloïdales, dû à Shih et collaborateurs. Ce modèle fait l'hypothèse d'une transition, lorsqu'on augmente la concentration en solide, d'un régime dit 'lien fort' à un régime dit 'lien faible'. À faibles concentrations (lien fort), la rigidité et la résistance de la pâte sont dominées par les propriétés internes des flocs fractals (des agrégats lâches de particules). À fortes concentrations au contraire (lien faible), ce sont les liens entre les flocs qui dominent. Cette transition est due au fait que les flocs sont de plus en plus petits et raides quand la concentration augmente. Si de nombreux systèmes ont été analysés dans la littérature à l'aide de ce modèle, la pâte de calcite est le premier système pour lequel cette transition est observée sans l'aide de stimulus extérieur, simplement par augmentation de la concentration de solide. Nous avons donc observé pour la première fois le minimum de γ_{cr} avec la concentration, prédiction majeure du modèle. Celui-ci nous a par ailleurs permis d'estimer la dimension fractale de la suspension dans les deux régimes, mettant en avant le changement de sa morphologie.

Une fois la suspension de calcite pure bien comprise, nous avons voulu piloter les propriétés mécaniques de la pâte via la modification des forces d'interaction entre particules par l'ajout d'ions dans la solution, susceptibles de modifier le pH, la force ionique de la solution ainsi que le potentiel Zêta à la surface des particules. Parmi les additifs inorganiques testés, ceux dont les effets sont les plus spectaculaires sont la chaux $Ca(OH)_2$ et la soude NaOH.

Immédiatement après préparation, la pâte préparée avec ajout de chaux montre une maniabilité fortement augmentée (G' diminué). Cet effet initial est dû à la dissolution de la chaux, qui libère des ions Ca^{2+} qui, en s'adsorbant à la surface des particules de calcite, augmente son potentiel Zêta, et diminue ainsi leur force d'attraction, comme nous l'avons constaté par des calculs d'interaction de type DLVO. La pâte réagit ensuite avec le CO_2 atmosphérique, et au bout d'environ 10 h, du fait de la précipitation de carbonate de calcium, la pâte retrouve des propriétés similaires à celles qui avait sans chaux (rigidité).

L'addition de soude au contraire transforme la pâte de calcite en un système très attractif, où toute répulsion électrostatique a disparu, permettant d'atteindre des valeurs de G' et γ_{cr}, très stables dans le temps. Nous avons alors mesuré la dynamique locale de la pâte à l'aide d'un dispositif, développé par Sébastien Manneville à l'ENS Lyon, couplant un montage de vélocimétrie ultrasonore à un rhéomètre de

géométrie Couette. Les mesures des profils de vitesse ont mis en évidence l'existence de bandes de cisaillement dans les pâtes en présence de soude, inexistantes pour les suspensions de calcite pure. Ce lien entre interaction inter-particule attractive et bande de cisaillement, s'il était connu dans les émulsions, n'avait encore jamais été observé dans les gels colloïdaux.

Maintenant que le comportement mécanique de la pâte de calcite pure et en présence d'ions est bien caractérisé et analysé, l'étude des modifications de ces propriétés par l'ajout d'additifs organiques (acides bi-caboxyliques, amino-acides, ...), présents dans le carbonate de calcium naturel ou artificiel, pourra être menée à bien avec confiance.

Contents

Introduction

Cementitious materials, both natural or artificial play a key role in our daily lives. The success of concrete lies in its abundant, inexpensive raw materials like limestone, sand and gravel. The most common concrete is primarily composed by ordinary Portland cement. Unfortunately its production contributes about 5% of global anthropogenic CO_2 emissions, mostly from a "fossil" origin, i.e. contained in the limestone rock, which produces carbon dioxide during the manufacturing process (calcination) [9]. The re-absorbing process of this "fossil" CO_2 is a very slow process that takes hundreds to thousands of years [9]. For these reasons the research of “green” or “low CO_2” concretes strongly developed in the last decade with different chemistry and mechanical properties [13]. Studies on concrete cover different fields as health care, e.g. biocompatible cement [14], construction heritage and conservation, e.g. low CO_2 cement [11], or oil and gas, e.g. CO_2 storage solution and oil extraction optimization [8].

The potential strong impact of these new materials on our environment, monuments and buildings, has led to the creation of our European Training Network (ETN) Horizon 2020, called *NanoHeal* [1]. This multidisciplinary group is composed of 6 European companies and 6 academic groups, working together combining: physics, chemistry, earth sciences, material science, civil engineering and petroleum engineering.

Training 15 PhD students, this program focuses on the interactions between a model mineral system —calcium carbonate— and simple organic molecules, to study mechanical properties of mineral materials, their durability, nano-confinement growth mechanisms and healing properties, spanning length-scales from atomic to macroscopic. The final goal of the project is to create the knowledge necessary to understand and improve the behavior of systems as diverse as rock reservoirs, biocompatible materials for bone cements, and construction materials. The applications cross many fields as biomedical, environmental, construction and conservation.

Calcite —the most stable polymorph of calcium carbonate— is one of the basic constituents of ancient and modern construction materials such as limestone and marble and the main raw material for concrete. For instance, calcite as limestone flour is used to produce high performance concrete with enhanced rheological properties [2]. Moreover, calcite slurry is one of the components of injection grouts for the restoration and consolidation of historical buildings and vernacular architecture [3]. Alternatively suspensions of colloidal calcite are used in industry as fillers (e.g. paper coating, toothpaste..).

In this context, the general objective of this PhD is to control the visco-elastic properties of calcite particle suspensions by tuning their microscopic interaction.

In particular, previous studies in the literature have focused on the flow properties of calcite paste to understand the mechanisms of superplasticizers [12, 4, 5, 7, 6]. However, little is known about their elastic properties. A large part of this PhD thesis is thus devoted to the characterization of the elastic regime of calcite paste both for pure calcite, which we consider as a reference system, and in presence

of ionic species. We first study the gel structure before changing the local interactions between particles. Finally, we investigate the role of attraction between calcite particles not only on the apparent flow response, but also on shear inhomogeneities.

The tools used in this research are two rheometers equipped with plate-plate and Couette geometries, an electroacoustic device to measure Zeta potential (ZetaProbe), a chemical speciation software (Visual MINTEQ), an optical technique called Diffusion Wave Spectroscopy (DWS) and an ultrasonic device (Ultrasonic Specle Velocimetry, USV) to follow the local dynamics of the sheared samples.

This PhD thesis consists in six chapters and 4 annexes. Chapter 1 illustrates the state of the art, reviewing the main theoretical aspects that support this PhD work. Materials and methodologies, i.e. protocols and device descriptions, are detailed in Chapter 2. The main results are presented in Chapters 3 to 5. They are presented as separate works, with the prospect of future publications for Chapters 4 and 5. In Chapter 3, we present our published results on the elastic properties of pure calcite paste [10] with supplementary information. Chapter 4 presents the physico-chemical role of additives, focusing on the reactivity of the pastes and its impact on elasticity. In Chapter 5, the influence of microscopic interaction on flow behavior is investigated. Chapter 6 is a general conclusion. Annex A presents intermediate results of Zeta potential measurements. Annexes B and C present additional elasticity measurements in presence of different ions (Annex B) or organic additives (dicarboxylic acids, Annex C). Annex D presents an explorative work on the mechanical properties of solid calcite cement.

The lack of basic information about the elastic properties of calcite paste (i.e. elastic behavior, yield strain..), pushed us into a fundamental study of the rheological properties of the pure suspension (no additives). Starting from a basic observation of the paste, we found that by mixing our nano-calcite powder with deionized water, we obtain a colloidal gel, weakly attractive, for a broad range of volume concentrations. This study of the role of particle concentration in itself brought new information on fractal gel physics. By playing on the addition of various ionic species, we have been able to tune both the reactivity and the electrostatic interactions between particles. This results in a temporal evolution of the elastic modulus of the colloidal gel, which can be linked to the evolution of the DLVO potential. Finally, for a very attractive system, we have evidenced shear bands upon flow for the first time for a colloidal suspension.

Bibliography

[1] http://www.nanoheal.uio.no.

[2] D. P. Bentz, A. Ardani, T. Barrett, S. Z. Jones, D. Lootens, M. A. Peltz, T. Sato, P. E. Stutzman, J. Tanesi, and W. J. Weiss. Multi-scale investigation of the performance of limestone in concrete. *Construction and Building Materials*, 75:1–10, 2015.

[3] B. Biçer-Şimşir, I. Griffin, B. Palazzo-Bertholon, and L. Rainer. Lime-based injection grouts for the conservation of architectural surfaces. *Studies in Conservation*, 54(sup1):3–17, 2009.

[4] G. Bossis, P. Boustingorry, Y. Grasselli, A. Meunier, R. Morini, A. Zubarev, and O. Volkova. Discontinuous shear thickening in the presence of polymers adsorbed on the surface of calcium carbonate particles. *Rheologica Acta*, 56(5):415–430, 2017.

[5] F. Dalas. *Influence des paramètres structuraux de superplastifiants sur l'hydratation, la création de surfaces initiales et la fluidité de systèmes cimentaires modèles*. PhD thesis, Dijon, 2014.

[6] F. Dalas, A. Nonat, S. Pourchet, M. Mosquet, D. Rinaldi, and S. Sabio. Tailoring the anionic function and the side chains of comb-like superplasticizers to improve their adsorption. *Cement and Concrete Research*, 67:21–30, 2015.

[7] F. Dalas, S. Pourchet, A. Nonat, D. Rinaldi, S. Sabio, and M. Mosquet. Fluidizing efficiency of comb-like superplasticizers: The effect of the anionic function, the side chain length and the grafting degree. *Cement and Concrete Research*, 71:115–123, 2015.

[8] J. Fredrich, J. Arguello, G. Deitrick, and E. de Rouffignac. Geomechanical modeling of reservoir compaction, surface subsidence, and casing damage at the Belridge diatomite field. Technical report, Sandia National Labs., Albuquerque, NM (US); Sandia National Labs., Livermore, CA (US), 2000.

[9] E. Gartner. Industrially interesting approaches to "low-CO_2" cements. *Cement and Concrete research*, 34(9):1489–1498, 2004.

[10] T. Liberto, M. Le Merrer, C. Barentin, M. Bellotto, and J. Colombani. Elasticity and yielding of a calcite paste: scaling laws in a dense colloidal suspension. *Soft matter*, 13(10):2014–2023, 2017.

[11] B. Lubelli and R. P. van Hees. Effectiveness of crystallization inhibitors in preventing salt damage in building materials. *Journal of cultural heritage*, 8(3):223–234, 2007.

[12] R. Morini. *Rhéologie de suspensions concentrées de carbonate de calcium en présence de fluidifiant*. PhD thesis, Université Nice Sophia Antipolis, 2013.

[13] J. L. Provis, P. Duxson, E. Kavalerova, P. V. Krivenko, Z. Pan, F. Puertas, and J. S. van Deventer. Historical aspects and overview. In *Alkali activated materials*, pages 11–57. Springer, 2014.

[14] A. Sellinger, P. M. Weiss, A. Nguyen, Y. Lu, R. A. Assink, W. Gong, and C. J. Brinker. Continuous self-assembly of organic–inorganic nanocomposite coatings that mimic nacre. *Nature*, 394(6690):256, 1998.

Chapter 1

State of the art

In this chapter, the basic theoretical concepts about calcite, soft matter and rheology are presented to give a general background for the other parts of the thesis. To deepen the different topics, the main references are provided.

Contents

1.1 Calcite: a complex chemical system

1.1.1 Crystallography

Calcium carbonate ($CaCO_3$) is a mineral, very abundant in the earth's crust and present in our daily life as chalk, limestone and marble [4]. It is common in sedimentary rocks formed from an extremely long sedimentation process of the shells of small fossilized snails or shellfish [22]. Calcium carbonate is a very widespread material crossing several industrial fields, from paper filling, through health and food production, to construction materials.

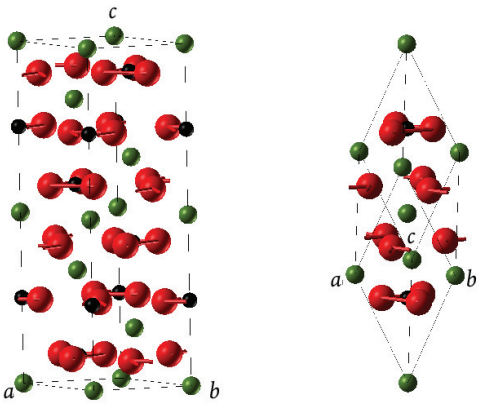

(i) Conventional cell *(i) Primitive cell*

Figure 1.1 – Courtesy of D. Carrasco de Busturia. View of the crystallographic conventional (i) and primitive (ii) cells of calcite. Whith: Ca ●, C ●, O ●. The primitive cell is rhombohedral and the crystallographic conventional cell is hexagonal.

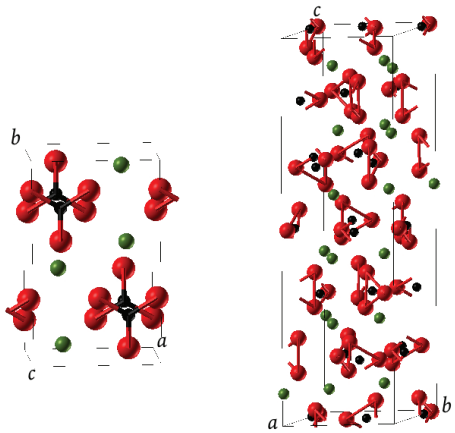

(i) Aragonite *(ii) Vaterite*

Figure 1.2 – Courtesy of D. Carrasco de Busturia. Crystallographic structures of aragonite (i) and vaterite (ii), with Ca ●, C ●, O ●.

Calcium carbonate has three polymorphs (crystal forms): *calcite* (rhombohedral) as in Figure 1.1, then *aragonite* (orthorhombic) and *vaterite* (hexagonal), as shown in Figure 1.2 [4]. Calcite is the most

stable polymorph of calcium carbonate. Aragonite and vaterite instead are two metastable phases. Aragonite can decompose in calcite on scales of $10^7 - 10^8$ years [54] or immediately by heating at temperatures in the range of $380 - 470°$ C [73]. Vaterite is less stable than aragonite, in fact the transformation in calcite occurs simply adding water [39, 76].

1.1.2 Solution chemistry

The aqueous carbonate system is very important for the environment, especially as component of the carbon cycle. Calcite-water suspension is a very rich and complex system. In fact many reactions are involved, all governed by the carbon dioxide equilibrium. For this reason, calcium carbonate dissolution and growth play a leading role in the control of the atmospheric CO_2 concentration, and thereby in climate change.

Calcite slightly dissolves in water (≈ 15 mg/L) as Ca^{2+} and CO_3^{2-}. The others related species in solution are: H_2CO_3, HCO_3^-, $CaHCO_3^+$, $CaOH^+$, $Ca(OH)_{2(aq)}$ and $CaCO_{3(aq)}$.

The detailed reactions are reported in Somasundaran and Agar (1967) [67]. The most important ones are listed below. A complete calcite chemical speciation is addressed in Section 2.4.

(1) $CaCO_3 + 2H^+ \longrightarrow Ca^{2+} + CO_2 + H_2O$ Calcite dissolution at low pH (≤ 6)

(2) $Ca^{2+} + 2HCO_3^- \rightleftharpoons CaCO_3 + CO_2 + H_2O$ Calcite precipitation/dissolution near neutral pH (≈ 8)

(3) $Ca^{2+} + CO_2 + 2OH^- \longrightarrow CaCO_3 + H_2O$ Calcite precipitation at high pH (≥ 10)

Assuming that the total amount of carbonates species: $[H_2CO_3]+[HCO_3^-]+[CO_3^{2-}]$ is a constant in water, it is possible to obtain the relative concentration evolution of each carbonate species as a function of the pH (Figure 1.3) [13] (CO_2 is assumed to always hydrate in H_2CO_3).

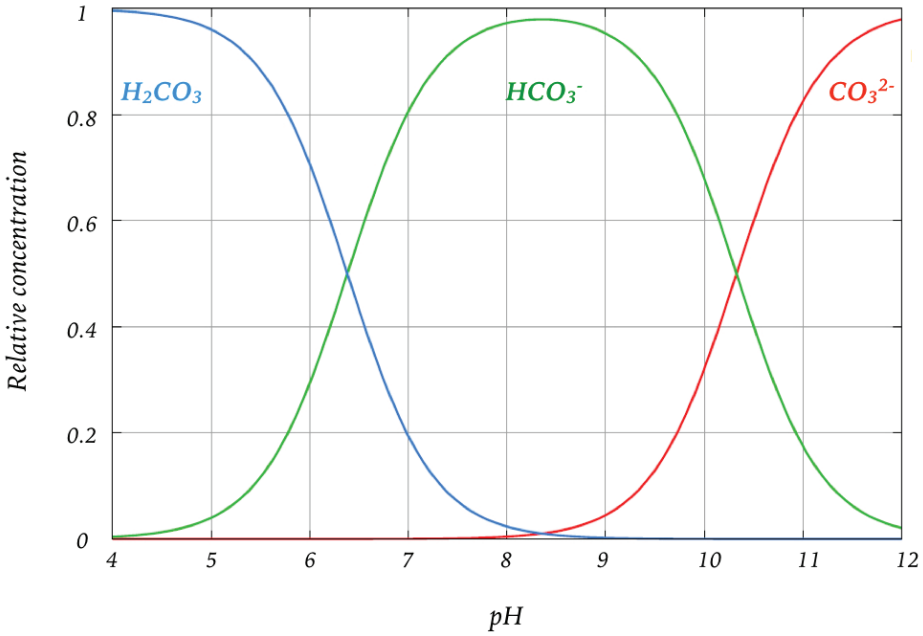

Figure 1.3 – Relative concentration of carbonate species as a function of pH. In geochemistry it is common to not distinguish the $CO_{2(aq)}$ and $H_2CO_{3(aq)}$.

The calcite suspension in contact with the atmosphere reach an equilibrium pH around $8.3 - 8.8$ [12],

where HCO_3^- is the dominant species. For higher pH values, reactions (2) and (3) start to prevail with a CO_2 uptake and the precipitation of calcium carbonate. At pH lower than the equilibrium one, calcium carbonate dissolution occurs and there is a release of CO_2.

To summarize calcite-water equilibrium is both CO_2 and ions sensitive. These two aspects form the basis of our investigation on calcite paste properties and are treated more into details in the next chapters.

1.2 Soft Matter: from simple bodies to complex fluids

1.2.1 Why "soft" matter?

In this chapter soft matter science is introduced, starting from a basic question: what does *soft* mean? Looking at the wide range of soft materials, from hard plastic to milk, this appellation does not match with our common idea of soft.

First soft matter includes a large class of materials (polymers, colloids, surfactants, foams, liquid crystals, etc.) that have mechanical properties between solid and liquid [38]. These systems are composed of small objects e.g. drops, bubbles, colloids with dimensions from a few nm to few mm. These objects constitute a dispersed phase distributed uniformly in a dispersion medium [66]. Soft matter often has some degree of self assembled ordering (short range) such as micelles or colloidal gels [38]. Then these systems have a multiscale structure that can go from a few nanometers to a macroscopic scale often with large structural units [28]. The interaction energies at small scale have the order of magnitude of k_BT, where k_B is the Boltzmann constant (1.3810^{-23} J/K) and T(K) is the temperature [38].

To conclude, the Nobel prize physicist Pierre-Gilles de Gennes defined soft matter as a class of materials that gives a large (non-linear) response to small perturbations, so easily deformable under an external force [23]. The main references to this section are [40, 42, 28, 38].

1.2.2 States of matter

The very well known basic states of matter are gases, liquids and solids. The final state depends on the balance between the thermal energy, k_BT, and the interaction energy between the components of the substance, E_{int}. Gas and liquid can be defined as *fluid* to indicate a substance without a fixed shape and easily deformable. Gases are isotropic fluids with a low density and minimal interparticle interaction due to the broad intermolecular distance. For an ideal gas composed of atoms, the average kinetic energy is $3/2\ k_BT$. To have a gas state, it is necessary that $k_BT \gg E_{\text{int}}$. Gases have an high relative mobility and can be characterized by their viscosity η, defined as the resistance to gradual deformation by shear stress or tensile stress.

On the other hand, solids are anisotropic, hard and high density materials (condensed phase) with a short intermolecular distance. Here $k_BT \ll E_{\text{int}}$. The solid structure is generally constituted by ordered molecules leading to a crystalline lattice. Amorphous solids (or glasses) are also possible in the case of lack of long-range order. Solids are not easily deformable due to their defined structure. They can be characterized by the *Young modulus E* that is a measure of the material stiffness as the ratio between stress and strain; the *shear modulus G* which define the material rigidity as the ratio between the shear stress and the shear strain, and also the *bulk modulus K* as the ratio between the pressure increase and

the resulting relative decrease of the volume [25].

Finally liquids are also isotropic fluids and condensed phase with a characteristic viscosity η. Their properties strongly depend on intermolecular forces. Liquids do not have a fixed structure, as solids, and their constitutive molecules are free to move. In fact $k_BT \approx E_{\text{int}}$ and the mobility μ can be calculated by the Stokes-Einstein equation ($\mu \approx 10^{-9}$ m^2/s/N). The liquid and solid states are the most relevant in the study of soft matter. Soft materials indeed can exhibit solid-like or liquid-like properties. These materials have a complex structure defined as self assembly that is at the origin of this intermediate behavior, as detailed in the following sections

1.2.3 Self assembly

As already mentioned one of the soft structure peculiarity is the possibility of self assembled ordering [38]. This spontaneous molecular association, as in micelles (Figure 1.4) or colloidal suspensions (Section 1.2.4), results in a structure soft and flexible. This fluid-like behavior is due to the weak nature of the interactions i.e. van der Waals, electrostatic, hydrophobic and hydrogen-bonding [42]. The size and the shape of the aggregates can be modified by external variation of the system acting on two levels: the aggregate interactions and the intermolecular forces inside the aggregate [42]. Moreover this self assembly process is driven by thermodynamic equilibrium. The system reaches the equilibrium when the Gibbs free energy is minimized (Equation (1.1)).

$$\mathscr{G} = U - TS + PV \tag{1.1}$$

Defining the chemical potential as $\mu = \frac{\partial G}{\partial N}\big|_{T,P}$, the aggregation is possible only when the single molecule has a chemical potential, μ_1, higher that the mean chemical potential of molecules in the aggregate, μ_n. Increasing the number of elements in the aggregate, n, decreases μ_n [42]. More specifically, there is a concentration value, called critical micelle concentration (CMC), at which surfactants self organize in micelles. This critical value is fixed comparing the entropic and energetic effects. In particular there is an energy gain (due to attractive interactions between molecules) despite a reduction in the entropy [24]. Also Brownian motion, due to thermal fluctuations, plays an important role in this aggregation process [38].

Self assembled systems can be constituted by amphiphiles, as surfactants, so molecules with a hydrophilic polar charged head and a hydrophobic carbon chain. These molecules assemble to form spherical (nm) , cylindrical (μm) or lamellar (μm) aggregates [42]. Figure 1.4 shows a spherical micelle, with the hydrophobic part (tail) concentrated in the center of the sphere and the hydrophilic part (head) in contact with the solution. Surfactants can also organize as inverted micelles, bilayer or bilayer vescicle depending on the solution conditions i.e. the electrolyte or lipid concentration, pH, or temperature [42]. The properties of the solution depend on the muddle of the resulting micelles.

1.2.4 Colloidal materials

Another example of self-assembly system is colloidal suspension in presence of attraction. The definition of colloid, from the Greek "kolla" (glue), covers a broad area of soft materials. Colloidal systems include gels, aerosols, suspensions and emulsions. The main characteristic is the coexistence of two phases (gas, liquid or solid): a dispersed one constituted by small droplets (emulsions) or particles (sus-

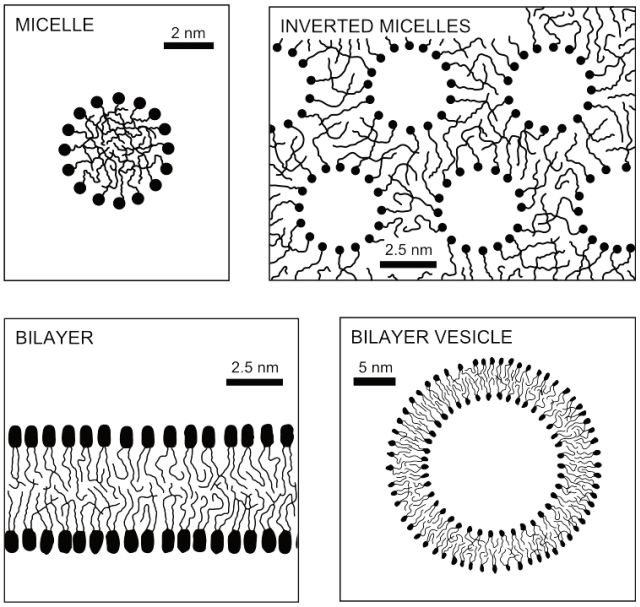

Figure 1.4 – Reproduced from [42]. Amphiphiles such as surfactants and lipids can associate into a variety of structures in aqueous solutions such as spherical micelles, inverted micelles, bilayer.... These can transform from one to another by changing the solution conditions such as the electrolyte or lipid concentration, pH, temperature and concentration of amphiphilic molecules. In most cases the hydrocarbon chains are in the fluid state allowing for the passage of water and ions through the narrow hydrophobic regions- for example, across bilayers. Most single-chained surfactants form micelles, while most double-chained surfactants form bilayers.

pensions) from nanometric to micrometric scale and a continuous fluid one. These systems have a high surface area to volume ratio, especially for smaller particles. This makes fundamental the study of the surface properties and the interaction between colloidal particles ($\sim k_{\mathrm{B}}T$) in the fluid medium [38]. Several forces define the final structure of the colloidal suspension. For "small" particles ($< \mu$m) thermal fluctuations promote dispersion and particle separation. This contribution interacts with an interparticle potential which can promote the colloid aggregation or dispersion, as discussed in the next chapters. Instead for "large" particles ($> \mu$m) also sedimentation and drag force start to play a role. In both cases the temperature is a key parameter as shown in the Stokes-Einstein Equation (1.2). Here, taking into account the Brownian motion, the diffusion coefficient, D, is a measure of the mean-squared displacement of the particle per unit time [38] (R is the radius of the spherical particle).

$$D = \frac{k_{\mathrm{B}}T}{6\pi\eta R} \tag{1.2}$$

Brownian force promotes dispersion of colloids whereas attractive forces such as van der Waals promotes aggregation. In particular, in the colloidal suspension, if van der Waals attractive forces (Figure 1.6) dominate, a colloidal gel is formed [15]. Here the interaction energy, E_{int} is bigger than $k_B T$. Generally colloid microscopical structure can be assumed as fractal flocs, defining a floc as "repetitive highly porous aggregate composed of smaller primary particles" [64]. The concept of fractal is addressed in the next section.

Fractals

Self assembly structures introduced before can be characterised by their *fractal dimension*. A fractal is a never ending pattern that repeats itself at different scales. This properties is called *self similarity* [48]. Fractal objects are scale invariant as showed in Figure 1.5 with the help of the Sierpinski triangles [38]. This set of equilateral triangles is repeated in the 2D space without filling it entirely.

Figure 1.5 – Sierpinski gasket: series of equilaterals triangles subdivided recursively to create an always more finer structure.

We can find fractals in nature i.e. trees, seashells or galaxies, but also in math i.e. the Mandelbrot set. Fractal dimension has been introduced to characterize the density of compaction of the structure, i.e. space-filling capacity. More clearly, how much space is occupied by an object in 1D, 2D or 3D? Fractal dimension, d_f links the mass M and the size r (A is a constant) [48] as following:

$$M(r) = Ar^{d_f} \tag{1.3}$$

The maximum value of the fractal dimension depends on the space dimension i.e. $d_f \leq 1$ in 1D, $1 \leq d_f \leq 2$ in 2D and $2 \leq d_f \leq 3$ in 3D. In real systems the fractal dimention is between 2 and 3. For colloids, if the aggregation is particle-cluster (Diffusion Limited Aggregation), typical $d_f \approx 2.6$ [40]. Cluster-cluster aggregation gives a $d_f \approx 2$ [40]. If there is an energy barrier (Reaction Limited Aggregation) the aggregate can be denser ($d_f = 2.86$ for haematite particles) [40].

In particular, in the aggregate which constitutes a colloidal gel, the number of the particles N follows a power law as in Equation (1.4), where ε is the floc characteristic size [15].

$$N \propto \left(\frac{\varepsilon}{R}\right)^{d_f} \tag{1.4}$$

1.2.5 Interparticle interactions

In colloidal systems and more generally in soft materials, interparticle forces play a relevant role in the stability and the final structure of these systems. We describe below the main forces such as van der Waals attraction, electrostatic forces, steric repulsion and depletion forces and their combination within the framework of Derjaguin, Landau, Verwey and Overbeek (DLVO) theory. The main references for this part are the books by Israelachvili [42] and Hunter [40].

Van der Waals attraction

Van der Waals forces are weak electrostatic forces that become relevant in interfacial phenomena and are at the origin of an attractive potential. This interaction has a polar origin and occurs between all the molecular dipoles, i.e. permanent, induced or instantaneous. Van der Waals interaction includes

all dipole interactions such as Keesom, Debye and London. Keesom force corresponds to the interaction between two permanent dipoles. Debye force is the force between a permanent dipole and the corresponding induced dipole. The dispersion force between instantaneously induced dipoles is called London force. These forces are at the origin of fluid cohesion.

Taking into account the different dipoles spatial configurations, the calculation of the interaction energy for all the three contributions (i.e. Keesom, Debye and London) leads to a scaling relation as D^{-6} (except for two high permanent dipoles). The resulting van der Waals energy between two dipoles, can be therefore expressed as:

$$E(r) = -\frac{C}{D^6} \tag{1.5}$$

were C is a coefficient and D the dipole separation distance.

We now turn to the interaction between two macroscopic bodies. Each body is constituted by dipoles. Then the total interaction is the sum of all dipole contributions. Assuming that the energies are additional and that there are no polar screening between the two objects, the van der Waals potential (energy per unit area) between two semi-infinite planes can be calculated as shown in Figure 1.6.

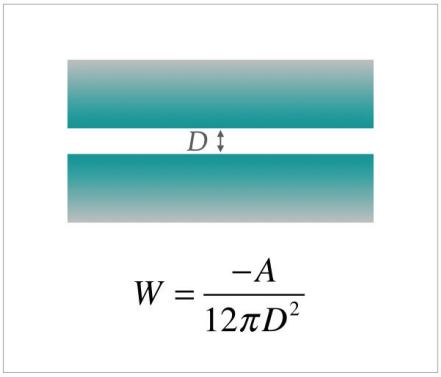

Figure 1.6 – Van der Waals interaction potential calculated on the basis of Hamaker pairwise additivity between two infinite surfaces.

A is the Hamaker constant whose expression is:

$$A = \pi^2 C \rho_1 \rho_2 \tag{1.6}$$

where C is the coefficient in the atom-atom pair interaction (the same as in Equation (1.5)) and ρ_1, ρ_2 are the number of atoms per unit volume in the two bodies. The Hamaker constant has the dimension of an energy, $A \simeq 10^{-19}$ J in vacuum and $A \simeq 10^{-21} - 10^{-20}$ J in solution ($\sim k_B T$). In vacuum condition $A > 0$, that corresponds to an attraction between the two interaction bodies. If there is a medium between two bodies with a permittivity equal to ε, this is taken into account in the coefficient C and also in A. The Hamaker constant is then: $A \propto (\varepsilon_1 - \varepsilon)(\varepsilon_2 - \varepsilon)$, where ε_1 and ε_2 are respectively the permittivity of the body 1 and 2. So in this case A can be positive (attractive potential) or negative (repulsive potential). For two identical particles we have always attraction, since $\varepsilon_1 = \varepsilon_2$ and $A \propto (\varepsilon_1 - \varepsilon)^2$.

Steric repulsion

Hard sphere repulsion becomes dominant for very short distance between two atoms or molecules. Reducing the separation distance, the electron orbitals of neighboring molecules start to interact. To prevent an overlapping of orbitals a strong repulsive force is developed. This phenomenon has a quantum mechanical origin, in fact according to the Pauli exclusion principle, two electrons cannot occupy the same quantum mechanical state and two atoms are unable to be in the same place at the same time [38]. This repulsion occurs between hard spheres because their internal structure cannot change with concentration while in soft spheres it can change due to the overlapping and deformation of the surfaces.

For atoms or molecules the combination between van der Waals attraction and the steric repulsion is empirically represented by Lennard-Jones energy, given by Equation (1.7):

$$E(D) = -\frac{C}{D^6} + \frac{B}{D^{12}} = 4\varepsilon\left[-\left(\frac{D_0}{D}\right)^6 + \left(\frac{D_0}{D}\right)^{12}\right] \tag{1.7}$$

here ε is the energy at the minimum point and provides a measure of how strongly the two atoms/molecules attract each other. D_0 is the distance at which the intermolecular energy between the two particles is zero. As shown in Figure 1.7 at very short distance, the repulsion between atoms prevails (orbitals-rejection) and rapidly decreases with increasing the separation distance, D, such as van der Waals contribution dominates. The potential energy minimum represents the equilibrium point between attractive and repulsive forces [38].

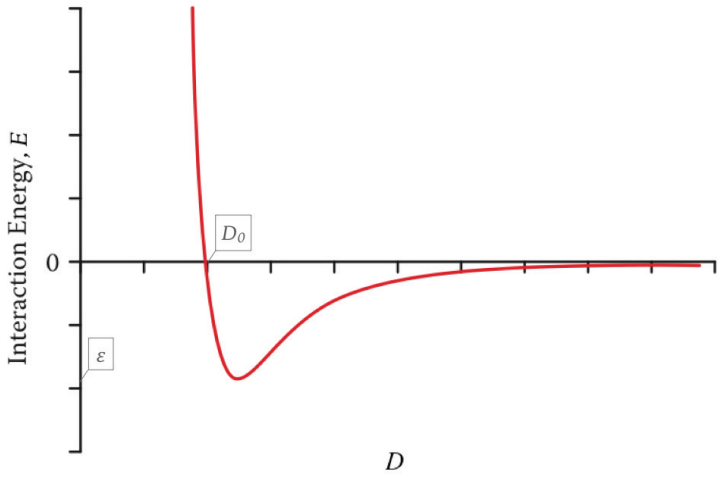

Figure 1.7 – Reproduced from [38]. Typical interaction energy (Lennard-Jones) between two atoms or molecules as a function of separation distance D. This interaction energy combines the van der Waals attraction and the hard sphere repulsion.

Electric double layer

In order to define the electrostatic forces between particles suspended in water, it is necessary to briefly recall what happens when a charged particle is inserted in an electrolyte solution. The particle charge results from the polarity of the solvent, the presence of salt and the consequent dissociated ions. Moreover, at the surface several phenomena are responsible for the charge i.e. dissociation/ionization of surface group, ionic impurities release and ions adsorption. The effect of a single (negative) colloid in solution is shown in Figure 1.8 and detailed in the following.

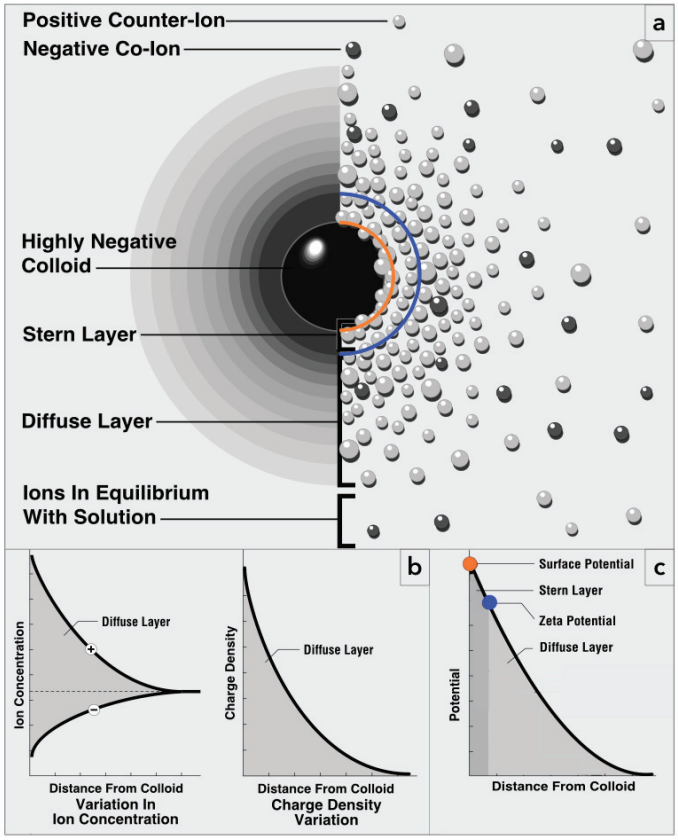

Figure 1.8 – Adapted from [74]. (a) Electric double layer (EDL) classification and distribution of positive and negative ions around the charged colloid (here negatively charged). (b) Variation of ion density through the diffuse layer. On left side is shown the single contribution of positive and negative ion concentrations as a function of the distance from the negative charged colloid. The net effect as difference between the two charge densities are represented on the right. (c) Potential all along the EDL. Both Surface (●) and Zeta potential (●) are defined in (a) and (c).

The colloidal particle is surrounded by *counter-ions* (positive in this specific case) forming a sticking layer around the surface, defined as the *Stern layer*. Moving from the surface, there is a counter ions charged atmosphere, called the *diffuse layer*. Both the Stern and the diffuse layer constitute the *Electric Double Layer* (EDL).

In the double layer the profile of concentration derives from the balance between the electrostatic forces (attraction towards the surface) and thermal fluctuation (diffusion). In particular the diffusion tends to homogenize the ions distribution. The EDL thickness is called *Debye length* (K^{-1}). Its value depends on the competition between the electrostatic attraction and the thermal motion and defines the electrostatic interaction range in the solution (as detailed in the next section). The concentration of counter-ions in the diffuse layer decreases with the distance from the colloid (Figure 1.8(b)). Oppositely the concentration of *co-ions* (here negative ions), strongly repelled in the surface surrounding, starts to increase in the diffuse layer, moving far from the colloid (Figure 1.8(b)).

Inside the EDL the electric field is non-zero but outside is equal to zero, in fact the double layer neutralizes the colloid charge (screening effect). The charge at the particle surface (Figure 1.8(a)) is defined as the *surface potential*, ψ_s (mV). This electrical potential decreases linearly through the Stern

layer and exponentially in the diffuse layer (Figure 1.8(c)). Due to the strong attraction of the counter-ions in the Stern layer, the only measurable potential is in reality the *Zeta potential*, ζ defined as the potential between the Stern and the diffuse layer (Figure 1.8(c)). Zeta potential corresponds in fact to the potential where the hydrodynamic boundary condition of no slip is satisfied. It is indeed located where the velocity of the colloid is equal to the one of the solvent medium. This means that the Stern layer sticks to the colloid, so by definition, ζ is the only measurable potential. For colloids which are not too highly charged ($e\psi_s < k_BT$, e electron charge) we can assume that $\zeta \approx \psi_s$.

In the next sections electrostatic forces and DLVO calculation are detailed.

Electrostatic forces

As already mentioned in the previous section, the presence of ions in the solution changes the electrostatic interaction between particles. In particular the ions electrostatic screening effect interacts with Coulomb potential. Coulomb force (Equation (1.8)) represents the attractive force between two opposite charges q_1 and q_2, or the repulsive force between two equal sign charge:

$$F_C = \frac{q_1 q_2}{4\pi\varepsilon_0 D^2} \tag{1.8}$$

were ε_0 is the permittivity of free space and D the separation between the charges [38].

The *Gouy-Chapman* theory describes the potential created by a charged surface in a solution, the ions distribution and the electrical field $\vec{E}$. Here the calculation for a simple case of a flat charged surface immersed into an electrolyte is reported. Combining the Maxwell and Poisson equations we obtain Equation (1.9):

$$\nabla \cdot \vec{E} = \frac{\rho}{\varepsilon} = -\triangle\psi \tag{1.9}$$

where ρ is the total electric charge density (total charge per unit volume), $\varepsilon = \varepsilon_0\varepsilon_r$ is the liquid permittivity and ψ the electric potential.

Thanks to the Boltzmann distribution of ions, we can express ρ as in Equation (1.10) and the ion concentration c as in Equation (1.11):

$$\rho = \rho_+ + \rho_- = z_+ e c_+ - z_- e c_- \tag{1.10}$$

$$c_\pm = c_\pm(0) e^{\mp \frac{z_\pm e\psi}{k_B T}} \tag{1.11}$$

where z is the ion valency and e the electron charge.

Assuming that the concentration in the electrolyte is 1:1 (i.e. salts like NaCl, KCl...), with $c_0 = c_+(0) = c_-(0)$ and $|z_+| = |z_-| = 1$, we can obtain the Poisson-Boltzmann expression for the electric potential (Equation (1.12)).

$$\triangle\psi = \frac{z_- e c_- - z_+ e c_+}{\varepsilon} = \frac{e c_0}{\varepsilon}\left(e^{\frac{e\psi}{k_B T}} - e^{\frac{-e\psi}{k_B T}}\right) = \frac{2ec_0}{\varepsilon}\sinh\left(\frac{e\psi}{k_B T}\right) \tag{1.12}$$

From Equation (1.12) and assuming that $\frac{e\psi}{k_B T} \ll 1$, i.e. $\psi \ll 25\,\text{mV}$ (Debye-Hückel limit), we can linearize the Poisson-Boltzmann equation to obtain the Debye-Hückel equation for the electric potential:

$$\triangle\psi = \frac{2e^2c_0}{\varepsilon k_B T}\psi = K^2\psi = \lambda_D^{-2}\psi \tag{1.13}$$

where λ_D is the Debye length ($K = \lambda_D^{-1}$) that, as already mentioned, gives the thickness of the electric double layer and the range of electrostatic interaction.

Equation (1.14) expresses the Debye length for a 1:1 electrolyte:

$$\lambda_D = \sqrt{\frac{\varepsilon k_B T}{2e^2c_0}} \tag{1.14}$$

The more general expression is given by Equation (1.15):

$$\lambda_D = \sqrt{\frac{\varepsilon k_B T}{2e^2 I}} \tag{1.15}$$

where the term I is the ionic strength, defined as $I = \sum_{i=1}^{n} c_i z_i^2$ In this specific condition of 1:1 electrolyte and for $\frac{e\psi}{k_B T} \ll 1$, it is possible to solve Equation (1.13) for the potential created by a charged surface (Equation (1.16)):

$$\psi(r) = \psi_s e^{-KD} \tag{1.16}$$

In the following, we consider objects not too highly charged, so we can consider $\psi_s = \zeta$.

DLVO theory

DLVO or Derjarguin-Landau-Verwey and Overbeek theory predicts the stability of colloidal suspensions by the combination of van der Waals attractive interaction and electrostatic repulsion. It is important to underline that, contrary to the electrostatic interactions, van der Waals interactions are largely insensitive to the variations of electrolyte concentration or pH [42].

Equation (1.17) and Figure 1.9 show respectively the expression and the plot of the total interaction energy per unit area by summing the attractive van der Waals contribution, W_a and the double layer repulsion, W_r, for two similarly charged planes at distance separation D.

$$W(D) = W_a + W_r \approx -\frac{A}{12\pi D^2} + 2\varepsilon K\zeta^2 e^{-KD} \tag{1.17}$$

In Figure 1.9, σ is the surface density of charges which is (in the Debye-Hückel limit) proportional to the ζ potential as: $\sigma = \zeta\varepsilon K$.

Remembering that to prevent the contact the steric repulsion always occurs, van der Waals contribution exceeds on double layer repulsion (primary minimum Figure 1.9) at short distance. An important parameter from the net DLVO interaction curve is the energy barrier as difference between the maximum and the secondary minimum. This barrier is generally compared with the typical thermal energy $k_B T$.

Varying the surface density of charge, σ, the energy barrier is modified. In particular for highly charged surface in dilute electrolyte the energy barrier is very high, resulting from a strong long-range repulsion [42]. Before the energy barrier there is a secondary minimum that becomes relevant in more concentrated electrolyte. In the case of high barrier, this lower minimum represents a weak "equilibrium" point in which the colloid is *kinetically stable* [42]. At low σ, also the barrier is reduced, leading to

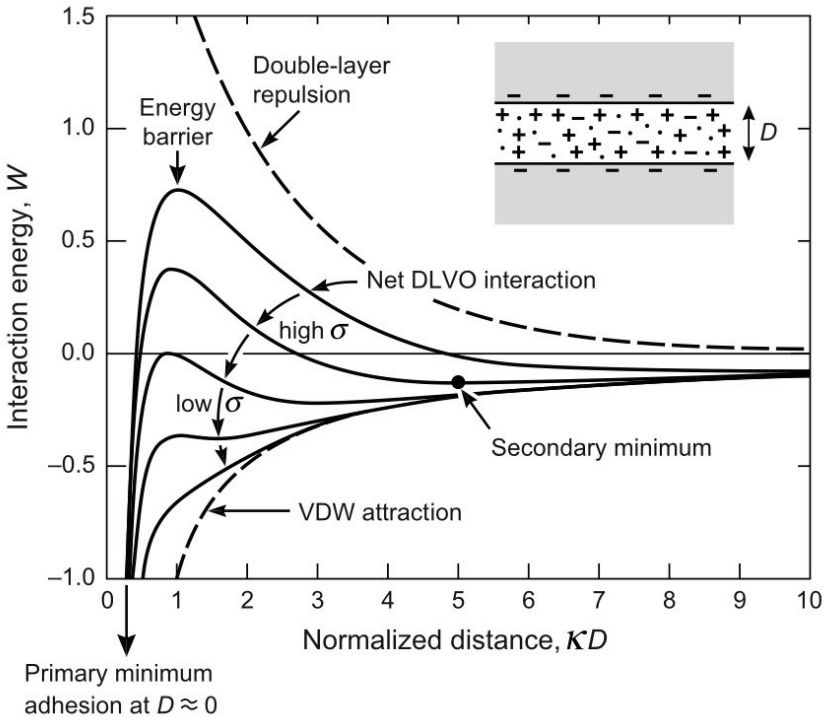

Figure 1.9 – Reproduced from [42]. Schematic DLVO interaction as a function of the normalized distance KD, for different values of σ, going from low to high charged surface.

coagulation and *flocculation*, making the colloid *unstable* [42].

In order to increase the attraction between two surfaces it is necessary to decrease the electrostatic repulsion by reducing the surface charge or the Debye length. This can be done by modifying the pH or the ions in solution.

Derjaguin approximation

To calculate the interaction between two curved surfaces, we can apply the Derjaguin approximation in the limit of small distances. This approximation allows to calculate the force (resp. energy) acting between two finite size bodies using the force (resp. energy) between two planar semi-infinite walls whose expression is known [26]. In particular, this approximation holds when the radii of curvature of the surfaces, R are large compared to the separation distance, D.

Using the Derjaguin approximation, the force $F(D)$ between two curved bodies as a function of the separation distance D has the following expression (Equation (1.18)):

$$F(D) = 2\pi R_{eff} W(D) \tag{1.18}$$

where $W(D)$ is the interaction energy per unit area between two semi-infinite planes and R_{eff} the effective radius. In particular, for two spheres of radii R_1, R_2, the $R_{eff} = R_1 \cdot R_2/(R_1 + R_2)$. Figure 1.10 shows the results of the total interaction energy $E_{tot} = \int F(D)\ \mathrm{d}D$, for two spheres and sphere-plane cases obtained with the Derjaguin approximation ($R_1, R_2 \gg D$).

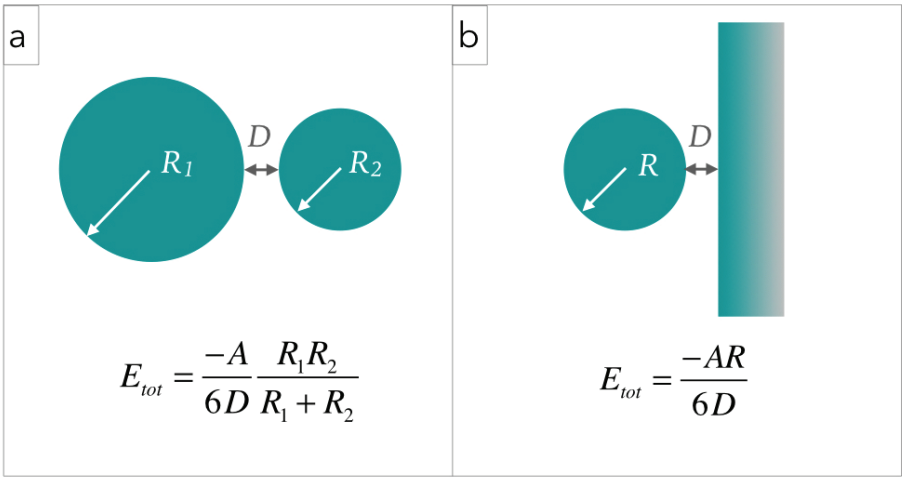

Figure 1.10 – Van der Waals total interaction energy between bodies of different geometries calculated with the Derjaguin approximation: (a) between two spheres with $R_1, R_2 \gg D$. (b) between a sphere and an infinite surface with $R \gg D$.

1.2.6 Non-DLVO forces

DLVO forces, such as attractive van der Waals and repulsive double-layer, at small surfaces or particles separations distance (closer than a few nanometers) generally cannot describe successfully all the interactions [42]. This can also be attributed to other non-DLVO forces (attractive, repulsive, oscillatory) that occur at short distance with a stronger contribution than the DLVO ones [42].

In this section the main non-DLVO forces are briefly recalled. The main reference of this section is the book of Israelachvili [42]

Oscillatory forces

Oscillatory (solvation) forces occur between two hard smooth or crystalline walls that confine a liquid that may structure into semiordered layers. Any attractive liquid-liquid or liquid- wall interaction is required. The solvation pressure can be expressed as in Equation (1.19):

$$P(D) = k_B T[\rho_s(D) - \rho_s(\infty)] = k_B T[\rho_m(D) - \rho_m(\infty)] \tag{1.19}$$

where ρ_s and ρ_m are respectively the ionic densities at each surface and the midplane, calculated when the surfaces are at a distance D or ∞ apart. Figure 1.11 shows the mechanism of solvation forces between two hard walls, confining molecules with molecular diameter σ.

In particular Figure 1.11 (a) outlines the two surfaces with in between layers of solvent molecules progressively squeezed out from g to a, applying a solvation pressure $P(D)$ as in Equation (1.19). In Figure 1.11 (b) is drawn a schematic variation of $P(D)$ with the distance D (few molecular diameters σ). The resulting oscillatory behavior corresponds to the ejection of several liquid layers. From g to a in fact, molecules layers are progressively squeezed out with an increasing applied solvation pressure. At very small separation, as the last layer of solvent molecules is finally expelled (contact between surfaces) a resulting adhesive force occurs (Figure 1.11 point a).

It is important to underline that liquid confinement between two surfaces is not enough to induce solvation forces. They arise because of the continuously disruption or change of the ordering molecular

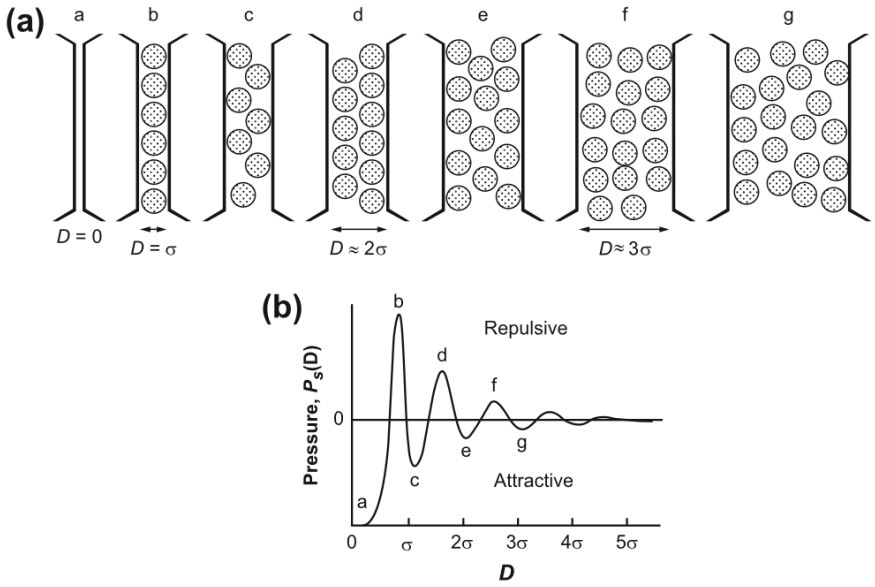

Figure 1.11 – Reproduced from Israelachvili [42]. (a) Modification of molecules layers between two hard walls with the separation distance D. (b) Corresponding (oscillatory) solvation pressure (schematic) as given by Equation (1.19). Note the multiple ("quantized") and progressively deeper adhesive minima at g, e, c, and a (contact). σ is here the molecular diameter.

layers, that vary the film thickness. In particular, they can withstand a finite compressive force at a finite separation even when the final contact is adhesive.

Moreover to have oscillatory solvation forces, both the liquid molecules and the surfaces need to have a high degree of order or symmetry. So molecule geometries and surface roughness can produce dramatic changes to solvation forces, even make them monotonic [35, 34].

Hydration forces

Hydration forces are solvation forces in aqueous systems and occur for hydrophilic surfaces. Hydrophilic surfaces mutually repel due to the ability of water to hydrogen bond and hydrate the surface, resulting in a repulsive osmotic pressure [41, 29]. The physical nature of these forces is not totally understood.

The repulsive hydration interaction potential (per unit area) between two hydrophilic surfaces is expressed as in Equation (1.20):

$$W(D) = +W_0 e^{-D/\lambda_0} \tag{1.20}$$

where W_0 depends on the surface hydration and λ_0 represents the decay length ($\approx$ 1 nm for 1:1 electrolytes [58]). We can distinguish between primary and secondary hydration forces [29].

Primary hydration forces are short-ranged ($\lambda_0 \approx 0.3$ nm [29]) and are observed for silica surfaces [37, 71]. They are due to surface hydration layers of protruding surface moieties (i.e. silicic acid groups extending $\approx$ 5 Å from the surface) [29]. This mechanism is similar to the steric repulsion created by polymer-functionalized surface (see steric stabilization in Section 1.2.6).

Secondary hydration forces instead are slightly longer-ranged ($\lambda_0 \approx 1$ nm [29]) and are due to the hydration of the solute i.e. counterions near charged surfaces. In this case the system studied is mica surfaces for which hydration forces increase with the hydration number of the cations: $Mg^{2+} > Ca^{2+} >$

$Li^+ \approx Na^+ > K^+ > Cs^+$[57, 59].

Hydration forces are relevant also for cement (C-S-H surface) [36]. Nevertheless, the wide range of volume concentration for which our calcite suspension forms a gel, suggests an attractive interaction between particles. For this reason we did not investigate shorter range repulsive force such as hydration forces.

Charge correlation forces

Charge correlation forces occur for highly charged surfaces (e.g. DNA [9] or C-S-H [44, 36]) and in presence of ions/counterions. Ions correlation results in an attractive force in a range of $\approx$ 1-2 nm [43, 36]. As the surface is highly charged, counter ions are attracted and "condense" on it (i.e. Manning condensation [49]).

This phenomenon leads to a quasi neutralization of the surface charge and the position of the condensed ions fluctuate. Moreover for two facing surfaces, the excess of condensed ions in some place (with respect to the Poisson-Boltzmann prediction [49]) leads to a deficit in other place [36]. In other words an excess of counterions on one side is correlated with a lack of counterions on the opposite side [44]. This charge displacement results in a strong attraction non predicted by classic mean-field electrostatic theory, so also two zero charged surfaces in average do attract each other [45].

In these systems the interaction between particles results from a competition between the entropic pressure, that is proportional to the counterions concentration at the mid-plane between two surfaces, and an attractive force, due to the counterions condensation at the surfaces [44]. In the case of high surface charge densities the attraction prevails to the entropy due to the accumulation of counterions at the surface [44]. In particular, Figure 1.12 [44] shows two surfaces of calcium-sylicate-hydrate C-S-H (i.e. network of nanoparticles inside the cement) immersed in a solution containing co-ions (OH^-) and counterions (Ca^{2+}).

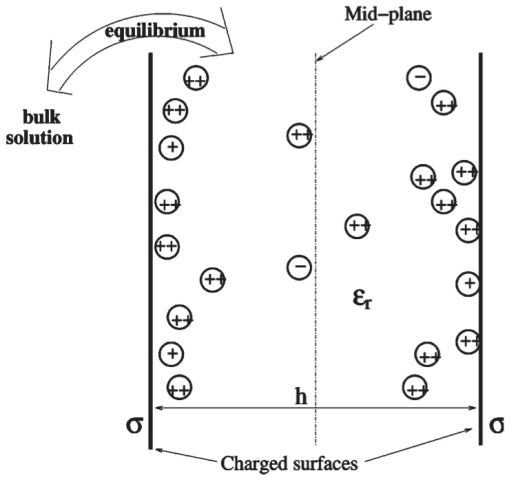

Figure 1.12 – Reproduced from Jönsson et al.(2005) [43]. Planar model system of two C-S-H particles (strongly negatively charged) with neutralizing mono and divalent counterions (Ca^{2+} represented as ++) as well as co-ions (OH^- represented as -). The system is thought to be infinite in two dimensions, and the surface charge density, σ, is assumed to be uniformly smeared out on the two confining surfaces. The confined solution contains both co- and counter-ions, whose concentrations are determined by the equilibrium with an infinite bulk solution. The dielectric permittivity, ε_r, is assumed to be uniform throughout space, and the whole system is electroneutral.

Close to the surfaces with charged densities σ, the counterions condense creating a local charge displacement. This short range (few nm) force is one of the contribution in the cement cohesion. In our case, calcite differs from cement behaving as a weak-attractive system. Our calcite surface charge density is certainly too low ($\psi_s < 25$ mV) to have an ion correlation contribution.

Role of polymer addition

Polymers can affect the behavior of suspensions, acting on interaction. We recall briefly the steric stabilization (repulsive effect) and depletion forces (attractive effect).

Steric stabilization is a repulsive interaction occurring between two polymer chains grafted on particles. In particular this effect occurs when particles approach each other. These polymers are constituted by an insoluble part (*anchor polymer*) and a soluble one (*stabilizing moieties*). The anchor polymer is adsorbed onto the particle and the soluble tail which projects away in the solution [40]. When two particles approach, the interaction is repulsive if the two chains are in good solvent condition. This phenomenon does not depend on the aqueous nature of the solution neither on the particles or electrolyte concentrations [40]. It is sensitive instead to temperature or pressure variations. Moreover its stability can be perturbed in bad solvent condition [40].

Depletion forces involve soluble *non-adsorbing* polymers whose gyration radius is smaller than the colloidal size. These forces occur at small separation distance between colloids, comparable with the size of the dissolved polymer molecules. The interactions between particles are modified by osmotic effect. In fact when two particles approach, the polymers in the solution move to surround them. The particles are then pushed by the osmotic pressure difference until flocculation [40]. In other words the polymers escape from the inter-particle space, due to steric repulsion, which makes the particles coagulate. This phenomenon can be extended to particles with different size. In this case the smaller particles act like the polymer and the bigger ones aggregate. In this case, the origin lies in the thermal motion of the smaller particles, that can collide and push together the larger colloids [38]. To control the aggregation, we can tune the size of the smaller particle or, in the case of polymer, the temperature (i.e. changing the radius of gyration) [38].

We have defined the main interactions that can bring to the formation of colloidal gels whose properties are intermediate between liquid and solid. In the next chapter we proceed with an overview of the study about the mechanical properties of fluids.

1.3 Rheology of complex fluids: a macroscopic approach

Why the only way to force mayonnaise to flow outside a bottle is to shake it? In our daily life we are dealing, also unconsciously, with rheology. In fact, when we are in contact with any product, we define it as viscous, creamy, gelatinous, rubbery, sticky, rigid, flexible, elastic etc., so we are evaluating its rheological nature. So πάντα ῥεῖ, everything flows!

In this section the main aspects of rheology and tools to study the mechanical properties are introduced. One of the interest of rheological experiments is to characterize the viscoelastic properties of complex systems as colloidal suspensions. The main references of this chapter are the books of Coussot [17], Larson [46] and Oswald [56].

1.3.1 Fundamental Rheological Concepts

Rheology is the science of the deformation and the flow of matter, under controlled testing conditions and it is applied to liquids, "soft solids" or solids. There are different types of deformation: compression, dilatation and shear. But in the following, we will focus only on the shear deformation that implies volume conservation.

Shear flow is the sliding of a material in which adjacent particles move over or past each other. Deformation or *strain*, is any transformation in the geometrical configuration of a body (e.g. shape, dimension) caused by external forces. Referring to Figure 1.13, we can define several quantities: the

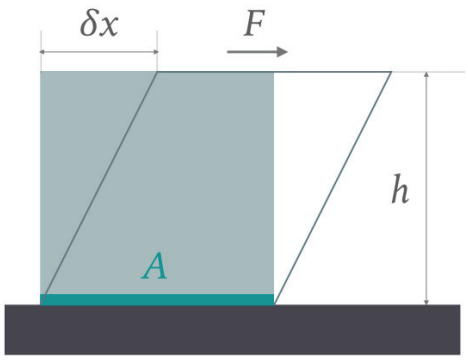

Figure 1.13 – Schematic drawing of a simple shear geometry.

strain as $\gamma = \delta x/h$, the shear rate as $\dot{\gamma} = d\gamma/dt$ and the shear stress as $\tau = F/A$, with A, the area of material parallel to the applied force vector. The range of material response goes from a solid like (ideal solid) to a liquid like (ideal fluid) behavior. These two extremes are characterized by two classical laws, respectively Hooke's and Newton's laws (i.e. Newtonian behavior).

As first, Hooke's law describes the behavior of an ideal elastic solid for which the mechanical response is proportional to the external force: $\tau = G\gamma$, were G, represents the elastic modulus and is measured in *Pa*.

Newtonian behavior for an ideal purely viscous fluid can be described with another proportional relation: $\tau = \eta\dot{\gamma}$. The viscosity η ($Pa\,s$) represents the resistance that the fluid opposes to the flow or deformation rate by shear stress. For a Newtonian fluid, η is a constant.

In both cases the material responds instantaneously to the imposed shear stress, independently of the associated time scale. The ideal solid can recover the initial state once the stress is removed, having an "infinite memory" about its first body configuration. Instead, the ideal fluid has no memory about its primitive structure and undergoes immediately a plastic irreversible deformation.

Once defined the main quantities linked to the mechanical characterization of a fluid, the next section presents the instrument — the rheometer— that we used to measure them.

1.3.2 Rheometer

Viscoelastic properties of fluid materials (i.e. suspensions, emulsions, pastes, polymer solutions..) can be measured by an instrument called rheometer. In Figure 1.14 (a) is shown a rheometer Anton Paar (MCR 301) and the most common geometries used for this equipment (detailed below).

Rotational rheometers are constituted by a rotor and a stator separated spatially by the gap ($\approx$ mm). The upper part is always equipped with a tool. If the rheometer is stress-imposed (Figure 1.14 (b))

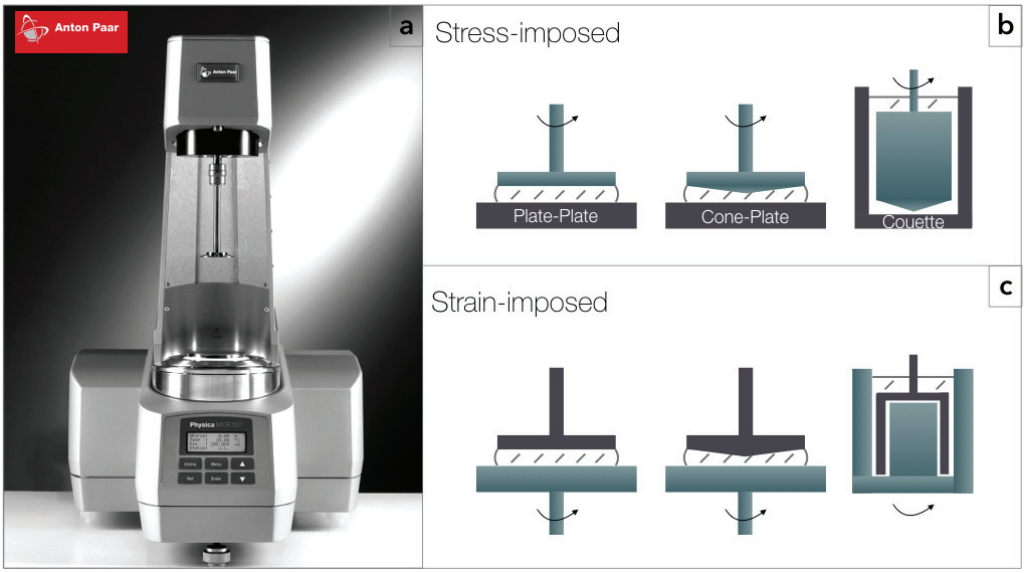

Figure 1.14 – (a) Picture of the rheometer MCR 301 by Anton Paar. Schematic geometries for a stress imposed (b) and strain imposed (c) rotational rheometer. For both rheometers (b) and (c), the torque sensor is located in the upper part of the machine.

the rotor, in the upper part, can move and measure the stress with the lower part (stator) fixed. In the strain-imposed rheometer (Figure 1.14 (c)) the lower part moves and the upper part allows to measure τ. Generally, the stress-imposed one is the more common because it is cheaper. But if one needs to measure mechanical properties at high frequency, it is better to use a strain-imposed rheometer to avoid the contribution of the motor inertia. In all cases the device imposes a rotation (resp. a torque) and measures the resulting torque (resp. deflection angle or speed). For each flow geometries, there are different conversion factors, applied by the rheometer software, to obtain the main rheological parameters (i.e. shear stress, deformation and shear rate from the torque and the angular velocity) and with which it calculates all the other viscoelastic parameters.

There exists two types of measurements: oscillation and rotational tests. Oscillation measurements give information about the viscoelastic behavior and the characterization of the undestroyed structure at rest (when performed at small deformation). Flow measurements (Section 1.3.3) are obtained with rotational measurements to investigate the flow behavior of the complex fluids under large deformation (Figure 1.18).

Coming back to Figure 1.14 (b), there are shown parallel disks (plate-plate), cone-plate and coaxial cylinders (Couette) geometries. A detailed review for each geometry can be found in [50]. Starting from flow measurements, parallel disks produce a linear variation of shear rate from zero at the center to a maximum at the edge, instead the cone-plate geometry maintains the same shear rate $\dot{\gamma}$ throughout the sample. In the Couette geometry the $\dot{\gamma}$ depends on the radial position, an average of the shear rate can be used when the ratio between the inner and outer radius is close to unity (narrow gap condition). For oscillatory measurements plate-plate or cone-plate geometries are usually used. For both a small amount of sample is required in comparison to the Couette geometry. For the plate-plate geometry it is easier to make the surfaces rough (e.g. stick sand paper to both sides) and for this reason it is used to avoid wall slip (Section 1.3.5). There are also many others complex geometries (i.e. helical, vane..) that make this instrument very versatile, although measurements can be difficult to interpret.

1.3.3 Rheological response of complex fluids

In Section 1.3.1 we defined the two ideal extreme behaviors, now we describe real fluids that are part of our daily life. These "complex fluids" exhibit an intermediate behavior between ideal solid and liquid. The transition from a solid to a liquid can be observed after a characteristic time or at large strain or deformation. Systems that strongly depend on time/frequency are defined as *viscoelastic* fluids and the systems whose properties mainly depend on the applied strain/deformation are defined as *yield-stress* fluids. Their properties can be investigated focusing on their linear behavior at "rest" (small amplitude oscillation measurements) or on their response to a continuous deformation (flow measurements).

Oscillation measurements

Viscoelastic fluids have both an elastic and a viscous responses that are quantified respectively by the storage modulus, G', and the loss modulus G''. Both quantities are frequency dependent.

To calculate these moduli, an oscillatory (sinusoidal) deformation (stress or strain) is imposed by a rheometer to the sample and the material response (strain or stress) is measured. As shown in Figure 1.15, δ is the phase angle or phase shift between the deformation $\gamma = \gamma_0 \sin(\omega t)$ and the response $\tau = \tau_0 \sin(\omega t + \delta)$.

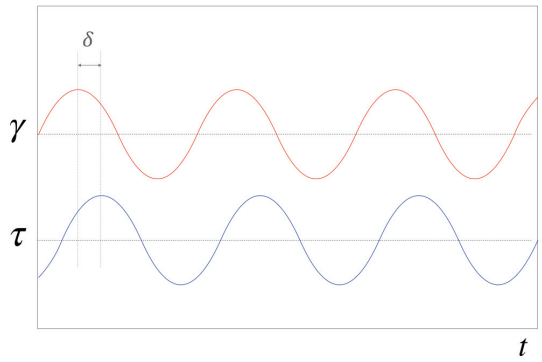

Figure 1.15 – Oscillatory deformation applied to the fluid γ and its response as shear stress τ. The phase angle between these two signals is δ.

If the stress and strain are in phase, we have a purely elastic material and if the phase lag is equal to $\pi/2$ we have purely viscous material. Viscoelastic materials show an intermediate behavior with a phase lag between 0 and $\pi/2$.

We can express the storage modulus G' and the loss modulus G'' as in Equations (1.21) and (1.22):

$$G' = \frac{\tau_0}{\gamma_0} \cos(\delta) \tag{1.21}$$

$$G'' = \frac{\tau_0}{\gamma_0} \sin(\delta) \tag{1.22}$$

We can also define the *shear complex modulus* G^* as the ratio between the complex stress τ^* and complex strain γ^*:

$$G^* = \frac{\tau^*(t)}{\gamma^*(t)} \tag{1.23}$$

Moreover G^* represents the complete response of a material to a periodic deformation: $G^* = G' + iG''$. The storage modulus G' describes the ability of the material to store energy upon deformation and release it when unloaded, this reversible deformation being typical of ideal solids. G' characterizes the elastic regime for all the complex fluids that, for a small range of deformations, act as an apparent solid. The loss modulus G'' instead represents the energy dissipation due to the internal friction linked to molecular motion.

A typical frequency sweep curve for a viscoelastic polymer (i.e. hydrophobic ethoxylated urethane HEUR associative polymer) is shown in Figure 1.16 [3]. In particular, G' and G'' are plotted as function

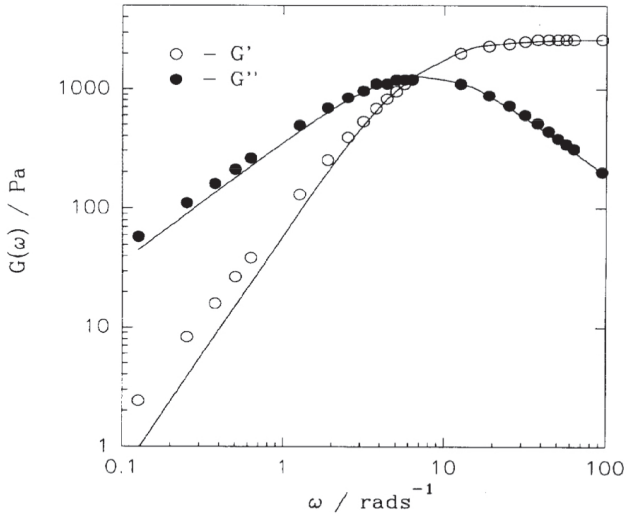

Figure 1.16 – Reproduced from Annable et al. (1993) [3]. Storage G' and loss G'' moduli as a function of the frequency ω, for a 7 % w/v HEUR (hydrophobic ethoxylated urethane) associative polymer. The solid lines are a fit to Maxwell model [46].

of frequency $\omega = 2\pi f$ and are perfectly described by the Maxwell model (solid lines), i.e. elastic spring connected in series with a viscous component [46].

For yield stress fluids (Section 1.3.4) instead, it is more interesting to trace the storage and loss modulus as a function of the applied strain γ, as shown in Figure 1.17.

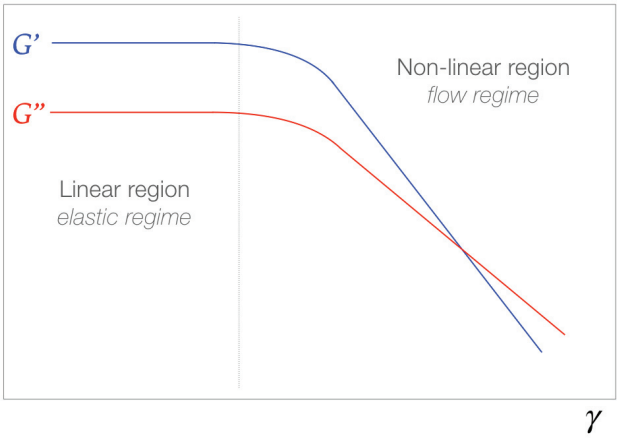

Figure 1.17 – Sketch from small amplitude oscillatory deformation. Storage G' and loss G'' moduli as a function of the deformation γ.

For gels at low strains, up to the end of linearity, G' is larger than G'' revealing the solid-like behavior of the system. In this linear region, at small deformations, both storage and loss moduli are constant with γ. At larger strains, the material starts to flow and both moduli drop dramatically until G'' becomes larger than G'. The system is in a non-linear regime with a liquid-like behavior. This kind of analysis defines the viscoelastic properties of the system "at rest" (small oscillatory deformation) characterizing the linear region in terms of G' and G'' and establishing the range in which we have a solid or a liquid like behavior. In general real fluids enter in this liquid regime for high values of deformation.

Flow measurements

The flow regime is characterized by the relationship between shear stress τ and the shear rate $\dot{\gamma}$. The *flow curve* is classically plotted as $\tau = f(\dot{\gamma})$ or as alternative $\eta = \tau/\dot{\gamma} = f(\dot{\gamma})$ as shown in Figure 1.18. Here, black lines represent the typical flow curves for both $\tau = f(\dot{\gamma})$ and $\eta = f(\dot{\gamma})$ for Newtonian fluids, red lines for shear thickening fluids, blue lines for shear thinning fluids and finally green line for yield stress (shear thinning) fluids.

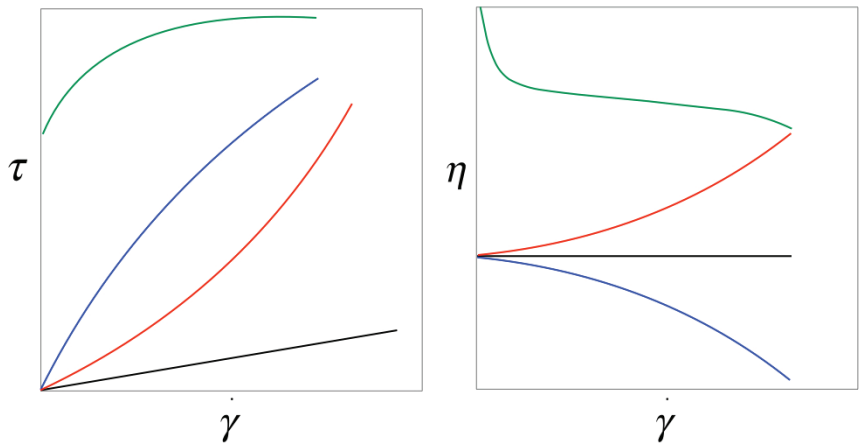

Figure 1.18 – Shear stress (τ) and shear viscosity (η) as function of the shear rate ($\dot{\gamma}$). Black lines represent Newtonian fluids, red lines shear thickening fluids, blue lines shear thinning fluids and green lines yield stress (shear thinning) fluids.

The Newtonian behavior for which $\tau = \eta\dot{\gamma}$, is observed for solvents such as water, oil, ethanol.... The majority of complex fluids are shear thinning, their viscosity decreases when the shear rate increases (blue lines in Figure 1.18). Shear thickening fluids are less common and the behavior is reverse, η increases with $\dot{\gamma}$ (red lines in Figure 1.18). Among shear thinning fluids, green lines in Figure 1.18 show a behavior typical for yield stress fluids. Above a certain critical stress, called yield stress τ_y, they flow and exhibit a shear thinning behavior. Below τ_y, there is no flow ($\dot{\gamma} = 0$). In fact they respond elastically. So depending on the applied stress they can exhibit a viscous, plastic or elastic behavior. This class of complex fluids will be detailed in the next Section 1.3.4.

1.3.4 Yield stress fluids

Yield stress fluids can be divided in *simple* yield stress fluids and *thixotropic* yield stress fluids [10].

Simple yield stress fluids are described under uniform flow in rheometrical geometries and without flow inhomogeneities. Uniform flow is defined by P. Coussot [16] as follows: "there exists a direction

along which the flow characteristics are identical in any plane perpendicular to this direction, the said direction can be specified by a straight line or a circular line; uniform flows are thus obtained through long straight conduits of any (constant) cross-section and in rotational geometries such as those used in rheometry (parallel disks, coaxial cylinders, cone and plate)". These simplifications allow a general description of yield stress fluids. The definition proposed by P. Coussot for yield stress is: "the stress associated with a steady flow at an infinitely small shear rate which, due to the finite deformation associated with the solid–liquid transition, would take an infinitely long time to reach"[16].

Yield stress fluids behave as a solid at rest until a critical deformation or a stress, called *yield stress*, for which the material starts to flow like a simple fluid. The peculiarity of these fluids is that they can recover their initial solid-like state and structure if left at rest. In these simplified conditions, simple yield stress fluids can be described with a continuous and monotonic constitutive equation: the Herschel-Bulkley law as in Equation (1.24) and sketched as in Figure 1.18 (green lines):

$$\begin{cases} \dot{\gamma} = 0, & \text{if } \tau < \tau_y \\ \tau = \tau_y + k\dot{\gamma}^n, & \text{if } \tau > \tau_y \end{cases} \tag{1.24}$$

where τ the shear stress, $\dot{\gamma}$ the shear rate, τ_y the yield stress, k the consistency and n the exponent of the power law; n is generally in the range of $[0.3-0.5]$ for simple yield stress fluids as carbopol gels, concentrated emulsions, kaolin suspensions [16]. With the same expression for $n=1$ we can obtain the Bingham fluids that have a linear shear stress on shear strain relationship i.e. clay suspensions, toothpaste, oil paint, molten chocolate etc... [5]. The typical values of shear rates and yield stress for simple yield fluids are respectively between 0.01 and 100 s^{-1} and 1 to 100 Pa [16].

Finally, for such systems, the more accurate method to characterize the value of the yield stress is a creep experiment in which different stresses are imposed and the resulting strain is measured. The smallest value of stress for which the system flows corresponds to the yield stress [75].

Thixotropic yield stress fluids have a discontinuous flow curve and a time dependent response. These materials show not only a yield stress, but also a critical shear rate, $\dot{\gamma}_c$. These suspensions, if $\dot{\gamma} < \dot{\gamma}_c$, cannot flow steadily in homogeneous conditions [10, 18]. Instead if $\dot{\gamma} > \dot{\gamma}_c$ a homogeneous flow is generally assured [10]. For thixotropic fluids the Herschel-Bulkley description is replaced by the discontinuous constitutive Equation (1.25) [10]:

$$\begin{cases} \dot{\gamma} = 0, & \text{if } \tau < \tau_y \\ \tau = k\dot{\gamma}^n, & \text{if } \tau > \tau_y \end{cases} \tag{1.25}$$

In jammed systems (volume fraction $\phi \approx 0.64$) many different materials show similar yielding properties. In fact in these highly packed suspensions the thermal motion has no significant role and the yield stress depends only to the network of interparticle contacts [14]. Adding attraction, these systems acquire a more complex dynamics, as in colloidal gel. In this case the yielding depends on the attractive interactions strength and the network rearrangements [70].

Generally yield stress materials show several flow inhomogeneities. The main flow heterogeneities (or artefacts) are detailed in the following Section 1.3.5.

1.3.5 Complex responses

Phenomena as *wall slip* and non uniform flow (i.e. inhomogeneities or *shear banding*) are typical of yield stress suspensions. This kind of artefacts affect the rheological measurements, invalidating the mechanical and flow characterization (i.e. yield stress, viscosity...). A general overview about yield stress fluids and their peculiarities i.e. artefacts are made by Coussot [16], Bonn et al. [10] and by Cloitre and Bonnecaze [14]. The velocity profiles across the gap (Couette geometry) corresponding to these artefacts are shown in Figure 1.19.

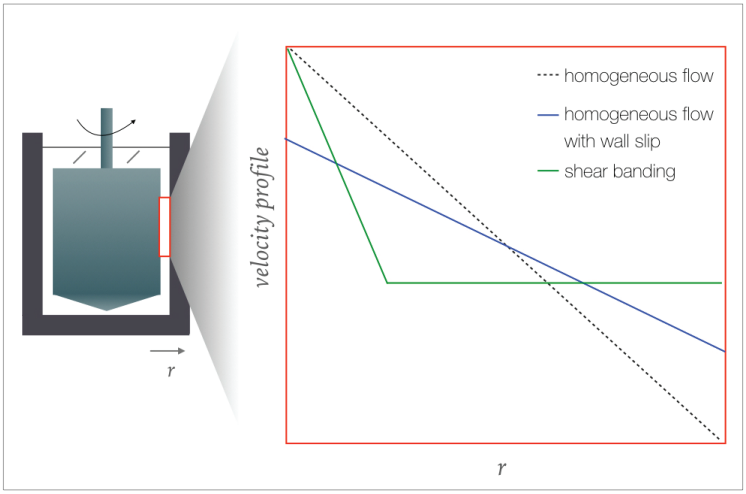

Figure 1.19 – Sketches of velocity profiles in a Couette geometry. Both homogeneous and inhomogeneous profiles (i.e. wall slip and shear banding) are showed along the gap.

Dashed line represents the velocity profile corresponding to a homogeneous flow. The blue line shows a homogeneous flow with slip at both walls and the green one, shear banding and slip at the stator wall. Both phenomena can occur at the same time. These two phenomena are detailed in the next sections. To detect and follow these inhomogeneities there are several techniques developed recently [10]. In particular Diffusion Wave Spectroscopy, (DWS) and Ultrasonic Speckle Velocimetry, (USV) are detailed in the next Materials and Methods chapter.

Wall slip

In Figure 1.19 we observe that the velocities at the walls (only the right wall for the shear banding profile) for the two solid lines differ from the case of homogeneous flow (dashed line). The no-slip boundary condition is not satisfied. As described by Bingham in 1922, this is mainly due to "a lack of adhesion between the material and the shearing surface. The result is that there is a layer of liquid, between the shearing surface and the main body of the suspension" [8]. In this thin lubricating layer between the suspension and the wall, the overall deformation is localized [14]. The physical origin of this wall slip phenomenon, for both rigid and soft particles, is well detailed by Cloitre and Bonnecaze [14]. The main mechanism proposed for rigid particles (Brownian or non-Brownian suspensions) are steric depletion— rigid particles cannot penetrate the wall, creating a thin layer ($\approx$ particle radius) with a different volume fraction comparing to the bulk— and particle migration due to the shear rate variation with the radial position in the Couette geometry.

For soft (deformable) particles, wall slip depends on roughness or surface chemistry. Both hydrophobic and hydrophilic surfaces determine the interaction at the solid boundaries. For hydrophobic surfaces, the weak attractive interaction results in a finite slip yield stress. Hydrophilic surfaces cause a repulsive interaction and a thin layer of water wet the surface, the system slips as soon as it is sheared. The signature of wall slip on the flow curve for a microgel suspension is showed in Figure 1.20.

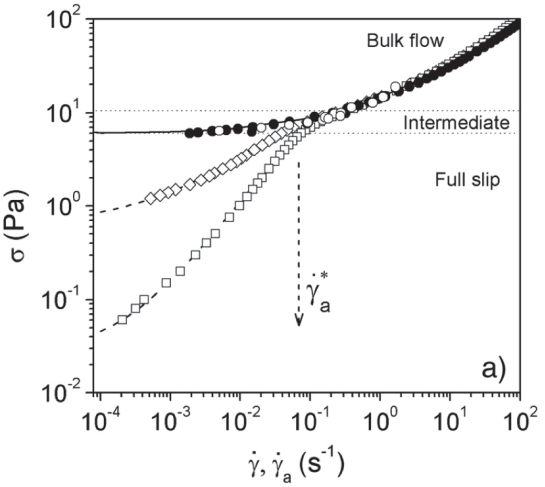

Figure 1.20 – Reported by [14, 63]. Generic signatures of wall slip represented for a concentrated microgel suspension in parallel plate geometry. a) Variations of the shear stress versus the true shear rate (no slip) or apparent shear rate (slip). When sheared with rough surfaces (•), the suspension exhibits a true yield stress and the flow curve is well described by the Herschel-Bulkley equation (-). With smooth polymer (◊) and glass surfaces (□), which are hydrophobic or hydrophilic respectively, the flow curves exhibits three regimes of flow. $\dot{\gamma}_a^*$ marks the onset of full slip; the equations of the dashed lines are of the form $\tau = \tau_s + k\,\dot{\gamma}_a^m$ with $\tau_s = 0.03$ and 0.6, $m = 0.92$ and 0.50 for the glass and polymer surfaces respectively. The local rheology data corrected from the effect of slip coincide with the flow curve in the absence of slip (○).

Three curves with different surfaces roughness and chemistry are compared. In particular, for high shear rate, all the flow curves coincide. Then below a certain value $\dot{\gamma}_a^*$, smooth surfaces lead to wall slip showing a kink in the flow curve and a slip yield stress $\tau_s < \tau_y$. At the contrary the flow curve obtained with the rough surface (full circles) follow the Herschel-Bulkley equation [14].

Another way to track the signature of wall slip is to verify the rheological dependency with the gap size. As shown in Figure 1.21 for the calcite colloidal suspension studied in our work, both smooth and rough surfaces show a gap-dependency of the elastic modulus (in the linear regime): G'_{lin} [47]. Increasing the gap size, the gap-dependency of the elastic modulus decreases, reaching a plateau. These results are in good agreement with the calculation made in the early work by Yoshimura and Prud'homme [72], reported for a parallel plates geometry in Equation (1.26). Upon increasing the gap width, h, the contribution of wall slip (slip velocity v_s) to the apparent deformation is reduced and consequently the apparent shear rate, $\dot{\gamma}_{\text{app}}$, approaches the effective one, $\dot{\gamma}_{\text{eff}}$.

$$\dot{\gamma}_{\text{app}} = \dot{\gamma}_{\text{eff}} + \frac{2v_s(\tau)}{h} \tag{1.26}$$

Emulsions and foams under flow show a similar gap-dependence [6]. To avoid wall slip different methods can be used. Firstly as already mentioned rough surfaces with a roughness comparable to the order

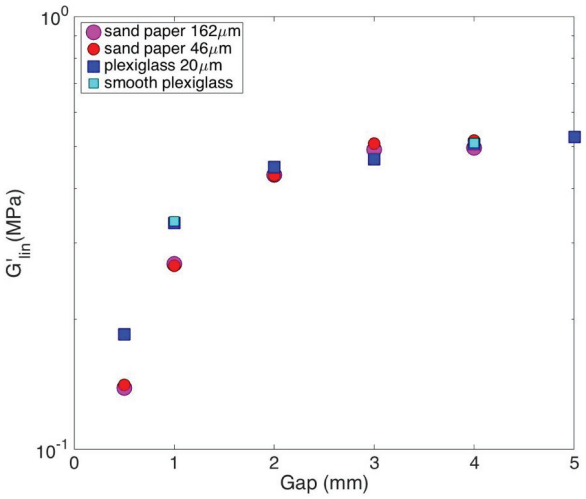

Figure 1.21 – Storage modulus in the linear regime G'_{lin} of calcite paste ($\phi = 20\%$) as a function of the gap size, for different smooth and rough surfaces.

of magnitude of the microstructure can be used [10], e.g. deformable objects (droplets in emulsions..). In this case the surface asperities avoid or destroy the lubricating film at the wall [14]. Another way is to use more specific geometries like vane or helical tools [14, 10]. Finally it is possible to play with the chemistry, tuning the surface interaction into attractive or repulsive, depending on the specific nature of the system [14]. In particular, the attraction between the surface and the complex fluid can lead to the suppression or reduction of slip.

Shear banding

Shear banding refers generally to flow inhomogeneities and occurs in disordered materials from complex fluids to rocks [7]. In particular, yield stress fluids (both simple and thixotropic) show stress heterogeneities.

In the case of simple yield stress fluids, flow inhomogeneities are not intrinsic and are linked only to stress heterogeneities resulting in shear localization [10]. Flow inhomogeneities can also depend on specific geometry conditions [10]. This happens for example, in a large gap of a Couette geometry, where consequently there is a large stress variation between the walls (i.e. rotor and stator). Therefore the lower stress value can be below the τ_y determining a non-shearing zone. Another example is a confined geometry with a gap width close to the characteristic microstructure size of the fluid, this can produce a local structure rearrangements showing a heterogeneous flow [10].

For thixotropic yield stress on the contrary, shear bands are intrinsic shear localization and geometry independent. They are linked to the existence of a critical shear rate as thixotropic yield stress fluids [10]. In Figure 1.19, the green line divides the gap region in two areas. The first is close to the rotor (left side) and flows like a liquid. The other one close to the stator is an arrested (or solid) region. This unstable flow corresponds to a range of critical strain between 0 and $\dot{\gamma}_c$ (corresponding to the sheared zone). The origin of shear bands for Brownian suspension is interpreted as a competition between spontaneous aging and shear-induced rejuvenation. Aging is linked with attractive interactions and promotes shear bands [10]. For dense non Brownian particles the origin of shear banding is linked to the competition between sedimentation, shear and volume fraction heterogeneities [10]. More details can be found in the review of Bonn et al. [10].

1.4 Calcite paste: a colloidal suspension with complex rheology

Calcite dispersed in water results in attractive interactions which promote aggregation of the calcite particles [2]. Literature on calcite suspensions focuses mainly on flow measurements, quantifying the variation of the yield stress τ_y (or the viscosity η) changing the particle interactions by superplasticizers addition [51, 53, 61, 19, 21, 20, 11].

In particular our calcite system is well described by DLVO forces, as detailed in Chapter 4. Then we assume that the non-DLVO forces presented above are not relevant in comparison to DLVO ones for the interactions between our calcite particles.

1.4.1 Zeta potential

At the microscopic level, Zeta Potential measurements determine the electrostatic (repulsive) contribution into DLVO calculation. The nature of interaction drives the final mechanical properties of suspension.

In the case of calcite paste, determining the Zeta potential is a complex problem. In the litterature in fact there is no consensus on both its value and sign. It is found to depend, among others, on pH, CO_2 pressure [55, 52, 27, 67], concentrations of solid calcite [65], specific surface area, concentration of other dissolved ions [61], and possible presence of impurities for natural calcite [69, 60]. An accurate and complete review of the Zeta potential on artificial and natural calcite is proposed by Al Mahrouqi et al. (2017) [1]. In Section 2.3.1 we propose a detailed explanation about the main chemical mechanisms on calcite surface, determining the value of Zeta potential.

1.4.2 Superplasticizers

Calcite suspensions are currently used [51, 61, 21, 20, 11] to mimic early age cementitious material, having surface and colloidal properties close to cement particles at the first steps of hydration i.e. specific surface area and particle size distribution [52].

In particular many studies [61, 21, 11] have investigated the role of superplasticizers on the rheology (i.e. flow properties) of calcite suspensions. The effects of superplasticizers in concrete is widely explained by R. Flatt in [31]. Superplasticizers are used to reduce the yield stress of concrete at constant solid content or to increase the solids content at constant yield stress, by steric repulsion between the grafted particles [68]. The adsorption of superplasticizers on cement particles reduces or eliminates the attractive interaction (van der Waals), that cause the yield stress.

Flatt and Bowen proposed a yield stress model for suspension called YODEL [32, 33]. This model can predict the yield stress of concentrated particulate suspensions taking into account volume fraction of solid, particle size and distribution, maximum packing, percolation threshold and interparticle forces. Dalas et al. [21] applied the YODEL to predict the fluidizing efficiency of superplasticizers (i.e. polycarboxylate grafted polyethylene oxide PCE) on calcite rheology (i.e. yield stress).

Bossis et al. [11] found a discontinuous shear thickening in presence of polyethylene oxide (PEO). In Figure 1.22 are showed two stress ramps for a calcite suspension $\phi = 0.68$ containing a polymer with a polymethacrylate backbone and side chains made of PEO called PCP 45.

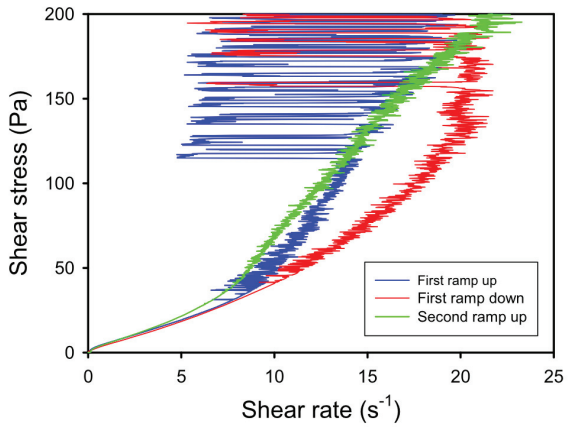

Figure 1.22 – Reproduced from [11]. First and second ramp of stress for a suspension at $\phi = 0.68$ with PCP45.

In this case, flow measurements made in a plate-plate geometry, for high calcite volume concentration, show hysteresis and large fluctuations for high shear stress i.e. bigger than 120 MPa. The instabilities of calcite flow, as show in Figure 1.22, suggest to couple rheological measurements with a setup allowing to follow the local dynamics as the Ultrasound Velocimetry (Section 2.2.4).

In our work, at first we evaluate the properties of pure calcite for both oscillation and flow measurements. Then we investigate the role of simple inorganic additives i.e. ionic species on mechanical properties of calcite suspensions. Results from these analysis are showed in Chapters 4 and 5.

1.4.3 Interactions

In literature there is no consensus also on the interaction forces between calcite surfaces. The attraction shown by calcite suspensions contradicts the recent results by Surface Force Apparatus (SFA) measurements [62, 27, 30], as shown in in Figure 1.23.

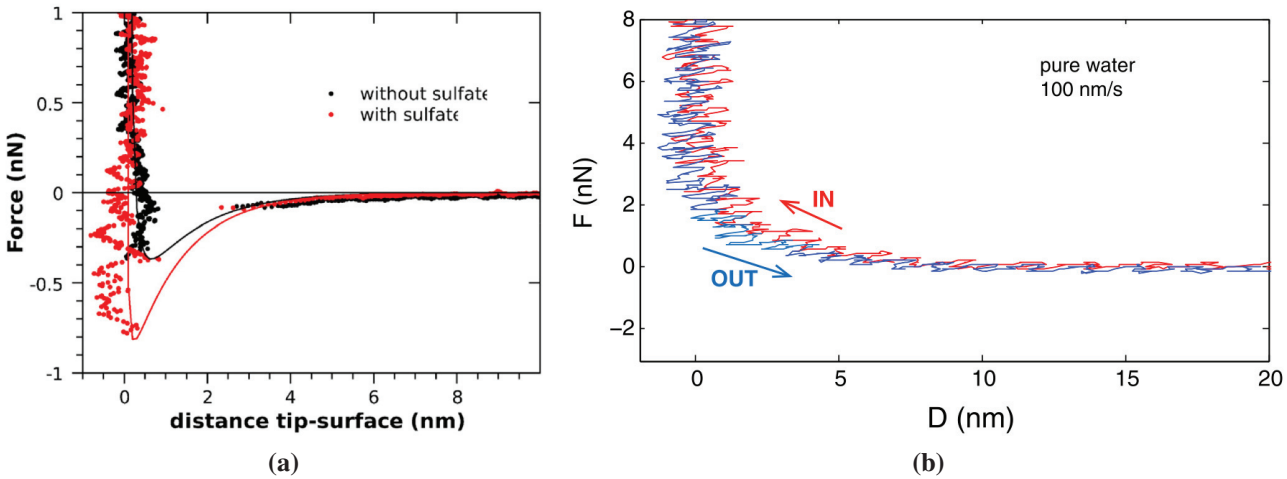

(a) (b)

Figure 1.23 – Reproduced from [61] (a) and [62] (b). (a) Effect of the sulfate ions on the force–distance curves between two calcite surfaces. Both curves show attraction. (b) Force curves measured using a single set of surfaces in water. In-runs are plotted as red lines, while out-runs are plotted in blue. A slight long-range repulsion out to approximately 5 nm is shown.

In particular in Figure 1.23 (a), Atomic Force Microscopy (AFM) force–distance curves between two calcite surfaces proposed by Pourchet et al. [61] exhibith attraction (with and without sulfate addition). Figure 1.23 (b) instead shows SFA force-curves between two calcite surfaces by Royne et al. [62] resulting in repulsion. Royne et al. [62] observed that this strong repulsive forces exceeds theoretical DLVO electric double layer. They attribute this repulsion at hydration forces acting between the highly hydrophilic calcite surfaces. Diao and Espinosa-Marzal [27] demonstrate that a mechanism of oscillatory forces (Section 1.2.6) occurs between two calcite surfaces due to the layering of water between them .

Very recent SFA work by Dziadkowiec et al. [30] underline the relevant role of roughness on the forces acting between the surfaces. They demonstrate that an increasing roughness results in a rise of the repulsive contact force. This is because of the higher mechanical work needed to compress multiple asperities on SFA loading. Moreover rugosity can decrease the cohesion between calcite grains weakening the system. Other theoretical studies in the group of F. Bresme (Imperial college, private communication) confirms the relevant role of rugosity in particle interactions.

A study of particle interaction on our calcite paste is addressed in Chapter 4.

Bibliography

[1] D. Al Mahrouqi, J. Vinogradov, and M. D. Jackson. Zeta potential of artificial and natural calcite in aqueous solution. *Advances in colloid and interface science*, 240:60–76, 2017.

[2] C. Allain, M. Cloitre, and M. Wafra. Aggregation and sedimentation in colloidal suspensions. *Physical review letters*, 74(8):1478, 1995.

[3] T. Annable, R. Buscall, R. Ettelaie, and D. Whittlestone. The rheology of solutions of associating polymers: Comparison of experimental behavior with transient network theory. *Journal of Rheology*, 37(4):695–726, 1993.

[4] J. W. Anthony, R. A. Bideaux, K. W. Bladh, and M. C. Nichols. *Handbook of Mineralogy, Volume V (Borates, Carbonates, Sulfates)*. Mineral Data Publishing, 2003.

[5] H. A. Barnes. The yield stress—a review or '$\pi\alpha\nu\tau\alpha\ \rho\varepsilon\iota$'—everything flows? *Journal of Non-Newtonian Fluid Mechanics*, 81(1-2):133–178, 1999.

[6] V. Bertola, F. Bertrand, H. Tabuteau, D. Bonn, and P. Coussot. Wall slip and yielding in pasty materials. *Journal of Rheology*, 47(5):1211–1226, 2003.

[7] R. Besseling, L. Isa, P. Ballesta, G. Petekidis, M. Cates, and W. Poon. Shear banding and flow-concentration coupling in colloidal glasses. *Physical review letters*, 105(26):268301, 2010.

[8] E. C. Bingham. *Fluidity And Plasticity*. Mcgraw-Hill Book Company,Inc, 1922.

[9] V. A. Bloomfield. Condensation of DNA by multivalent cations: considerations on mechanism. *Biopolymers*, 31(13):1471–1481, 1991.

[10] D. Bonn, M. M. Denn, L. Berthier, T. Divoux, and S. Manneville. Yield stress materials in soft condensed matter. *Reviews of Modern Physics*, 89(3):035005, 2017.

[11] G. Bossis, P. Boustingorry, Y. Grasselli, A. Meunier, R. Morini, A. Zubarev, and O. Volkova. Discontinuous shear thickening in the presence of polymers adsorbed on the surface of calcium carbonate particles. *Rheologica Acta*, 56(5):415–430, 2017.

[12] J. Bridge and R. Demicco. *Earth surface processes, landforms and sediment deposits*. Cambridge University Press, 2008.

[13] J. N. Butler. *Carbon dioxide equilibria and their applications*. CRC Press, 1991.

[14] M. Cloitre and R. T. Bonnecaze. A review on wall slip in high solid dispersions. *Rheologica Acta*, 56(3):283–305, 2017.

[15] P. Coussot. Rheophysics of pastes: a review of microscopic modelling approaches. *Soft Matter*, 3(5):528–540, 2007.

[16] P. Coussot. Yield stress fluid flows: A review of experimental data. *Journal of Non-Newtonian Fluid Mechanics*, 211:31–49, 2014.

[17] P. Coussot. *Rheophysics*. Springer, 2016.

[18] P. Coussot, J. Raynaud, F. Bertrand, P. Moucheront, J. Guilbaud, H. Huynh, S. Jarny, and D. Lesueur. Coexistence of liquid and solid phases in flowing soft-glassy materials. *Physical review letters*, 88(21):218301, 2002.

[19] F. Dalas. *Influence des paramètres structuraux de superplastifiants sur l'hydratation, la création de surfaces initiales et la fluidité de systèmes cimentaires modèles*. PhD thesis, Dijon, 2014.

[20] F. Dalas, A. Nonat, S. Pourchet, M. Mosquet, D. Rinaldi, and S. Sabio. Tailoring the anionic function and the side chains of comb-like superplasticizers to improve their adsorption. *Cement and Concrete Research*, 67:21–30, 2015.

[21] F. Dalas, S. Pourchet, A. Nonat, D. Rinaldi, S. Sabio, and M. Mosquet. Fluidizing efficiency of comb-like superplasticizers: The effect of the anionic function, the side chain length and the grafting degree. *Cement and Concrete Research*, 71:115–123, 2015.

[22] J. Dana, C. Hurlbut, and C. Klein. *Manual of Mineralogy*. Wiley international edition. Wiley, 1977.

[23] P.-G. de Gennes. Soft matter: the birth and growth of concepts. *Twentieth Century Physics. London*, 1593, 1995.

[24] P.-G. de Gennes and F. Brochard-Wyart. *Gouttes, bulles, perles et ondes*. Belin, 2015.

[25] M. De Jong, W. Chen, T. Angsten, A. Jain, R. Notestine, A. Gamst, M. Sluiter, C. K. Ande, S. Van Der Zwaag, J. J. Plata, et al. Charting the complete elastic properties of inorganic crystalline compounds. *Scientific data*, 2:150009, 2015.

[26] B. V. Derjaguin. Untersuchungen über die reibung und adhäsion, IV. *Colloid & Polymer Science*, 69(2):155–164, 1934.

[27] Y. Diao and R. M. Espinosa-Marzal. Molecular insight into the nanoconfined calcite–solution interface. *Proceedings of the National Academy of Sciences*, 113(43):12047–12052, 2016.

[28] M. Doi. *Soft Matter Physics*. Oxford University press, 2013.

[29] S. H. Donaldson Jr, A. Røyne, K. Kristiansen, M. V. Rapp, S. Das, M. A. Gebbie, D. W. Lee, P. Stock, M. Valtiner, and J. Israelachvili. Developing a general interaction potential for hydrophobic and hydrophilic interactions. *Langmuir*, 31(7):2051–2064, 2014.

[30] J. Dziadkowiec, S. Javadi, J. E. Bratvold, O. Nilsen, and A. Røyne. Surface forces apparatus measurements of interactions between rough and reactive calcite surfaces. *Langmuir*, 2018.

[31] R. Flatt and I. Schober. Superplasticizers and the rheology of concrete. In *Understanding the rheology of concrete*, pages 144–208. Elsevier, 2012.

[32] R. J. Flatt and P. Bowen. Yodel: a yield stress model for suspensions. *Journal of the American Ceramic Society*, 89(4):1244–1256, 2006.

[33] R. J. Flatt and P. Bowen. Yield stress of multimodal powder suspensions: an extension of the YODEL (Yield Stress mODEL). *Journal of the American Ceramic Society*, 90(4):1038–1044, 2007.

[34] L. J. D. Frink and F. van Swol. Solvation forces between rough surfaces. *The Journal of chemical physics*, 108(13):5588–5598, 1998.

[35] M. L. Gee and J. N. Israelachvili. Interactions of surfactant monolayers across hydrocarbon liquids. *Journal of the Chemical Society, Faraday Transactions*, 86(24):4049–4058, 1990.

[36] A. Gmira, M. Zabat, R.-M. Pellenq, and H. Van Damme. Microscopic physical basis of the poromechanical behavior of cement-based materials. *Materials and Structures*, 37(1):3–14, 2004.

[37] A. Grabbe and R. G. Horn. Double-layer and hydration forces measured between silica sheets subjected to various surface treatments. *Journal of Colloid and Interface Science*, 157(2):375–383, 1993.

[38] L. S. Hirst. *Fundamentals of Soft Matter Science*. CRC Press, 2013.

[39] K. Hosoi, T. Hashida, H. Takahashi, N. Yamasaki, and T. Korenaga. Low temperature solidification of calcium carbonate through vaterite-calcite wet transformation. *Journal of materials science letters*, 15(9):812–814, 1996.

[40] R. J. Hunter. *Foundations of colloid science*. Oxford university press, 2001.

[41] J. Israelachvili and H. Wennerström. Role of hydration and water structure in biological and colloidal interactions. *Nature*, 379(6562):219, 1996.

[42] J. N. Israelachvili. *Intermolecular and Surface Forces*. Academic press, 2011.

[43] B. Jönsson, A. Nonat, C. Labbez, B. Cabane, and H. Wennerström. Controlling the cohesion of cement paste. *Langmuir*, 21(20):9211–9221, 2005.

[44] B. Jönsson, H. Wennerström, A. Nonat, and B. Cabane. Onset of cohesion in cement paste. *Langmuir*, 20(16):6702–6709, 2004.

[45] P. Kékicheff and O. Spalla. Long-range electrostatic attraction between similar, charge-neutral walls. *Physical review letters*, 75(9):1851, 1995.

[46] R. G. Larson. The structure and rheology of complex fluids. 150, 1999.

[47] T. Liberto, M. Le Merrer, C. Barentin, M. Bellotto, and J. Colombani. Elasticity and yielding of a calcite paste: scaling laws in a dense colloidal suspension. *Soft matter*, 13(10):2014–2023, 2017.

[48] B. B. Mandelbrot. *The fractal geometry of nature*, volume 982. Freeman, San Francisco, 1982.

[49] G. S. Manning. Limiting laws and counterion condensation in polyelectrolyte solutions i. colligative properties. *The journal of chemical Physics*, 51(3):924–933, 1969.

[50] J. Mewis and N. J. Wagner. *Colloidal suspension rheology*. Cambridge University Press, 2012.

[51] N. Mikanovic and C. Jolicoeur. Influence of superplasticizers on the rheology and stability of limestone and cement pastes. *Cement and concrete research*, 38(7):907–919, 2008.

[52] N. Mikanovic, K. Khayat, M. Pagé, and C. Jolicoeur. Aqueous $CaCO_3$ dispersions as reference systems for early-age cementitious materials. *Colloids and Surfaces A: Physicochemical and Engineering Aspects*, 291(1-3):202–211, 2006.

[53] R. Morini. *Rhéologie de suspensions concentrées de carbonate de calcium en présence de fluidifiant*. PhD thesis, Université Nice Sophia Antipolis, 2013.

[54] I. L. Moudrakovski. Recent advances in solid-state NMR of alkaline earth elements. In *Annual reports on NMR spectroscopy*, volume 79, pages 129–240. Elsevier, 2013.

[55] P. Moulin and H. Roques. Zeta potential measurement of calcium carbonate. *Journal of colloid and interface science*, 261(1):115–126, 2003.

[56] P. Oswald. *Rhéophysique: Ou comment coule la matière*. Belin, 2005.

[57] R. Pashley. DLVO and hydration forces between mica surfaces in Li^+, Na^+, K^+, and Cs^+ electrolyte solutions: A correlation of double-layer and hydration forces with surface cation exchange properties. *Journal of Colloid and Interface Science*, 83(2):531–546, 1981.

[58] R. Pashley. Hydration forces between mica surfaces in electrolyte solutions. *Advances in Colloid and Interface Science*, 16(1):57–62, 1982.

[59] R. Pashley and J. Israelachvili. DLVO and hydration forces between mica surfaces in Mg^{2+}, Ca^{2+}, Sr^{2+}, and Ba^{2+} chloride solutions. *Journal of Colloid and Interface Science*, 97(2):446–455, 1984.

[60] A. Pierre, J. Lamarche, R. Mercier, A. Foissy, and J. Persello. Calcium as potential determining ion in aqueous calcite suspensions. *Journal of dispersion science and technology*, 11(6):611–635, 1990.

[61] S. Pourchet, I. Pochard, F. Brunel, and D. Perrey. Chemistry of the calcite/water interface: Influence of sulfate ions and consequences in terms of cohesion forces. *Cement and Concrete Research*, 52:22–30, 2013.

[62] A. Røyne, K. N. Dalby, and T. Hassenkam. Repulsive hydration forces between calcite surfaces and their effect on the brittle strength of calcite-bearing rocks. *Geophysical Research Letters*, 42(12):4786–4794, 2015.

[63] J. R. Seth, C. Locatelli-Champagne, F. Monti, R. T. Bonnecaze, and M. Cloitre. How do soft particle glasses yield and flow near solid surfaces? *Soft Matter*, 8(1):140–148, 2012.

[64] W.-H. Shih, W. Y. Shih, S.-I. Kim, J. Liu, and I. A. Aksay. Scaling behavior of the elastic properties of colloidal gels. *Physical Review A*, 42(8):4772, 1990.

[65] D. Siffert and P. Fimbel. Parameters affecting the sign and magnitude of the electrokinetic potential of calcite. *Colloids and surfaces*, 11(3-4):377–389, 1984.

[66] D. K. Smith. Soft matter science—a historical overview with a supramolecular perspective. *Supramolecular Chemistry: From Molecules to Nanomaterials*.

[67] P. Somasundaran and G. Agar. The zero point of charge of calcite. *Journal of Colloid and Interface Science*, 24(4):433–440, 1967.

[68] N. Spiratos, M. Pagé, N. Mailvaganam, V. Malhotra, and C. Jolicoeur. Superplasticizers for concrete: Fundamentals. *Technology and Practice*, 2003.

[69] N. Vdović. Electrokinetic behaviour of calcite—the relationship with other calcite properties. *Chemical Geology*, 177(3-4):241–248, 2001.

[70] J. Vermant and M. Solomon. Flow-induced structure in colloidal suspensions. *Journal of Physics: Condensed Matter*, 17(4):R187, 2005.

[71] G. Vigil, Z. Xu, S. Steinberg, and J. Israelachvili. Interactions of silica surfaces. *Journal of Colloid and interface science*, 165(2):367–385, 1994.

[72] A. Yoshimura and R. K. Prud'homme. Wall slip corrections for Couette and parallel disk viscometers. *Journal of Rheology*, 32(1):53–67, 1988.

[73] S. Yoshioka and Y. Kitano. Transformation of aragonite to calcite through heating. *Geochemical Journal*, 19(4):245–249, 1985.

[74] Zeta-Meter. Zeta-potential: A complete course in 5 minutes. *Zeta-Meter Inc*, pages 1–8, 1997.

[75] X. Zhang, E. Lorenceau, P. Basset, T. Bourouina, F. Rouyer, J. Goyon, and P. Coussot. Wall slip of soft-jammed systems: A generic simple shear process. *Physical review letters*, 119(20):208004, 2017.

[76] G.-T. Zhou, Q.-Z. Yao, S.-Q. Fu, and Y.-B. Guan. Controlled crystallization of unstable vaterite with distinct morphologies and their polymorphic transition to stable calcite. *European Journal of Mineralogy*, 22(2):259–269, 2010.

Chapter 2

Materials and methods

In this chapter, we describe all the materials and methods used during my PhD to obtain the results presented in this thesis.

Contents

2.1 Calcite powder and paste characterization

Calcite paste is obtained by dispersion of precipitated calcium carbonate (Socal 31, SOLVAY) powder in deionized water.

The data sheet of this product describes Socal 31 powder as an ultrafine precipitated calcium carbonate, white and odourless powder. The particle size ranges from 20 to 100 nm and the average particle dimension is around 70 nm. The crystal structure is rhombohedral with a cubic crystal shape. The density of Socal 31 is $\rho = 2710\,\mathrm{kg/m^3}$, its specific surface area 17 $\mathrm{m^2/g}$ and it is produced in Salin de Giraud, France.

To obtain calcite suspensions, the powder is dispersed in water with a vortex stirrer (Ultra Turrax TD300) used at mixing rate of 5800 rpm. As shown in Figure 2.1 the suspension appears white (as the powder) and it scatters light due to the mismatch of refractive index between water and calcite. The strong scattering suggests the existence of heterogeneities (i.e. aggregates) at the micrometric scale, larger than the initial nanometric particles [23]. Calcite paste behaves as a yield stress fluid as we can see in Figure 2.1, in fact it does not spread when in contact with a surface (both horizontal and vertical).

(a) **(b)**

Figure 2.1 – Images of calcite paste at an intermediate volume concentration $\phi = 20\%$. The spatula flat end size is ≈ 3 cm.

We define the volume concentration ϕ as the volume of calcite over the total volume. The mechanical characterization of calcite suspensions is made for a volume concentration range: $5 - 30\,\%$. This wide range of volume concentrations, for which we have properties between a solid and a liquid, suggests that we have a colloidal paste with attractive interactions. This aspect is detailed in Chapter 4. The pH of the pure calcite suspensions measured with a pH-meter HANNA edge on fresh paste, slightly increases with the volume concentration and is in the range of $8.7 - 8.9$, typical for calcite water suspensions in equilibrium with the atmosphere [7].

2.1.1 Inorganic additives

We first study the mechanical properties of pure calcite paste [25]. Then we investigate the role of simple additives on the mechanical properties (Chapter 4). We study the effects of the following species: calcium hydroxide ($Ca(OH)_2$), calcium chloride ($CaCl_2$), hydrochloric acid (HCl) and sodium hydroxide (NaOH). All the chemicals are from Sigma Aldrich. The solutions are prepared by dissolving all the mentioned species in deionized water, at the concentrations detailed in Table 2.1. As already shown in Section 1.1, the dissolution of calcite starts for a pH lower than 8. Deionized water has a pH of

7 or lower if it is in contact with the atmosphere, due to the dissolution of carbon dioxide from the atmosphere. At this pH value it is expected that calcite dissolves slightly upon dispersion. To avoid this effect, we conducted several measurements with calcium hydroxide solutions. In particular we found that the addition of 3 mM of $Ca(OH)_2$ into deionized water increases the pH of the initial solution up to 8, avoiding the initial calcite dissolution. For this reason, we added this quantity to all solutions (i.e. NaOH, $CaCl_2$ and HCl).

2.1.2 Microscopic characterization of calcite powder and paste

In order to characterize the calcite powder and have more information about the paste structure, we performed several characterizations: Cryogenic X-Ray Photoelectron Spectroscopy (CryoXPS), Electron microscopy: Transmission Electron Microscopy (TEM), Scanning Electron Microscopy (SEM), Atomic Force Microscopy (AFM). The CryoXPS and SEM measurements were made during my secondment at the University of Copenhagen (KU, Chemistry department) with Kim Dalby (SEM) and Nicolas Bovet (CryoXPS). All the others measurements were carried out at the ILM of Lyon with Nicholas Blanchard (TEM) and Agnès Piednoir (AFM).

Firstly, CryoXPS is a surface sensitive technique allowing to investigate the composition and the structure ($\approx$ 10 nm) of the electric double layer (Section 1.2.5). The centrifuged wet paste is quickly vitrified on a sample stub cooled down to -170° C and irradiated with a beam of X-rays while kept at -150° C [35]. An XPS spectrum is obtained by measuring the intensity of electrons ejected from the surface by the X-rays at a given kinetic energy (KE). Then the binding energy (BE) of these electrons are calculated as $BE = E_{X-ray} - KE$ [35]. We used binding energies which are specific of each element, to determine the composition of the surface, a few nm solid and 1-2 nm of solution. A typical XPS spectrum for the C 1s peak (i.e. binding energy reference for a thin surface carbon layer [17]) obtained for a dried pure calcite paste is shown in Figure 2.2. Two peaks constitute the spectrum, the main one at 290.1 eV (92 %) corresponds to the carbonate group (-CO_3, i.e. $CaCO_3$) [40] and the second one at around 285.5 eV (8 %) represents the generic bond between two carbons (i.e. organic impurities). Due to the high level of the calcite peak, we consider our calcite as rather pure.

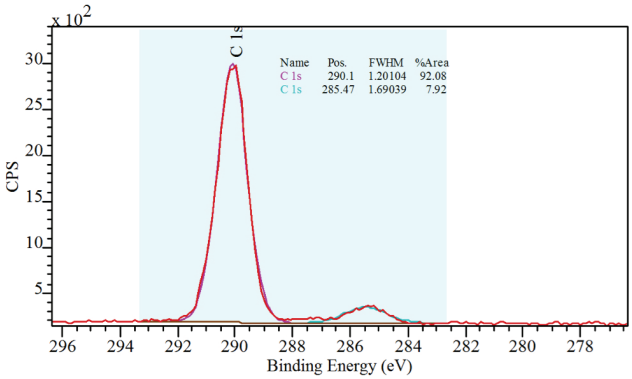

Figure 2.2 – Carbon 1s XPS spectrum for pure calcite dried paste. The first peak (92%) is attributed to the carbonate group -CO_3 bond. The second one (8%) is the generic bond between two carbons.

Then optical, electron and atomic force microscopy techniques are used to characterize the microstructure of our paste. A very general outline of the techniques is given before going on to the measurement details. Standard (optical) microscopy uses white visible light and a system of lenses to produce

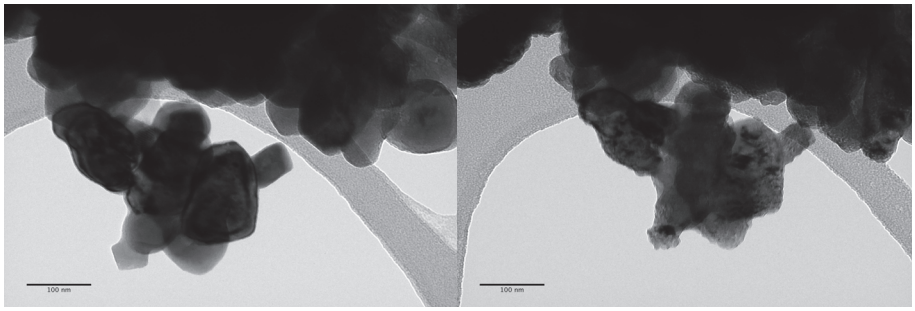

(a) **(b)**

Figure 2.3 – TEM images of calcite powder. (a)-(b) Images of the same area. Image (b) was acquired less that one minute after image (a). Scale bar equal to 100 nm. (a)-(b) Images acquired at 80 kV.

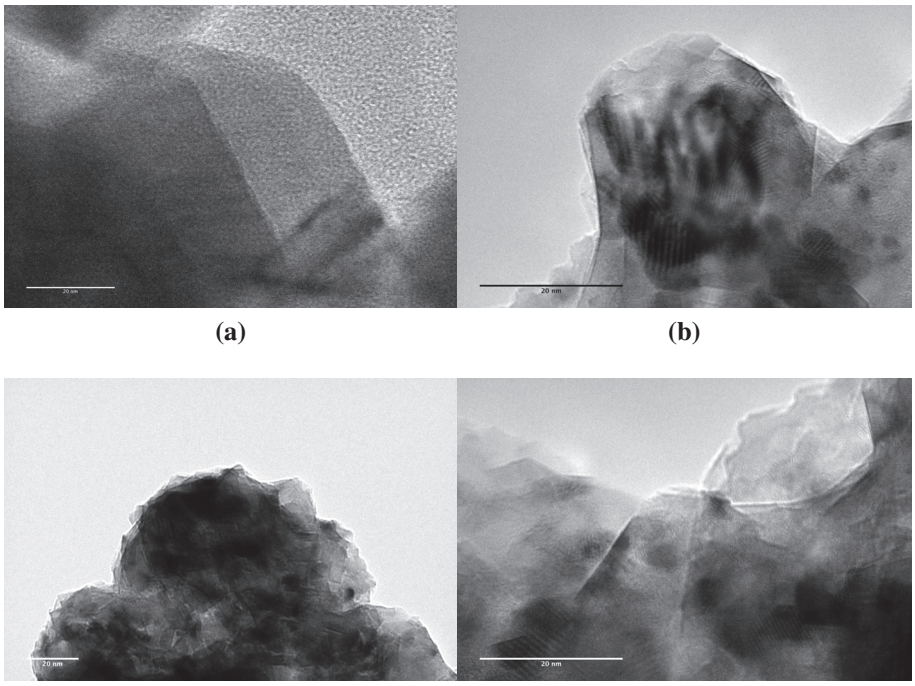

(a) **(b)**

(c) **(d)**

Figure 2.4 – TEM images of pure calcite powder. A small amount of particles are suspended in ethanol and one drop of the resulting suspension is placed on a copper grid. Scale bar equal to 20 nm. (b)-(d) Images acquired at 80 kV or 120 kV for (a).

a magnified image of the specimen. The limitation of this technique is the resolution which is given by the light wavelength [34].

Electron microscopy instead uses a beam of accelerated electrons to create an image of the specimen. Due to the short electron wavelength, electron microscopy can image the surface, generally covering a size range from few millimiters to fractions of nm (in classical TEM) [44].

In particular Scanning Electron Microscopy (SEM) is based on inelastically scattered electrons, focusing on sample surface and composition (i.e. morphology) with a maximal resolution of a few nanometers [44].

Transmission Electron Microscopy (TEM) instead is based on transmitted electrons and provides the details about the internal composition of the sample (i.e. morphology, grain boundaries, defects..).

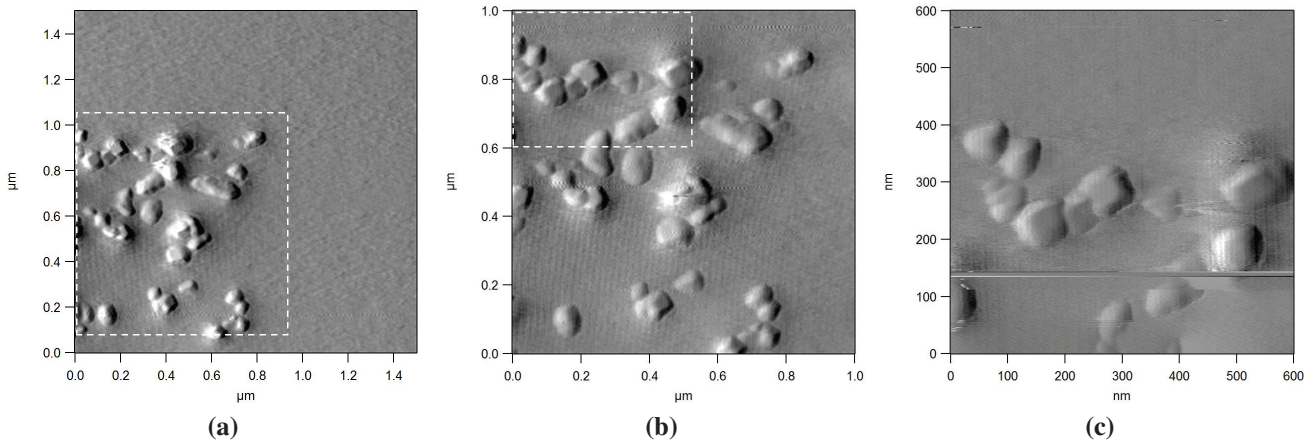

Figure 2.5 – AFM error signal images of calcite powder. Particles are fixed directly on the glass surfaces with a double tape. From (a) to (c), zoom in the outlined white area.

The maximal resolution depends on both microscope mode and use and is around a fraction of nm [44].

Atomic Force Microscopy (AFM) or scanning probe microscopy is constituted by a cantilever with a sharp tip which scans systematically across a sample surface to make force measurement, imaging, or manipulation. AFM can reach a very high resolution on the order of a fraction of nanometer [6], depending on the tip size.

Now we turn to the characterization of the powder and the paste. Transmission Electron Microscopy (TEM) images were acquired to obtain information on the shape of the calcite particles. The results are showed in Figures 2.3 and 2.4. In order to image the sample by TEM, a very small quantity of calcite powder is dispersed in ethanol and a drop of this suspension is dropped on to a holey carbon film supported by a 3.05 mm diameter 400 mesh copper grid. The point-to-point resolution of the JEOL 2100 TEM operated at 120 kV is 0.3 nm. The atomic step of calcite is also 0.3 nm [39]. The resolution of TEM can therefore display the calcite surface condition. We operate with a nominal magnification in the range of 40kx to 150kx, and a beam energy of 80 or 120 keV. Images (a) and (b) of Figure 2.3, are acquired successively (after less than a minute) with the same operating conditions. Comparing these two images, we can easily notice that the surface of the particles has been altered. In fact, the beam damaged the calcite surface by making it rougher. In Figure 2.4, we thus rely on the images acquired in a very short exposure time for which we can clearly distinguish atomic facets i.e. straight lines interpreted as the edge of the rhomboedral structure. Assuming that the time of exposition of the TEM beam damaged only partially the surface, we can consider that our particles have facets with approximately smooth surfaces. This aspect is crucial in the analysis of particle-particle interaction, as detailed in Chapter 4. From these images, we can also estimate the radius of curvature R$\sim$10 nm of the edge of the particles.

Another technique used to verify the surface condition and in particular to confirm the observations made with the TEM measurements (i.e. smooth surface with atomic facets), is AFM. A small quantity of calcite powder has been spread on a reticulated double tape, previously placed upon a glass microscope slide. In our measurement, the AFM works in “intermittent contact” mode to limit the lateral forces between the tip and the calcite nano-crystals. The tip, with a radius of curvature of about twenty nanometers, scans the surface and line by line provides its topographic map. Figure 2.5 shows three images: (c) is a zoom of (b) which is a zoom of (a) as outlined by white areas. All are “error signal”

images. The error signal is the deviation from the setpoint of the feedback loop and it highlights the contrasts and the shapes of small details. On these images, we can observe particles which are fixed as they fell on the tape. They do not necessarily have a flat facet parallel to the support and may have sunk more or less into the adhesive of the tape. From Figure 2.5, despite the small particle size of our nano-calcite, we can say that some of particles are parallelepipeds, with dimensions larger than 50 nm. They appear rounded on the image because of the convolution between the particles and the tip, whose dimension is close to the size of the nano-crystals. This artifact makes it difficult to define the shape of objects. But in AFM, the resolution in z (vertical) direction does not depend on the tip size, and is $\approx$10 nm. We therefore conclude that, (at the scale of $\approx$ 10 nm), the facets observed are not rough and could be rectangular crystal plane. All of these observations are in good agreement with the TEM results.

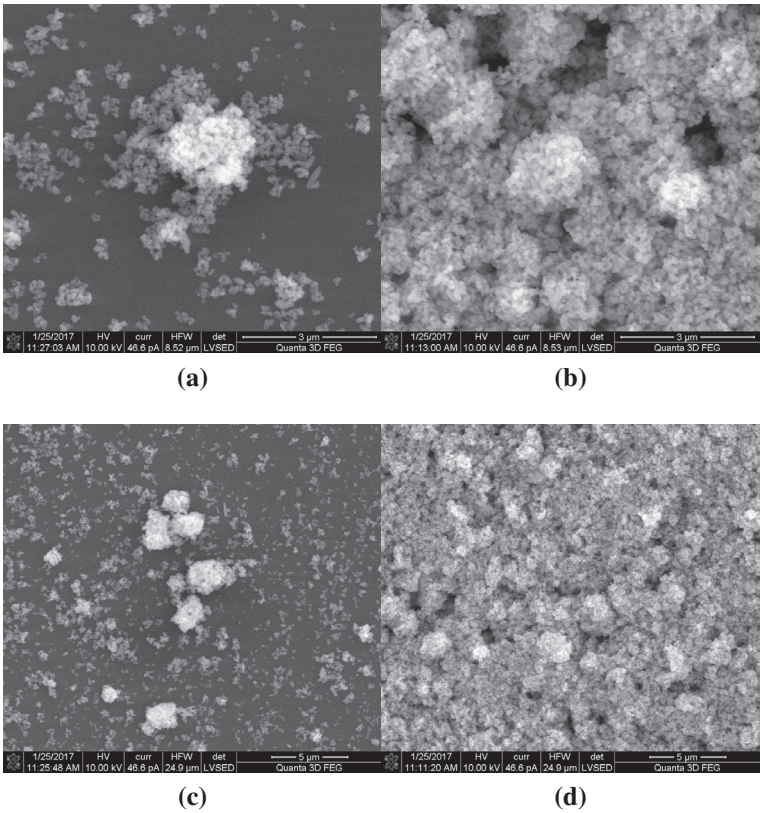

Figure 2.6 – SEM images of pure calcite paste (ϕ=20%). Scale bar equal to 3 μm for (a) and (b) and 5 μm for (c) and (d).

To study how the particles organize in the paste, we used SEM and optical microscopy images. A thin sheet of a calcite fresh sample is pressed between two microscope slides and imaged. SEM images are made with calcite suspension at $\phi = 20\%$. Figure 2.6 shows the morphology of pure calcite aggregates at the micron scale. In particular, Figure 2.6 (a) and (c) represent the less crowded area of the dried sample that still shows a high quantity of nano calcite primary particles. In particular in these two images, aggregates of particles around $\approx 1-2\,\mu$m are easily identifiable. Using Figure 2.6 (b), we can calculate a typical particle size distribution. Using the software imageJ, within 100 particles the maximum measured size is 125 nm, the minimum one is 22 nm and the mean 75 nm.

Figure 2.7 shows the cumulative distribution of calcite particle size from which we can extrapolate

the intercepts for 10 %, 50 % and 90 % as D10= 56 nm, D50= 73 nm and D90= 96 nm. This estimation matches very well with the particle dimension provided by SOLVAY (average diameter 70 nm).

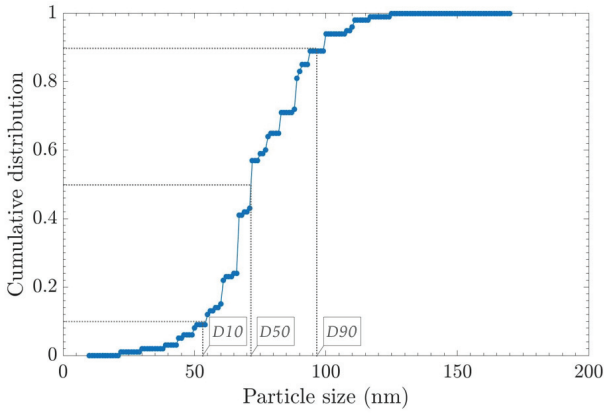

Figure 2.7 – Cumulative distribution of calcite particle size (D50=73 nm).

Finally, optical microscopy on calcite paste at $\phi = 10\,\%$ (Figure 2.8) shows the presence of big aggregates. The more common aggregate size is $\approx$ 10-30 μm as shown in Figure 2.8 (a) and (b). A few very large aggregates (100-200 μm) are also detected (Figure 2.8 (c) and (d)).

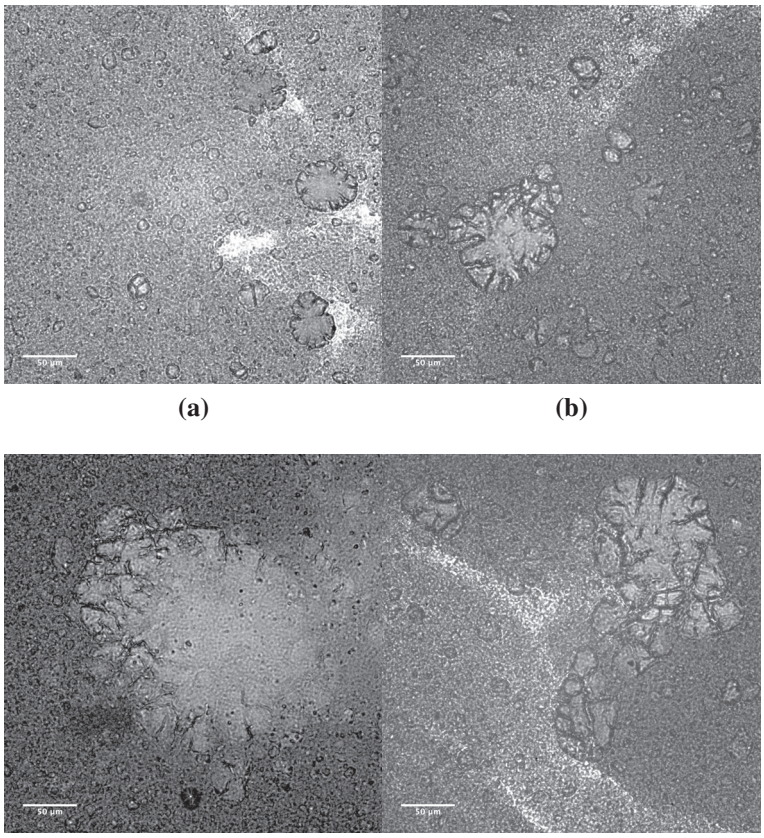

Figure 2.8 – Optical microscopy images of a pure calcite paste $\phi = 10\,\%$. Images (a) and (b) show the most characteristic aggregate-size found. Bigger aggregates as in (c) and (d) are more rare. (a)-(d) Scale bar equal to 50 μm.

To sum up before moving to rheological measurements, we have verified the purity of the powder by CryoXPS measurements. Then the size and the shape of particles are observed by optical, electron and atomic microscopy. The detected atomic facets are in line with the rhombohedral geometry. We calculate a mean particle diameter which confirm the size of $\approx$ 70 nm. Moreover, particles organize as micron-size aggregates ($\approx$ 10-30 μm), and sometimes form very few large clusters ($\approx$ 100-200 μm).

2.2 Rheological measurements and local shear measurements

In this section, we describe the rheological tests used to characterize macroscopically the mechanical properties of the paste.

First, we performed oscillation tests to obtain the viscoelastic properties of the paste with a classical rheometer in a plate-plate geometry. To characterize the homogeneity of the deformation, we use Diffusion Wave Spectroscopy (DWS), an optical technique which we briefly introduce.

Second, we investigate the flow behavior of the suspensions, using a Couette geometry coupled with Ultrasonic Speckle Velocimetry (USV). This setup allows to record velocity profiles inside the gap at the same time as the rheological measurements. More details of the protocols and the techniques are given in the following sections.

2.2.1 Viscoelasticity

Rheological experimental setup

To characterize the viscoelastic properties of calcite suspensions, oscillatory deformations are imposed by a stress-controlled rotational rheometer, Anton Paar MCR 301 (Figure 1.14). We opt for a plate-plate geometry with an upper (respectively lower) plate diameters of 36 mm (respectively 64 mm). Samples are protected with a closed moisture chamber to avoid drying. The width of the gap between the plates ranges from 0.5 to 5 mm. For low volume concentration, $\phi \leq 10\%$, the optimal gap (and the maximum gap reachable) is 1.5 mm. For gap width bigger than 1.5 mm, the suspension spreads on the lower plate and looses the contact with the upper plate. Varying the gap width between 1 and 1.5 mm we obtain the same rheological results. For high volume concentration, $\phi \geq 15\%$, the maximum reachable gap width is 4 mm. To limit the influence of slip, we always choose a gap width as large as possible and for which we have checked that the results are gap independent (Section 1.3.5). In all cases, the gap dimension is larger than the typical size of aggregates formed by calcite particles (Figure 2.6). We also study the effects of different surface plates as shown in Figure 1.21. The final choice is a plate covered by sand papers with typical roughness of 46 μm (P320). These optimal conditions (i.e. gap and rugosity) are used to avoid slip phenomena. We detail the complete study of both gap and surface influence on rheological measurements in Section 3.1 [25]. Moreover, we verify the homogeneity of shear deformation in the linear regime (i.e. at low γ), using an optical technique called Diffusion Wave Spectroscopy, presented in Section 2.2.2.

Oscillation test protocol

We use two protocols, α and β constituted by the same three steps: *pre-shear* (PS), *time structuration* (TS) and *amplitude sweep* (AS). As shown in Figure 2.9 the difference between the two protocols lies in

the duration of the time structuration step. It is typically 5 min for α and 10 h for β.

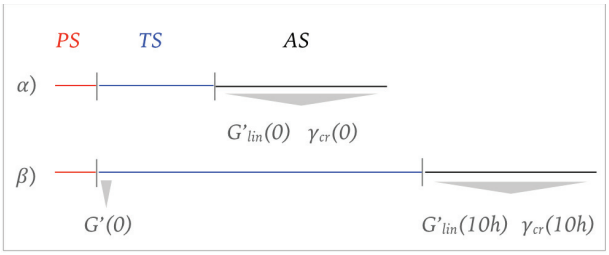

Figure 2.9 – Descriptions of the protocols used to measure viscoelasticity. Pre-shear (PS), time structuration (TS) and amplitude sweep (AS). Arrows indicate quantities extracted from each step.

More precisely, the *pre-shear* consists in a one minute imposed shear rate of $\dot{\gamma} = 10\,\mathrm{s}^{-1}$, in order to start all experiments with comparable initial conditions.

During the *time structuration*, a small and constant deformation of $\gamma = 0.01\,\%$ is imposed, at frequency equal to $f = 1\,\mathrm{Hz}$. The system, thanks to this low value of deformation, can restructure and rebuilt the aggregates that may have been destroyed by the pre-shear. This recovering is confirmed by the increase of G' just after the pre-shear step, ending in a constant plateau value (for pure calcite) after one minute, as shown in Figure 2.10.

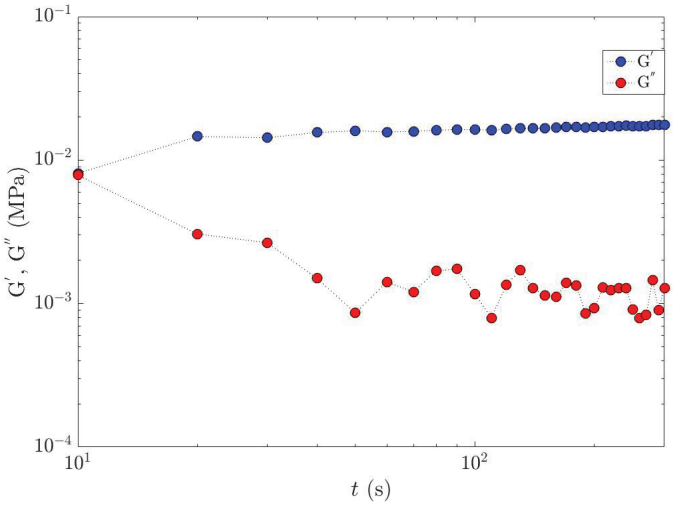

Figure 2.10 – Short time structuration step: evolution of the storage and loss moduli, G' and G'' for a pure calcite suspension (ϕ=10 %) just after a pre-shear of 1 min at $\dot{\gamma} = 10\,\mathrm{s}^{-1}$.

As already mentioned, this resting step can have two different durations: *a)* 5 min or *b)* 10 h. For protocol α the intent of the time structuration step is to give enough time to the sample to restore the initial sample conditions after the strong shear. For protocol β, the aim is to follow the time evolution of the sample in contact with the atmosphere. In this step we recorded the temporal evolution of the values of the storage and loss moduli, G' and G'', as shown in Figure 2.11.

The final step, the *amplitude sweep*, consists in an oscillatory deformation at imposed frequency ($f = 1\,\mathrm{Hz}$) with an increasing strain, $\gamma_0 = 0.001 - 10\,\%$, or an increasing stress in the range of $\tau = 1 - 3000\,\mathrm{Pa}$.

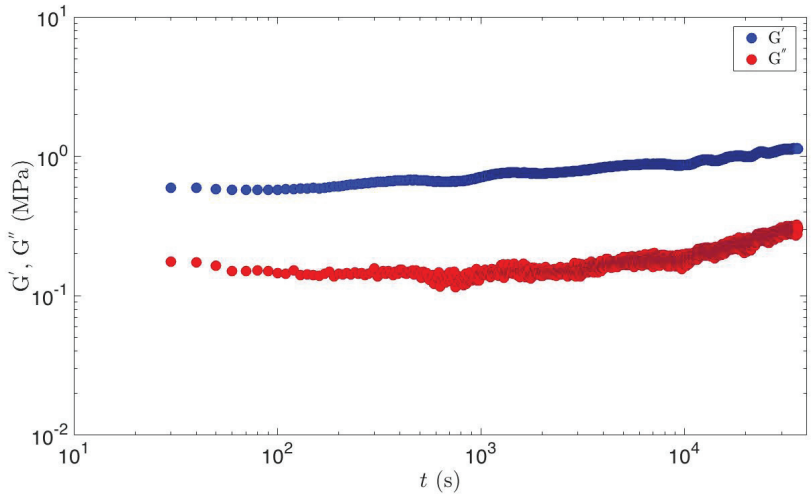

Figure 2.11 – Long time structuration step: evolution of the storage and loss moduli, G' and G'' for a pure calcite suspension (ϕ=20 %) just after a pre-shear of 1 min at $\dot{\gamma} = 10\,\mathrm{s}^{-1}$.

Figure 2.12 shows the typical amplitude sweep curve for controlled strain or stress. For both curves the storage and the loss moduli, G' and G'', are plotted as a function of the deformation γ. The two curves are constant in the linear regime (low γ). Beyond linearity small increments of applied stress correspond to large variations of measured strains. This explains why very few points are measured for the stress-imposed protocol ($\gamma > 10^{-2}$ %). However, working with a stress-imposed rheometer, the resulting curves are less noisy for stress controlled measurements, especially at low strains, and the entire measurement is also less time consuming (no rheometer feedback). Since we are interested in the characterization of the end of linearity (arrow in Figure 2.12), we have mostly used the stress controlled protocol.

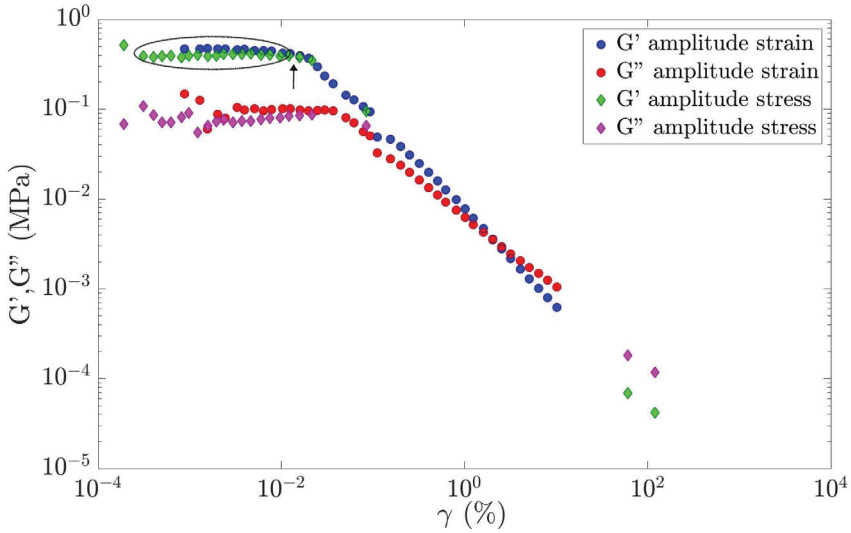

Figure 2.12 – Typical amplitude sweep ($\phi = 20$ % and $f = 1$ Hz): storage and loss moduli, G' and G'', as a function of the deformation γ. The circled region denotes the linear storage modulus G'_{lin} and the arrow indicates the end of linearity as $\gamma = \gamma_{\mathrm{cr}}$. We show results obtained at both controlled stress (diamonds) and strain (circles).

Sample	α	ϕ_α **(%)**	β	ϕ_β**(%)**
Pure	•	5-30	•	10-20
3 mM **Ca(OH)**$_2$	•	20	•	10-20
15 mM **Ca(OH)**$_2$	•	20	•	10-20
30 mM **Ca(OH)**$_2$	•	20	•	10-20
50 mM **Ca(OH)**$_2$	•	20	•	10-20
100 mM **Ca(OH)**$_2$	•	20		
1 mM **HCl** + 3 mM Ca(OH)$_2$	•	20		
5 mM **HCl** + 3 mM Ca(OH)$_2$	•	20		
50 mM **HCl** + 3 mM Ca(OH)$_2$	•	20		
100 mM **HCl** + 3 mM Ca(OH)$_2$	•	20	•	20
47 mM **CaCl**$_2$ + 3 mM Ca(OH)$_2$	•	20		
97 mM **CaCl**$_2$ + 3 mM Ca(OH)$_2$	•	20		
94 mM **NaOH** + 3 mM Ca(OH)$_2$	•	10-20	•	10-20

Table 2.1 – List of all the tested samples. Columns α and β indicate the protocol applied to the sample. ϕ_α and ϕ_β columns show the tested volume concentration range in each protocol.

In particular, from Figure 2.12 we can obtain the quantities of interests for our further analysis which are the *linear storage modulus*, G'_{lin} and the *critical strain*, γ_{cr}. At low strains, we have a linear regime in which both moduli, G' and G'', are constant with γ (elastic-like behavior). Moreover the storage modulus G' is typically one order of magnitude larger than the loss modulus G'', revealing the solid-like behavior of the pastes. In this plateau regime, circled in Figure 2.12, the storage modulus is defined as linear storage modulus (G'_{lin}). This value is a measure of the rigidity of the system. At larger strains, both moduli drop dramatically, $G' \approx G''$ and the material yields and becomes liquid-like. To characterize the onset of plasticity, we extract the strain at the end of linearity denoted as γ_{cr} (critical strain). This point, marked with an arrow in Figure 2.12, corresponds to a storage modulus which is $10-15\,\%$ lower than the value in the elastic regime G'_{lin}. We also denote $\tau_{\text{cr}} = G'_{\text{cr}}\,\gamma_{\text{cr}}$ the corresponding critical stress.

In Table 2.1 we summarize the experimental measurements. For each sample, the protocol used is specified (α or β) with the corresponding volume concentration range ϕ_α or ϕ_β. In particular, for protocol α four repeated measurements were performed for each concentration, with a new sample loading for each measurement. For protocol β, we performed only one measurement due to their long duration (10 h). The mechanical characterization of pure calcite paste with protocol α and $\phi_\alpha = 5-30\,\%$ constitutes the object of the Chapter 3. All other data are analyzed in Chapter 4, where we investigate the influence of specific ions on calcite surface interactions and their impact on calcite paste rheology.

2.2.2 Diffusive Wave Spectroscopy

During oscillation measurements, the local shear dynamics is characterized with an optical technique called Diffusion Wave Spectroscopy (DWS), briefly introduced in this section.

The main reference for this section is the seminal article of Pine et al. (1988) [31]. In the following the DWS technique is briefly outlined together with the experimental setup used in our experiments. DWS was born out of necessity to extend classical dynamic light scattering (DLS) to thick (opaque) systems which exhibit multiple scattering. Both techniques exploit the ability of suspensions (i.e. colloids, foams, emulsions...) to scatter light revealing interesting information about their dynamics.

The light passes through the suspension, its path is deviated as it meets the particles that have a size

comparable with the light wavelength (≈ 500 nm).

The multiple scattering of light is usually described by a random walk of step length ℓ^* e.g. $\ell^* \approx 200\ \mu$m for 0.5 μm polystyrene spheres in water at $\phi = 1$ % [31]. The various light paths interfere to form a speckle pattern i.e. a random interference figure.

The temporal evolution of the speckle is a signature of the sample dynamics and it is quantified through a temporal autocorrelation function. Originally, DWS "exploits the diffusive nature of the transport of light in strongly scattering media to relate the temporal fluctuation of multiply scattered light to the motion of the scatterers" [31]. So DWS allows the calculation of the particles diffusion coefficient inside opaque mediums. The autocorrelation function, in this case, is calculated as the temporal average of a single speckle. A natural evolution of this technique consists in time and space resolved measurements using multi-speckle averaging [8, 13, 24].

DWS setup and protocol

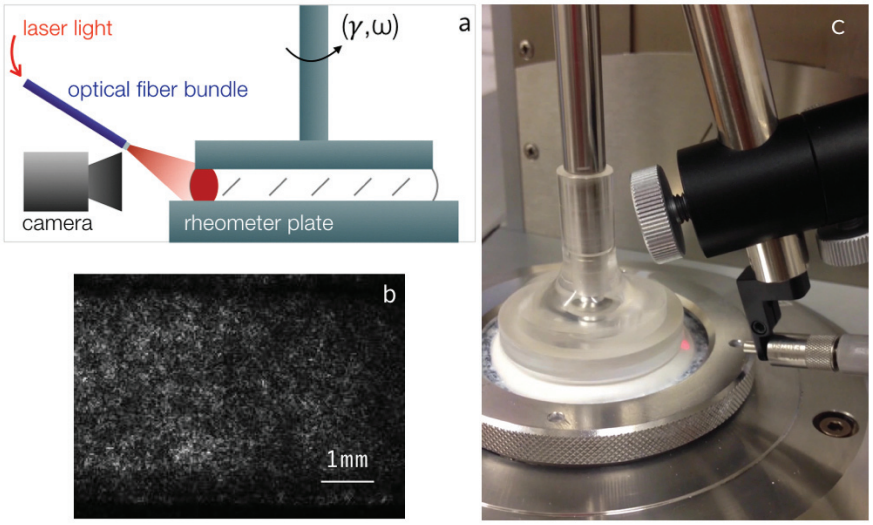

Figure 2.13 – Sketch (a) and photograph (c) of the experimental setup. (b) Image of the sample with the speckle pattern created by the light backscattered from the sample.

As already mentioned in Section 2.2.1, diffusive wave spectroscopy is used in order to characterize the local shear dynamics across the rheometer gap for amplitude sweep measurements on pure calcite paste. The experimental setup is shown in Figure 2.13. It corresponds to a backscattering geometry. Coherent light from a He-Ne laser (wavelength $\lambda_0 = 632$ nm) is sent onto the side of the rheometer cell thanks to an optical fiber bundle. The illuminated zone is a few millimeters wide and we image the sample surface from the side with a camera (IDS UI) and objective. A speckle interference pattern is created (Fig. 2.13b), whose temporal evolution reveals the relative motion of light scatterers, hence the inner dynamics of the sample, namely the shear oscillations. Videos are made during amplitude sweep experiments similar to the ones used for the elasticity measurements (last step of protocol α). The sample oscillation is $f = 10$ Hz, while the video acquisition frequency is fixed at 50 Hz, with an exposure duration of 20 ms.

Protocol To analyse the recordings, we use time and space resolved correlation spectroscopy [8, 13, 24]. After background subtraction, we first define rectangular areas of interest (AOI) of area 20×200 square pixels (approximately 0.6×6 mm^2) at different positions z across the gap (see Figure 2.14). For each area, we calculate at each time the following autocorrelation function:

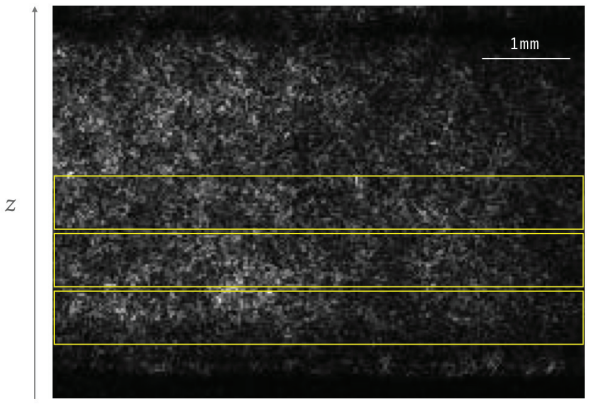

Figure 2.14 – Images of a speckle pattern for which we outlined (in yellow) examples of rectangular areas of interest at various positions z across the gap.

$$F(t,\Delta t,z) = \frac{2\langle I_t I_{t+\Delta t}\rangle - \langle I_t\rangle^2 - \langle I_{t+\Delta t}\rangle^2}{\langle I_t^2\rangle + \langle I_{t+\Delta t}^2\rangle - \langle I_t\rangle^2 - \langle I_{t+\Delta t}\rangle^2} \tag{2.1}$$

where I_t is the pixel intensity at time t, $\langle ...\rangle$ denotes the average over the AOI and Δt is a delay time, which is an integer multiple of the time interval between successive frames ($\Delta t = n \times 20$ ms). In the following, we only consider the case $\Delta t = 20$ ms.

In the absence of motion inside the sample, F is equal to 1, but its value decreases as the light scatterers are sheared past each other. For a simple shear oscillatory flow, the DWS theory predicts [46, 5, 43]:

$$F(t,\Delta t,z) = \exp\left[-2k\ell^*\Gamma|\Delta\gamma|\sqrt{2/5}\right] \tag{2.2}$$

where $\Gamma \approx 2$ is a numerical prefactor, k is the light wavenumber in the medium (here water), ℓ^* is the light transport mean free path and $\Delta\gamma = \gamma(t+\Delta t) - \gamma(t) \approx \dot{\gamma}(t)\Delta t$ is the change in deformation during the delay Δt. The variations in F are determined by the ratio between the variation of optical paths $\approx \ell^*|\Delta\gamma|$ during Δt over the light wavelength $2\pi/k$.

If we now write that the strain varies periodically, i.e. $\gamma = \gamma_0\cos(2\pi f t)$, and further assume that $\Delta t f \ll 1$ (slow dynamics compared to the delay Δt), we can simplify the above expression to:

$$\begin{aligned} F(t,\Delta t,z) &= \exp\left[-4\pi\sqrt{2/5}k\ell^*\Gamma\gamma_0 f\Delta t\,|\sin(2\pi f t)|\right] \\ &\approx 1 - 4\pi\sqrt{2/5}k\ell^*\Gamma\gamma_0 f\Delta t\,|\sin(2\pi f t)| \end{aligned} \tag{2.3}$$

in the limit $k\ell^*\gamma_0 \ll 1$. The time and space resolved autocorrelation function F thus provides a measurement of the absolute value of the actual shear deformation rate inside the sample. Figure 2.15 shows the autocorrelation function F as a function of time t for different positions z across the gap for a pure calcite paste at $\phi = 20\%$. We find that $F(t)$ is periodic as expected from Equation (2.3) and that it barely changes with the position z.

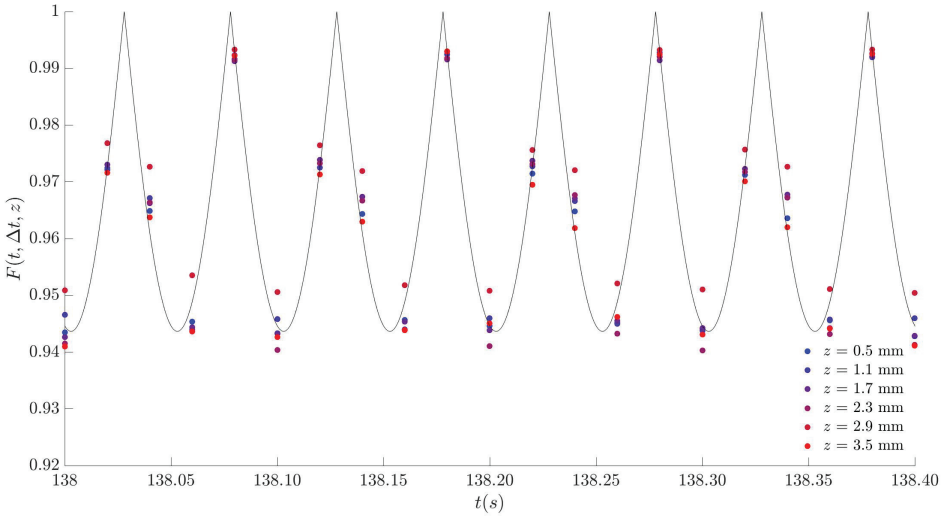

Figure 2.15 – Autocorrelation function $F(t,\Delta t,z)$ as a function of time t for different positions z across the gap, for a pure calcite paste at $\phi = 20\%$. The frequency is $f = 10Hz$ and the apparent shear strain is $\gamma = 9.6 \cdot 10^{-3}\%$. The delay Δt is fixed to 20 ms. The origin of times is the same as in Figure 3 of [25] reproduced in Chapter 3. The black line is a guide for the eye and corresponds to $F(t) = \exp(-A|\sin(2\pi ft + \phi)|)$ (Equation (2.3)).

The optical data thus allow us to check that the strain is homogeneous across the sample (z), and to compare it to the macroscopic strain applied by the rheometer geometry. Further results of DWS measurements are shown and discussed in Section 3.1.

2.2.3 Flow measurements

In order to have a complete characterization of the rheology of our suspension, we also perform flow measurements using Ultrasonic Speckle Velocimetry (USV). This entire work is carried out at the ENS of Lyon, in collaboration with and under the supervision of Sebastien Manneville. The calibration procedures is performed by Brice Saint-Michel and Vincent Dolique. For those experiments, a Couette geometry is coupled to an ultrasonic device in order to follow at the same time the rheological behavior and the local dynamic of the sheared sample. In particular this ultrasonic setup allows one to measure the velocity profiles inside the gap, as detailed in Section 2.2.4. Then we can detect the possible artefacts such as slippage or shear banding (Figure 1.19). This device is described in detail in Gallot et al. (2013) [15]. A brief summary is made in the following section.

Experimental setup

As shown in Figure 2.16 (c), the stress-imposed rheometer (ARG2, TA instruments) is equipped with a transparent Couette cell composed of a PMMA (poly methyl methacrylate, or plexiglass) rough rotor ($\approx$15 μm) and a PMMA smooth stator. The radii of the geometry are $R_1 = 23$ mm and $R_2 = 25$ mm respectively for the inner and outer cylinder (gap $R_2 - R_1 = 2$ mm). On top of the Couette cell, a lid reduces the contact with the atmosphere. To provide acoustic coupling and maintain a constant temperature, the Couette cell is immersed in a large water tank connected to a water bath (Figure 2.16) [15]. The temperature is maintained at $20.2 \pm 0.1^\circ$ C.

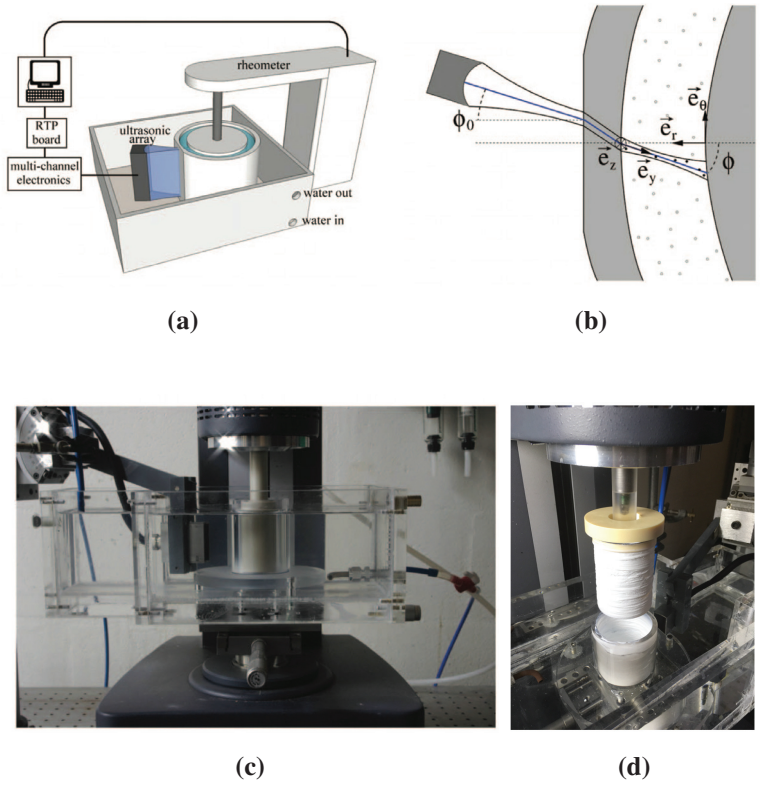

Figure 2.16 – Adapted from Gallot et al.(2013) [15]. Sketches and pictures of the experimental setup. (a) Three-dimensional general view showing the Couette geometry coupled to the ultrasonic device. (b) Top view of the gap of the Couette cell together with the path of the acoustic beam and the representation of the different axes and angles. (c) Picture showing the water tank with the ultrasonic transducer facing a smooth, transparent Couette geometry with dimensions: $R_1 = 23$ mm and $R_2 = 25$ mm. (d) Picture of the Couette geometry at the end of a flow measurement on calcite paste.

Flow protocol

The protocol starts with a pre-shear step imposing the same starting conditions for all studied systems. Then a series of constant shear rate steps is imposed to the calcite paste. These shear steps are coupled with ultrasonic speckle velocimetry measurements. For each shear step, we fix a testing time, $t_{\dot{\gamma}}$ defined as the duration of the shear step and the USV time, t_{USV} defined as the interval for which USV are recorded. After each step, the linear storage modulus is recorded to check the possible evolution of the paste properties. The final test consists in two flow curves with decreasing and increasing shear rates. More precisely, the protocol is composed by:

1. Pre-shear: one minute at $\dot{\gamma} = 10\,\mathrm{s}^{-1}$ and one minute at $\dot{\gamma} = -10\,\mathrm{s}^{-1}$;

2. Recording of the linear storage modulus: three minutes at $\gamma = 0.05\,\%$ and at frequency $f = 1$ Hz;

3. Shear rate steps series at: $\dot{\gamma} = 10 - 20 - 50 - 20 - 10\,\mathrm{s}^{-1}$. During each step USV are recorded. For each shear step, there is a specific USV acquisition time and testing time, listed in Table 2.2. After each step, the value of the linear storage modulus is recorded as in 2);

4. Shear rate steps series at: $\dot{\gamma} = 10 - 20 - 50 - 100 - 50 - 20 - 10 - 5 - 2\,\mathrm{s}^{-1}$, similar to 3);

5. Flow curve with a decreasing shear rate ramp from $\dot{\gamma} = 100 - 1\ \mathrm{s}^{-1}$, 10 s/point and 15 points/decade ("Descending ramp");

6. Flow curve with a increasing shear rate ramp from $\dot{\gamma} = 1 - 100\ \mathrm{s}^{-1}$, 10 s/point and 15 points/decade ("Ascending ramp");

7. Same as 2).

$\dot{\gamma}$ (s^{-1})	t_{USV} (s)	$t_{\dot{\gamma}}$ (s)
1	60	120
2	30	90
5	15	70
10	10	60
20	5	15
50	3	5
100	2	4

Table 2.2 – List of the specific USV acquisition time t_{USV} and shear rate testing time $t_{\dot{\gamma}}$ for each shear rate step $\dot{\gamma}$ (points 3 and 4 of the protocol).

Table 2.2 summarizes the time during which USV are recorded ("USV time") and the times for each shear rate step ("testing time"). We decide to apply a decreasing testing time as the shear rate increases to impose a roughly constant deformation. We fix these times such as the total deformation per step is around $\gamma = 3 \cdot 10^4\ \%$. Depending on the system and the properties, we change the protocol performing only step 3 or 4, as specified in Chapter 5.

Figure 2.17 shows the typical flow curves obtained for a pure calcite paste ($\phi = 10\ \%$) for a decreasing/increasing $\dot{\gamma}$.

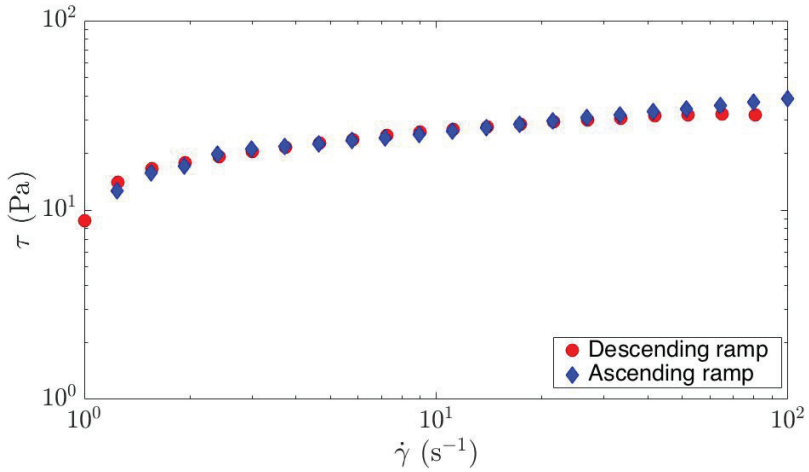

Figure 2.17 – Typical flow curve for a decreasing and increasing shear rate ramps (pure calcite, $\phi = 10\ \%$): shear stress, τ as a function of the shear rate $\dot{\gamma}$.

Examples of velocity profiles obtained during the shear rate steps are shown in Section 2.2.4, together with the explanation of ultrasonic speckle velocimetry technique. In Table 2.3 we summarize all investigated samples specifying the volume concentration range.

Samples	ϕ range (%)
Pure	10-20
30 mM **Ca(OH)$_2$**	10
50 mM **Ca(OH)$_2$**	10-15
100 mM **HCl** + 3 mM Ca(OH)$_2$	10
94 mM **NaOH** + 3 mM Ca(OH)$_2$	8-15

Table 2.3 – List of all studied samples and the corresponding volume concentration range.

2.2.4 Ultrasonic speckle velocimetry

We briefly recall the setup and the principles of ultrasonic speckle velocimetry (USV) technique. A complete explanation can be found in the papers of Manneville et al. (2004) [26] and Gallot et al. (2013) [15].

Ultrasonic imaging follows the dynamics of the flow between the two cylinders of the Couette geometry. Moreover, this kind of measurements gives information about the evolution of spatial distribution of the acoustic tracers during flow and detects the possible flow inhomogeneities i.e. wall slip or shear banding (Figure 1.19).

An ultrasonic scanner is composed by:

1. A probe which transmits and receives the ultrasonic signal. An ultrasonic transducer converts electrical signals into ultrasound and vice-versa though piezoelectric crystals;

2. An electric system which drives the transducer, generates the transmitted impulse, receives the probe echo and treats the signal;

3. A system for displaying the images from the ultrasound scanner.

In this specific case the ultrasonic probe is custom-made and is constituted by 128 piezoelectric transducers with a total active length of 32 mm. The probe, as shown in the setup (Figure 2.16), is centered in the middle of the Couette height to have a focal spot as a thin rectangular slice of 32 mm height, 2 mm length and 300 μm thickness [15]. Moreover it is necessary to fix the transducer array angle not equal to zero but $\phi_0 \approx 5^\circ$ relative to the normal of the outer cup (Figure 2.16 (b)). This angle allows one to measure the projection of the azimuthal velocity along the USV axes [15] and then to estimate the velocity inside the gap, provided a calibration performed with a Newtonian fluid (i.e. suspension of polystyrene spheres in water).

Depending on the investigated system, it can be necessary to add tracers (i.e. glass beads). The backscattered signal results in an ultrasonic speckle reflecting the scatterer distribution along the ultrasonic beam [15]. Then velocity profiles are obtained by correlating the ultrasonic speckle signal in time. In fact, this apparatus detects the positions of the particles at different times and calculate the corresponding velocity. More precisely, Figure 2.18 describes how the variation of the speckle signal is recorded between two times, T and $T + \delta T$. Figure 2.18 (a) shows a typical backscattered signal of a dilute suspension of polystyrene in water, normalized by the maximum amplitude [26]. The first backscattered signal corresponds to the stator (violet area in Figure 2.18 (a)) and the last one to the rotor (green area in Figure 2.18 (a)). Figure 2.18 (b) correspond to a zoom of the signal shown in Figure 2.18 (a) in a range of time around t= 14 μs (pink rectangle). The two curves correspond to the USV signal

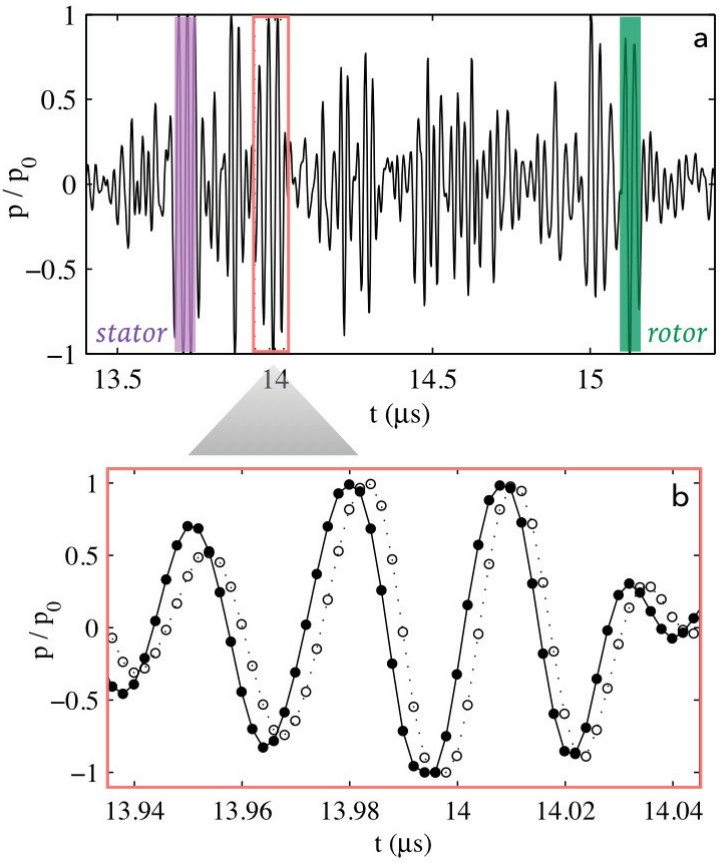

Figure 2.18 – Adapted from Manneville et al.(2004) [26]. (a) Speckle signal recorded in a 1 % wt suspension of polystyrene spheres in water. The voltage $V(t)$ from the transducer output is directly proportional to the acoustic pressure $p(t)$. The signal is normalized by its maximum value V_0, which yields $V/V_0 = p/p_0$, where p_0 is the maximum pressure. The sampling frequency is $f_s = 500\,\mathrm{MHz}$ and the recorded signal is 1000 points long. The rotor velocity is $v_0 = 23.5\,\mathrm{mm\,s^{-1}}$. (a) The violet area represents the first backscattered signal and corresponds to the stator. The green area instead represents the last backscattered signal and corresponds to the rotor. (b) Zoom over 4 acoustic periods of the speckle signal p/p_0 in (a), corresponding to the rectangle around $t = 14\,\mu$s. Bullets (•) correspond to the speckle signal p_T, shown in (a), received after a pulse is sent at time T. Open circles (○) correspond to the signal $p_{T+\delta T}$ recorded over the same time window after a second pulse which is sent 1 ms later at time $T + \delta T$. The motion of the scatterers results in a shift to the right of the signal i.e. the scatterers move away from the transducer.

obtained at T (•) and $T + \delta T$ (○). They result from the interferences coming from scatterers within the gap. The resulting velocity is calculated as $v_y = \delta y/\delta T$ where $\delta y \approx 0.5\,c\,\delta t$ and δt is the time shift due to the scatterer displacement at position $y \approx 0.5\,c\,t$ in the gap, with c the speed of sound.

In summary, the ultrafast scanner through plane wave imaging together with rheometry gives a "two dimensional time-resolved characterization of the shear flow of soft materials" [15]. In fact, thanks to the ultrasonic speckle technique, informations about the position and the velocity of the particles are obtained at the same time with global rheological data in the Couette geometry (shear rate, shear stress, viscosity) [15]. The time resolution is down to 1 ms and space resolution is around 100 μm in radial direction and 250 μm in vertical direction.

We use this setup for calcite paste because the suspension is opaque and white as shown in Sec-

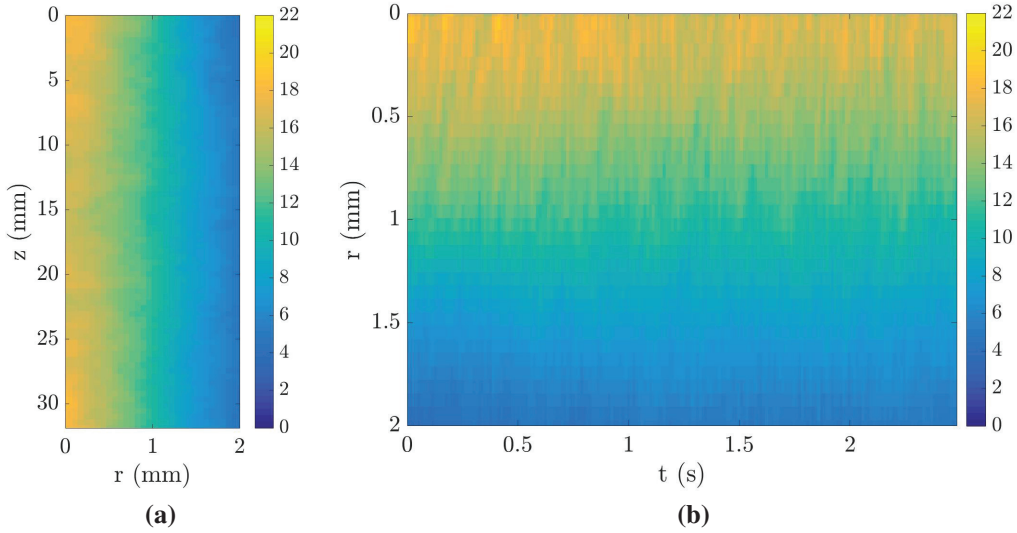

Figure 2.19 – Velocity map images for pure calcite paste ($\phi = 10\,\%$). Color bar refers to the velocity in mm/s. Blue is the minimum value and yellow the maximum one.(a) Example of a time-average velocity map as a function of (r, z). This diagram verifies the velocity spatial homogeneity along the imaging plane, z is the height and r is the distance across the gap ($r = 0$ rotor, $r = 2$ mm stator). (b) Spatio-temporal diagram which shows the velocity averaged in z. This map along r as a function of the USV acquisition time, t, helps to estimate the stationarity of the velocity profiles.

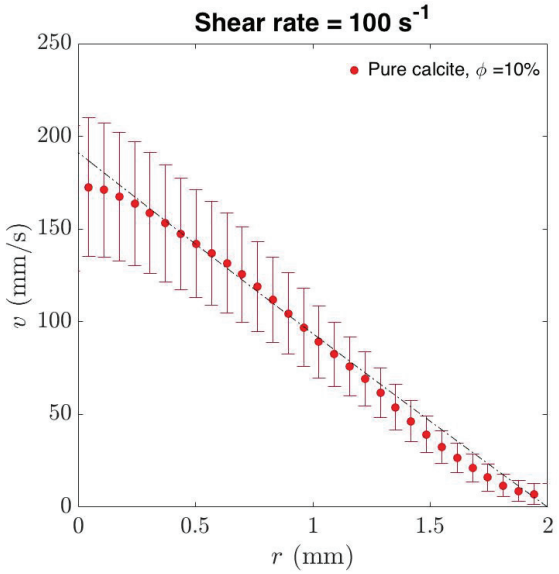

Figure 2.20 – Typical velocity profile, v, along the gap, r, for a pure calcite sample ($\phi = 10\,\%$). The error bar is due to the variation of the velocity in the vertical direction. The shear rate is equal to $\dot{\gamma} = 100\,\mathrm{s}^{-1}$

tion 2.1, making impossible the use of classical optical techniques such as Particle Image Velocimetry (PIV). Moreover the use of ultrasonic tracers is not necessary here because calcite scatters very well ultrasound due to the big aggregates naturally formed in the suspension, as shown in Figure 2.8.

Thanks to ultrasonic velocimetry, we can obtain time averaged velocity maps, as shown in Figure 2.19 (a) or averaged in z as shown in Figure 2.19 (b). Time-averaged velocity maps show how the velocity profiles change along the window probed by ultrasound. In Figure 2.19 (a), z is the investigated

height and r is the position along the gap. As expected, at $r = 0$ mm (rotor position), the velocity is maximal (yellow) all along z and it is zero in correspondence of the stator position $r = 2$ mm (deep blue). With this diagram $v(z,r)$ the velocity spatial homogeneity can be verified.

Second, by averaging across z position, we can obtain a spatio-temporal diagram $v(r,t)$. This diagram allows one to check the stationarity of the velocity (Figure 2.19 (b)). Finally, for each z position, the velocity $v(r,t)$ is averaged over time obtaining $v(r)$. Then the spatial vertical dispersion of the velocity $v(r)$ is calculated. We verified that all velocity profiles are identical along z. A typical velocity profile for pure calcite ($\phi = 10\,\%$) is shown in Figure 2.20. In fact the local shear rate is quite homogeneous and is equal to the imposed shear rate $\dot{\gamma} = 100\,\mathrm{s}^{-1}$. In the following, we consider only velocity profiles stationary with time and homogeneous in z. Velocity profiles and flow rheology results are detailed in Chapter 5.

2.3 Zeta potential

The strength and the range of the inter-particle interaction is at the origin of the mechanical properties of the pastes. As already mentioned, the fact that we obtain a solid-like paste ($G' \gg G''$) even at small solid fraction ($\phi = 5\,\%$) suggests attractive interactions between calcite particles. The interaction potential is generally constituted by two main actors: Van der Waals attraction and electrostatic repulsion (Section 1.2.5). On the one hand the van der Waals attraction is mainly characterized by a Hamaker constant of $\sim 2 \times 10^{-20}$ J [3]. On the other hand, the repulsion arising from the electrostatic double layer depends on the Debye length (hence the concentrations of dissolved ions), and on the Zeta potential ζ of the particles. Both parameters depend on whether the solution is at equilibrium with atmospheric carbon dioxide, as detailed in Section 1.1. In particular, in the litterature there is no consensus on the value and on the sign of the Zeta potential of calcite paste or suspension. It is found to depend, among others, on pH, CO_2 pressure [28, 27, 9, 37], solid calcite concentrations [36], concentration of other dissolved ions [33], specific surface area and possible presence of impurities for natural calcite [42, 30]. An accurate and complete review of the Zeta potential of artificial and natural calcite is proposed by Al Mahrouqi et al.(2017) [2]. A brief summary of the main chemical mechanisms at the calcite surface, which determine the value of the Zeta potential is presented in Section 2.3.1. Moreover, direct measurements of Zeta potential are made on our calcite suspensions to estimate the interparticle interactions. Section 2.3.2 presents protocols and techniques used to measure ζ. Finally Section 2.4 details the chemical speciation and the characterization of the ionic strength I and then of the Debye length.

2.3.1 Zeta potential in aqueous calcite system

The main adsorption sites on calcite surface in water, at pH between $8-11$ (typical of our pastes), are made of ionic and neutral sites such as: $>Ca^+$, $>CO_3^-$, $>Ca(OH_2)^+$, $>Ca(O)^-$, $>CO_3(OH_2)^-$, >CaOH, $>CO_3H$ etc.. [40, 16, 32]. This list of surface sites is composed by $-Ca^+$, $-CO_3^-$ and their hydrated forms. In fact, the ions OH^- and H^+ are naturally attracted on the calcite surface [40, 16]. Moreover with these possible active sites, positive and negative ions can be attracted from the solution to the calcite surface. In particular the positive sites attract HCO_3^-, CO_3^{2-} and the negative ones mostly Ca^{2+}. Previous articles also underline that Ca^{2+} (with CO_3^{2-}) is a potential determining ion (PDI) in aqueous calcite suspension [14, 30] and can have a preferential adsorption on calcite surface [20]. This means

that the value of Zeta potential, in a calcite-water system presenting several ionic species, is determined mainly by the amount of Ca^{2+} ions, due to its strong adsorption on calcite surface. Figure 2.21 shows a schematic representation of the electrical double layer at the calcite–water interface for a calcite mineral in aqueous solution [2]. The Stern layer, already introduced in Section 1.2.5 is here further detailed in three planes as a function of the distance x from the calcite surface. In particular, the 0-plane at $x = 0$, attached to the surface, corresponds to the hydrolysis layer, where H and OH are chemi-bonded to the bulk ions (i.e. ions at the calcite surface, Figure 2.21) [38, 2]. The plane at $x = 1$ is the inner Helmholtz plane (IHP), which is the plane passing though the centers of the adsorbed ions and the outer Helmholtz plane (OHP), at $x = 2$ which passes through the solvated ions centers [45]. Looking at Figure 2.21 (b), the calcite surface ($x = 0$) is negatively charged due to the hydrolysis layer (i.e. surface complexation within the hydrolisis layer), as predicted in the complexation model of [19]. Instead the Zeta potential measured at the shear plane has a positive sign due to the adsorption of potential determining ions, especially Ca^{2+}.

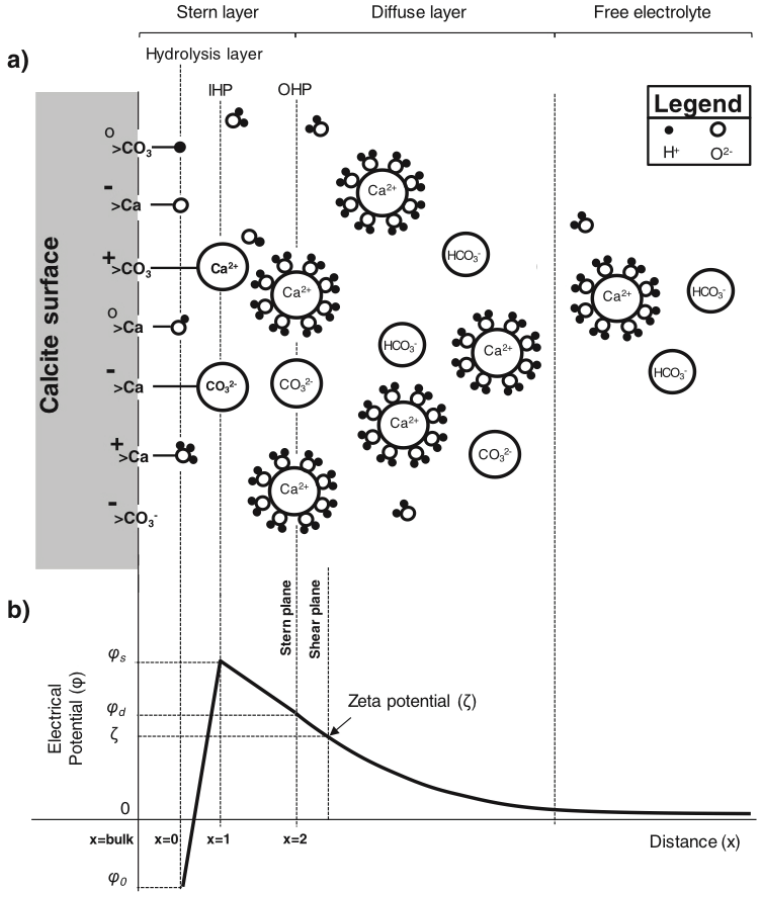

Figure 2.21 – Adapted from Al Mahrouqi et al. (2017) [2].(a) A schematic representation of the electrical double layer at the calcite–water interface. The surface speciation sites are from [40, 16, 32]. The Stern layer is described by three planes. The 0-plane ($x = 0$) corresponds to the hydrolysis layer where H and OH are chemi-bonded to the bulk ions [38]. The 1-plane (x = 1) denotes inner-sphere complexes and corresponds to the inner Helmholtz plane (IHP), while the 2-plane (x = 2) denotes outer-sphere complexes and corresponds to the outer Helmholtz plane (OHP) [45]. (b) A schematic representation of the variation of the electrical potential with distance from the mineral surface. Here the mineral surface is negatively charged, consistent with the surface complexation model of [19], but the Zeta potential is positive because of adsorption of the lattice PDIs (potential determining ions) Ca^{2+} and CO_3^{2-}.

The effect of others ions on calcite-water interface is described in Chapter 4, together with the analysis of Zeta potential measurements on calcite suspensions.

2.3.2 Zeta potential measurements

Zeta potential measurements can be carried out in very dilute suspension by electrophoretic method or directly on the concentrated paste by electroacoustic measurements [22]. For our experiments we tested both techniques, introduced in the following sections.

Zeta potential of dilute suspensions

Zeta potential measurements in very dilute calcite suspensions are made using an apparatus called Zeta-Sizer Nano (Malvern). This instrument allows to measure both size distribution (0.3 nm to 10 μm) by Dynamic Light Scattering technique and Zeta potential measurements by electrophoresis technique (Electrophoretic Light Scattering EDL).

A 20 % volume concentration calcite sample is diluted to $\phi = 0.2$ % with three different solutions: deionized water, saturated calcite solution and a saturated calcite solution with 3 mM of calcium hydroxide. Once the paste is diluted, the resulting suspension is maintained in contact with the atmosphere for more than 15 minutes. During this time the calcite powder sediments. Then the suspension supernatant is picked up for a Zeta potential measurement. The final concentration in the instrument cell is too low to be able to detect single particle or aggregate displacement. The sample is placed in a viewing chamber called electrophoresis cell. Then an electric field is applied. The charge or Zeta potential of the particles is determined by electrophoretic mobility measurement of the particles using Laser Doppler Velocimetry (LDV) [4]. More precisely under the applied electric field, charged particles move toward the electrode of opposite charge. The force of the electric field is then balanced by the viscous drag on the particle. The electrophoretic mobility is equal to $\mu_e = V/E$ where V is the particle velocity (μm/s) and E is the electric field strength (V/cm). Both quantities are known and the Zeta potential ζ can be calculated by the Henry equation [4]:

$$\mu_e = \frac{2\varepsilon\zeta f(Ka)}{3\eta} \tag{2.4}$$

where ε is the dielectric constant, η the suspension viscosity and $f(Ka)$ Henry's function with a the particle radius and $K = \lambda_D^{-1}$. If the EDL thickness is much smaller than the particle radius, $Ka \gg 1$ ($f(Ka) = 1.5$), obtaining the Helmholtz-Smoluchowski equation [4, 21]:

$$\mu_e = \frac{\varepsilon\zeta}{\eta} \tag{2.5}$$

On the contrary, if the EDL thickness is much bigger than the particle radius, $Ka \ll 1$ ($f(Ka) = 1$), and the μ_e can be express with the Hückel equation [4, 21]:

$$\mu_e = \frac{2\varepsilon\zeta}{3\eta} \tag{2.6}$$

In our case the Helmholtz-Smoluchowski equation can be used in fact $Ka = 2.5 - 35$ for the different tested systems. With this device, ζ, ε, η and pH can be changed directly in the cell by circulating two solutions, one at 0.1 M of NaOH and the other at 0.1 M of HCl. The quantity of added solution for the

titration is regulated directly by the instrument. The data from Zeta-Sizer measurements are collected in Annex A. These results obtained on very dilute suspensions cannot be directly compared with rheological measurements performed on concentrated calcite paste due to the change in pH, ions concentrations and solid concentration. For this reason, we decided to measure the values of Zeta potential directly in the paste with electroacoustic technique.

Zeta potential of concentrated systems

The application of ultrasound allows the characterization of concentrated opaque samples. ZetaProbe instrument (DT-310 Dispersion Technology) is used to obtain Zeta potential measurements on concentrated calcite suspensions ($\phi = 10\,\%$). These tests have been carried out at the ISTEC center of Faenza (Italy) by Anna Luisa Costa and Davide Gardini.

The used electroacoustic methods is named colloidal vibration current (CVI) [29, 11]. Here an acoustic wave is applied to the suspension. Then the sample produces an electric signal that is converted in a dynamic mobility and therefore in Zeta potential.

In this case the electrophoretic mobility of colloidal particles can be described by the Smoluchowski equation in the form which is valid in concentrated systems [10]:

$$\mu_e = \frac{\varepsilon\zeta}{\eta}\frac{K_s}{K_m} \tag{2.7}$$

where K_s is the macroscopical conductivity of the suspension and K_m is the conductivity of the medium outside the EDL (i.e. solution without particles), both reported in [10]. The dynamic mobility is calculated within the Smoluchowski Dynamics Electroacoustic Limit (SDEL) [11, 12]:

$$\mu_d = \frac{\varepsilon\zeta}{\eta}\frac{K_s}{K_m}\frac{(\rho_p - \rho_s)\cdot\rho_m}{(\rho_p - \rho_m)\cdot\rho_s} \tag{2.8}$$

where ρ is the density with the index p for particle, m for medium and s for the system (ρ_s is a function of ρ_p and ρ_m). Further details can be found in [11, 12].

With this instrument (ZetaProbe), the pH can be varied by adding NaOH and HCl solutions. However it is not possible to measure the particle size that is an input data that in our case was set at 100 nm.

Once the Zeta potential is known, and in order to calculate the DLVO potential, we need to characterize the ionic composition of the solute.

2.4 Chemical speciation

In order to quantify the chemical equilibrium of our calcite suspensions, a fully description of their ionic composition is calculated with the speciation freeware Visual MINTEQ [1]. The aim of the program is to simulate equilibria and speciation of inorganic solutes in natural water.

As first we describe the complete equilibrium reactions in calcite-water system and then we specify the procedure used for the MINTEQ calculation.

2.4.1 Calcite equilibrium reactions

As already introduced in Section 1.1, the carbonate equilibria depend strongly on the pH and on the dissolved carbon dioxide. For pH above 10, dissolved CO_2 is in the form of carbonate CO_3^{2-} and for pH below 10 in the form of bicarbonate HCO_3^- (Figure 1.3). Moreover as detailed in Somasundaran and Agar [37], calcite once dissolved in water produces several chemical species such as: H_2CO_3 (carbonic acid), HCO_3^-, CO_3^{2-}, Ca^{2+}, $CaHCO_3^+$, $CaOH^+$, $Ca(OH)_{2(aq)}$ and $CaCO_{3(aq)}$ involving in the following reactions:

(1) $CaCO_{3(s)} \rightleftharpoons CaCO_{3(aq)}$ $K_1 = 10^{-5.09}$
(2) $CaCO_{3(aq)} \rightleftharpoons Ca^{2+} + CO_3^{2-}$ $K_2 = 10^{-3.25}$
(3) $CO_3^{2-} + H_2O \rightleftharpoons HCO_3^- + OH^-$ $K_3 = 10^{-3.67}$
(4) $HCO_3^- + H_2O \rightleftharpoons H_2CO_3 + OH^-$ $K_4 = 10^{-7.65}$
(5) $H_2CO_3 \rightleftharpoons CO_{2(g)} + H_2O$ $K_5 = 10^{1.47}$
(6) $Ca^{2+} + HCO_3^- \rightleftharpoons CaHCO_3^+$ $K_6 = 10^{0.82}$
(7) $CaHCO_3^+ \rightleftharpoons H^+ + CaCO_{3(aq)}$ $K_7 = 10^{-7.90}$
(8) $Ca^{2+} + OH^- \rightleftharpoons CaOH^+$ $K_8 = 10^{1.40}$
(9) $CaOH^+ + OH^- \rightleftharpoons Ca(OH)_{2(aq)}$ $K_9 = 10^{1.37}$
(10) $Ca(OH)_{2(aq)} \rightleftharpoons Ca(OH)_{2(s)}$ $K_{10} = 10^{2.45}$

in particular, the calcite dissolution is described by reactions (1) and (2), the carbonate equilibria by reactions (3) to (5) and the calcium hydroxide dissolution by reactions (8) to (10).

Most of the studied samples (listed in Table 2.1) have a pH higher than 10. In this case the prevalent species in solution are Ca^{2+}, CO_3^{2-} and OH^-, with the corresponding equations deduced from those above:

(*a*) $Ca^{2+} + CO_3^{2-} \rightleftharpoons CaCO_{3(s)}$ $K_a = 10^{8.34}$ from (1) and (2).
(*b*) $CO_{2(g)} + 2\,OH^- \rightleftharpoons CO_3^{2-} + H_2O$ $K_b = 10^{9.85}$ from (3), (4) and (5).
(*c*) $Ca^{2+} + 2\,OH^- \rightleftharpoons Ca(OH)_{2(s)}$ $K_c = 10^{5.22}$ from (8), (9) and (10).

Moreover we add calcium hydroxide (portlandite) up to 50 mM. The solubility limits of solid calcium hydroxide is around 20 mM [18]. In our experimental conditions, i.e. in presence of high concentration of calcite, MINTEQ calculates a maximum solubility of 19 mM. For amounts of $Ca(OH)_2$ higher than 19 mM, the exceeding calcium hydroxide remains as solid in the solution easily reacting with the carbon dioxide from the atmosphere to precipitate calcite [41] as:

(*d*) $Ca(OH)_{2(s)} + CO_{2(g)} \longrightarrow CaCO_{3(s)} + H_2O$

reaction (d) is written as an irreversible reaction (i.e. products favorite reaction). We calculate from reactions (1)-(5) and (8)-(10) an equilibrium constant of $K_d = 10^{13}$ (for $K \gg 1$ products are always favorites). The transformation of solid portlandite to solid calcite is thus favored as long as the activity of CO_2 in the air a_{CO_2} is larger than K_d^{-1}, which is the case for atmospheric carbon dioxide (a_{CO_2} = 0.00038).

2.4.2 MINTEQ calculation

Visual MINTEQ input criteria can be: pH or ionic strength, partial pressure of carbon dioxide (pCO_2), temperature and components of the problem (i.e. concentrations or molarities). To obtain the chemical speciation at our experimental conditions, pH measurements of the different suspensions are made immediately after sample preparation. The measured pH is between 6.5 and 12.7 ± 0.2. In this range, the dominant form of calcium in solution is Ca^{2+} and for the carbon dioxide is CO_3^{2-} or HCO_3^- depending on pH (Section 1.1).

For all systems, calcite is imposed in MINTEQ as an *infinite solid phase*. This is justified by the fact that the quantity of precipitated or dissolved calcite is small compared to the initial concentration (3.35 M for $\phi = 10\%$).

Our experimental conditions lie between equilibria with and without atmosphere. Indeed during the sample preparation, the paste is inevitably in contact with the carbon dioxide. Then to obtain in MINTEQ the pH measured experimentally, CO_2 is inserted as CO_3^{2-} component (input). MINTEQ then calculates the ionic concentrations to satisfy the above chemical equilibria (1-10) (and water dissociation) as well as charge balance. Imposing the CO_2 pressure is also possible. The results of the calculation are equivalent.

In order to better understand the mode of operation of MINTEQ, two cases are detailed in the following: pure calcite and calcite with 30 mM of calcium hydroxide. Table 2.4 reports the results for the two systems.

	pH_{meas}	$[CO_2]_{diss}$ (mM)	$[Ca^{2+}]$ (mM)	I (mM)
Pure calcite	8.9	0.21	0.24	0.73
30 mM $Ca(OH)_2$	11.8	26.40	3.30	10.20

Table 2.4 – Chemical speciation for pure calcite and calcite with 30mM of calcium hydroxide for $\phi = 10\,\%$. In particular measured pH (pH_{meas}) and dissolved carbon dioxide $[CO_2]_{diss}$ are input values. Concentration of ions $[Ca^{2+}]$ and ionic strength I are the most relevant output values.

In the case of pure system, the inputs are: calcite as infinite solid phase and 0.27 mM of CO_3^{2-}. Asking for a mass and charge balance we obtain the measured pH and the complete chemical speciation.

The inputs for the system with 30 mM of $Ca(OH)_2$ are: calcite as infinite solid phase, 30 mM of Ca^{2+}, 26.4 mM of CO_3^{2-} and also portlandite $Ca(OH)_{2(s)}$ as *possible solid phase*. The last input allows to precipitate portlandite if we are over the limit of solubility of calcium hydroxide. It is also possible to incorporate 30 mM of portlandite directly as a *finite solid phase*.

Moreover we recalculated the values in Table 2.4 by resolving the relevant reactions for each systems i.e. $(a), (b), (c)$ for the samples containing $Ca(OH)_2(s)$. Contrary to MINTEQ we used concentrations instead of activities but the final values are very similar.

The resulting chemical equilibrium is essential to calculate the ionic strength of the calcite suspensions then the Debye length and consequently the DLVO interaction (Section 1.2.5). Results for chemical speciation are presented in Chapter 4.

Bibliography

[1] Visual minteq version 3.1, https://vminteq.lwr.kth.se.

[2] D. Al Mahrouqi, J. Vinogradov, and M. D. Jackson. Zeta potential of artificial and natural calcite in aqueous solution. *Advances in colloid and interface science*, 240:60–76, 2017.

[3] L. Bergström. Hamaker constants of inorganic materials. *Advances in colloid and interface science*, 70:125–169, 1997.

[4] S. Bhattacharjee. DLS and zeta potential-what they are and what they are not? *Journal of Controlled Release*, 235:337–351, 2016.

[5] D. Bicout and G. Maret. Multiple Light Scattering in Taylor-Couette Flow. *Physica A*, 210:87, 1994.

[6] G. Binnig, C. F. Quate, and C. Gerber. Atomic force microscope. *Physical review letters*, 56(9):930, 1986.

[7] J. Bridge and R. Demicco. *Earth surface processes, landforms and sediment deposits*. Cambridge University Press, 2008.

[8] L. Cipelletti, H. Bissig, V. Trappe, P. Ballesta, and S. Mazoyer. Time Resolved Correlation : A new tool for studying temporally heteroheneous dynamics. *J. Phys.: Condens. Matter*, 15:S257, 2003.

[9] Y. Diao and R. M. Espinosa-Marzal. Molecular insight into the nanoconfined calcite–solution interface. *Proceedings of the National Academy of Sciences*, 113(43):12047–12052, 2016.

[10] A. S. Dukhin, V. Shilov, and Y. Borkovskaya. Dynamic electrophoretic mobility in concentrated dispersed systems. Cell model. *Langmuir*, 15(10):3452–3457, 1999.

[11] A. Dukhin, V. Shilov, H. Ohshima, and P. Goetz. Electroacoustic phenomena in concentrated dispersions: New theory and CVI experiment. *Langmuir*, 15(20):6692–6706, 1999.

[12] A. Dukhin, V. Shilov, H. Ohshima, and P. Goetz. Electroacoustic phenomena in concentrated dispersions: Effect of the surface conductivity. *Langmuir*, 16(6):2615–2620, 2000.

[13] A. Duri, D. A. Sessoms, V. Trappe, and L. Cipelletti. Resolving Long-Range Spatial Correlations in Jammed Colloidal Systems Using Photon Correlation Imaging. *Phys. Rev. Lett.*, 102(8):085702, 2009.

[14] T. Foxall, G. C. Peterson, H. M. Rendall, and A. L. Smith. Charge determination at calcium salt/aqueous solution interface. *Journal of the Chemical Society, Faraday Transactions 1: Physical Chemistry in Condensed Phases*, 75:1034–1039, 1979.

[15] T. Gallot, C. Perge, V. Grenard, M.-A. Fardin, N. Taberlet, and S. Manneville. Ultrafast ultrasonic imaging coupled to rheometry: Principle and illustration. *Review of Scientific Instruments*, 84(4):045107, 2013.

[16] C. Geffroy, A. Foissy, J. Persello, and B. Cabane. Surface complexation of calcite by carboxylates in water. *Journal of Colloid and Interface science*, 211(1):45–53, 1999.

[17] G. Greczynski and L. Hultman. C 1s peak of adventitious carbon aligns to the vacuum level: Dire consequences for material's bonding assignment by photoelectron spectroscopy. *ChemPhysChem*, 18(12):1507–1512, 2017.

[18] D. Green and R. Perry. *Perry's Chemical Engineers' Handbook, 8^{th} Edition*. McGraw Hill professional. McGraw-Hill Education, 2007.

[19] F. Heberling, T. P. Trainor, J. Lützenkirchen, P. Eng, M. A. Denecke, and D. Bosbach. Structure and reactivity of the calcite–water interface. *Journal of colloid and interface science*, 354(2):843–857, 2011.

[20] Y. C. Huang, F. M. Fowkes, T. B. Lloyd, and N. D. Sanders. Adsorption of calcium ions from calcium chloride solutions onto calcium carbonate particles. *Langmuir*, 7(8):1742–1748, 1991.

[21] R. J. Hunter. *Foundations of colloid science*. Oxford university press, 2001.

[22] R. J. Hunter. *Zeta potential in colloid science: principles and applications*, volume 2. Academic press, 2013.

[23] A. Kurokawa, V. Vidal, K. Kurita, T. Divoux, and S. Manneville. Avalanche-like fluidization of a non-brownian particle gel. *Soft Matter*, 11(46):9026–9037, 2015.

[24] M. Le Merrer, S. Cohen-Addad, and R. Höhler. Bubble Rearrangement Duration in Foams near the Jamming Point. *Physical Review Letters*, 108(18):188301, 2012.

[25] T. Liberto, M. Le Merrer, C. Barentin, M. Bellotto, and J. Colombani. Elasticity and yielding of a calcite paste: scaling laws in a dense colloidal suspension. *Soft matter*, 13(10):2014–2023, 2017.

[26] S. Manneville, L. Bécu, and A. Colin. High-frequency ultrasonic speckle velocimetry in sheared complex fluids. *The European Physical Journal-Applied Physics*, 28(3):361–373, 2004.

[27] N. Mikanovic, K. Khayat, M. Pagé, and C. Jolicoeur. Aqueous $CaCO_3$ dispersions as reference systems for early-age cementitious materials. *Colloids and Surfaces A: Physicochemical and Engineering Aspects*, 291(1-3):202–211, 2006.

[28] P. Moulin and H. Roques. Zeta potential measurement of calcium carbonate. *Journal of colloid and interface science*, 261(1):115–126, 2003.

[29] R. O'Brien, D. Cannon, and W. Rowlands. Electroacoustic determination of particle size and zeta potential. *Journal of Colloid and Interface Science*, 173(2):406–418, 1995.

[30] A. Pierre, J. Lamarche, R. Mercier, A. Foissy, and J. Persello. Calcium as potential determining ion in aqueous calcite suspensions. *Journal of dispersion science and technology*, 11(6):611–635, 1990.

[31] D. Pine, D. Weitz, P. Chaikin, and E. Herbolzheimer. Diffusing wave spectroscopy. *Physical review letters*, 60(12):1134, 1988.

[32] O. Pokrovsky and J. Schott. Surface chemistry and dissolution kinetics of divalent metal carbonates. *Environmental science & technology*, 36(3):426–432, 2002.

[33] S. Pourchet, I. Pochard, F. Brunel, and D. Perrey. Chemistry of the calcite/water interface: Influence of sulfate ions and consequences in terms of cohesion forces. *Cement and Concrete Research*, 52:22–30, 2013.

[34] T. G. Rochow and P. A. Tucker. *Introduction to microscopy by means of light, electrons, X rays, or acoustics*. Springer Science & Business Media, 2013.

[35] A. Shchukarev and M. Ramstedt. Cryo-XPS: probing intact interfaces in nature and life. *Surface and Interface Analysis*, 49(4):349–356, 2017.

[36] D. Siffert and P. Fimbel. Parameters affecting the sign and magnitude of the electrokinetic potential of calcite. *Colloids and surfaces*, 11(3-4):377–389, 1984.

[37] P. Somasundaran and G. Agar. The zero point of charge of calcite. *Journal of Colloid and Interface Science*, 24(4):433–440, 1967.

[38] S. Stipp. Toward a conceptual model of the calcite surface: hydration, hydrolysis, and surface potential. *Geochimica et Cosmochimica Acta*, 63(19-20):3121–3131, 1999.

[39] S. Stipp, C. Eggleston, and B. Nielsen. Calcite surface structure observed at microtopographic and molecular scales with atomic force microscopy (AFM). *Geochimica et Cosmochimica Acta*, 58(14):3023–3033, 1994.

[40] S. L. Stipp and M. F. Hochella. Structure and bonding environments at the calcite surface as observed with X-ray photoelectron spectroscopy (XPS) and low energy electron diffraction (LEED). *Geochimica et Cosmochimica Acta*, 55(6):1723–1736, 1991.

[41] K. Van Balen. Understanding the lime cycle and its influence on historical construction practice. In *Proceedings of the First International Congress on Construction History*, volume 20, page 24. Instituto Juan de Herrera Universidad Politécnica de Madrid, 2003.

[42] N. Vdović. Electrokinetic behaviour of calcite—the relationship with other calcite properties. *Chemical Geology*, 177(3-4):241–248, 2001.

[43] F. Wintzenrieth, S. Cohen-Addad, M. Le Merrer, and R. Höhler. Laser-speckle-visibility acoustic spectroscopy in soft turbid media. *Phys. Rev. E*, 89(1):012308, January 2014.

[44] S. Wischnitzer. *Introduction to electron microscopy*. Elsevier, 2013.

[45] M. Wolthers, L. Charlet, and P. Van Cappellen. The surface chemistry of divalent metal carbonate minerals; a critical assessment of surface charge and potential data using the charge distribution multi-site ion complexation model. *American Journal of science*, 308(8):905–941, 2008.

[46] X.-L. Wu, D. J. Pine, P. M. Chaikin, J. S. Huang, and D. A. Weitz. Diffusing-wave spectroscopy in a shear flow. *J. Opt. Soc. Am. B*, 7(1):15–20, January 1990.

Chapter 3

Elastic properties of pure calcite paste

In this chapter, our results on elastic properties of pure calcite paste is presented and detailed with the article *Elasticity and yielding of calcite paste: scaling law in a dense colloidal suspension*, published in 2017 in Soft matter [6]. In Section 3.2 supplementary information to the publication are added.

Contents

3.1 Soft Matter Publication

Elastic measurements such as viscoelastic moduli G', G'' or critical (yield) strain, are performed on the pure calcite suspensions for a wide range of volume concentrations. Here the yielding point is defined as the deformation at the end of the linear regime, well detected due to a clear transition from a solid-like to liquid-like behavior. One of the aim of this study is to extract microscopic information from the macroscopic mechanical properties. Thanks to the model proposed by Shih et al. (1991) [9] for fractal colloidal gels, we manage to link the macroscopic response to the microstructure of the calcite paste, in particular calculating the fractal dimension of the gel structure.

Journal Name

ARTICLE TYPE

Cite this: DOI: 10.1039/xxxxxxxxxx

Elasticity and yielding of calcite paste: scaling laws in a dense colloidal suspension

Teresa Liberto*[a], Marie Le Merrer[a], Catherine Barentin[a,c], Maurizio Bellotto[b] and Jean Colombani[a]

Received Date
Accepted Date

DOI: 10.1039/xxxxxxxxxx

www.rsc.org/journalname

We address the mechanical characterization of calcite paste as a model system to investigate the relation between microstructure and macroscopic behavior of colloidal suspensions. The ultimate goal is to achieve a control of the elastic and yielding properties of calcite which will prove valuable in several domains, from paper coating to paint manufacture and eventually in the comprehension and control of the mechanical properties of carbonate rocks. Rheological measurements have been performed on calcite suspensions for a wide range of particle concentrations. The calcite paste exhibits a typical colloidal gel behavior, with an elastic regime and a clear yield strain above which it enters a plastic regime. The yield strain shows a minimum when increasing the solid concentration, connected to a change of the power law scaling of the storage modulus. In the framework of the classical fractal elasticity model for colloidal suspensions of Shih et al. [*Phys. Rev. A*, 1990, **42**, 4772], we interpret this behavior as a switch with the concentration from the strong-link regime to the weak-link regime, which had never been observed so far in one well-defined system without external or chemical forcing.

1 Introduction

Calcite is the most stable polymorph of calcium carbonate ($CaCO_3$)[1] and an extremely widespread mineral. It is found in many igneous, metamorphic and sedimentary rocks as an accessory mineral and it can also have biochemical origin. Moreover, calcite is the principal constituent of limestone, chalk and marble, extremely common rocks and one of the largest carbon repositories on our planet[2]. The mechanical and optical properties of calcite and its availability make it one of the most widely used minerals as a construction material, abrasive, agricultural soil treatment, extender for pigments, excipient for pharmaceuticals and more. In many uses like filler for paper manufacture or building materials, calcite is ground to powder and dispersed in aqueous solutions, resulting in the formation of a paste, i.e. a yield stress fluid, solid-like under low stresses but flowing at large stresses[3–5]. However, most of the previous works on calcite paste rheology have focused on the influence of organic additives on flow properties, driven by applications in cement and paper industries, while the elasticity and yielding of pure calcite paste remain almost unexplored.

Typical calcite particles are found in the range of microns if obtained from grinding or tens to hundreds of nanometers if obtained by precipitation, and can thus be considered as colloids. Microscopically, in presence of attractive interactions, colloids aggregate into fractal flocs. For a sufficiently high concentration, the flocs interconnect and form a network called gel, similar to the network of blobs in polymeric gels, which confers the paste an elastic-like behavior[6]. The elastic properties of the suspension depend on those of the flocs and on the links between them. Shih et al.[6] and subsequently Wu and Morbidelli[7] have proposed a model to describe the power-law dependence of the mechanical properties of colloidal gels versus the solid concentration based on the floc structure and organization, which has been successfully used to interpret the elastic and plastic behaviors of many such gels[8–19]. One of the main predictions of this model is that, when the colloid concentration increases, a transition in the mechanical properties of the material is expected between two scaling laws. Surprisingly, despite the widespread utilization of this acclaimed model, this central feature has never been observed experimentally in the absence of external or chemical forcing.

We use conventional rheology to characterize both the elastic and yielding behavior of calcite colloidal gels, for volume concentrations varying in the range $5\% \leq \phi \leq 30\%$. At $\phi \approx 20\%$ we evidence a striking change in the dependency upon concentration of the yield strain, separating the elastic and plastic regimes, correlated to a change in the power law dependence of the elastic

[a] *Institut Lumière Matière, Université de Lyon, Université Claude Bernard Lyon 1, Domaine scientifique de la Doua, 6 Rue Ada Byron, 69622 Villeurbanne cedex (France)*
[b] *Dipartimento di Chimica, Materiali ed Ingegneria Chimica "G. Natta", Politecnico di Milano, Piazza Leonardo da Vinci 32, 20133 Milano (Italy)*
[c] *Institut Universitaire de France (France)*
* *E-mail:teresa.liberto@univ-lyon1.fr*

modulus upon concentration. These results constitute a complete validation of the above model of the mechanics of colloidal suspensions in the full range of concentrations[6], whereas up to now only parts of the model were used for one well-defined unforced system.

This article is organized as follows. In section 2, sample preparation, rheological and optical measurements are described. In section 3, after ruling out the effect of slippage as a rheological artefact, the influence of calcite concentration on elasticity and yielding is studied in detail. In section 4, the results are discussed and analysed along the model of Shih et al.[6], which allows to characterize the microstructure of the calcite paste, i.e, the fractal dimension and the size of the flocs constituting the paste as a function of the concentration.

2 Materials and Methods

2.1 Sample preparation

A calcite dense colloidal suspension was obtained by dispersion of Socal 31 calcite powder (Solvay, average particle diameter 60 nm, density $\rho = 2710$ kg/m^3), in distilled water. The range of volume concentrations is $\phi = 5-30\%$. The volume concentrations are deduced from the powder weight and calcite density. Sample preparation was carried out in a vortex stirrer (Ultra Turrax TD300). The homogenization process required five minutes mixing at an increasing mixing rate (4500-5800 rpm) on increasing volume concentration. Immediately after mixing, the suspension appears white because it scatters light due to the mismatch of refractive index between water and calcite. The strong scattering suggests the existence of heterogeneities at the micrometric level, larger than the initial nanometric particles[20]. The pH-range of the calcite suspensions, measured on fresh paste, slightly increases with ϕ in the range $8.7-8.9$, typical for calcite water suspensions[21].

2.2 Rheological Measurements

The viscoelastic properties were determined using oscillatory deformation applied by a stress-controlled rotational rheometer (Anton Paar MCR 301). The measurements were performed in a plate-plate (PP) geometry at room temperature. Upper and lower plate diameters respectively of 36 mm and 64 mm were used. The dimension of the gap, in the range $0.5-5$ mm, was chosen much bigger than the average diameter of the nanoparticles and of the heterogeneities (i.e. flocs), in the aim to obtain bulk rheological properties (Fig. 1a). More precisely, we studied the influence of the gap width ranging from 0.5 to 5 mm on the local deformation field and on the rheological measurements. Four repeated measurements were performed for every concentration, with a new sample loading for each measurement.

To characterize the viscoelastic response of the paste, we extract from the measurements the storage modulus (G') and the loss modulus (G''), defined as follows[22]:

$$G^* = G' + iG'' \quad (1)$$

where G^* is the complex modulus corresponding to the ratio between the complex stress τ^* and complex strain γ^*:

$$\tau^*(t) = G^*\gamma^*(t) \quad (2)$$

The entire experimental protocol consists in a preparation phase and a measurement one. The preparation phase includes two steps: pre-shear and time structuration. The pre-shear consists in a 1 minute imposed shear rate of $\dot{\gamma} = 10$ s^{-1}, in order to start from comparable initial conditions for each sample. The time structuration is a 5 minutes small amplitude oscillation step at imposed deformation $\gamma_0 = 0.01\%$ and frequency $f = 1$ Hz. During this resting time, the sample restores the colloidal interactions that were destroyed in the pre-shear step and thus recovers rigidity, as indicated by the increase of the storage modulus G' which reaches a constant plateau after one minute. The measurement phase is an amplitude sweep in oscillatory regime at imposed frequency ($f = 1$ Hz or $f = 10$ Hz), with increasing deformations in the range: $\gamma_0 = 0.001-10\%$ or increasing stress in the range: $\tau = 1-300$ Pa. The two different amplitude sweeps give equivalent results, although the stress amplitude sweep is less noisy, since we work with a stress-controlled rheometer. During this step, the values of the stress and strain are acquired by the rheometer, from which the viscoelastic moduli are computed.

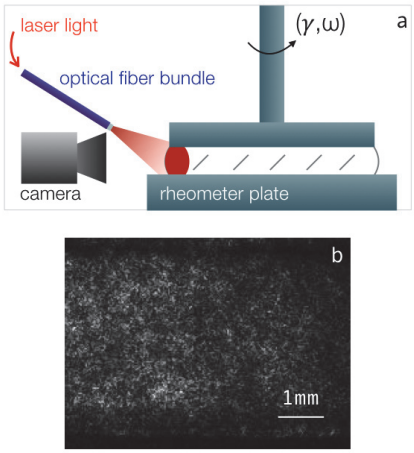

Fig. 1 (a) Sketch of the experimental setup. (b) Image of the sample with the speckle pattern created by the light backscattered from the sample.

2.3 Data analysis

At low strains, up to the end of linearity, we find that the elastic modulus G' is typically one order of magnitude larger than the loss modulus G'', revealing the elastic-like behavior of the paste (Fig. 2). Besides, at small deformations, the system reacts linearly such that the storage and loss moduli are constant. In this plateau regime, the linear storage modulus G'_{lin} can thus be estimated unambiguously.

At larger strains, the material yields and becomes liquid-like, and both moduli drop dramatically (Fig. 2). The purpose of our paper is to explore in detail the gel destructuration, i.e. the

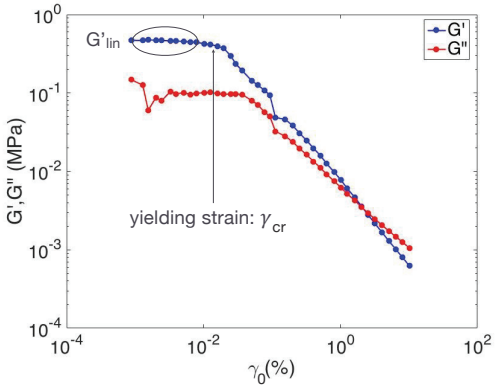

Fig. 2 Typical amplitude sweep measurement ($\phi = 20\%$, $f = 1$ Hz, 46 μm-rough sand paper plates): storage G' and loss G'' moduli as a function of the deformation γ_0.

onset of plasticity. To characterize it, we estimate the end of the linear regime by a critical strain γ_{cr}, which corresponds to the value of γ_0 for which the storage modulus is 10%-15% lower than the value in the elastic regime G'_{lin}. We also denote τ_{cr} the corresponding critical stress.

2.4 Shear characterization with Diffusing-Wave Spectroscopy

Since our samples are highly turbid and strongly scatter light, we have also used an optical probe based on Diffusing-Wave Spectroscopy (DWS) techniques[23] to characterize the local shear dynamics across the rheometer gap. Coherent light from a He-Ne laser (wavelength $\lambda_0 = 632$ nm) is sent onto the side of the rheometer cell thanks to an optical fiber bundle. The illuminated zone is a few millimeters wide and we image the sample surface from the side with a camera (IDS UI) and objective. The experimental setup is shown in Fig. 1a.

A speckle interference pattern is created (Fig. 1b), whose temporal evolution reveals the relative motion of light scatterers, hence the inner dynamics of the sample, namely the shear oscillations. Videos are made during stress sweep experiments similar to the ones used for the elasticity measurements at $\phi = 20\%$. The sample oscillation is $f = 10$ Hz, while the video acquisition frequency is fixed at 50 Hz, with an exposure duration of 20 ms. To analyse the recordings, we use time and space resolved correlation spectroscopy[24–26]. After background subtraction, we first define rectangular areas of interest (AOI) of area 20×200 square pixels (approximately 0.6×6 mm^2) at different positions z across the gap. For each AOI, we calculate at each time the following autocorrelation function:

$$F(t,\Delta t,z) = \frac{2\langle I_t I_{t+\Delta t}\rangle - \langle I_t\rangle^2 - \langle I_{t+\Delta t}\rangle^2}{\langle I_t^2\rangle + \langle I_{t+\Delta t}^2\rangle - \langle I_t\rangle^2 - \langle I_{t+\Delta t}\rangle^2} \tag{3}$$

where I_t is the pixel intensity at time t, $\langle ...\rangle$ denotes the average over the AOI and Δt is a delay time, which is an integer multiple of the time interval between successive frames ($\Delta t = n \times 20$ ms). In the following, we only consider the case $\Delta t = 20$ ms.

In the absence of motion inside the sample, F is equal to 1, but its value decreases as the light scatterers are sheared past each other. For a simple shear oscillatory flow, the DWS theory predicts[27–29]:

$$F(t,\Delta t,z) = \exp\left[-2k\ell^*\Gamma|\Delta\gamma|\sqrt{2/5}\right] \tag{4}$$

where $\Gamma \approx 2$ is a numerical prefactor, k is the light wavenumber in the medium (here water), ℓ^* is the light transport mean free path and $\Delta\gamma = \gamma(t+\Delta t) - \gamma(t) \approx \dot\gamma(t)\Delta t$ is the change in deformation during the delay Δt. If we now write that the strain varies periodically, i.e., $\gamma = \gamma_0\cos(2\pi f t)$, and further assume that $\Delta t f \ll 1$ (slow dynamics compared to the delay Δt), we can simplify the above expression to

$$\begin{aligned} F(t,\Delta t,z) &= \exp\left[-4\pi\sqrt{2/5}k\ell^*\Gamma\gamma_0 f\Delta t\,|\sin(2\pi f t)|\right] \\ &\approx 1 - 4\pi\sqrt{2/5}k\ell^*\Gamma\gamma_0 f\Delta t\,|\sin(2\pi f t)| \end{aligned} \tag{5}$$

in the limit $k\ell^*\gamma_0 \ll 1$. The time and space resolved autocorrelation function F thus provides a measurement of the absolute value of the actual shear deformation rate inside the sample. F thus oscillates with time and its average over one period $T = 1/f$ reads:

$$F_0(z) = \langle F(t)\rangle_T \approx 1 - 8\sqrt{2/5}k\ell^*\Gamma\gamma_0 f\Delta t \tag{6}$$

$F_0(z)$ enables us to check the homogeneity of the deformation along z, as detailed below. Besides, the sensitivity of the method to the amplitude of the shear oscillations γ_0 is for instance revealed in Fig. 3, which corresponds to a stress sweep experiment, for which we calculate the spatial average of F_0:

$$F_m = \langle F_0(z)\rangle_z \tag{7}$$

Fig. 3a shows F_m as a function of time, while Fig. 3b shows the corresponding values of imposed stress and apparent deformation extracted from the rheological measurements. As increasing stresses are applied to the paste, the deformation increases, and the measured autocorrelation value F_m, starting from the value ≈ 1, decreases step by step (Fig. 3a), until a more important drop (at ≈ 160 s), corresponding to the onset of the liquid-like behavior, emphasized by the sharp increase in deformation γ_0 (Fig. 3b). The optical data thus allow us to estimate the variation of local strain, which can be compared to the macroscopic strain applied by the rheometer geometry.

3 Results

In this section, we first characterize the elasticity and the yielding of the calcite paste for a given concentration. In particular, the effect of slippage of the paste is analyzed and ruled out. Other rheological artefacts[30] such as flow inhomogeneity and sample aging are also discussed. Then the influence of the paste concentration on the elastic modulus and on the yielding point is studied in detail.

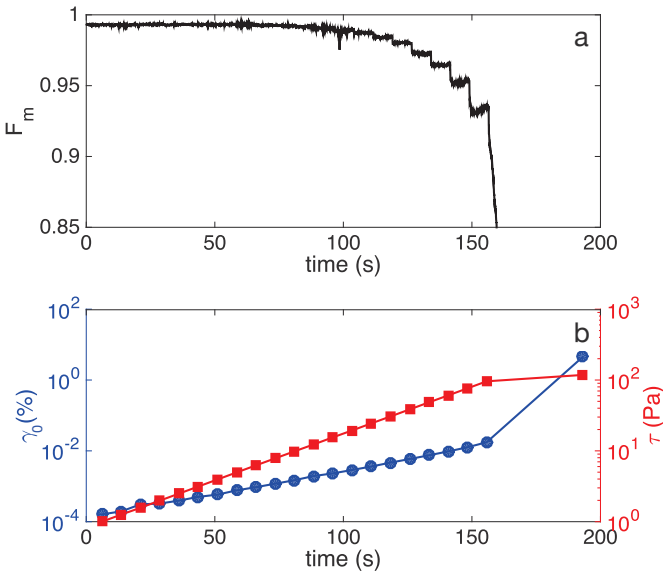

Fig. 3 Typical stress sweep experiment: (a) optical signal F_m and (b) rheological data (applied strain, blue circles and stress, red squares) as a function of time. F_m denotes the value of $F(t,\Delta t)$, for $\Delta t = 20$ ms, spatially averaged and smoothed over one oscillation period (0.1 s) to extract the continuous component of the oscillating signal. The calcite volume concentration is $\phi = 20\%$ and the gap width is 4 mm with 20μm-rough PMMA plates.

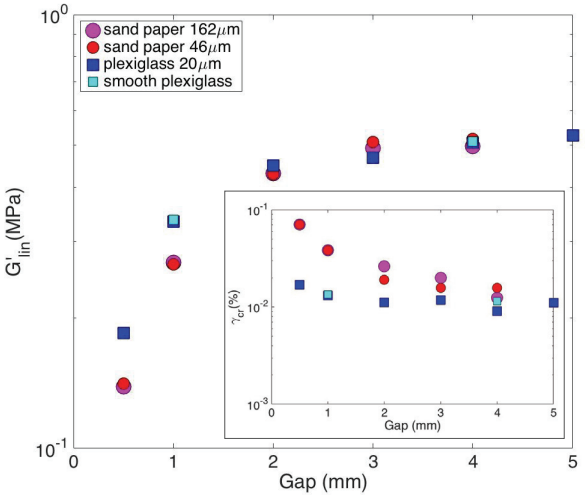

Fig. 4 Linear storage modulus G'_{lin} as a function of the gap width for different surfaces for a volume concentration of $\phi = 20\%$ and frequency $f = 1$ Hz. The standard deviation for the G'_{lin} values is 15 %. In the inset is represented the critical strain γ_{cr} at the same conditions with a standard deviation less than 25%.

3.1 Influence of surfaces and gap width

An important aspect to investigate is the wall aptitude to drag the paste. In general, to prevent slippage, a rough surface is recommended. The choice of roughness should be adequate to provide sufficient grip, keeping an accurate and well defined geometry, without secondary flows[31]. In our case, we tested four different surfaces: sand papers with typical roughness of 162 μm and 46 μm and PMMA smooth and with roughness 20 μm. If the surface prevents slippage we expect the local rheological quantities (stress and strain) to be independent of the gap. We thus tested the different surfaces at various gap widths, from 0.5 to 5 mm.

Fig. 4 shows the variation of the estimated G'_{lin} and γ_{cr} as a function of the gap width, for the different surfaces and $\phi = 20\%$. G'_{lin} first increases with the gap width, then saturates for widths larger than ≈ 3 mm. In the same time, γ_{cr} decreases, then also saturates. This gap-dependency suggests that slip at the plate walls might be non-negligible for gaps smaller than 3 mm. For a given applied stress, we expect a combination of the actual deformation of the sample γ_{real} and slip at the walls. If we denote δ_{top} and δ_{bottom} the slip distance on the top and bottom plates of the rheometer, the deformation imposed by the rheometer is $\gamma_{\text{app}} = \gamma_{\text{real}} + (\delta_{\text{top}} + \delta_{\text{bottom}})/h$ where h is the gap width. Hence, the larger the gap, the smaller the contribution of slip to the total deformation, which is consistent with the measurements of Fig.4.

This effect seems more pronounced for sand papers than for PMMA. This could be due to specific interactions between calcite and silica (sand) or PMMA[32,33]. To evidence the presence of slip at smaller gaps, we performed optical DWS measurements to compare the deformation inside the sample at two different gap widths (1 and 4 mm). Figure 5 shows the optical signal F_m (averaged spatially and over one oscillation period), as a function of the apparent deformation imposed by the rheometer, for the 2 different gap widths. For each gap, two experiments are shown to illustrate the reproducibility of the optical measurement. For the 4 mm gap, we find that F decreases roughly linearly with the strain applied by the rheometer γ_0^{app}, as expected from Eq.6. On the contrary, for the 1 mm gap, the optical decorrelation is much reduced, indicating that the actual deformation in the sample is lower than expected from the motion of the rheometer plate: this is characteristic of slip of the paste at the walls, thus confirming our interpretation of Fig. 4.

Consequently, all the measurements shown below have been performed with sand paper plates (roughness 46 μm) at a gap width of 4 mm, except for pastes of low concentrations ($\phi \leq 10\%$). Such pastes cannot remain in large gap cells, and a smaller gap width of 1 mm have then been used, always checking the independence of the data upon gap (see appendix).

3.2 Deformation homogeneity

At large gaps (4 mm), the optical DWS signal can be calculated at different positions across the gap, in order to check the deformation homogeneity. More precisely, we extract the value of $F(t,\Delta t = 20\text{ ms},z)$ for different positions z and average it over one oscillation period to obtain the continuous component F_0. Figure 6 shows the variation of F_0 as a function of z, for 3 different strains γ_0, in the solid-like regime of the paste, for the experiment of Fig. 3. The origin of z is taken at the top plate. We find that F_0 decreases as γ_0 increases, as seen above. Besides, we notice that F_0 is independent of the position z, thus ruling out shear banding effects in the elastic regime[34]. Note that we have taken

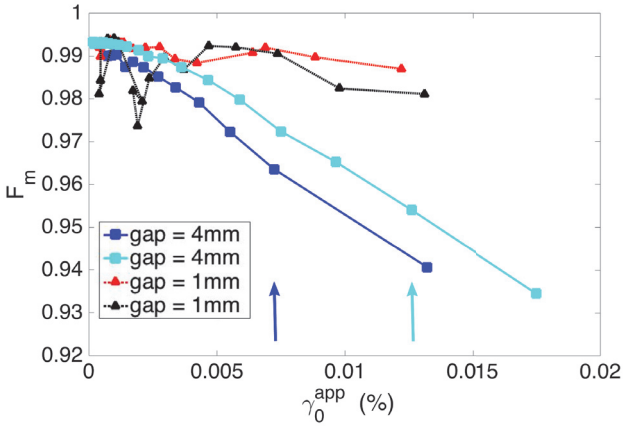

Fig. 5 Comparison between optical and rheological measurements: optical signal F_m as a function of the strain applied by the rheometer γ_0^{app}, for two different gap widths: 1 mm (red and black triangles) and 4 mm (blue and light blue squares). The arrows indicate the end of the elastic regime for 4 mm gap experiments. The calcite volume concentration is $\phi = 20\%$ and the experiments are performed with 20 μm-rough PMMA plates.

care here to illuminate the sample as homogeneously as possible, to get a clean optical signal in the whole gap. However, we have also noticed that, in the liquid-like regime, conversely to the solid-like one, shear localization occurs, as can be directly seen on the picture of Fig. 6(c), where the deformed region appears blurred, because in this case the temporal evolution of the speckle pattern is much faster than the camera exposure time 20 ms[35].

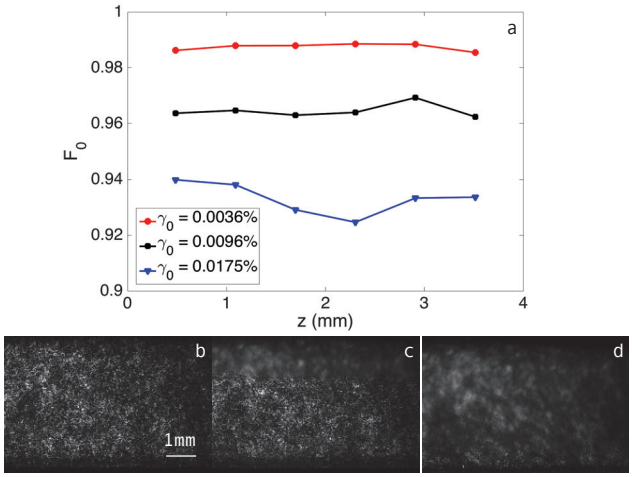

Fig. 6 (a) Optical signal F_0, as a function of position z in the gap, for various strains in the experiment of Fig. 3. F_0 denotes the value of F averaged over an oscillation period. (b,c,d) Images of the speckle pattern for applied stresses $\sigma = 5$ Pa (b) and $\sigma = 144$ Pa (c,d). The blurred zone shows where deformation is localized. The shear band is smaller right after the stress has been set to the value $\sigma = 144$ Pa (c) than after one minute (d).

3.2.1 Influence of sample age

To quantify the aging phenomena, we measured the value of G'_{lin} and γ_{cr} for different ages of the same sample. As shown in Fig. 7 we find that the value of G'_{lin} only increases of 25% within one month. Looking at this result and taking into account the value of the standard deviation on G'_{lin} measurement, equal to 15%, we can consider the effect of the aging as non significant. The same conclusion can be drawn from the evolution of γ_{cr}.

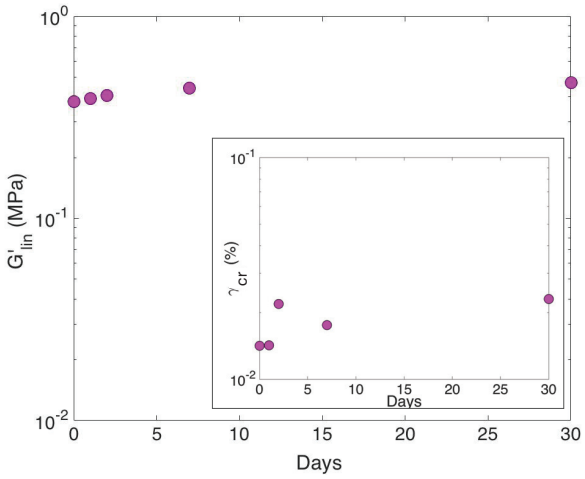

Fig. 7 Aging analysis: linear storage modulus at 20% volume concentration ϕ, frequency 1 Hz and 4 mm gap. The standard deviation of G'_{lin} is 15%. In the inset is represented the critical strain γ_{cr} in the same conditions with a standard deviation less than 25%. These experiments are performed with 46 μm-rough sand paper plates.

3.3 Influence of calcite volume fraction on elasticity and yielding

Now that we have identified working conditions enabling to avoid the main rheological artifacts, we can focus safely on the influence of the calcite volume fraction ϕ on the elastic modulus G'_{lin} and the critical strain for yielding γ_{cr}, as shown in Fig. 8 for the frequency $f = 1$ Hz. In Fig. 8a we see that G'_{lin} constantly rises with ϕ. In this logarithmic plot, the rise shows a smaller slope at larger concentrations. This change of slope occurs at $\phi \approx 20\%$. More strikingly, Fig. 8b shows that γ_{cr} varies in a non-monotonic way with ϕ and exhibits a minimum for $\phi \approx 20\%$. Finally, the stress at yielding τ_{cr} also shows a two-slopes scaling behavior with ϕ (Fig. 8c, in logarithmic scales), the change occurring at the same volume fraction.

In the appendix, we also show the data obtained at $f = 10$ Hz, which exhibit the same behavior.

4 Discussion

In the standard fractal elasticity model of colloidal suspensions, proposed initially by Shih et al.[6], the gel network is viewed as closely packed fractal flocs. A floc is a repetitive highly porous aggregate composed of smaller primary particles[36]. The rigidity and strength of the gel are assumed to be dominated by the weakest element of its network. At low volume fraction, each

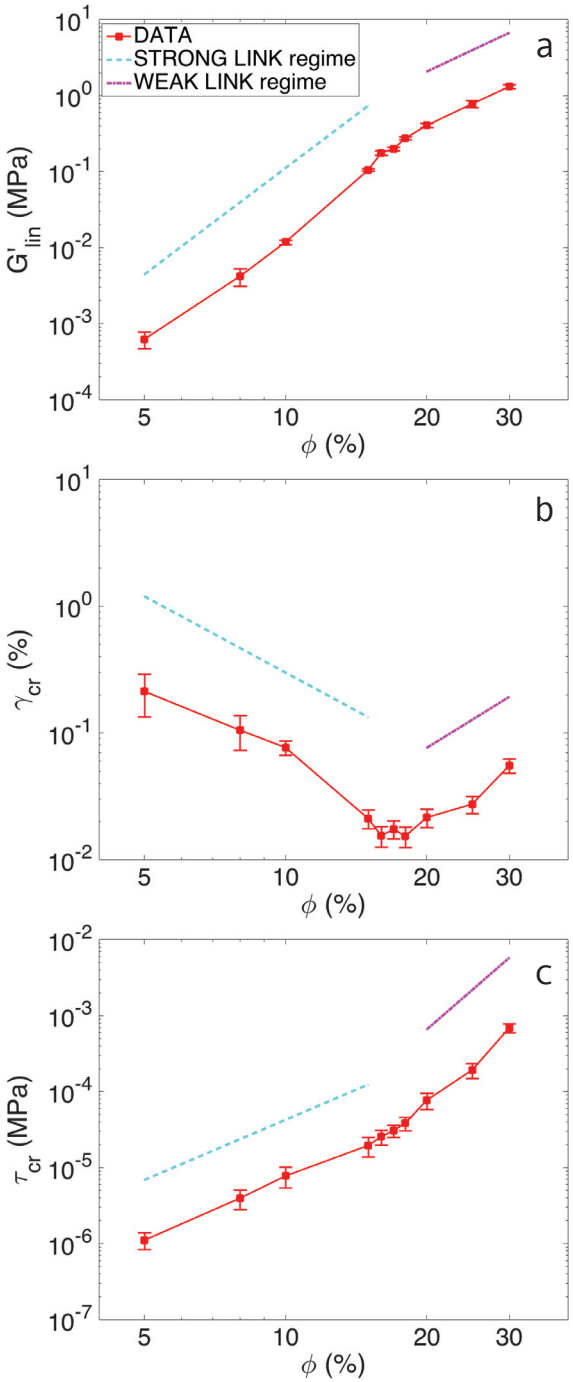

Fig. 8 (a) Linear storage modulus G'_{lin}, (b) critical strain γ_{cr} and (c) critical stress τ_{cr} versus the volume concentration ϕ measured at frequency 1 Hz (red symbols). The blue dashed lines (resp. purple solid lines) show the scaling laws fitted in the strong link (resp. weak link) regime. These experiments are performed with 46 μm-rough sand paper plates.

floc is highly porous and deformable, and is the weakest element. The inter-floc links are as strong as the flocs, and the regime is called strong-link (SL). Conversely, at higher volume fraction, the flocs are denser and stiffer: the weakest element is therefore the inter-floc link and the regime is called weak-link (WL). Wu and Morbidelli[7] re-elaborated this theory introducing an intermediate behavior, called transition regime (TR) to describe continuously the change of mechanical response and scaling laws as a function of the concentration. Several examples of strong-link regime systems are reported: suspensions of alumina[6,11] or silica[10,12], nanocomposites made of linear low density polyethylene (LLDPE) and clay[9] or polyester and exfoliated graphite[8]. Conversely, fewer materials exhibit the weak-link regime like protein solutions[17,18] or mixture of colloids and polymers[19]. Note that the weak-link scenario is equivalent to double-step yielding, which has been reported for this latter system[37,38] and attractive microgels[39]: the first yield point corresponds to the network destruction and formation of individual clusters, and the second yield point to the cluster fragmentation.

Among all the investigated systems, the shift from WL to SL regimes has rarely been observed, and always with changing the external or chemical conditions. One can cite the case of mixture of surfactants and silica colloid, forced to sweep from WL to SL by changing the length of the surfactant hydrophobic chain[13], magnetorheological fluids, forced by an applied magnetic field[14], protein gel prepared from eggs white, forced by changing the pH[15] and waxy oil system, forced by heating[16]. The model by Shih et al. proposes power law scalings of the elastic modulus G', critical strain γ_{cr}, and critical stress τ_{cr} with ϕ, as follows:

$$G' \propto \phi^A, \tag{8a}$$

$$\gamma \propto \phi^B, \tag{8b}$$

$$\tau \propto \phi^C. \tag{8c}$$

with scaling exponents:

$$A = \frac{(d-2)+(2+x)(1-\alpha)}{d-d_{\text{f}}}, \tag{9a}$$

$$B = \frac{1-(2+x)(1-\alpha)}{d-d_{\text{f}}}, \tag{9b}$$

$$C = \frac{d-1}{d-d_{\text{f}}}. \tag{9c}$$

Here d represents the Euclidean dimension (equal to 3), d_{f} the fractal dimension of the flocs and x the fractal dimension of the particle chains (backbone). Note that, from Eq (2), C is equal to $A+B$. The value of x is difficult to estimate and is usually assumed to be in the range of $1-1.3$[40]. The quantity α is a parameter quantifying the state of the gel, defined by Wu and Morbidelli[7], varying from 0 to 1; $\alpha = 0$ corresponds to a SL regime, $\alpha = 1$ to a WL regime and intermediate values to TR regimes. If A and C remain positive whatever the value of α, B turns from negative to positive when α changes from 0 to 1. Thereby, according to this model, the critical strain of a dense colloidal suspension should exhibit a minimum with increasing the concentration.

Quite unexpectedly, despite the wide use of this model, this feature has up to now never been observed experimentally with-

Table 1 Parameters of the colloidal gel model obtained from the fit of the experimental results for $f = 1$ Hz (Fig. 8a, b and c) with equations 8 and 9, taking $x = 1$.

ϕ range	α	A	B	A+B	C	d_f	Regime
$5\% \leq \phi \leq 15\%$	0.14	4.65	-2.05	2.60	2.63	2.23	strong link
$15\% \leq \phi \leq 20\%$	0.69	4.50	0.19	4.69	4.64	2.57	transition
$20\% \leq \phi \leq 30\%$	0.96	2.90	2.29	5.19	5.36	2.61	weak link

Table 2 Parameters of the colloidal gel model obtained from the fit of the experimental results for $f = 10$ Hz, (Fig. 10b and d) with equations 8 and 9, taking $x = 1$.

ϕ range	α	A	B	A+B	C	d_f	Regime
$5\% \leq \phi \leq 17\%$	0.34	4.74	-1.57	3.17	3.17	2.37	strong link
$17\% \leq \phi \leq 25\%$	0.67	4.68	-0.05	4.63	4.77	2.57	transition
$25\% \leq \phi \leq 30\%$	1.06	2.30	3.39	5.69	5.59	2.65	weak link

out external forcing. Turning to our results, we recognize immediately from Fig. 8 that the mechanical properties of the calcite paste show a power-law behavior changing with concentration exactly as predicted by the colloidal suspension model, with two identified domains separated by a narrow transition zone associated to a minimum of the yield strain observed for $\phi \approx 15-20\%$. This analysis therefore shows that our system ruptures first inside the flocs at low concentration (SL) and between the flocs at higher concentration (WL).

As a further confirmation of the fact that the calcite paste enters the WL regime, we have performed amplitude sweep experiments up to a 1000% deformation. We have thereby observed a double-step yielding for $\phi = 30\%$(see Appendix and Fig. 11). This behavior is characteristic of other attractive weak-link gels[37–39], where the first yielding, here for $\gamma_{cr} \sim 0.05\%$, is a signature of the inter-floc rupture, as predicted by the model, and the second one, here for $\gamma_0 \sim 5\%$, corresponds to the fragmentation of the flocs.

The very low value of the first yielding strain γ_{cr} is a further clue of the gel being inside the WL regime. Indeed values of γ_{cr} lower than 0.1% are characteristic of WL systems, like BSA gels[17], magnetofluids[14], or gelled waxy oils[16], whereas they are unusual in SL sytems.

A second important information can be derived from the evolution of the yield stress with concentration. According to Eq.8c and Eq.9c, the exponent C of the power law evolution of this quantity depends exclusively on d_f. Therefore the change of slope shown in Fig.8c should be a consequence of a change of fractal dimension d_f of the gel network with the evolution of the concentration. With this in mind, we have fitted our experimental data of elastic modulus G'_{lin} and yield strain γ_{cr} with Eq (8)a and b, to get exponents A and B in the three domains (SL, TR and WL), choosing $x = 1$. We have then solved Eq. (9)a and b, to get d_f and α in each domain. Table 1 shows the values of the exponents of the power laws, of the fractal dimension d_f of the gel, and of the transition parameter α in the 3 concentration domains. Table 2 also shows the results obtained at the frequency $f = 10$ Hz, which show a very similar behavior. The values of α inform us that, as expected, the low concentration range corresponds to a strong-link regime ($\alpha \simeq 0$), the high concentration range to a weak-link regime ($\alpha \simeq 1$), and the concentrations in-between to a transition regime. The fractal dimension of the gel obtained in the 3 regimes are comparable to values from the literature[6,7]. This dimension is notably larger at higher concentration due to the more crowded structure of the flocs.

The fractal theory proposes a scaling relation between the typical cluster size D and the mean diameter a of the particles which are here assumed to be spherical[41] :

$$\phi \sim \phi_0 (D/a)^{-(3-d_f)} \tag{10}$$

where ϕ_0 is the maximum packing fraction. With $\phi_0 = 64\%$ (random close packing) and using the values of d_f from Table 1, we obtain $D/a = 27$ for the extreme value of SL regime and $D/a = 7$ for the extreme value of WL. These values give an idea of the structure of the gel network, that we have sketched in Fig. 9.

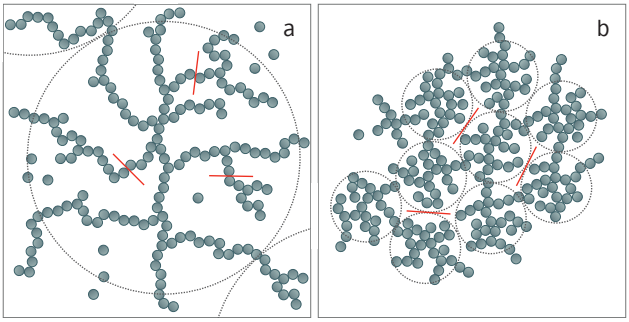

Fig. 9 (a) Strong link structure corresponding to $d_f = 2.23$ at low volume fraction, (b) Weak link structure corresponding to $d_f = 2.61$ at high volume fraction. Dashed lines represent the flocs at rest and solid lines are the probable rupture points in the two regimes.

The model of Shih et al.[6] was used numerous times to describe different kinds of colloidal systems. The novelty of our results is to show, for the first time, a complete experimental verification of the model going from the strong link regime to the weak-link regime by increasing the concentration. This verification was carried out with a pure material, varying only the solid particle fraction, without any other external or chemical modification, in contrast with previous works from the literature[13–16]. Moreover the fractal dimension and the size of the flocs extracted thanks to the model in the SL and WL regimes are consistent with what is known from colloidal gels.

The question arises why the calcite paste is the only system

investigated so far that crosses both regimes. Although it is too early to answer firmly, clues can be found in the literature. In general, large (micron-size) particles are in the SL regime [11]. For small particles ($\sim 10\,$nm), both regimes are encountered, SL at small concentration ($\phi \leq 10\%$) [6,12] and WL at high concentration ($\phi \geq 15\%$) [17]. The calcite particles are small ($\simeq 60\,$nm), and we find a transition between SL and WL in the range expected from the literature ($\phi \sim 15-20\%$). Therefore, it is likely that the calcite paste is the only studied system exhibiting the transition because it is made of particles being both small, and with an attraction strong and short-ranged that enables both to form a gel at low concentration and remain a homogeneous paste at high concentration.

5 Conclusion

The mechanical properties of calcite suspensions in water have been investigated through dynamic rheological measurements. The variation of both the elastic modulus in the small deformation linear domain $G'_{\rm lin}$ and the yield strain $\gamma_{\rm cr}$ (end of the elastic regime) with the solid concentration have been measured. The absence of measurement artifacts such as wall slip effects or heterogeneous deformation fields has been ascertained by optical measurements based on multiple light scattering. The trends of $G'_{\rm lin}$ and $\gamma_{\rm cr}$ with the solid volume fraction evidence the presence of two different scaling laws: $G'_{\rm lin}$ shows a change in exponent while $\gamma_{\rm cr}$ goes through a minimum for the same range of solid content.

This feature can be interpreted in the framework of the fractal elasticity model of colloidal suspensions of Shih et al. [6,7]. This model assumes a transition from a regime where elasticity and yielding are dominated by the fractal floc properties at low concentration (strong link regime), to a regime where they are dominated by the links between the flocs (weak link regime), when the flocs become smaller and stiffer as the solid concentration increases. We stress on the fact that this is the first observation of the transition from the strong-link to the weak-link regime in one simple and unperturbed system, predicted by the original model. This interpretation enables to evidence an increase of the fractal dimension of the flocs with increasing solid fraction, pointing to a change of the aggregation with concentration.

This thorough characterization of the elastic and yielding behavior of calcite paste is the first step to understand the particle-particle interactions, and control it through adsorption of organic molecules. This could lead to improve the mechanical properties of building materials such as their ductility. More fundamentally, the flow features (e.g. shear-banding, transient regime or wall slip) rise many open questions which require further studies.

Appendix

Protocol and frequency dependence

Fig. 10 presents all the results of the amplitude sweep at different frequencies and experimental conditions. Fig. 10a and c show experiments made at $f = 1\,$Hz and Fig. 10b and d at $f = 10\,$Hz. As already mentioned, we have verified the gap dependence for the concentration range $\phi = 5-30\%$. For $\phi < 10\%$ only experiments with small gap ($\sim 1\,$mm) are possible because, for higher gaps, the fluidity of the paste makes it flow outside the gap. In the same figure are also compared the results at 4 mm gap width and without pre-shear. In most of our experiments, a pre-shear is applied to ensure similar initial conditions and a better reproducibility of the results. However, the few measurements obtained without pre-shear gave very similar results, thus showing a weak effect of the protocol applied to the paste. Concerning the frequency dependence, the results are comparable in term of linear storage modulus $G'_{\rm lin}$, critical strain $\gamma_{\rm cr}$ and critical stress $\tau_{\rm cr}$, as a function of the volume concentration ϕ. For both frequencies, $f = 1\,$Hz and $f = 10\,$Hz, the transition between strong link to weak ling regime occurs as shown in Fig. 10.

Large amplitude deformation

To better analyze the yielding and flow mechanism of the calcite paste, we have performed amplitude sweep experiments for deformations up to 1000% at three different volume concentrations (10, 20 and 30%) as shown in Fig. 11. The data obtained at the highest concentration ($\phi = 30\%$) clearly exhibit a two-step yielding, which is consistent with the weak-link scenario for this concentration: the first yield point is associated with the breaking of bonds between clusters, while the second yield point corresponds to the fragmentation of the clusters. However this double-yielding process has no effect on the study of the onset of plasticity, which is the aim of our study. In the strong-link regime ($\phi = 10\%$ and 20%) , the cluster destructuration occurs at several length scales so that there is no reason to expect two distinct yield points, consistently with our observations.

Acknowledgements

This project has received funding from the European Union Horizon 2020 research and innovation program under the Marie Skłodowska-Curie grant agreement No.642976-NanoHeal Project. The results of this paper reflects only the author's view and the Commission is not responsible for any use that may be made of the information it contains. We also thank S. Manneville and B. Saint-Michel for stimulating discussions.

References

1 A. Putnis, *An introduction to mineral sciences*, Cambridge University Press, 1992.
2 *Mineral and Rocks*, ed. J. R. Wilson, Systematic Mineralogy, 2010.
3 P. Coussot, *Soft Matter*, 2007, **3**, 528–540.
4 R. Morini, *PhD thesis*, Université Nice Sophia Antipolis, 2013.
5 F. Dalas, S. Pourchet, A. Nonat, D. Rinaldi, S. Sabio and M. Mosquet, *Cement and Concrete Research*, 2015, **71**, 115–123.
6 W.-H. Shih, W. Y. Shih, S.-I. Kim, J. Liu and I. A. Aksay, *Physical Review A*, 1990, **42**, 4772.
7 H. Wu and M. Morbidelli, *Langmuir*, 2001, **17**, 1030–1036.
8 H. Kim and C. W. Macosko, *Macromolecules*, 2008, **41**, 3317–3327.

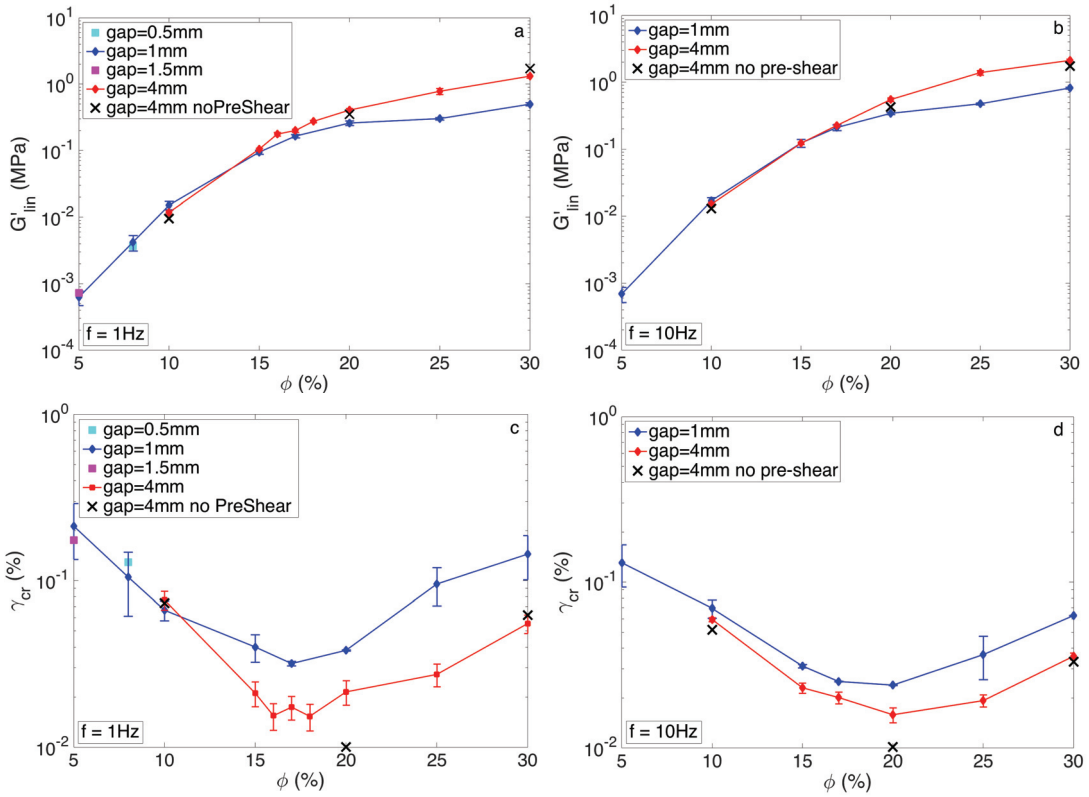

Fig. 10 Influence of gap width and pre-shear: (a) linear storage modulus at frequency 1Hz, (b) linear storage modulus at frequency 10Hz, (c) critical strain at 1Hz, (d) critical strain at 10Hz. These experiments are performed with 46 μm-rough sand paper plates.

9 A. Durmus, A. Kasgoz and C. W. Macosko, *Polymer*, 2007, **48**, 4492–4502.

10 C. Rueb and C. Zukoski, *Journal of Rheology*, 1997, **41**, 197–218.

11 G. M. Channell and C. F. Zukoski, *AIChE Journal*, 1997, **43**, 1700–1708.

12 P. Cassagnau, *Polymer*, 2008, **49**, 2183–2196.

13 H. Asai, A. Masuda and M. Kawaguchi, *Journal of colloid and interface science*, 2008, **328**, 180–185.

14 J. Segovia-Gutiérrez, C. Berli and J. De Vicente, *Journal of Rheology*, 2012, **56**, 1429–1448.

15 M. O. Eleya, S. Ko and S. Gunasekaran, *Food Hydrocolloids*, 2004, **18**, 315–323.

16 F. Yang, C. Li, C. Li and D. Wang, *Energy & Fuels*, 2013, **27**, 3718–3724.

17 T. Hagiwara, H. Kumagai and K. Nakamura, *Food Hydrocolloids*, 1998, **12**, 29–36.

18 S. Ikeda, E. A. Foegeding and T. Hagiwara, *Langmuir*, 1999, **15**, 8584–8589.

19 M. Laurati, G. Petekidis, N. Koumakis, F. Cardinaux, A. B. Schofield, J. M. Brader, M. Fuchs and S. U. Egelhaaf, *The Journal of chemical physics*, 2009, **130**, 134907.

20 A. Kurokawa, V. Vidal, K. Kurita, T. Divoux and S. Manneville, *Soft Matter*, 2015, **11**, 9026–9037.

21 J. Bridge and R. Demicco, *Earth surface processes, landforms and sediment deposits*, Cambridge University Press, 2008.

22 R. G. Larson, *The structure and rheology of complex fluids*, Oxford university press New York, 1999, vol. 150.

23 D. A. Weitz and D. J. Pine, in *Dynamic Light Scattering*, ed. W. Brown, Clarendon, Oxford, 1993, ch. 16, p. 652.

24 L. Cipelletti, H. Bissig, V. Trappe, P. Ballesta and S. Mazoyer, *Journal of Physics: Condensed Matter*, 2003, **15**, S257.

25 A. Duri, D. A. Sessoms, V. Trappe and L. Cipelletti, *Physical Review Letters*, 2009, **102**, 085702.

26 M. Le Merrer, S. Cohen-Addad and R. Höhler, *Physical Review Letters*, 2012, **108**, 188301.

27 X.-L. Wu, D. J. Pine, P. M. Chaikin, J. S. Huang and D. A. Weitz, *Journal of the Optical Society of America B*, 1990, **7**, 15–20.

28 D. Bicout and G. Maret, *Physica A*, 1994, **210**, 87.

29 F. Wintzenrieth, S. Cohen-Addad, M. Le Merrer and R. Höhler, *Physical Review E*, 2014, **89**, 012308.

30 R. H. Ewoldt, M. T. Johnston and L. M. Caretta, *Complex Fluids in Biological Systems*, Springer, 2015, pp. 207–241.

31 C. Combes, S. Tadier, H. Galliard, S. Girod-Fullana, C. Charvillat, C. Rey, R. Auzély-Velty and N. El Kissi, *Acta biomaterialia*, 2010, **6**, 920–927.

32 J. R. Seth, C. Locatelli-Champagne, F. Monti, R. T. Bonnecaze and M. Cloitre, *Soft Matter*, 2012, **8**, 140–148.

33 T. Gibaud, C. Barentin and S. Manneville, *Physical Review Let-*

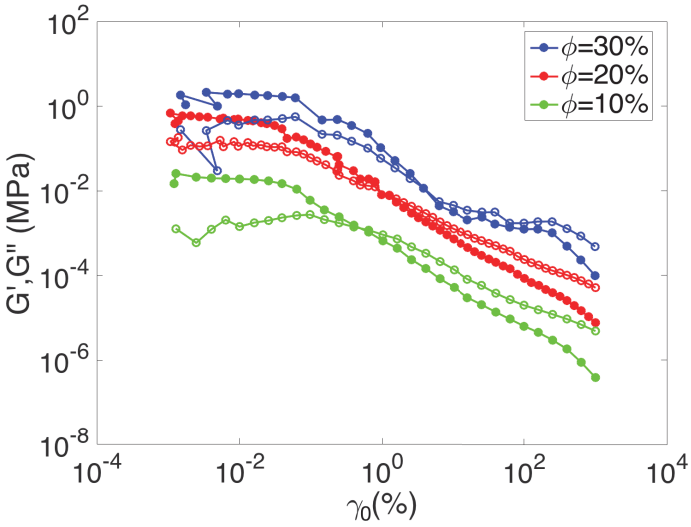

Fig. 11 Amplitude sweep at 30%, 20% and 10% volume concentration (gap width 4 mm, 46 μm-rough sand paper plates). Full circles represent the G' values and the empty circles the G'' values. For $\phi = 30\%$ in the weak-link regime, a second yield strain can be observed at $\gamma_0 \simeq 100\%$.

ters, 2008, **101**, 258302.

34 Y. Guo, W. Yu, Y. Xu and C. Zhou, *Soft Matter*, 2011, **7**, 2433.

35 R. Bandyopadhyay, A. S. Gittings, S. S. Suh, P. K. Dixon and D. J. Durian, *Review of Scientific Instruments*, 2005, **76**, 093110.

36 P. Jarvis, B. Jefferson and S. A. Parsons, *Reviews in Environmental Science and Bio/Technology*, 2005, **4**, 1–18.

37 M. Laurati, S. Egelhaaf and G. Petekidis, *Journal of Rheology*, 2011, **55**, 673–706.

38 N. Koumakis and G. Petekidis, *Soft Matter*, 2011, **7**, 2456–2470.

39 Z. Shao, A. S. Negi and C. O. Osuji, *Soft Matter*, 2013, **9**, 5492.

40 A. G. Marangoni *et al.*, *Fat crystal networks*, 2005, 413–440.

41 R. Buscall, P. D. Mills, J. W. Goodwin and D. Lawson, *Journal of the Chemical Society, Faraday Transactions 1: Physical Chemistry in Condensed Phases*, 1988, **84**, 4249–4260.

3.2 Supplemental information to the publication

In this section, supplementary informations on the publication [6] are provided. In particular we detail the robustness of our results with respect to the used protocol and to our critical strain definition. Indeed the preparation and the history of a soft material sample are known to have potentially a considerable influence on its mechanical behavior [4]. We also go through the yield strain definition in the literature.

3.2.1 Effect of shear history

The protocol α used to measure the viscoelastic properties of calcite paste is detailed in Section 2.2.1 and is recalled in Figure 2.9: it is composed by steps of pre-shear, time structuration and amplitude sweep. The effect of pre-shear step is already presented in Section 3.1 (appendix). To summarize, we can say that the pre-shear does not affect too much the final viscoelastic properties but ensures similar initial conditions and reduces the dispersion of the data.

In this section we test other protocols that change the shear history of the sample and we evaluate the effect of such protocol modifications on the results.

a) As first the usual pre-shear step (one minute at $\dot{\gamma} = 10\,\mathrm{s}^{-1}$) is substituted by a new pre-shear step, with a decreasing pre-shear rate ramp from $\dot{\gamma} = 10\,\mathrm{s}^{-1}$ to $\dot{\gamma} = 0.01\,\mathrm{s}^{-1}$, during around seven minutes (ten seconds for each point). Time structuration and amplitude sweep steps remain unchanged. Figure 3.1 shows the value of G' obtained with the two pre-shear protocols in all the range of volume concentration (5 to 30 %).

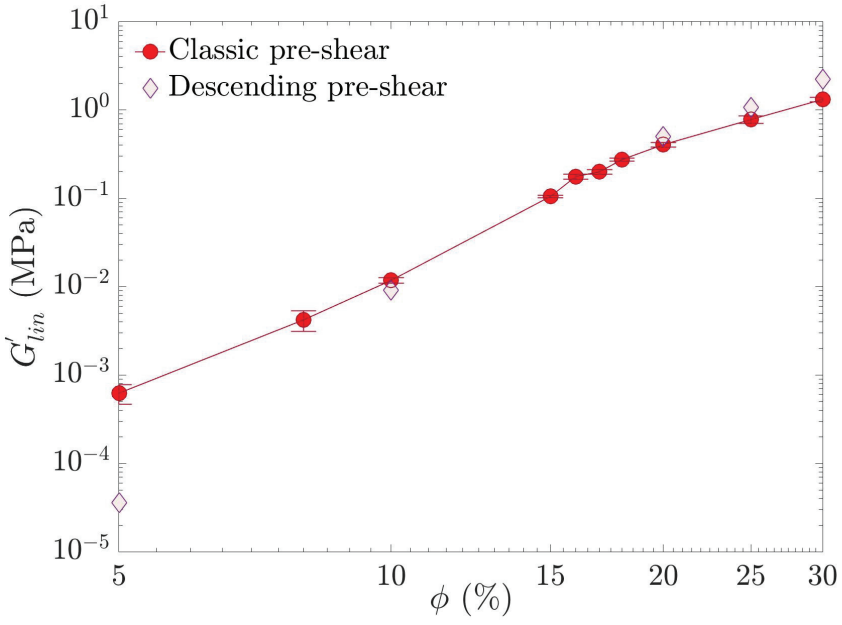

Figure 3.1 – Linear storage modulus, G'_{lin} as a function of the pure calcite volume concentration, ϕ. Comparison between two protocols: one with the usual pre-shear (one minute at $\dot{\gamma} = 10\,\mathrm{s}^{-1}$) and the other one with a descending pre-shear as a shear rate ramp from $\dot{\gamma} = 10\,\mathrm{s}^{-1}$ to $\dot{\gamma} = 0.01\,\mathrm{s}^{-1}$.

No significant effect of the pre-shear step is detected except for $\phi = 5\,\%$. At the lowest volume concentration in fact, strong sedimentation occurs during the descending pre-shear step, that allows to understand the lowering value of G'_{lin}. All the others points show similar values of linear storage

modulus. However, the descending pre-shear has an impact on the γ_{cr} only for the sample at $\phi = 10\,\%$ as shown in Figure 3.2 (purple curve).

In order to investigate the effect of the mixing process, the second modified protocol consists in making a progressive descending mixing rate in the ultraturrax (Section 2.2.1) during five minutes, followed directly by the amplitude sweep measurement. Here pre-shear and time structuration steps are suppressed. This protocol was tested on the sample at $\phi = 10\,\%$, for which the critical strain was very sensitive to the pre-shear protocol. Results are shown in Figure 3.2. In the legend, descending mixing *top* and *bottom*, denote two measurements performed on the same batch for the slowing down mixing protocol. But the difference between top and bottom lies in where we collect the calcite paste in the tube. The (small) difference in G' in certainly due to the sedimentation. The critical strain for these two samples (top and bottom) is almost the same.

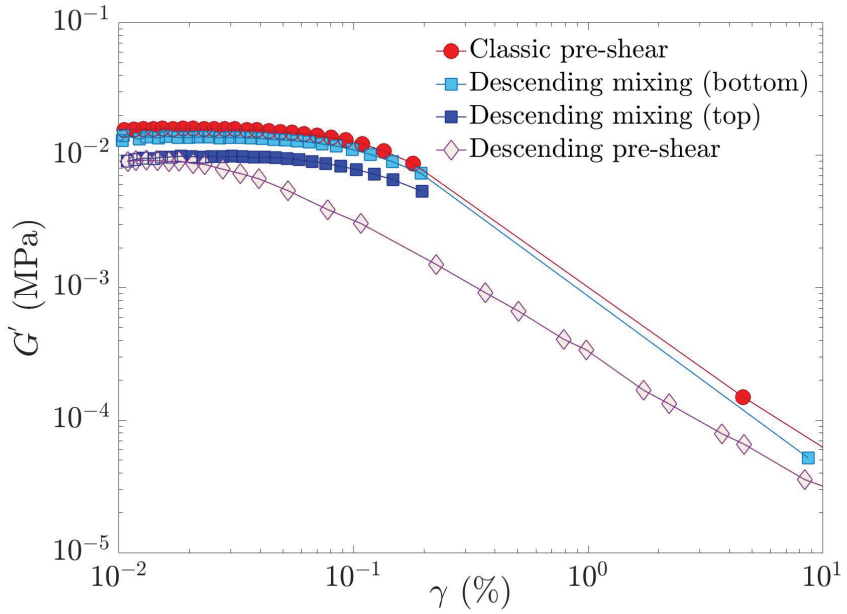

Figure 3.2 – Storage modulus G' as a function of the strain amplitude γ, for different protocols, at $\phi = 10\,\%$. Classic pre-shear is compared with the descending pre-shear protocol and with the descending mixing one. In particular top and bottom entries are two measurements on the same sample and correspond to the position of the collected material in the preparation tube.

To summarize a descending pre-shear does not affect the value of the storage modulus except for very low concentration ($\phi = 5\,\%$), so elasticity is robust to different protocols. However a descending pre-shear can affect the critical strain for $\phi = 10\,\%$. Modifying the mixing process, the homogeneity of the sample is not achieved for $\phi = 10\,\%$ and is worst for higher volume fraction resulting in samples impossible to test, i.e. powder not well homogenized with the solution. In conclusion these modifications undermine the accuracy of the rheological measurements.

3.2.2 Robustness of the definition of the critical strain

As already mentioned in Section 2.2.1, the critical strain γ_{cr} is defined as the strain value at the end of the storage modulus linearity. It is calculated in correspondence of a storage modulus value, which differs from the linear storage modulus, G'_{lin} of about $10 - 15\,\%$. To verify the robustness of this estimation of

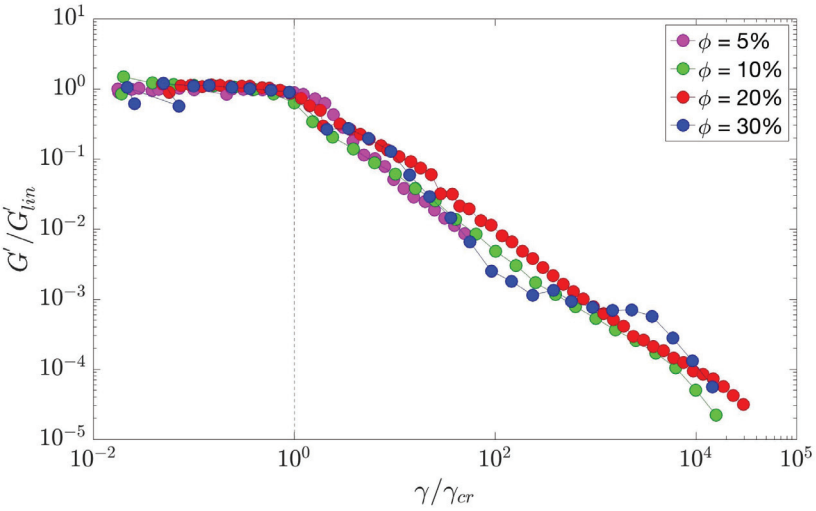

Figure 3.3 – Normalized storage modulus G'/G'_{lin} versus the normalized deformation $\gamma/\gamma_{\text{cr}}$ for a volume concentration between 5 and 30 %. Within the linear regime all the curves collapse on a master curve.

the critical strain, we plot the normalized storage modulus, G'/G'_{lin} versus the normalized deformation, $\gamma/\gamma_{\text{cr}}$ in Figure 3.3 for different volume concentration ranging from 5 to 30 %. As expected, in the linear regime, $\gamma/\gamma_{\text{cr}} \leq 1$, all the curves acquired at different ϕ, collapse on a same master curve. This confirms the robustness of the chosen estimation of critical strain that does not depend on ϕ.

3.2.3 Yield strain definitions

In our publication we refer to the limit of the linearity as the yield or critical strain γ_{cr}. In the literature, the yield strain has not an unanimous definition. For clarity, in the following section, a few examples are presented.

Definitions of yield strains in experiments

We take as an example the work of Koumakis et al. (2010) [5], on two step yielding in attractive colloids. The system studied here is a mixture of hard spheres and a linear polymer which induces short range depletion attraction. This mixture behaves as an attractive gel at low volume concentration of particles ($\phi = 0.10$) and as an attractive glass at higher concentration ($\phi = 0.60$).

In Figure 3.4 the experimental curves are shown for the entire volume concentration range of $\phi = 0.10 - 0.60$ (dynamic stress sweeps). In particular, the authors define several remarkable strains: the first yield point, γ_1, the crossing point yield, γ_{co}, and the second yield point, γ_2 (only for $\phi \geq 0.2$). These strains are traced in the yellow boxes of Figure 3.4 together with the critical strain γ_{cr} that we used in our analysis for the violet curves ($\phi = 0.6$). More precisely Koumakis et al. (2010) [5], define the first and second yields as the two distinct peaks of G'' and the γ_{co} as the yield strain at the crossover point where the loss and storage moduli are equal ($G = G''$). This crossover strain is frequently defines as the "yield strain" [8].

In the next section, we present the microscopic rupture scenarios associated with these different yield strains.

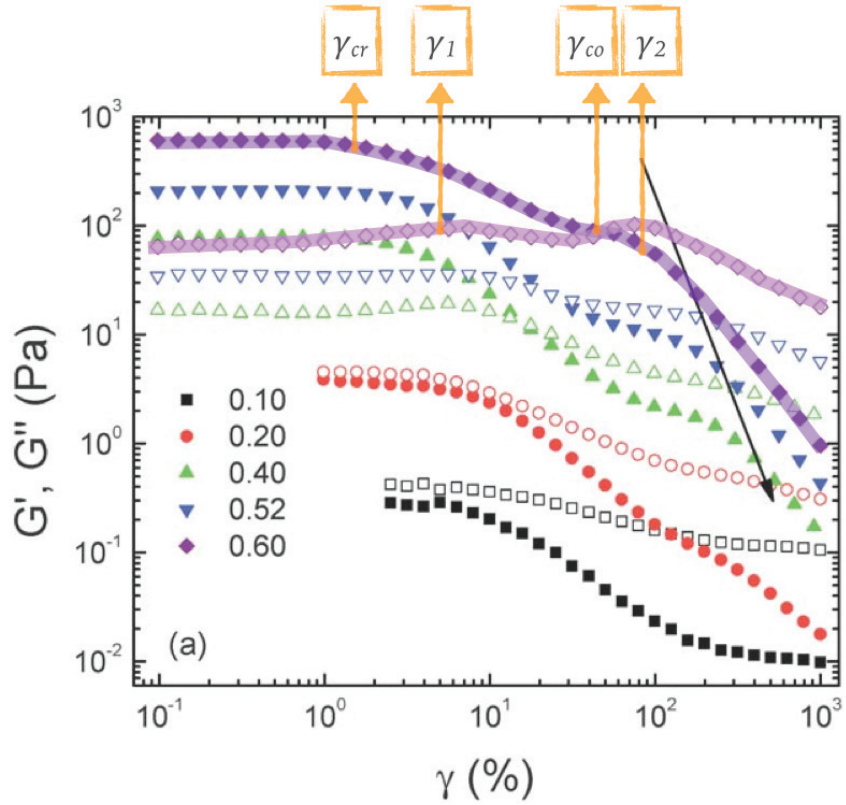

Figure 3.4 – Adapted from Koumakis et al.(2010) [5]. Dynamic strain sweep at $\omega = 10\,\mathrm{rad\,s^{-1}}$ for five different volume fractions with equal attraction strength (the arrow shows the approximate shift of the second G'' peak with decreasing volume fraction). The storage and loss moduli trends for $\phi = 0.6$ are underlines (violets lines) to define all the possibles yields in [5]. In particular γ_{cr} is the deformation at the end of linearity, γ_1 the first yield point, γ_{co} the deformation at the crossover point and γ_2 the second yield point. The plain symbols correspond to G' and empty symbols to G''.

Microscopic pictures

The pioneering theoretical and experimental studies by Shih et al. [9, 8], describe the scaling behavior of the elastic properties of colloidal gel. Here the structure is described at rest, within the limit of linearity and above the gelation threshold. In these conditions the fractal nature of the flocs dominates. Considering the structure of the gel as collection of flocs (fractals objects), Shih et al. found two distinct regimes with different floc structure i.e. strong and weak link, as sketched in Figure 3.5 (a)-(b). Initially this scaling theory was developed for polymer gel, to relate elastic properties and network structure and subsequently was successfully applied to numerous fractal gels (colloids, proteins,..) [2, 1, 7, 3].

The model assumes that colloidal and polymer gels have similar structures in which flocs correspond to polymer blobs and constitute the repeating unit in the sample volume. The fractal dimension d_f is linked to both particle concentration ϕ and average floc size ξ (defined as D in the article [6]) as: $\xi \approx a\,\phi^{1/(d_f-d)}$, where a is the particle diameter and d is the euclidean dimension equal to 3 [9]. In order to link the elastic constant to the floc size, Shih at al. consider the backbone as a linear chain of springs with ξ as a radius of gyration. With these assumptions, they express the elastic constant K of a system of size L as in Equation (3.1).

$$K \sim \left(\frac{L}{\xi}\right)^{d-2} K_\xi = \frac{K_\xi}{\xi} L \quad \text{(for d = 3)} \tag{3.1}$$

Where K_ξ is the elastic constant of the backbone. We can derive the elastic modulus G as: $G \sim K/L$. At the scale of particle-particle bond, they consider the rigidity k_0 (associated with bending motion K_0 as $k_0 = K_0/a^2$) and the force F_c at which the bond breaks.

Two regimes are then considered. In the **strong link** regime, the flocs are very deformable and their rigidity $K_\xi \sim (a/\xi)^{2+x} k_0$ (assuming a linear backbone with a fractal dimension x) determines that of the network:

$$G \sim \frac{K_\xi}{\xi} \sim \frac{k_0}{a} \phi^{(d+x)/(d-d_f)} \tag{3.2}$$

Looking at the definition of the elastic constant, large ξ correspond to weaker flocs. The end of the linear regime corresponds to a bond breaking inside the floc, such that $F_c \sim K_\xi \Delta\xi$:

$$\gamma_c \sim \frac{\Delta\xi}{\xi} \sim \frac{F_c}{k_0 a} \phi^{-(1+x)/(d-d_f)} \tag{3.3}$$

In the **weak link** regime, the weakest parts of the network are the bonds between flocs, of rigidity k_0. The elastic modulus then reads (in 3D):

$$G \sim \frac{k_0}{\xi} \sim \frac{k_0}{a} \phi^{(d-2)/(d-d_f)} \tag{3.4}$$

and the critical strain is such that $F_c \sim k_0 \xi \gamma_c$ or

$$\gamma_c \sim \frac{F_c}{k_0 a} \phi^{1/(d-d_f)} \tag{3.5}$$

Figure 3.5 sketches the two regimes: the strong (interfloc) link regime (a) is constituted by big deformable flocs acting as weak springs; the weak (interfloc) link regime (b) presents smaller flocs acting as hard spheres. The elastic constant (i.e. storage modulus) is lower in the case of strong link than in the case of the weak link regime. Moreover in Figure 3.5 (a)-(b) the red solid lines show the rupture associated with the critical strain at the limit of elasticity: inner-floc breaks for the strong link regime and inter-flocs breaks for the weak link one.

Table 3.1 sums up the two regimes, weak and strong link, in terms of volume fraction ϕ, fractal dimension d_f, ratio between floc and particle size ξ/a and floc deformation.

	Strong-link	**Weak-link**
ϕ	$\leq 15\,\%$	$\geq 20\,\%$
d_f	2.23	2.61
ξ/a	27	7
Deformation	intra-floc	inter- flocs

Table 3.1 – Summary of the conditions for the weak-link and the strong-link regimes for our pure calcite paste, ϕ is the volume fraction, d_f the fractal dimension and ξ/a the ratio between floc and particle size [6].

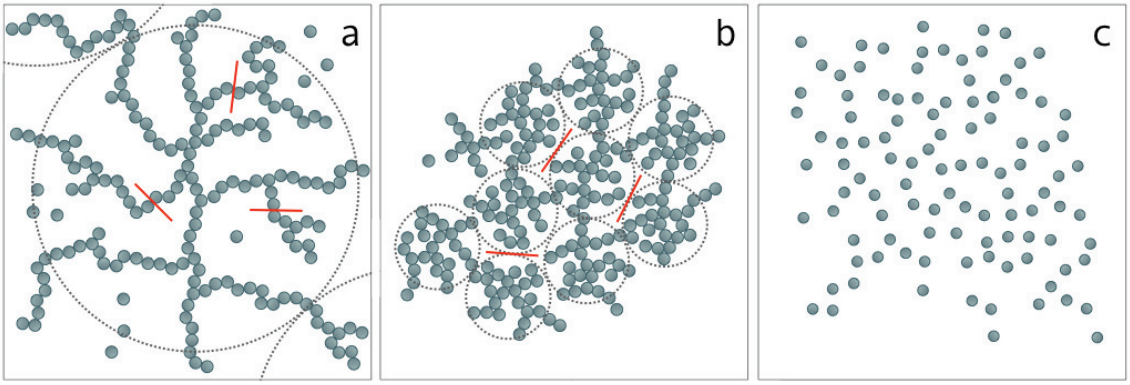

Figure 3.5 – Sketch of strong link (a) and weak link (b) structures in which dottet lines represent the flocs at rest. Solid lines show the rupture mechanism associated with the critical strain at the limit of elasticity. (c) Common condition for both strong and weak link after the extensive breaking of all links in correspondence to the yield (crossover) point.

Moreover, in a subsequent paper published in 1999, Shih et al. also focus on what they call the "yield strain", corresponding to the crossover strain γ_{co} as defined in [5] and represented in Figure 3.4.

They assume that at the crossover, there is an extensive breaking of the network (all bonds broken), such that $\gamma_{co} \sim F_c/(k_0 a)$ as Figure 3.5 (c).

In this picture, the elastic modulus and the end of linearity both depend on the microscopic interactions (local bending rigidity k_0 and critical force F_c) and on the network structure (solid volume fraction and fractal dimension). However, the yield strain is expected to depend only on the microscopic interactions. In the following chapter, we come back to the microscopic interactions discussed for instance in Shih et al 1999. [8].

Going back to the work by Koumakis et al. (2010) [5], we can investigate at the microscale the mechanisms associated with the yield points. In particular, referring to Figure 3.4, they identify the first yield, γ_1, as the in-cages or inter-clusters bonds breaking, and the second yield, γ_2, as the breaking of cages or clusters (i.e. clusters fragmentation). This study is made mostly on high volume concentrations suspensions, so for systems more comparable with the weak-link regime of Shih [9, 8].

Actually, the rupture mechanism associated to γ_1 is the same as associated to γ_{cr} in the weak link regime. This mechanism is shown in the sketch of Figure 3.6, from b_1 to b_2 (violet box). Moreover Figure 3.6, presents the effect of timescale of deformation versus typical time of aggregation in the system. Inside the violet box the double yielding rupture mechanism is presented, the first yield corresponding to the floc separation ($b_1 \rightarrow b_2$), while the second yield correspond to the breaking of the flocs in smaller parts ($b_2 \rightarrow b_3$). Decreasing the time scale of deformation (increasing $\omega, \dot{\gamma}$) they obtain a total floc breaking, as in c_3 (orange dashed line). Moreover from c_1 to c_2 we can observe a mechanism similar to the critical strain in the Shih's strong link regime.

Making a comparison with our system, for $\phi = 30\,\%$, we already showed that a double yielding appears (Figure 3.7). This result is consistent with Koumakis [5] which shows that this double yield behavior appear at high ϕ, and with the weak-link scenario for this concentration.

Finally we can compare the effect of the frequency in our system with the picture proposed by Koumakis (Figure 3.6). We find that strong-link is favored at higher frequency. In fact as shown in Figure 3.8, for $\phi = 20\,\%$ at $f = 1\,\text{Hz}$ our system behaves as a gel in the weak-link regime (Figure 3.6 b_1-b_3), while at $f = 10\,\text{Hz}$ it behaves as in the strong link one (Figure 3.6 c_1-c_2). This implies a shift of

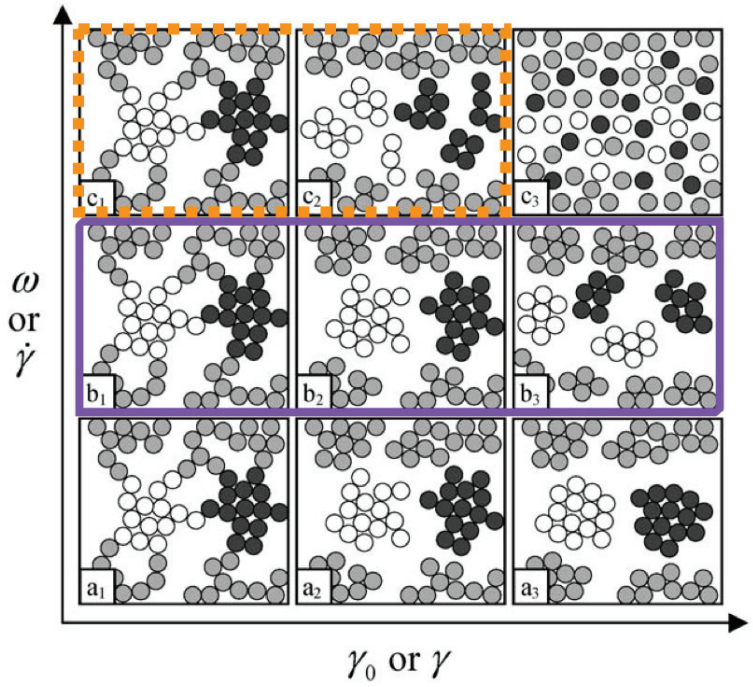

Figure 3.6 – Reproduced from Koumakis et al. (2010) [5]. Structure representation of an attractive gel at rest and under shear. Increasing from left to right is the applied strain in both steady (γ) and oscillatory (γ_0) experiments. Increasing from bottom to top is the shear rate ($\dot{\gamma}_0$) or frequency of oscillation. The scheme describes how different regimes of strain rate and applied strain lead to different structural properties under shear.

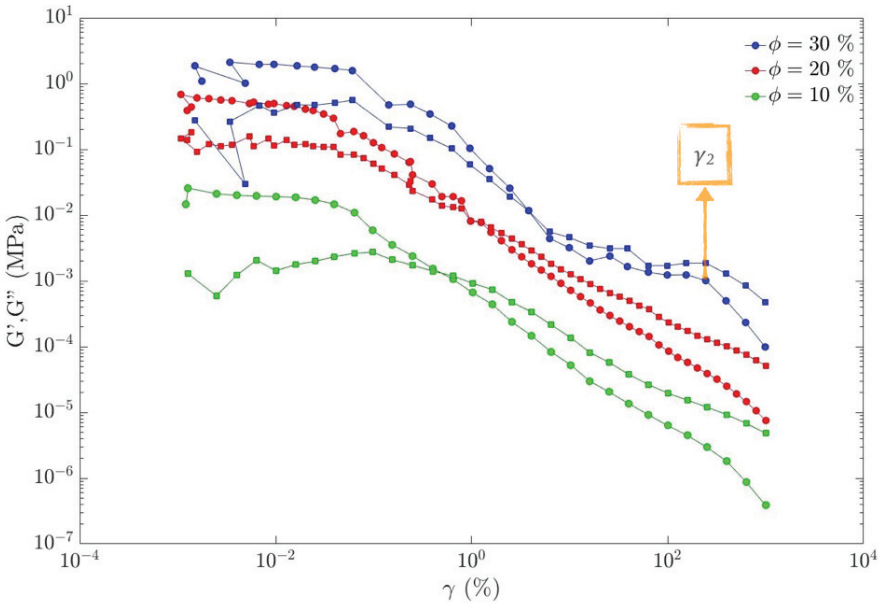

Figure 3.7 – Amplitude sweep at 30 %, 20 % and 10 % volume concentration. Full circles represent the G' values and the full squares the G'' values. For $\phi = 30$ %, in the weak-link regime, a second yield strain can be observed at $\gamma_0 \approx 100$ %.

the minimum γ_{cr} toward higher ϕ when frequency increases. This is in good agreement with the effect proposed by Koumakis at high frequency.

To conclude, in Figure 3.5 we have simply adapted Shih's sketch in order to provide a microscopic

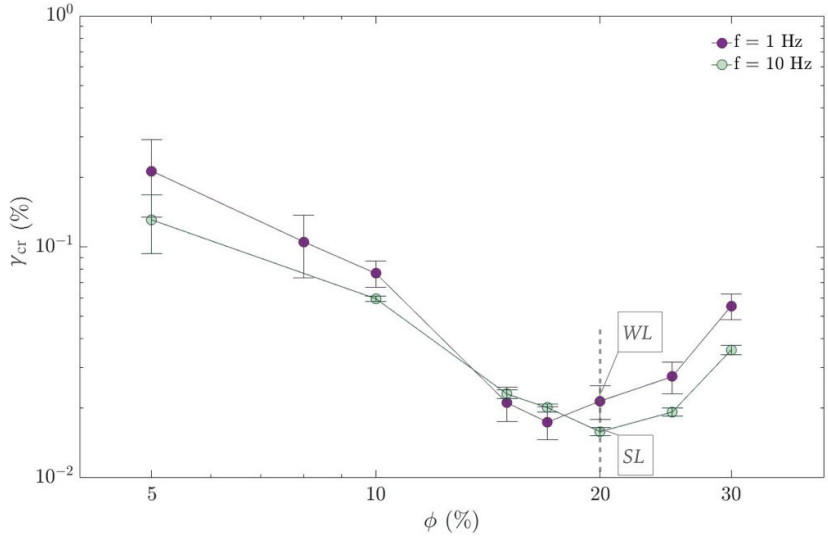

Figure 3.8 – Effect of frequency on the limit of linearity deformation value, γ_{cr} for pure calcite suspensions in a volume concentration range from 5 to 30 %.

view, representative of the fractal dimension and floc size of our calcite paste. These sketches are valid at rest (i.e. at small oscillatory deformation), contrary to the ones in the article from Koumakis, which characterize the behavior of their gel under shear (Figure 3.6). Whereas our system behaves completely differently from the colloid-polymer mixture investigated by Koumakis, we found common deformation and rupture mechanisms, giving an overview of the generality of this description of fractal gels.

In this chapter the influence of the concentration of calcite suspensions on their mechanical behavior is well analyzed, without any modifications of the chemistry of the system. We focused our analysis in the elastic regime, taking as yield point the limit of linearity, as it is well characterized due to the bad reproducibility of our system behaviors after this linear regime. We observed two regimes, as predicted by Shih et al. [9], respectively at low (strong-link) and high (weak-link) volume concentration. Increasing ϕ also the fractal dimension rises. In the weak-link regime the deformation occurs inside the flocs, in the strong-link regime between the flocs.

In the next chapter we focus mainly on the influence of additives (i.e. simple ionic species) on both mechanical properties and interparticles forces.

Bibliography

[1] P. Cassagnau. Melt rheology of organoclay and fumed silica nanocomposites. *Polymer*, 49(9):2183–2196, 2008.

[2] G. M. Channell and C. F. Zukoski. Shear and compressive rheology of aggregated alumina suspensions. *AIChE Journal*, 43(7):1700–1708, 1997.

[3] T. Hagiwara, H. Kumagai, and K. Nakamura. Fractal analysis of aggregates in heat-induced BSA gels. *Food Hydrocolloids*, 12(1):29–36, 1998.

[4] A. Helal, T. Divoux, and G. H. McKinley. Simultaneous rheoelectric measurements of strongly conductive complex fluids. *Physical Review Applied*, 6(6):064004, 2016.

[5] N. Koumakis and G. Petekidis. Two step yielding in attractive colloids: transition from gels to attractive glasses. *Soft Matter*, 7(6):2456–2470, 2011.

[6] T. Liberto, M. Le Merrer, C. Barentin, M. Bellotto, and J. Colombani. Elasticity and yielding of a calcite paste: scaling laws in a dense colloidal suspension. *Soft matter*, 13(10):2014–2023, 2017.

[7] J. Segovia-Gutiérrez, C. Berli, and J. De Vicente. Nonlinear viscoelasticity and two-step yielding in magnetorheology: A colloidal gel approach to understand the effect of particle concentration. *Journal of Rheology (1978-present)*, 56(6):1429–1448, 2012.

[8] W. Y. Shih, W.-H. Shih, and I. A. Aksay. Elastic and yield behavior of strongly flocculated colloids. *Journal of the American Ceramic Society*, 82(3):616–624, 1999.

[9] W.-H. Shih, W. Y. Shih, S.-I. Kim, J. Liu, and I. A. Aksay. Scaling behavior of the elastic properties of colloidal gels. *Physical Review A*, 42(8):4772, 1990.

Chapter 4

Role of ionic additives on paste elasticity

In order to control the mechanical properties of calcite paste, it is necessary to understand the role of the interaction forces that occur between $CaCO_3$ particles and how to modify them. In this regard, this chapter describes the physico-chemical influence of inorganic additives (i.e. simple ions) on the calcite paste and its consequences on the paste elasticity.

Contents

4.1 Introduction

4.1.1 Linking macroscopic rheology to particle interaction models

In the previous chapter, we have presented the characterization of the elastic domain of calcite suspensions for a wide range of volume concentrations [8]. Introducing the model of Shih et al. (1990) [15], we have described the variation of the floc structures at low and high volume concentrations from the scaling relations of the storage modulus and critical strain with ϕ.

In this chapter, we want to tune the elasticity with particle interactions, by adding simple ions, as detailed in the following section. We present below two models which link macroscopical and microscopical behaviors [14, 3].

Firstly, Shih et al. [14] investigate the yield forces between two particles within the framework of DLVO interactions under high attractive conditions (i.e. no secondary minimum in DLVO potential). Both the radial (x) and the lateral (y) motion between two particles are analyzed, as shown in Figure 4.1, were r_0 and s_0 are respectively the center-to-center and surface-to-surface distances. at equilibrium.

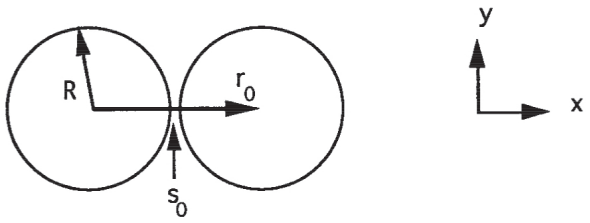

Figure 4.1 – Reproduced from Shih et al. (1999) [14]. Schematic of the coordinates of a two-particle system with r_0 and s_0 respectively the center-to-center and surface-to-surface distances.

Figure 4.2 shows the attractive interparticle forces F in both directions for different values of the Zeta potential ζ proposed by [14]. The authors argue that the force in the lateral direction shows a maximum (i.e. $-F_y^{max}$ in Figure 4.2 (b)) and an elastic-like ($F = ky$) behavior for small y.

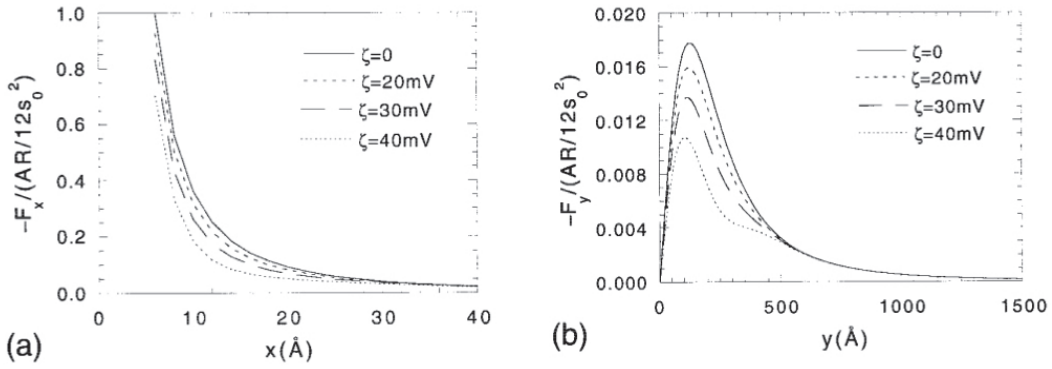

Figure 4.2 – Reproduced from Shih et al. (1999) [14].(a) $-F_x$ versus x where F_x is the restoring force in the radial direction between two particles with various ζ. (b) $-F_y$ versus y where F_y is the restoring force in the lateral direction y between two particles with various ζ. Both F_x and F_y were obtained numerically from the full DLVO interaction energy for alumina particles of $R = 200$ nm. For calculation details see [14]. Note that $-F_x$ decreases monotonically as x increases, whereas $-F_y$ exhibits a maximum at an intermediate $y = y_{max}$. Moreover, y_{max} decreases as ζ increases.

Once demonstrated that the elasticity is due to the lateral (shear) displacement between particles, the authors express the storage modulus G', the yield strain γ_y and the yield stress τ_y as a function of ζ:

$$G'(\zeta) = G_y'^0(1-\alpha\zeta^2) \tag{4.1}$$

$$\gamma_y(\zeta) = \gamma_y^0(1-0.5\alpha\zeta^2) \tag{4.2}$$

$$\tau_y(\zeta) = \tau_y^0(1-1.5\alpha\zeta^2) \tag{4.3}$$

where the 0 superscript denotes that $\zeta = 0$ and $\alpha \propto \lambda_D^{-1}$:

$$\alpha = \left(\frac{2\pi\varepsilon_0\varepsilon_w}{\lambda_D}\frac{e^{-k_B s_0}}{1+e^{-k_B s_0}}\right) \Big/ \left(\frac{A}{12s_0^2}\right) \tag{4.4}$$

where ε_0 is the vacuum permittivity, ε_w the water dielectric constant and A is the Hamaker constant.

A second class of models [2, 17, 12, 3] assumes that the yield stress arises from the DLVO interaction which resists to stretching (i.e. radial displacement).

In particular Flatt and Bowen [3] propose a model called Yield Stress mODEL (YODEL), already mentioned in Section 1.4, in which they also express the shear yield stress as a function of interparticle forces finding a similar expression compared to Equation (4.3):

$$\frac{\tau_y}{\tau_y^{max}} = 1 - \frac{24\pi\varepsilon\varepsilon_0 H^2}{\lambda_D A(1+e^{-H/\lambda_D})}\zeta^2 \tag{4.5}$$

where ε is the relative dielectric constant of the continuous phase and $H = f(\phi)$ is the non-zero minimum separation distance between particles ("contact"). This term is also proportional to the inverse of the Debye length.

In this chapter, we now seek to relate the experimental rheological values to computed DLVO interactions.

4.1.2 Studied systems

To understand the physical and chemical mechanisms that drive the surface modifications, we decide to analyze separately several ionic species that change the pH and the ionic strength of the calcite suspension.

In particular we study the effects of the following species: calcium hydroxide ($Ca(OH)_2$), sodium hydroxide (NaOH), hydrochloric acid (HCl), calcium chloride ($CaCl_2$), as detailed in Table 2.1, Section 2.2.1. These species have already been studied in the literature [4, 10, 6, 9, 11], but not all at the same time for the same system and in a narrow range of molar composition.

Chemical speciation modelling with the software MINTEQ is performed for all the samples in order to identify the main reactions taking place and the main ions in the solution at equilibrium with calcite. We investigate a wide space of parameters, including strong variations of pH —from 6.5 to 12.7— and ionic strength —from $I = 10^{-3}$ to 1 M. These broad ranges are tested to reach the best conditions in

terms of rigidity and deformation of the paste, compared to the pure calcite one [8].

Due to the complexity of the physico-chemical analysis we report in this chapter only the data series for which we have a complete understanding: calcium and sodium hydroxide. All other data are presented in Annex B. For clarity we remind in Table 4.1 the samples described in this chapter, their related protocols and volume concentration range. To briefly recall: the first protocol, α), is composed of a pre-shear, a short time structuration (5 min) and an amplitude sweep. The other one β) is constituted by a pre-shear, a long time structuration (10 h) and an amplitude sweep (see Section 2.2.1 for more details). In particular we mainly focus on suspensions at ϕ=10 % for which Zeta potential measurements have been performed.

Samples	α	ϕ_α **(%)**	β**)**	ϕ_β**(%)**
Pure	•	10-20	•	10-20
3 mM **Ca(OH)**$_2$	•	20	•	10-20
15 mM **Ca(OH)**$_2$	•	20	•	10-20
30 mM **Ca(OH)**$_2$	•	20	•	10-20
50 mM **Ca(OH)**$_2$	•	20	•	10-20
94 mM **NaOH** + 3 mM Ca(OH)$_2$	•	10-20	•	10-20

Table 4.1 – List of selected samples. Columns α and β indicate the applied protocols and ϕ_α and ϕ_β the tested volume concentration range in each protocol.

4.2 Calcium hydroxide

Calcium hydroxide ($Ca(OH)_2$) production is briefly introduced presenting the "lime cycle" (or calcium carbonate cycle). Calcium carbonate based materials are commonly used in the construction field since antique Egypt [16]. Figure 4.3 (a) shows the classic manufacture and setting of lime (calcium oxide or hydroxide). The main reactions driving the lime cycle [16] are detailed in Figure 4.3 (b).

Starting from calcium carbonate, also called limestone, a calcination process at very high temperature (800-1200°C) produces calcium oxide, also defined as burnt or quick lime. In presence of water, CaO can hydrolyze becoming calcium hydroxide, $Ca(OH)_2$, also called portlandite or slaking lime. This reaction releases heat (exothermic). $Ca(OH)_2$ once exposed to the atmosphere reacts to form $CaCO_3$, captures CO_2 and releases water (Section 2.4.1). The carbonation of hydrated lime requires the presence of adsorbed water and the calcium carbonate formation is thus affected by the relative humidity [13].

4.2.1 Elasticity of calcite paste with calcium hydroxide: temporal evolution and carbonation

We present the long term evolution of the elastic modulus of calcite paste with calcium hydroxide obtained with protocol β. The sample is maintained in a moisture chamber for 10 hours. We focus on samples at $\phi = 10\,\%$, the effect of calcite concentration is discussed later in this chapter. Figure 4.4 shows the temporal evolution for various concentrations of calcium hydroxide added to the paste. To simplify the discussion, we introduce the term c as the concentration of the inserted calcium hydroxide into the calcite paste.

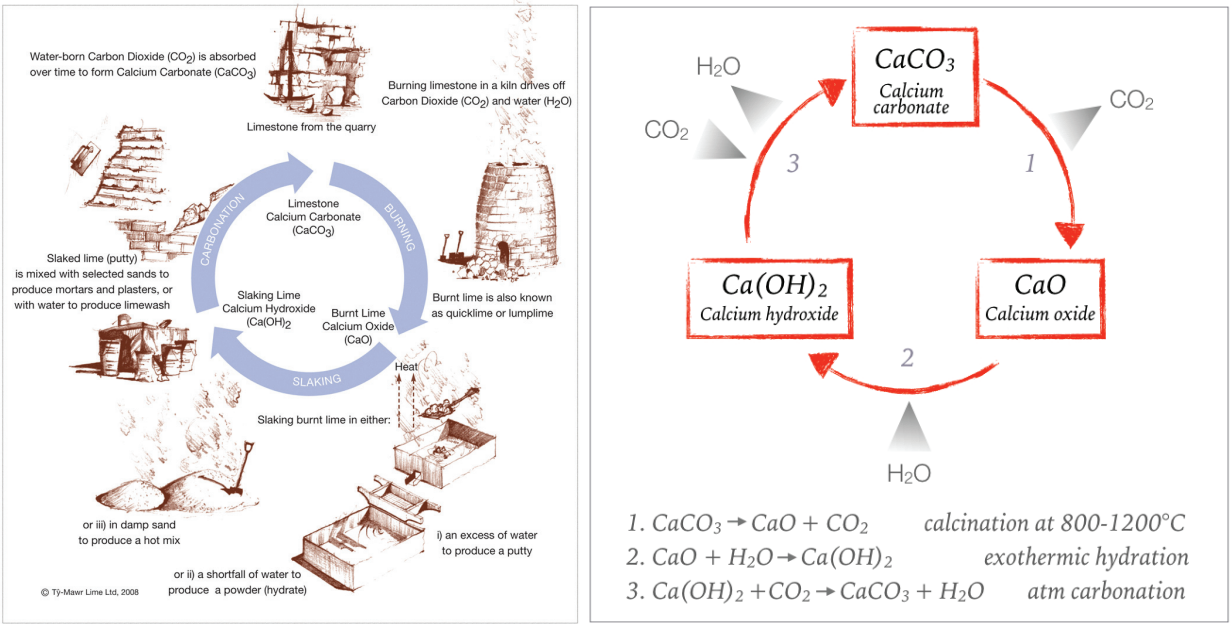

(a) **(b)**

Figure 4.3 – The lime cycle. (a) Image representing the processes of the classic manufacture and setting of lime (© Tŷ-Mawr Lime Ltd, 2008). (b) Description of the main reactions constituting the lime cycle.

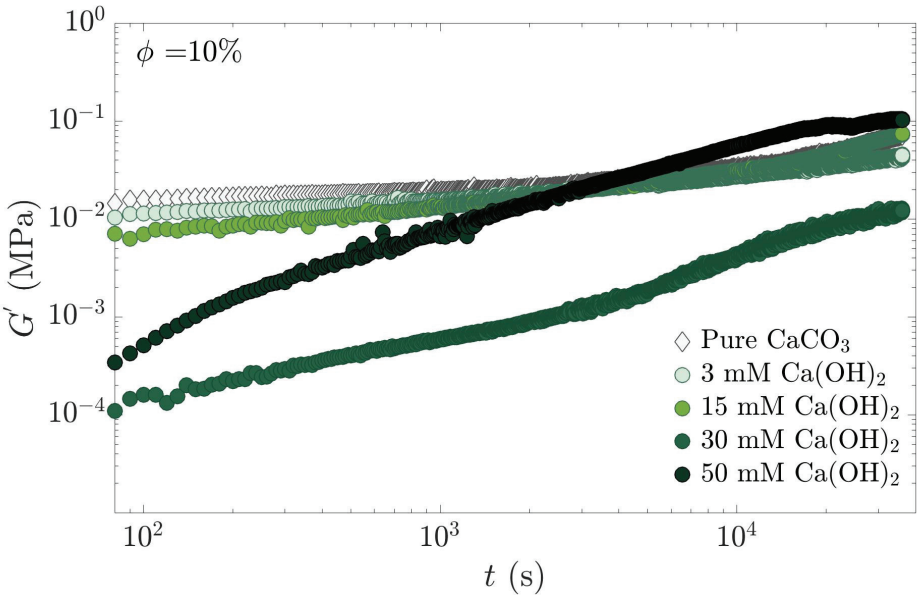

Figure 4.4 – Time evolution of the storage modulus G' of $\phi = 10\,\%$ calcite suspensions, for increasing $Ca(OH)_2$ concentrations.

Two behaviors are observed: pure calcite paste and paste containing $c = 3$ and 15 mM present a slow increase of G' with time whereas suspensions with $c = 30$ and 50 mM show a large increase. Then inserting calcium hydroxide lead to a global decrease in the initial linear storage modulus $G'(0)$. More precisely, the elastic modulus in the sample with $c = 30$ mM is lower than for the one with $c = 50$ mM. We thus observe a non monotonic trend of $G'(0)$ with c.

We know from the lime cycle that $Ca(OH)_2$ strongly reacts with the atmospheric CO_2, producing

calcite. We thus suspect that this temporal evolution is linked to the dynamics of carbonation and CO_2 uptake from the atmosphere. In our setup the sample is protected by a moisture chamber, but the CO_2 access is not totally prevented.

To test this idea, we try to limit the contact of the sample with carbon dioxide. We surround the gap between the two plates of the rheometer geometry with oil, as shown in Figure 4.5 (a). Oil is added after the sample loading. We test both colza and paraffin oils with a sample containing $c = 50$ mM. Figure 4.5 (b) and (c) show the lower plate at the end of the test (10 h), i.e. when the upper plate is removed, respectively for colza and paraffin oils. Both plates are covered with sand (red colored) paper.

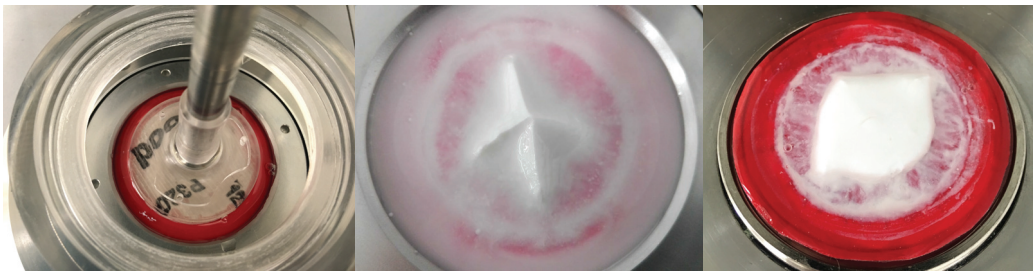

(a) **(b)** **(c)**

Figure 4.5 – (a) Picture of plate-plate geometry for which oil is added all around the gap, once the sample is loaded. (b)-(c) Pictures of the lower plate, respectively for colza and paraffin oils, at the end of the sample evolution (10 h) and once the upper plate is removed. Both plates are covered with sand (red colored) paper.

From Figure 4.5 (b) we can notice that the colza oil mixes with the calcite paste and is not suitable for our purpose. Figure 4.6 thus compares suspensions obtained for $c = 50$ mM with and without paraffin oil around the sample.

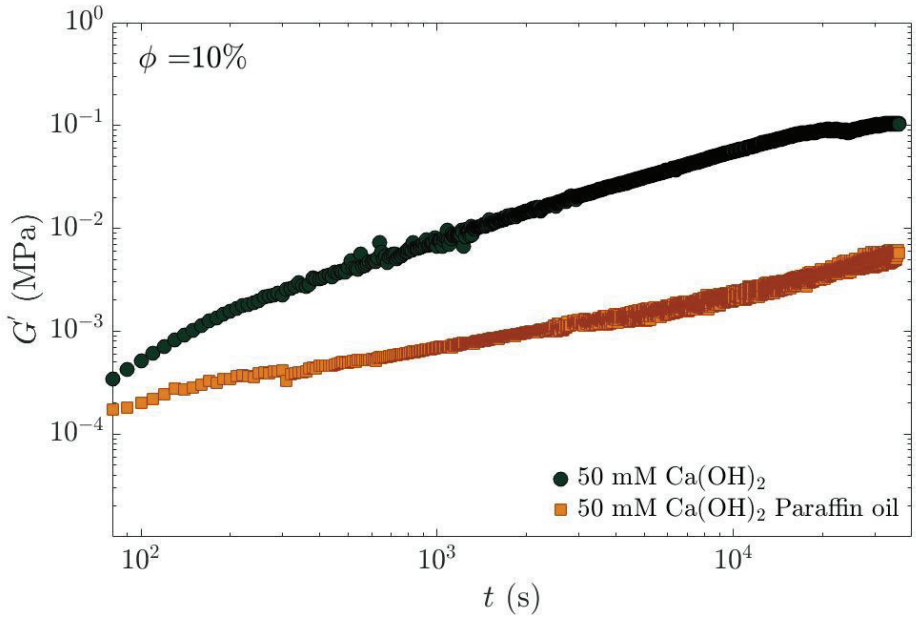

Figure 4.6 – Time evolution of the storage modulus of calcite suspension with 50 mM of $Ca(OH)_2$ for $\phi = 10\,\%$. In one case, paraffin oil is added around the plate-plate geometry to reduce the contact with the CO_2.

The sample with paraffin oil exhibits a slower evolution of the storage modulus in time than the sample without paraffin oil, whose rim is in contact with the atmosphere. These results confirm the key role of CO_2 in presence of calcium hydroxide and more general in carbonate equilibria, as already discussed in Sections 1.1 and 2.4.1. We will come back to this point later in this chapter.

To go one step further, a complete chemical speciation is calculated for each sample with the software Visual MINTEQ using the protocol presented in Section 2.4. The pH used for the chemical speciation are the ones measured in Faenza, before the Zeta potential tests. Every precaution were taken to reduce the contact with the CO_2 during the preparation and shipment of the $\phi = 10\,\%$ samples. The samples were kept well sealed until the measurements, that took place 3-4 days after the preparation. We verify a pH difference between the fresh samples and the ones measured in Faenza within the pH-measurement incertitude ± 0.2.

Table 4.2 shows the MINTEQ chemical speciation for $\phi = 10\,\%$, for various initial calcium hydroxide concentration c.

	No atmosphere		Atm pressure		Exp. condition t(0)		Exp - No atm
c (mM)	pH	Ca^{2+}(mM)	pH	Ca^{2+}(mM)	pH_{meas}	Ca^{2+}(mM)	Δsolid(mM)
0	9.9	0.12	8.2	0.51	8.9	0.24	-0.12
3	11.7	2.8	8.2	0.51	10.3	0.15	2.9
15	12.4	11.8	8.2	0.51	11.0	0.55	14.5
30	12.4	14.2	8.2	0.51	11.8	3.3	26.4
50	12.4	14.2	8.2	0.51	12.4	13.0	33.0

Table 4.2 – MINTEQ chemical speciation for $\phi = 10\,\%$ samples, increasing c. Values of pH and calcium ions concentration Ca^{2+} are reported for our experimental condition and in the two extreme cases of a system without atmosphere and in equilibrium with the atmosphere. Δsolid is the calcite solid variation between the system at the experimental condition and without atmosphere ($\Delta\text{solid} < 0$ correspond to dissolution and $\Delta\text{solid} > 0$ to precipitation).

In particular, we report the values of pH and calcium ion concentration Ca^{2+} for our experimental conditions and in the two extreme cases: a system without atmosphere and in equilibrium with the atmosphere (pCO_2=0.00038 atm). The column: "Exp. condition t(0)", represents the chemical analysis made at the experimental pH (fresh paste). Here the concentration of dissolved CO_2 and ionic species concentrations are intermediate between the absence of atmosphere and the equilibrium condition with atmosphere. We find that the experimental values are closer to the equilibrium with no atmosphere. This is because the exchange with CO_2 is limited during sample storage before the experiments.

Finally the last column Δsolid represents the calcite solid variation between the system at the experimental condition and without atmosphere. $\Delta\text{solid} < 0$ corresponds to a dissolution of calcite and $\Delta\text{solid} > 0$ a precipitation of $CaCO_3$. Note that the solubility limit of calcium hydroxide is around 20 mM [5]. MINTEQ calculation for our calcite-portlandite system gives a value of 19 mM.

From Table 4.2 we can observe that the final equilibrium conditions (i.e. atmospheric pressure) for all samples are identical. We will come back to this point later in this chapter.

4.2.2 Fresh paste behavior

Chemical speciation

The other initial chemical conditions for our calcite suspensions are recapitulated in Table 4.3.

c (mM)	pH_{meas}	ζ (mV)	Ca^{2+} (mM)	I (mM)	λ_D (nm)
0	8.9	9.3±0.99	0.24	0.73	11.1
3	10.3	10.9±0.11	0.15	0.47	13.8
15	11.0	12.5±0.12	0.55	1.7	7.3
30	11.8	18.6±1.4	3.3	10.2	3.0
50	12.4	18.6±0.28	13.0	43.2	1.4

Table 4.3 – Values obtained by MINTEQ chemical speciation (Ca^{2+}, I) with pH and Zeta potential ζ measurements for $\phi = 10\,\%$ samples, increasing $Ca(OH)_2$ concentration c. The Debye length λ_D is calculated from the ionic strength I values.

More precisely this table reports the values of measured pH and Zeta potential ζ, the values obtained from MINTEQ calculations for the concentration of calcium ions Ca^{2+} and ionic strength I, and the calculated Debye length $\lambda_D \propto 1/\sqrt{I}$. All data correspond to $\phi = 10\,\%$ suspensions with increasing c in the initial conditions.

Zeta potential

In Figure 4.7, Zeta potential values are plotted as a function of the corresponding Ca^{2+} concentration in the suspensions. The measurements are carried out at ϕ = 10 %.

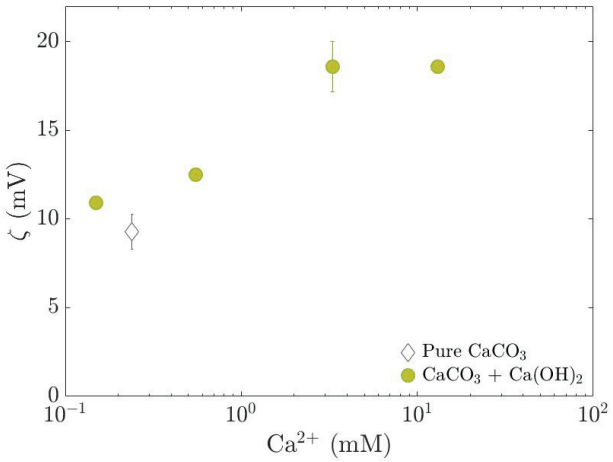

Figure 4.7 – Zeta potential, ζ, as a function of the concentration of calcium ions Ca^{2+}.

Zeta potential ζ increases then saturates with the amount of calcium ions, except for pure calcite. The raise of ζ is due to the adsorption of Ca^{2+} ions on the calcite surface. We thus confirm the role of calcium as a potential determining ion [4, 10]. More generally the Zeta potential is determined by the relative quantities of potential determining ions (PDI) (Ca^{2+}, CO_3^{2-}). PDI are the ones that adsorb preferentially on the calcite surface [1]. These ions are calculated by MINTEQ at our experimental conditions as specified in Table 4.4. Carbonate CO_3^{2-} ions are reported with bicarbonate HCO_3^- and

OH^- ones (carbonate equilibria). We also calculated a potential determining ions ratio $[Ca^{2+}]/[CO_3^{2-}]$ to compare the positive and the negative charge contribution in the solution. An increase in PDI ratio results in a larger quantity of Ca^{2+} which influences ζ by raising the positive charge.

c (mM)	CO_3^{2-} (mM)	HCO_3^- (mM)	OH^- (mM)	PDI ratio
0	$1.8 \cdot 10^{-2}$	$4.2 \cdot 10^{-1}$	$8.6 \cdot 10^{-3}$	13.1
3	$2.8 \cdot 10^{-2}$	$2.7 \cdot 10^{-2}$	$2.1 \cdot 10^{-1}$	5.2
15	$8.7 \cdot 10^{-3}$	$1.6 \cdot 10^{-3}$	1.1	63.2
30	$2.3 \cdot 10^{-3}$	$5.8 \cdot 10^{-5}$	6.9	$1.4 \cdot 10^{3}$
50	$1.1 \cdot 10^{-3}$	$5.5 \cdot 10^{-6}$	30.1	$1.2 \cdot 10^{4}$

Table 4.4 – Values obtained by MINTEQ chemical speciation at the experimental conditions, increasing $Ca(OH)_2$ concentration c. The potential determining ions (PDI) ratio is defined in the text.

In the case of pure calcite, the PDI ratio is higher than the sample with 3 mM of calcium hydroxide due to the initial calcite dissolution. Adding calcium hydroxide, the calcite is not dissolving and the main potential determining ion in the suspension is Ca^{2+} coming from $Ca(OH)_2$ dissolution. For these samples the amount of carbonate CO_3^{2-} is very low and decreases with increasing c. In fact, the raise of c results in a continuous increasing of the PDI ratio.

In the following, our results are compared with the previous work by Pourchet et al. [11]. They measured the Zeta potential for calcite suspensions with a particle size of 7μm and a solid fraction of about 10 %. Both $Ca(OH)_2$ and $CaCl_2$ are used as a source of calcium ions. In Figure 4.8 we superpose our results (green dots) to the points obtained by Pourchet et al. [11] for both calcium hydroxide (closed symbols) and calcium chloride (open symbols) addition.

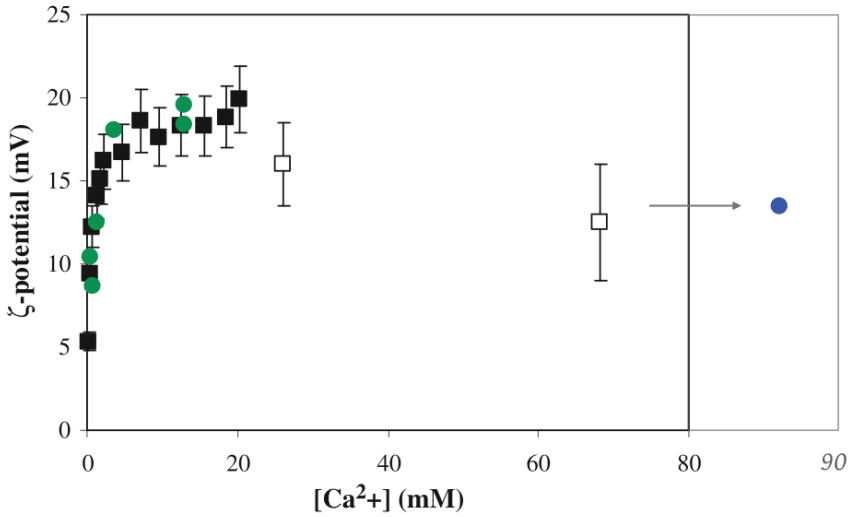

Figure 4.8 – Adapted from Pourchet et al. [11]. Zeta potential ζ of the calcite suspension as a function of the calcium ion concentration. Comparison between ζ measurements from [11]: closed (calcium hydroxide) and open symbols (calcium chloride) and our suspensions with calcium hydroxide (green points) and calcium chloride (blue point). The error for our point is at most 1 mV.

Our results agree perfectly with the data of Pourchet et al. [11] although obtained at different ionic strengths.

We add a point at $c = 100$ mM with a corresponding $\zeta = 19.6$ mV. The measure of pH for this point (12.7) is higher than 12.4 (i.e. maximum pH reachable at portlandite saturation without atmosphere).

We do not explain this pH-value and we decide to take the same chemical speciation as at pH= 12.4. Moreover we also add $CaCl_2$, obtaining $\zeta = 13$ mV for $[Ca^{2+}] = 87$ mM (blue dot). Both points are in perfect agreement with the trend shown in Figure 4.8.

Moreover, Figure 4.8 shows that the Zeta potential reaches a plateau for a calcium concentration value less than 10 mM. Pourchet et al. correlated it with a plateau in the calcium adsorption for the same concentration $[Ca^{2+}] \sim 10$ mM (measured by Atomic Emission Spectroscopy) [11]. Above this Ca^{2+} value, the weak decrease in ζ is attributed to an electrostatic screening [9, 6, 11].

Elastic modulus at ϕ=10 % and micro-macro link: comparison with existing models

The storage modulus of the fresh paste $G'(0)$ recorded at the beginning of the long time structuration tests (Figure 4.4), is reported in Figure 4.9 as a function of c. A minimum of $G'(0)$ is observed for the sample containing 30 mM of $Ca(OH)_2$.

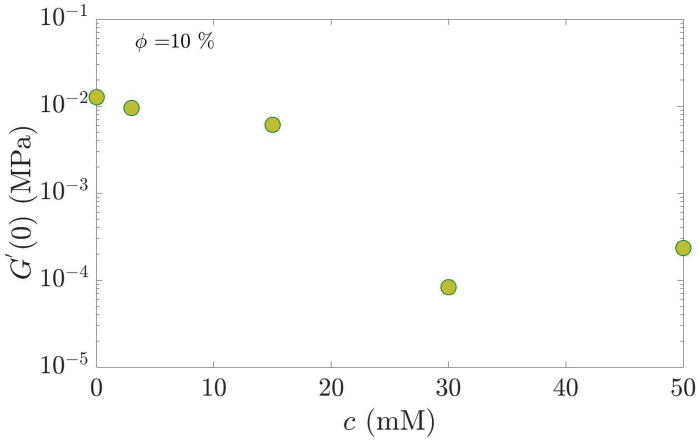

Figure 4.9 – Initial storage modulus $G'(0)$ as a function of c. We observe a minimum of $G'(0)$ for the sample containing 30 mM of initial $Ca(OH)_2$.

We can compare this non-monotonic behavior exhibiting a minimum with the interaction model predictions by Shih et al. (1999) [14] and by Flatt and Bowen (2006) [3] discussed above. Both models predict a dependency of the yield properties as ζ^2/λ_D. In particular from Equations (4.1) to (4.3) and (4.5), G', γ_y and τ_y decrease if the term ζ^2/λ_D increases. From Table 4.3, we find that the value of ζ^2/λ_D, in our experimental system, increases with c, as shown in Figure 4.10. In particular, increasing c from 30 to 50 mM, ζ is almost the same while λ_D is divided by 2. The increase of ζ^2/λ_D cannot explain the non monotonic dependence of the storage modulus in Figure 4.9, in particular the increase of $G'(0)$ from 30 to 50 mM of $Ca(OH)_2$.

To better understand this behavior now we estimate the complete DLVO interaction in the fresh paste.

4.2.3 DLVO interactions in calcite paste

Role of physico-chemistry

In order to link the macroscopic properties with microscopic interaction and to understand the influence of different ions on mechanical properties, DLVO calculations are made for various geometries [7]. As

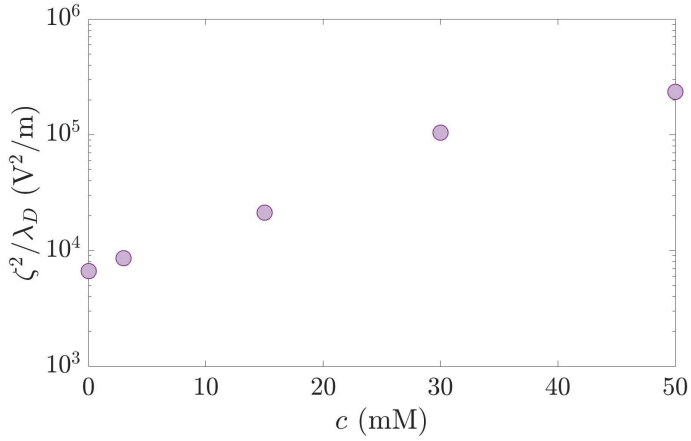

Figure 4.10 – Values of ζ^2/λ_D as a function of c.

already detailed in Section 1.2.5, DLVO interaction is calculated by the combination of attractive van der Waals and electrostatic repulsion contributions. In particular, as the particles have facets as shown in Section 2.1.2, we first consider the interactions between two calcite planes. The potential per unit area W_{DLVO} reads:

$$W_{DLVO} = -\frac{A}{12\pi x^2} + \frac{2\varepsilon_w \zeta^2}{\lambda_D} e^{-x/\lambda_D} \tag{4.6}$$

where x is the distance between the two planes and ε_w the water permittivity. We compare the interaction potential to $k_B T/a^2$.

Figure 4.11 shows the results of DLVO calculation for a plane-plane geometry, for increasing value of inserted calcium hydroxide, c. The Debye length is estimated from chemical speciation (MINTEQ) and Zeta potential is given by measurements detailed in Table 4.3.

For pure calcite the potential is weakly attractive with a barrier of the order of $k_B T$. Increasing c, the repulsion barrier increases to around 17 $k_B T$ for $c = 30$ mM then drops (below zero) for $c = 50$ mM. However, the potential estimated at 50 mM is very sensitive to the pH value used for chemical speciation. To illustrate this we plot in Figure 4.11 two curves for the $c = 50$ mM: a solid line for the measured pH$=$ 12.4 and a dashed line for a pH$=$ 12.2. The difference between the two curve shows the impact on the barrier of the error bar on the measured pH$=$ 12.4$\pm$0.2.

To go one step further, for a pH ranging from 10 to 12.5, we estimate the maximum value of the plane-plane interaction potential $W_{\max}$ (shown in red in Figure 4.11 for $c = 30$ mM).

To obtain the Zeta potential values in all the pH range, we interpolate our experimental data of ζ (red points) versus pH as shown in Figure 4.12 (a). The values of λ_D are calculated with MINTEQ (through ionic strength) for different pH at equilibrium with calcite. The evolution of ionic strength as a function of pH is showed in Figure 4.12 (b). The final plot of $W_{\max}$ (compared with $k_B T/a^2$) is shown in Figure 4.12 (c).

Figure 4.12 (b) shows the strong sensitivity of the ionic strength with the pH in the range 11.5-12.5, as well as the value of $W_{\max}$ (Figure 4.12 (c)). More precisely, $W_{\max}$ goes through a maximum around 15 $k_B T$ for a pH of 11.8, as for the sample containing 30 mM of $Ca(OH)_2$ (Figure 4.11). This is consistent with the much lower elastic modulus measured for this system. At pH $\gtrsim$ 10, the raise of the pH results in an increase of ζ. Consequently the repulsion and $W_{\max}$ increase. At pH $\lesssim$ 12.4, ζ is constant with

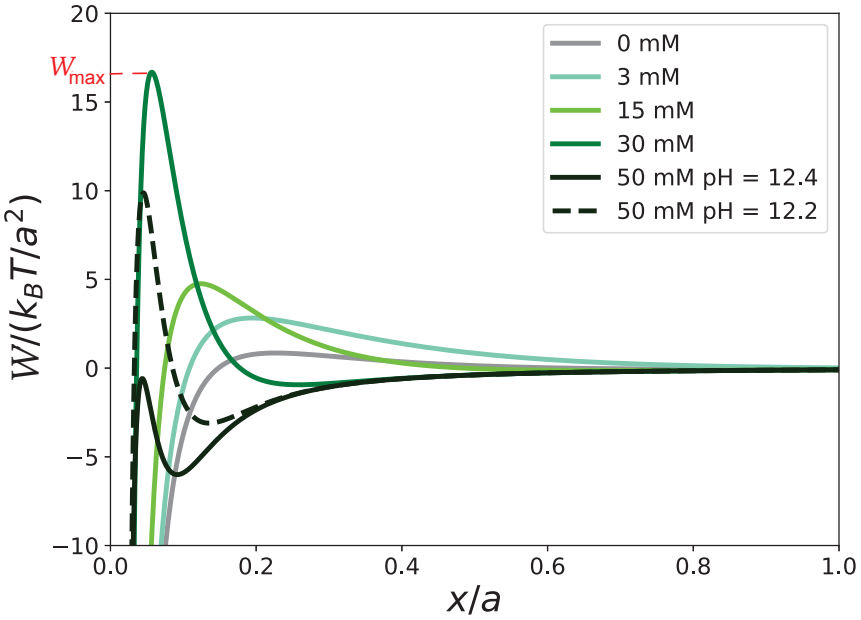

Figure 4.11 – Plane-plane (normalized) interaction potentials as a function of the distance normalized by the particle size a. The various curves correspond to calcite suspensions containing an increasing concentration of calcium hydroxide. For 50 mM of $Ca(OH)_2$, two curves at different pH are plotted to show the sensitivity of the interaction to the pH value (measured at ± 0.2). In red, we highlight the maximum value of the potential interaction W_{max}, for the sample containing 30 mM of calcium hydroxide.

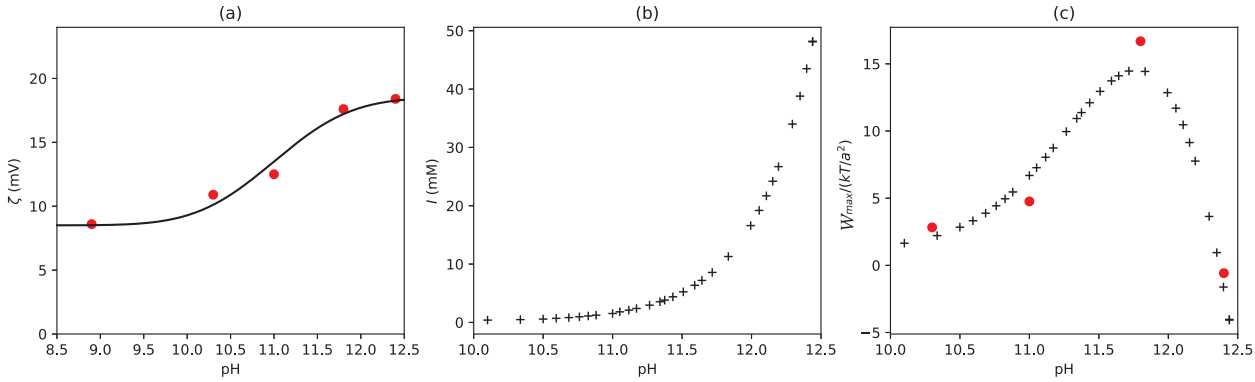

Figure 4.12 – (a) Interpolation of Zeta potential ζ with the pH obtained from experiments (red) points. (b) Ionic strength as a function of pH. Values obtained for a calcite-portlandite system by MINTEQ chemical speciation. (c) Maximum potential W_{max} as a function of pH, the crosses correspond to the ζ-fit and the red points are the ones calculated with Zeta potential measurements.

the pH and the ionic strength strongly increases. This implies a stronger electrostatic screening and a decrease of W_{max}.

Role of geometry

We also explore the role of the geometry of the particles on the interaction potential. The calculation for plane-plane (facet-facet) is reported above and the ones for the edge-facet and the vertex-facet in-

teractions are reported below. These three geometries are tested to simulate the contact between two rhombohedral particles.

The interaction between an edge and a facet can be calculated as the DLVO interaction potential between a plane and a cylinder of radius R. Here the radius R is taken as the radius of curvature of the calcite edges ($\sim$10 nm according to TEM images). Using the Dejarguin approximation ($R \gg x$) the potential is:

$$W_{DLVO,L} = -\frac{A\sqrt{R}}{12\sqrt{2}x^{3/2}} + 2\sqrt{2\pi}\varepsilon_w\zeta^2\sqrt{R/\lambda_D}\,e^{-x/\lambda_D} \tag{4.7}$$

where $W_{DLVO,L}$ is the DLVO potential per unit length, assuming $R \gg \lambda_D$. This potential per unit length is compared to k_BT/a.

We also assume that the interaction between a vertex and a facet is similar to the interaction between a sphere and a plane. In the Derjaguin approximation this total energy reads:

$$E_{DLVO} = -\frac{AR}{24x} + \pi\varepsilon_w R\zeta^2 e^{-x/\lambda_D} \tag{4.8}$$

where E_{DLVO} is the DLVO energy. This energy is compared to k_BT.

The influence of geometry is displayed in Figure 4.13 for the most repulsive system at $c = 30$ mM, respectively for plane-plane, edge-plane and vertex-plane geometries.

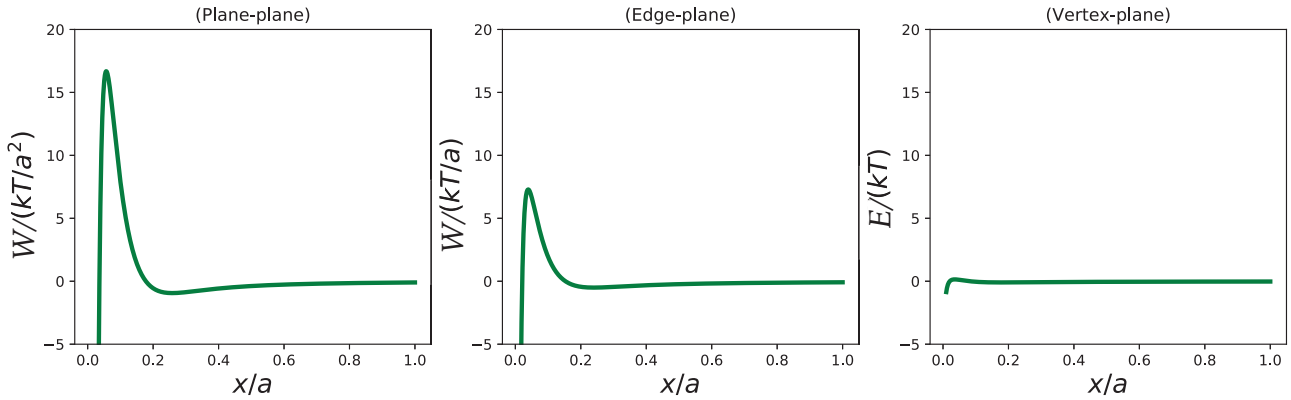

Figure 4.13 – Plane-plane, edge-plane and vertex-plane DLVO interactions for a calcite suspension with $c = 30$ mM and ϕ=10 %.

The repulsion observed for the plane-plane configuration is attenuated in the edge-plane one, until almost disappeared for the vertex-plane geometry. This behavior suggests that the nature of the interaction depends strongly on the geometry. In particular, for this sample we can imagine a weak attraction when a vertex comes close to a facet and a repulsion between facets. This weak attraction could be sufficient to maintain a gel-like structure with a weak solid behavior ($G' > G''$).

Evolution of DLVO interactions with carbonation

As already mentioned, Table 4.2 shows that adding $Ca(OH)_2$ even in a wide range of molarity, leads to the same final equilibrium. This can be explained with the chemistry of the systems, as already introduced in Section 2.4.1. At contact with carbon dioxide, calcium ions precipitate as calcite. This leads to dissolution of the remaining solid portlandite, as shown in the following reactions:

$$\text{(I)}\quad CO_{2(g)} + 2OH^- \rightleftharpoons CO_3^{2-} + H_2O \qquad K_I = 10^{9.85}$$
$$\text{(II)}\quad Ca(OH)_{2(s)} \rightleftharpoons Ca^{2+} + 2OH^- \qquad K_{II} = 10^{-5.22}$$
$$\text{(III)}\quad Ca^{2+} + CO_3^{2-} \rightleftharpoons CaCO_{3(s)} \qquad K_{III} = 10^{8.34}$$

In a first stage, for c larger than the solubility limit ($c \approx 20$ mM), solid portlandite remains in the suspension (reaction II) and both $[Ca^{2+}]$ and pH are fixed. In a second stage, once all the portlandite is dissolved, the pH decreases due to further CO_2 dissolution (reaction I). The carbonates coming from the atmosphere precipitate with calcium ions as calcite (reaction III); This lowers the calcium concentration.

For the different samples, the amount of precipitated calcite (once the equilibrium with the atmosphere is reached) is reported as a solid variation (Δsolid) in Table 4.2.

In order to verify the evolution of the sample containing 50 mM of $Ca(OH)_2$ (Figure 4.4), we maintain the suspension (open batch $\sim$ 100 mL) in a closed chamber for three days. The humidity is fixed by a saturated solution of NaCl, to avoid the drying of the paste. Then we measure the Zeta potential obtaining 17.50 mV. This ζ reduction (from 18.6 to 17.5 mV), even small, confirms that the amount of calcium ions in the suspension is getting lower due to the reaction with carbon dioxide (Figure 4.8). We can also observe that the evolution for a high quantity of calcite paste ($\sim$ 100 mL) is very slow in comparison with the one measured for a small amount of sample ($\sim$ 1 mL) in the rheometer gap (Figure 4.4). This is probably due to the surface to volume ratio which is larger in the rheometer (≈ 6 cm^{-1}) than in the tube (≈ 0.2 cm^{-1}).

We also follow the evolution of pH with pure calcite and for $c = 30$ and 50 mM. (Figure 4.14) at $\phi = 20\,\%$. The pH of the pure calcite barely decreases with time sample shows a minor reduction

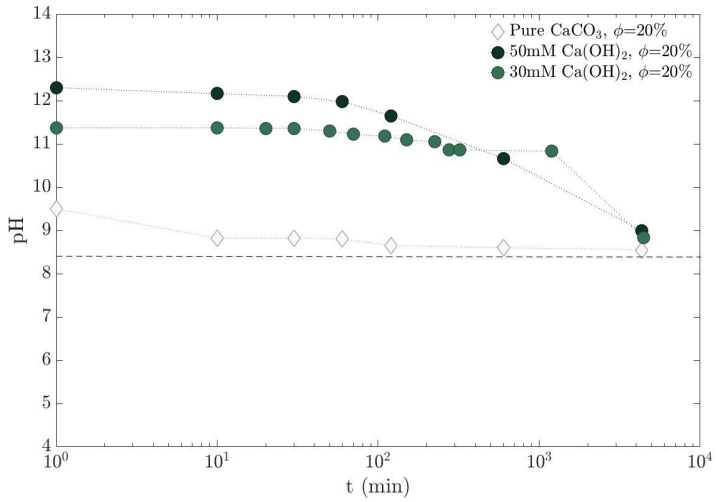

Figure 4.14 – Time evolution of pH for calcite pastes at $\phi = 20\,\%$: pure calcite paste and suspension with 30 and 50 mM of $Ca(OH)_2$. The black dashed line represents the pH value at the equilibrium with atmosphere, calculated by MINTEQ.

with time. The initial pH for this sample is not so different from the equilibrium value (dashed line in Figure 4.14). For the sample with calcium hydroxide, we observe a progressive pH-decrease to reach the equilibrium pH-value after three days, as shown in Figure 4.14. The sample for which we show the evolution is at $\phi = 20\,\%$. The overall behavior remains the same also at lower volume concentration

(i.e. $\phi = 10\,\%$) with a different evolution time. We will come back to this evolution in Section 4.2.4 comparing the two concentrations.

We can conclude that both ζ and pH decrease once the suspension is in contact with the atmospheric carbon dioxide. Now, looking at Figure 4.12 (a), going from right to left the pH decreases from 12.4 to 8.9 and ζ reduces from 18.6 to 9.3 mV. This implies that the various samples obtained at different concentration c, represent progressively evolving steps of the same initial system at pH= 12.4 (saturated in portlandite without atmosphere) as CO_2 is supplied from the atmosphere. Referring to Figure 4.12 (c), the initial (portlandite saturated) system is placed on the right and presents a weak repulsion. Once the CO_2 is inserted, this system "moves" to the left in the curve with a gradual decrease of both pH and ζ. This causes first an increase of the repulsion until $W_{\max} = 17$ mV. Then at pH < 11.8, the repulsion drops until the equilibrium with the CO_2 (pH ≈ 8). In this final state, we have a weakly attractive pure calcite paste.

4.2.4 Effect of calcite volume fraction

The same rheological analysis is made for $\phi = 20\,\%$ calcite suspensions at various concentrations of initial portlandite c. In particular the temporal evolution of the elastic modulus is shown in Figure 4.15. We also made one sample at $c = 100$ mM but the final paste was too liquid to allow measurements at the same gap width (4 mm).

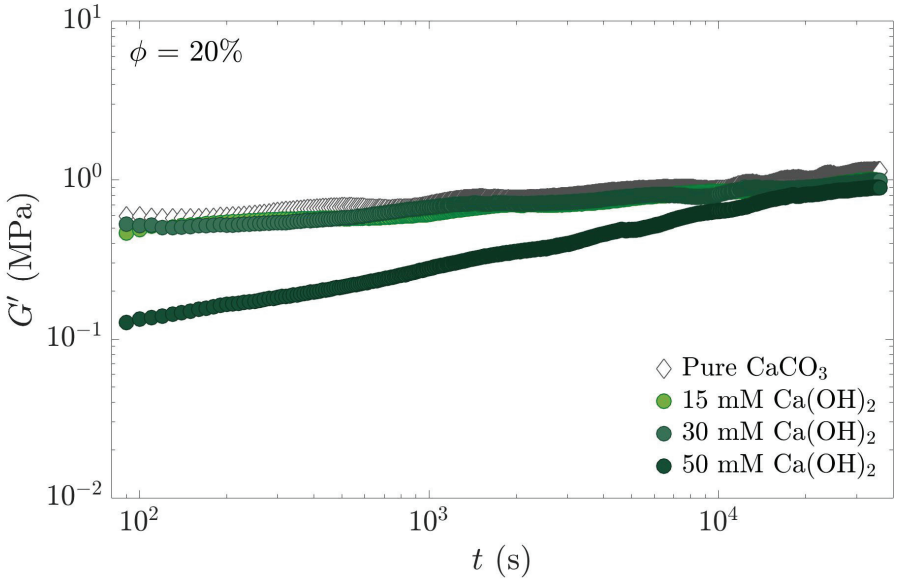

Figure 4.15 – Time evolution of the storage modulus of $\phi = 20\,\%$ calcite suspensions, increasing $Ca(OH)_2$ concentration.

At this solid volume fraction a strong evolution of G' is observed only for the paste prepared at $c = 50$ mM. The results of the pH measurements on the fresh paste are collected in Table 4.5 and compared to those obtained at $\phi = 10\,\%$.

For each c we find that the pH for $\phi = 20\,\%$ is equal or smaller than for $\phi = 10\,\%$. This pH difference probably explains the different elastic behaviors observed at $\phi = 10$ and $20\,\%$, i.e. for $10\,\%$ both $c = 30$ and 50 mM have a smaller initial storage modulus, whereas at $20\,\%$, $G'(0)$ decreases only for $c = 50$mM. To explain this effect, we can note that a small variation in pH can significantly change the energy barrier

c (mM)	$pH_{10\%}$	$pH_{20\%}$
0	8.9	8.8
3	10.3	10.2
15	11.0	11.0
30	11.8	11.4
50	12.4	12.0

Table 4.5 – Values of pH, measured for the fresh samples at $\phi = 10\,\%$ and $\phi = 20\,\%$, increasing $Ca(OH)_2$ concentration c.

of the sample, as shown in Figure 4.12 (c). This effect is more pronounced from pH ranging from 11.8 to 12.4.

More precisely, for $\phi = 10\,\%$ we find that the repulsion is maximum for $c = 30$ mM at pH= 11.8, which results in a lower storage modulus. For $\phi = 20\,\%$, it is the $c = 50$ mM sample which has the pH (12.0) closer to that of the maximum repulsion (11.8). Consistently we observe that G' is the lowest at $c = 50$ mM among all the data at $\phi = 20\,\%$, for all lower c we suspect that the repulsion is low enough for the elastic response to be comparable and slowly evolving with time.

Going back to the discussion of pH evolution, measurements of pH at different instants are acquired for pure calcite, and for $c = 30$ and 50 mM. In particular for the sample with 30 mM of $Ca(OH)_2$ both concentration: 10 and 20 %, are tested. Samples were maintained in contact with the atmosphere in an open batch for 3 days (covered with a pierced aluminum foil after 4 h). Results are shown in Figure 4.16. The black dashed line represents the pH value at the equilibrium with atmosphere, calculated by MINTEQ.

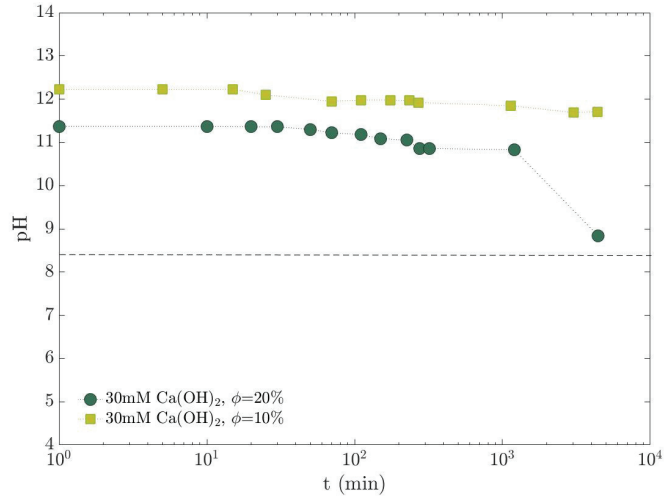

Figure 4.16 – Time evolution of pH for calcite pastes containing 30 mM of $Ca(OH)_2$ at $\phi = 20$ and $= 10\,\%$. Black dashed line represents the pH value at the equilibrium with atmosphere, calculated by MINTEQ.

After 3 days, the sample at $\phi = 20\,\%$ reach a similar pH, close to the one at the equilibrium (calculated by MINTEQ), while the sample at $\phi = 10\,\%$ still has a pH around 12. Although the geometry and the surface to volume ratio are very different from those of the rheometric cell, this suggests that the CO_2 dissolution is faster at $\phi = 20\,\%$ than that at $\phi = 10\,\%$. This could be due to differences in available calcite area ($5{\cdot}10^3$ m^2/L for $\phi = 10\,\%$ and $1.1{\cdot}10^4$ m^2/L for $\phi = 20\,\%$) where the precipitation of calcite

can take place.

To be more precise the reactivity of the paste is ruled by coupled dynamics: the diffusion of the atmospheric CO_2 in the air and of ions in the solution, the dissolution of solid portlandite and the precipitation of calcite which depends also on the amount of $CaCO_3$ surface available.

Moreover, regarding the mechanical properties in time, the rheometer in the plate-plate geometry gives us an averaged response between the edge (in contact with the atmosphere) and the inner part of the sample. This averaged result should depend strongly on all the diffusion-dissolution-precipitation dynamics mentioned above. Further studies will be necessary to define which of these mechanisms is controlling the entire evolution.

4.2.5 Ion effects on critical strain

In this section are reported all the results on the critical strain for both $\phi = 10$ and $20\,\%$. In particular Table 4.6 shows values of γ_{cr}, measured for samples at $\phi = 10\,\%$ and $\phi = 20\,\%$ after 10 h. These values are acquired during the amplitude sweep, after 10 h of time structuration, as detailed in Section 2.2.1 and Figure 2.9.

c (mM)	$\gamma_{cr\,10\%}(10\text{ h})$ (%)	$\gamma_{cr\,20\%}(10\text{ h})$ (%)
0	0.070	0.065
3	0.057	-
15	0.091	0.056
30	0.033	0.085
50	0.042	0.249

Table 4.6 – Value of γ_{cr}, measured for samples at $\phi = 10\,\%$ and $\phi = 20\,\%$ (increasing $Ca(OH)_2$ concentration c) after 10 h.

The values do not show a clear trend for both concentrations. Note that, since the pastes should all have the same chemical composition at long times, we would expect the same yield strain for all the samples. This is probably due to the slow and different chemical evolution in the suspension that is not completed after 10 h.

Figure 4.17 shows the values of the initial critical strain (i.e. amplitude sweep for α protocol Section 2.2.1 and fig. 2.9) for increasing c at $\phi = 20\,\%$. We find that $\gamma_{cr}(0)$ increases continuously with c.

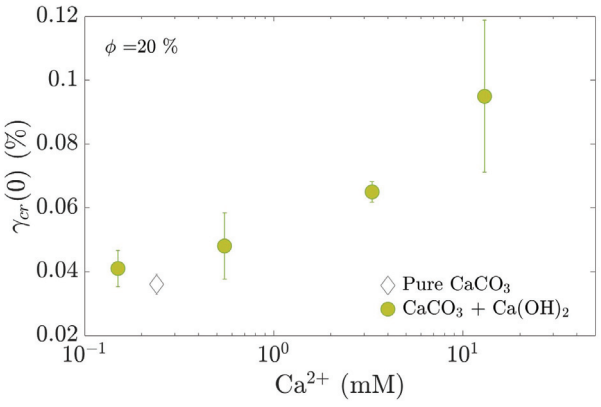

Figure 4.17 – Initial critical strain $\gamma_{cr}(0)$ at increasing Ca^{2+} concentration for $\phi = 20\,\%$.

The large error bar for the sample with 50 mM of $Ca(OH)_2$ is due to the strong evolution of the sample in the first minutes. Typical amplitude sweeps measurements take around 20-30 min. Moreover the critical strain increases as the elastic modulus decreases. This contrasts with the prediction of Shih et al. [14] for which both quantities have the same variation as ζ increases.

To sum up the results concerning the critical strain, we observe an increase of γ_{cr} as c increases. This initial tendency is not understood now. The values of γ_{cr} (10 h) are difficult to relate because the samples evolve on slightly different time scales.

Finally, we find that the addition of high concentration of calcium hydroxide causes a strong temporal evolution of the elasticity due to the samples carbonation. DLVO calculation shows that the nature of the attraction strongly depends on both pH and calcium concentration. In particular the repulsion goes through a maximum at pH$\approx$ 12. The differences of G' between samples and upon time can be linked to the amplitude of the repulsion which evolves with time.

4.3 Sodium hydroxide

Sodium hydroxide, NaOH, is an inorganic compound also known as caustic soda. It is a strong base totally dissociated in water. In fact, its solubility is around 1090 g/L [5].

In our case we decide to add 94 mM of NaOH with 3 mM $Ca(OH)_2$. Originally, calcium hydroxide was added to increase the pH and avoid an initial dissolution of calcite upon dispersion. Here in particular, adding NaOH, the pH increases without calcite dissolution. Nevertheless we still add calcium hydroxide to the system with NaOH, to compare it with all the others samples containing additives (Annex B).

4.3.1 Mechanical responses

Figure 4.18 shows the evolution of pure calcite (white diamonds) and calcite with sodium hydroxide (red squares) in time for both $\phi = 10\%$ and $\phi = 20\%$. For $\phi = 10\%$, also the sample with calcite containing 3 mM $Ca(OH)_2$ is inserted. As in the previous section, these curves result from the time structuration of the protocol β (10 h at $\gamma = 0.01$ % and $f = 1$ Hz).

The evolution of the elastic modulus remains limited (compared to Figure 4.4 for calcium hydroxide), especially for $\phi = 20$ %. Looking at $\phi = 10$ %, the elastic modulus of the sample with NaOH is higher than the other two while the evolution is very similar. Applying to these samples both protocols α and β, we also acquire the values of critical strain. Following the nomenclature defined in Figure 2.9, results are shown in Table 4.7. We find that the addition of sodium hydroxide increases the critical strain, at both short and long times and for both concentrations (ϕ =10 and 20 %).

	ϕ = 10 %		ϕ = 20 %	
Sample	γ_{cr} (0)	γ_{cr} (10 h)	γ_{cr} (0)	γ_{cr} (10 h)
Pure $CaCO_3$	0.077	0.070	0.035	0.065
94 mM NaOH + 3 mM $Ca(OH)_2$	0.146	0.126	0.096	0.249

Table 4.7 – Comparison between the critical strain at the initial time γ_{cr} (0) and after 10 h γ_{cr} (10 h) on pure calcite and calcite with NaOH for both $\phi = 10$ and 20 %.

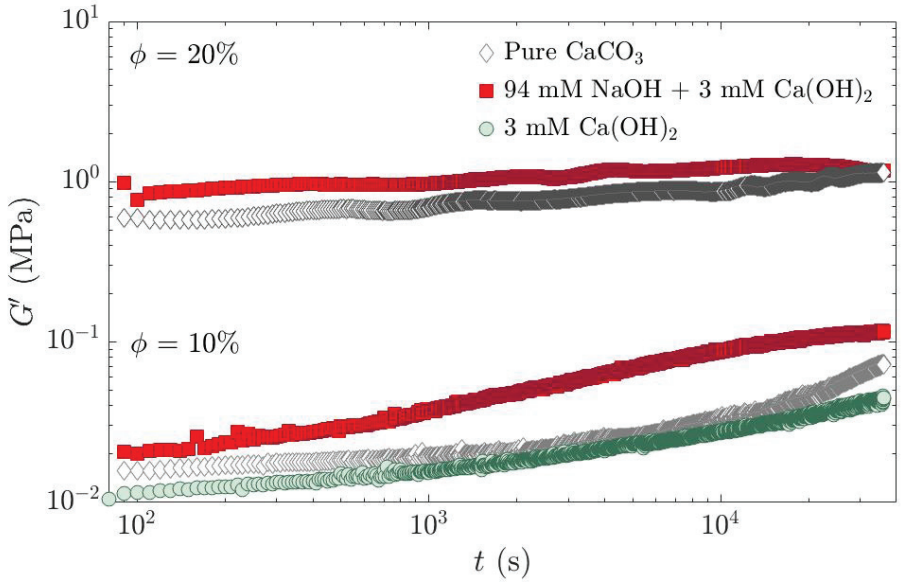

Figure 4.18 – Time evolution of the storage modulus for pure calcite and calcite with NaOH suspensions at both $\phi = 10\%$ and $\phi = 20\%$. In particular at $\phi = 10\%$, the evolution of the sample with 3 mM $Ca(OH)_2$ is also shown.

The evolution of the critical strain depends on the calcite volume fraction ϕ. For $\phi = 10\,\%$ it is roughly constant while it is multiplied by a factor 2 for $\phi = 20\,\%$. This could be due to different reactivities of the pastes although the evolution of the elastic modulus is less striking than in the case of calcium hydroxide.

4.3.2 Microscopic interaction: chemical speciation and DLVO

The MINTEQ chemical analysis for the pure sample and with NaOH are detailed in Table 4.8.

	No atmosphere		Atm pressure		Exp. condition t(0)	
Sample	pH	Ca^{2+}(mM)	pH	Ca^{2+}(mM)	pH_{meas}	Ca^{2+}(mM)
Pure calcite	9.92	0.12	8.23	0.51	8.90	0.24
94 mM NaOH + 3 mM $Ca(OH)_2$	12.86	1.78	9.70	$1.30 \cdot 10^{-3}$	12.7	$1.8 \cdot 10^{-3}$

Table 4.8 – MINTEQ chemical speciation for pure calcite and calcite with sodium hydroxide at $\phi = 10\,\%$. Values of pH and calcium ions concentration Ca^{2+} are reported for our experimental condition and in the two extreme cases of a system without atmosphere and in equilibrium with the atmosphere.

The measured pH before Zeta potential measurement for $\phi = 10\,\%$ is 12.7. A comparable pH value (12.6) is obtained for the fresh sample at $\phi = 20\,\%$. In the suspension without contact with the atmosphere, Na^+ and OH^- ions prevail, due to the complete dissociation of NaOH (while reducing OH^- and pH). The CO_2 uptake produces carbonate and bicarbonate ions which are involved in two reactions:

$$\text{(I)}\quad Na^+ + HCO_3^- \rightleftharpoons NaHCO_3 \qquad K_I = 10^{-0.19}$$
$$\text{(II)}\quad Na^+ + CO_3^{2-} \rightleftharpoons NaCO_3^- \qquad K_{II} = 10^{0.9}$$

Then, at equilibrium with the atmosphere, the pH decreases at the expense of HCO_3^-, CO_3^{2-}, $NaCO_3^-$ and

$NaHCO_3$ (sodium bicarbonate) production. In this situation, the positive charge of Na^+ ions (86 mM) is mostly balanced with the negative ions: HCO_3^- (37 mM), CO_3^{2-} (19 mM) and $NaCO_3^-$ (11 mM). The concentration of Ca^{2+} ions has a very low value ($\sim 10^{-3}$ mM) due to the precipitation of calcium carbonate.

Again our experimental condition lies between the condition without atmosphere and in equilibrium with atmosphere. In our experimental conditions, the positive charge of Na^+ ions (86 mM) is balanced with the negative ions: OH^- (52 mM), CO_3^{2-} (13 mM) and $NaCO_3^-$ (8 mM). From this chemical speciation we calculate the ratio of the concentrations of the PDI. We find that the Ca^{2+} concentration is very low in comparison with the CO_3^{2-} one (PDI ratio$\approx 10^{-4}$). We therefore expect a negative value of ζ. In fact, Zeta potential measurement for a sample containing NaOH and $\phi = 10\,\%$, gives a value of $\zeta = -2.4 \pm 0.025$ mV ($\zeta = 9.3 \pm 0.99$ mV for pure calcite).

At our experimental conditions we also calculate the ionic strength $I = 90$ (mM) and the corresponding Debye length $\lambda_D = 1$ nm.

With both ζ potential measurement and the ionic strength calculation from the chemical speciation, we can determine the DLVO interaction between two facets as specified in Section 4.2.3.

Figure 4.19 shows the interaction energy for pure calcite and calcite with NaOH.

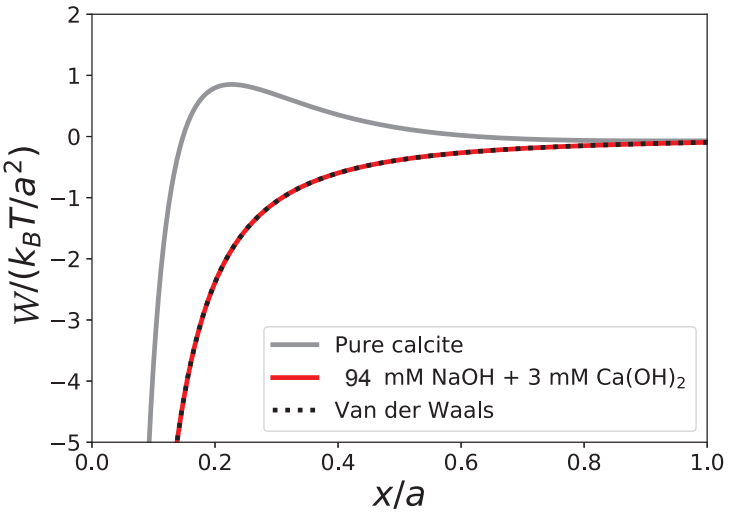

Figure 4.19 – Interaction potential (plane-plane) for pure $CaCO_3$ (gray) and $CaCO_3$ with sodium hydroxide (red). The dashed line shows the contribution of van der Waals attraction.

For pure calcite, as already observed, the potential shows a low barrier ($\sim 1 k_B T$) and is thus weakly attractive. Adding NaOH the electrostatic repulsion vanishes with $\zeta = -2.4$ mV and the repulsion is strongly screened ($\lambda_D \approx 1$ nm). Attraction is dominant and the energy profile is coincident with pure van der Waals attraction.

To sum up, sodium hydroxide addition to calcite paste makes the system more attractive, lowering both ζ and λ_D. Comparing to pure calcite, the sample containing NaOH increases both elasticity G' and the yield or critical strain γ_{cr}. This tendency is in a good agreement with the one described in the interactions models (Section 4.1.1) proposed by Shih et al. [14] and Flatt and Bowen [3]. This is not surprising as these models have been proposed for strongly attractive systems.

The effect of this attractive interaction of flow properties will be discussed in the next chapter.

4.3.3 Conclusion

To understand the physico-chemical mechanisms that occur in the calcite-portlandite system and the influence of ion addition on calcite properties requires several tools: rheological measurements, chemical speciation calculations and Zeta potential measurements.

Concerning the influence of calcium hydroxide on the mechanical properties and on the microscopic interaction, we observe that, in a first step, $Ca(OH)_2$ releases calcium ions that adsorb at the calcite surface, increasing its positive charge and ζ. The energy barrier value is very sensitive to pH. A slight variation of pH induces a different amount and kind of ions in the suspensions, affecting ζ and I, leading to a maximum in the repulsive energy barrier. Adding various quantities of calcium hydroxide, the overall effect (with respect to the pure calcite) is a (non-monotonic) decrease of the elasticity. We find the elastic modulus $G'(0)$ varies qualitatively as the inverse of the energy barrier W_{max} in the DLVO interaction.

Once in contact with CO_2, the systems evolve by carbonation, decreasing both pH and calcium ions. After reaching the equilibrium with the atmosphere, we expected to have the same system constituted of pure calcite.

The influence of sodium hydroxide is easier to understand. The attraction raises once NaOH is added. This is due to both the screening effect of released ions (high I) and the decrease of Zeta potential due to the high concentration of negative potential determining ions (carbonate) compared to positive ones (calcium). Both elastic and yielding properties (G' and γ_{cr}) are increased. Moreover the system evolves more slowly with time.

Bibliography

[1] D. Al Mahrouqi, J. Vinogradov, and M. D. Jackson. Zeta potential of artificial and natural calcite in aqueous solution. *Advances in colloid and interface science*, 240:60–76, 2017.

[2] B. A. Firth and R. J. Hunter. Flow properties of coagulated colloidal suspensions: III. the elastic floc model. *Journal of Colloid and Interface Science*, 57(2):266–275, 1976.

[3] R. J. Flatt and P. Bowen. Yodel: a yield stress model for suspensions. *Journal of the American Ceramic Society*, 89(4):1244–1256, 2006.

[4] T. Foxall, G. C. Peterson, H. M. Rendall, and A. L. Smith. Charge determination at calcium salt/aqueous solution interface. *Journal of the Chemical Society, Faraday Transactions 1: Physical Chemistry in Condensed Phases*, 75:1034–1039, 1979.

[5] D. Green and R. Perry. *Perry's Chemical Engineers' Handbook, 8^{th} Edition*. McGraw Hill professional. McGraw-Hill Education, 2007.

[6] Y. C. Huang, F. M. Fowkes, T. B. Lloyd, and N. D. Sanders. Adsorption of calcium ions from calcium chloride solutions onto calcium carbonate particles. *Langmuir*, 7(8):1742–1748, 1991.

[7] J. N. Israelachvili. *Intermolecular and Surface Forces*. Academic press, 2011.

[8] T. Liberto, M. Le Merrer, C. Barentin, M. Bellotto, and J. Colombani. Elasticity and yielding of a calcite paste: scaling laws in a dense colloidal suspension. *Soft matter*, 13(10):2014–2023, 2017.

[9] R. Nyström, M. Lindén, and J. B. Rosenholm. The influence of Na^{+}, Ca^{2+}, Ba^{2+}, and La^{3+} on the ζ potential and the yield stress of calcite dispersions. *Journal of colloid and interface science*, 242(1):259–263, 2001.

[10] A. Pierre, J. Lamarche, R. Mercier, A. Foissy, and J. Persello. Calcium as potential determining ion in aqueous calcite suspensions. *Journal of dispersion science and technology*, 11(6):611–635, 1990.

[11] S. Pourchet, I. Pochard, F. Brunel, and D. Perrey. Chemistry of the calcite/water interface: Influence of sulfate ions and consequences in terms of cohesion forces. *Cement and Concrete Research*, 52:22–30, 2013.

[12] P. J. Scales, S. B. Johnson, T. W. Healy, and P. C. Kapur. Shear yield stress of partially flocculated colloidal suspensions. *AIChE Journal*, 44(3):538–544, 1998.

[13] S. Shih, C. Ho, Y. Song, and J. Lin. Kinetics of the reaction of $Ca(OH)_2$ with CO_2 at low temperature. *Industrial and Engineering Chemistry Research*, 38(4), 1999.

[14] W. Y. Shih, W.-H. Shih, and I. A. Aksay. Elastic and yield behavior of strongly flocculated colloids. *Journal of the American Ceramic Society*, 82(3):616–624, 1999.

[15] W.-H. Shih, W. Y. Shih, S.-I. Kim, J. Liu, and I. A. Aksay. Scaling behavior of the elastic properties of colloidal gels. *Physical Review A*, 42(8):4772, 1990.

[16] K. Van Balen. Understanding the lime cycle and its influence on historical construction practice. In *Proceedings of the First International Congress on Construction History*, volume 20, page 24. Instituto Juan de Herrera Universidad Politécnica de Madrid, 2003.

[17] Z. Zhou, M. J. Solomon, P. J. Scales, and D. V. Boger. The yield stress of concentrated flocculated suspensions of size distributed particles. *Journal of Rheology*, 43(3):651–671, 1999.

Chapter 5

Flow behavior and influence of colloidal interactions

After the characterization of the viscoelastic properties (i.e. G',G'') of the calcite pastes, we now study the flow properties of such systems by measuring the flow curves and the velocity profiles inside the sheared sample. In this chapter, we also investigate the influence of additives on the flow properties, one of the aim being to study the influence of the interaction forces between $CaCO_3$ particles on the macroscopic properties. We thus compare the flow curves and the velocity profiles of pure calcite paste and of calcite paste with some of the additives already studied in Chapter 4. In particular we focus on the comparison between the pure system and the one containing sodium hydroxide, as explained below.

Contents

5.1 Investigated systems

In Table 5.1, we list all the systems that we have tested. However the pastes containing calcium hydroxide or hydrochloric acid (c, d and e in Table 5.1) exhibit a strong temporal evolution of their properties such as the flow curve or viscoelastic moduli. So we mainly concentrate our study on two systems macroscopically stable in time: pure calcite and calcite with sodium hydroxide (NaOH) (a and b in Table 5.1). Section 5.4 at the end of this chapter is nevertheless devoted to the other systems (c, d and e in Table 5.1).

Samples	ϕ **range (%)**
a) Pure	10-20
b) 94 mM **NaOH** + 3 mM $Ca(OH)_2$	8-15
c) 30 mM **Ca(OH)$_2$**	10
d) 50 mM **Ca(OH)$_2$**	10-15
e) 100 mM **HCl** + 3 mM $Ca(OH)_2$	10

Table 5.1 – List of all the studied samples and the corresponding volume concentration range.

Concerning pure calcite and calcite with NaOH, we already know from Chapter 4 that the temporal evolution of the storage modulus $G'(t)$ remains limited (Figure 4.18), so that we can assume viscoelastic properties merely constant with time. Moreover, from a microscopic point of view, we observe that adding sodium hydroxide to calcite paste induces a decrease in both the zeta potential ζ and on the Debye length λ_D, changing the DLVO interaction, as recalled in Table 5.2. In particular, the calcite paste with sodium hydroxide is a purely attractive system whereas the interaction between particles inside pure calcite exhibits a small barrier of energy $W_{max} \sim 1\,k_BT$ (i.e. weak attractive system). The DLVO calculation for both systems is showed in Figure 4.19.

	ζ (mV)	W_{max}	λ_D (nm)
Pure $CaCO_3$	8.6	$1\,k_BT$	11.1
94 mM NaOH + 3 mM $Ca(OH)_2$	-2.4	strong attraction	0.99

Table 5.2 – Comparison between pure calcite and calcite with NaOH. Zeta potential ζ values are measured for calcite suspensions at $\phi = 10\%$. W_{max} is the calculated DLVO energy barrier between the maximum and the primary minimum. The Debye length λ_D is calculated from the ionic strength I values.

The values of Zeta potentials used in the DLVO calculations have been measured with pastes at $\phi = 10\%$, so that we have decided to conduct the flow measurements with calcite pastes at the same volume concentration.

5.2 Flow measurements and USV tracking

Before presenting in detail the flow properties of pure calcite and calcite with NaOH, we briefly recall the experimental setup and the protocol. Both are extensively presented in Section 2.2.3.

The setup is composed of a rheometer equipped with a Couette geometry, coupled to an ultrasonic device. Its 128 piezoelectric transducers allow us to follow the local dynamics of the sheared sample. To obtain flow curves and velocity profiles at different shear rates, we use the following protocol:

1. Pre-shear: one minute at $\dot{\gamma} = 10\,\mathrm{s}^{-1}$ and one minute at $\dot{\gamma} = -10\,\mathrm{s}^{-1}$;
2. Linear storage modulus recording: three minutes at $\gamma = 0.05\,\%$ and $f = 1\,\mathrm{Hz}$;
3. Series of shear rate steps at: $\dot{\gamma} = 10 - 20 - 50 - 20 - 10\,\mathrm{s}^{-1}$. During each step, USV data are recorded. Each shear step is characterized by a specific USV acquisition time and shearing time, listed in Table 2.2. After each step, the value of the linear storage modulus is recorded as in 2);
4. Series of shear rate steps at: $\dot{\gamma} = 10 - 20 - 50 - 100 - 50 - 20 - 10 - 5 - 2\,\mathrm{s}^{-1}$, similar to 3);
5. Flow curve with a decreasing shear rate ramp from $\dot{\gamma} = 100 - 1\,\mathrm{s}^{-1}$, 10 s/point and 15 points/decade ("Descending ramp");
6. Flow curve with a increasing shear rate ramp from $\dot{\gamma} = 1 - 100\,\mathrm{s}^{-1}$, 10 s/point and 15 points/decade ("Ascending ramp");
7. Same as 2).

5.2.1 Flow curves

Figure 5.1 shows the flow curves for pure calcite (a) and calcite with sodium hydroxide (b) at $\phi = 10\,\%$.

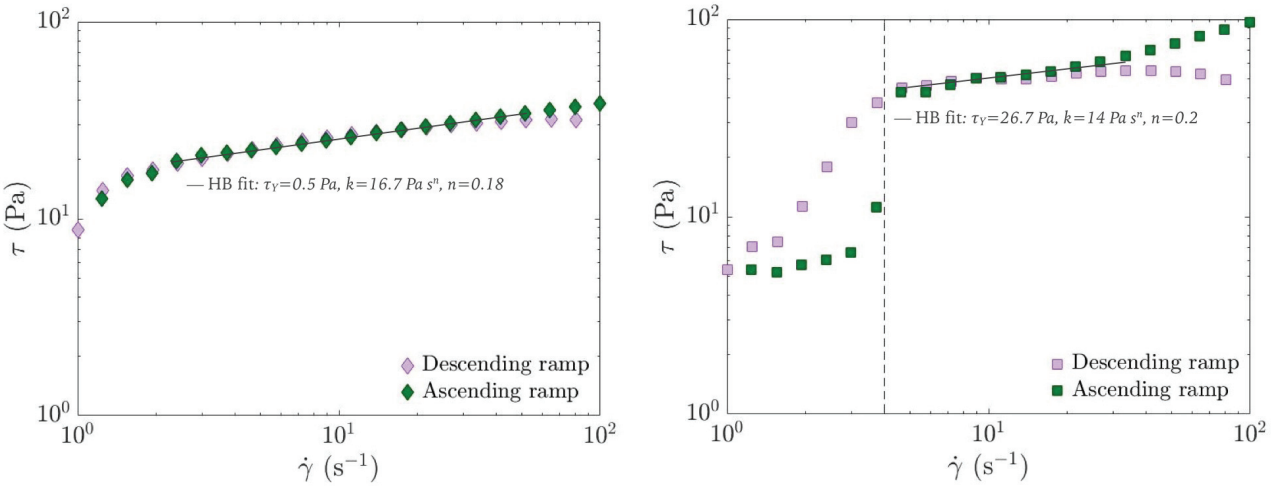

Figure 5.1 – Flow curves for a decreasing shear rate ramp from $\dot{\gamma} = 100 - 1\,\mathrm{s}^{-1}$ (descending ramp) and an increasing shear rate ramps from $\dot{\gamma} = 1 - 100\,\mathrm{s}^{-1}$ (ascending ramp). Comparison between two samples: (a) pure calcite and (b) calcite with 94 mM of NaOH and 3 mM of $Ca(OH)_2$. Both samples are at $\phi = 10\,\%$. (b) The dashed line corresponds to $\dot{\gamma} = 4\,\mathrm{s}^{-1}$, below which the hysteresis is important. For both figures, black lines correspond to the Herschel-Bulkley (H-B) fit of the data obtained in absence of wall slip and in the range of shear rates for which the descending and ascending flow curves coincide.

The flow curves are obtained with both a descending ramp of shear rates from $\dot{\gamma} = 100$ to $1\,\mathrm{s}^{-1}$ and an ascending ramp from $\dot{\gamma} = 1$ to $100\,\mathrm{s}^{-1}$. For each applied shear rate $\dot{\gamma}$, the shear stress τ is recorded after 10 s.

For both samples, we observe at low shear rate ($\dot{\gamma} \leq 4\,\mathrm{s}^{-1}$), a strong dependence of the shear stress with the shear rate which is associated to wall slip phenomena. This effect is more pronounced with

sodium hydroxide showing a hysteresis between the ascending and the descending curves for $\dot{\gamma} \leq 4\,s^{-1}$ (dashed line in Figure 5.1(b)). Due to this hysteresis, we chose to compare the flow curves of the two samples (pure calcite and calcite with NaOH) only for $\dot{\gamma} \geq 4\,s^{-1}$ and obtained with the descending ramps which are more reproducible than the ascending ones. For both samples, at higher $\dot{\gamma}$, the shear stress increases slowly with the shear rate exhibiting a strong shear-thinning behavior.

The two flow curves are compared in Figure 5.2 (a), where we plot the viscosity η $(= \tau/\dot{\gamma})$ as a function of the shear rate for the two samples. Both viscosities are close, slightly smaller for the pure calcite paste. To compare the two systems, we also measure the elastic behavior by storage modulus acquisition. The results are presented in Figure 5.2(b) and correspond to the measurement of G' after a series of shear rate steps.

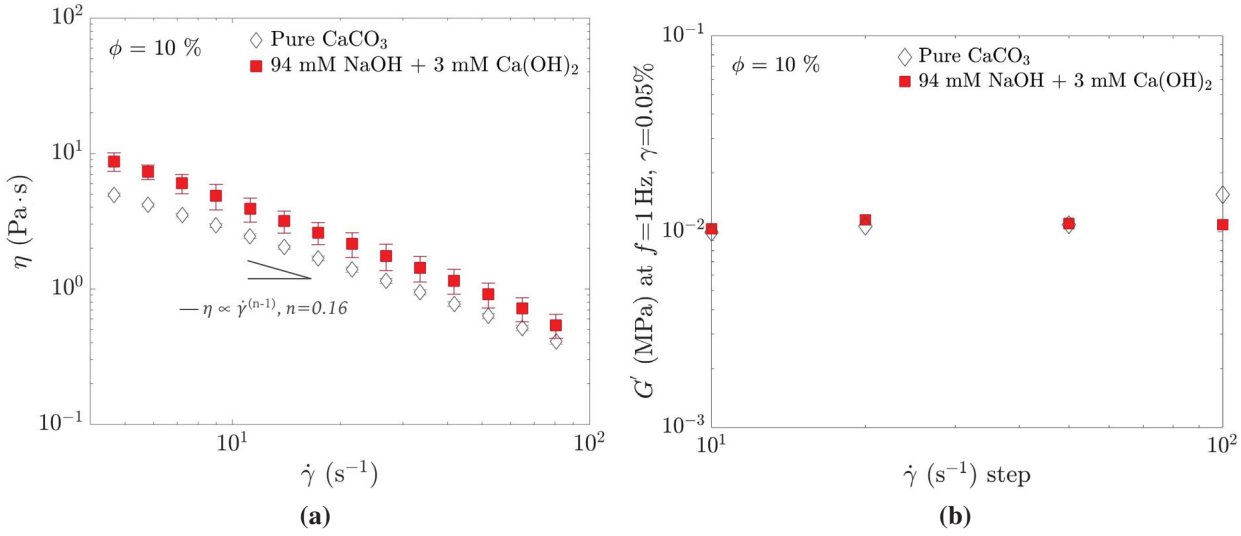

Figure 5.2 – Comparison between two samples: pure calcite and calcite with NaOH ($\phi = 10\,\%$). (a) Flow curve for a decreasing shear rate ramp from $\dot{\gamma} = 100 - 4\,s^{-1}$. The viscosity, η is plotted as a function of $\dot{\gamma}$. Black lines correspond to the power-law fit of $\eta(\dot{\gamma})$. The obtained n is in good agreement with the H-B fit of Figure 5.1.(b) Storage modulus values G' (measured after each shear rate step as specified in point 3 of the protocol) as a function of the shear rate applied prior to viscoelastic measurements, $\dot{\gamma}$ (of the step).

The two systems are characterized by similar elastic moduli ($G' \sim 10^{-2}$ MPa). Those values obtained in a Couette geometry with an ARG2 rheometer are in good agreement with the ones measured in rough plate-plate geometry with a MCR 301. More precisely, in a rough plate-plate geometry, we measured for pure calcite, $G'_{pure}(0) \simeq 1.6 \cdot 10^{-2}$ MPa and for calcite with NaOH, $G'_{NaOH}(0) \simeq 2 \cdot 10^{-2}$ MPa. The values of rigidity for the two samples in the two geometries show a difference (especially for the sample with NaOH) certainly due to the existence of slip in the Couette geometry, whose stator is smooth, whereas both plates are covered with sand paper. This explanation is reinforced by the fact that flow curves obtained with calcite with NaOH evidence more slip than the ones obtained with pure calcite, as shown for low $\dot{\gamma}$ in Figure 5.1.

To summarize the results of Figure 5.2, pure calcite and calcite with NaOH at $\phi = 10\%$ exhibit comparable apparent rheological values (identical G' and similar $\eta(\dot{\gamma})$).

To compare the local properties (i.e. velocity profiles) of two sheared systems characterized by the same macroscopic average viscosity (Figure 5.2), we adjust the volume concentrations of the samples.

To do so, we fix the volume concentration of the NaOH sample at $\phi = 10\,\%$ and we explore for the pure calcite paste different concentrations ranging from $\phi = 10\,\%$ to $12\,\%$. Then we choose the concentration for which the flow curve is the closest to the one of $\phi = 10\,\%$ NaOH sample.
Figure 5.3 shows the comparison between flow curves for pure calcite in a concentration range of $\phi = 10 - 12\,\%$ and calcite with sodium hydroxide at $\phi = 10\,\%$. The best match is obtained with a pure calcite at $\phi = 11\,\%$.

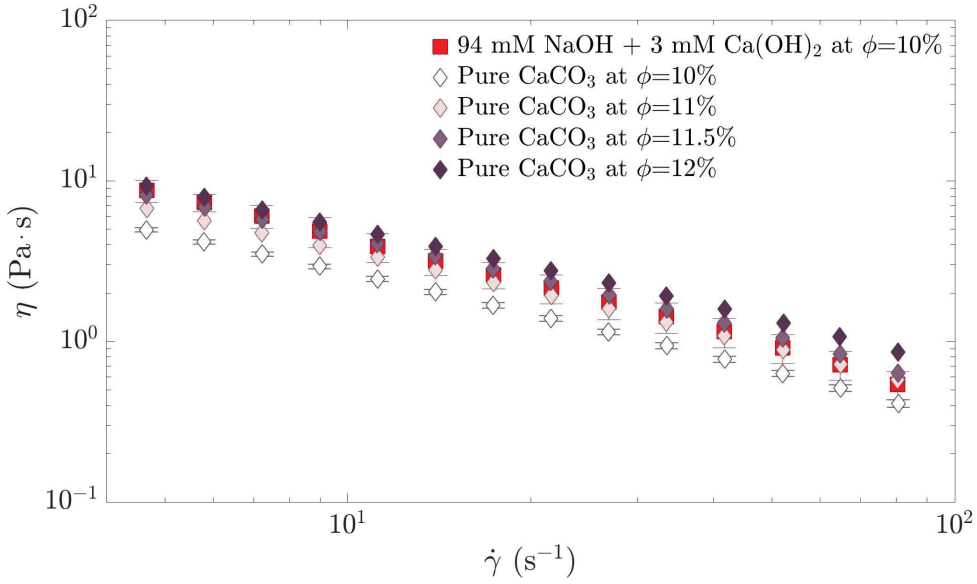

Figure 5.3 – Flow curves (viscosity η as a function of the shear rate $\dot{\gamma}$) for different samples obtained with a decreasing shear rate ramp from $\dot{\gamma} = 100 - 4\,\mathrm{s}^{-1}$: comparison between pure calcite in a concentration range of $\phi = 10 - 12\,\%$ and calcite with NaOH at $\phi = 10\,\%$.

Therefore, in the following, we shall compare the velocity profiles measured with pure calcite at $\phi = 11\,\%$ and calcite with NaOH at $\phi = 10\,\%$.

5.2.2 Velocity profiles

As already mentioned, the ultrasonic velocimetry technique is used to follow the local dynamics of the samples, during imposed shear rate steps, ranging in our study from $\dot{\gamma} = 100$ to $1\,\mathrm{s}^{-1}$. The ultrasonic region of interest is a rectangular slice of $z_{max} = 3\,\mathrm{cm}$ height and $r_{max} = 2\,\mathrm{mm}$ length (gap width). The acquisition of velocity profiles is detailed in Section 2.2.4. The raw velocity data from the 128 channels (on z) are a function of (z, r, t). If we average the velocity over time, we obtain a $v(z,r)$ diagram, which allows us to check that velocities are homogeneous along the vertical direction z. Averaging over z, instead, leads to a spatio-temporal velocity map $v(r,t)$. With such a diagram, we can check the flow stationarity.

Typical time averaged and spatio-temporal velocity maps are shown in Figure 5.4, for an intermediate shear rate, $\dot{\gamma} = 20\,\mathrm{s}^{-1}$. In particular (a)-(b) are respectively the time averaged and the spatio-temporal velocity maps for the pure calcite at $\phi = 11\%$. Images (c)-(d) are the same velocity maps for a calcite with sodium hydroxide sample at $\phi = 10\%$.

For both systems, the time-average velocity maps (a) and (c) show that the velocities are respectively homogeneous and quasi-homogeneous spatially along z, and the spatio-temporal velocity maps (b,d)

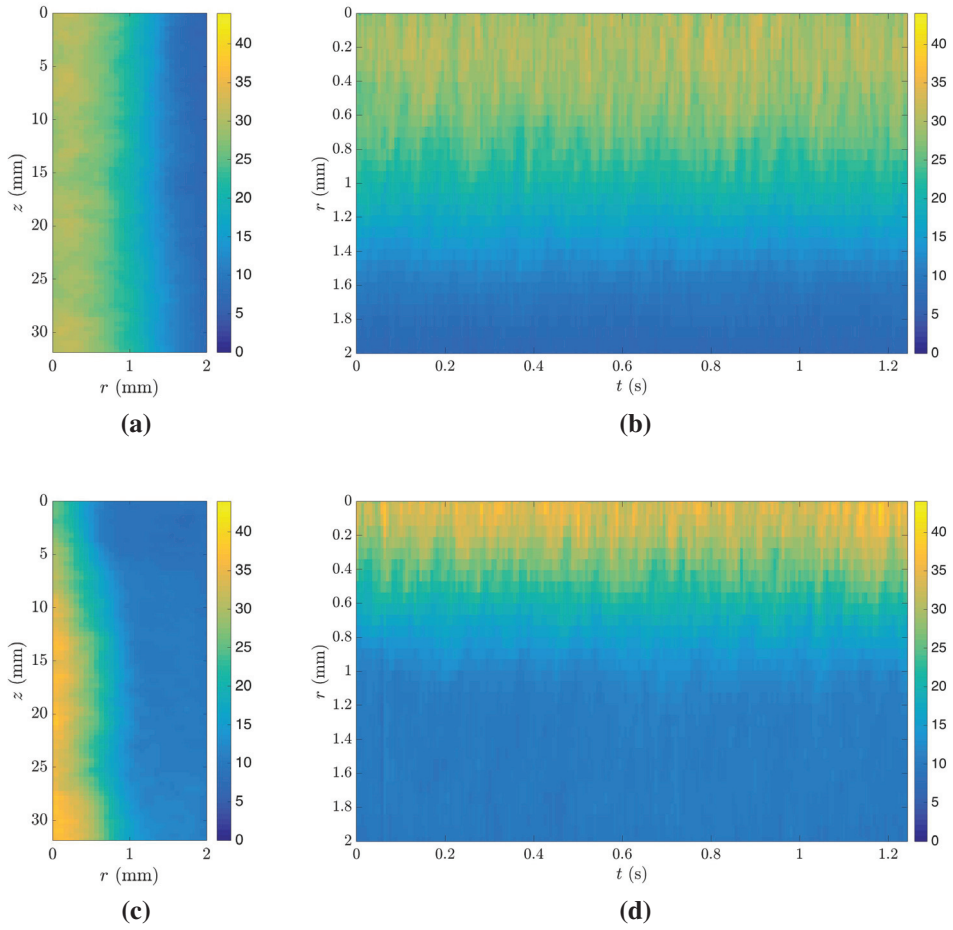

Figure 5.4 – Time-averaged (a,c) and spatio-temporal (b,d) velocity maps at $\dot{\gamma} = 20\,\mathrm{s}^{-1}$. (a-b) Pure $CaCO_3$ sample at $\phi = 11\%$. (c-d) $CaCO_3$ with NaOH sample at $\phi = 10\%$. Color bar refers to the velocity in mm/s. Blue is the minimum value of the velocity and yellow the maximum one.

show that the flow is stationary.

Note that we sometimes observed spatially inhomogeneous (along z) time-averaged velocity maps such as the one shown on Figure 5.5 (b). In fact comparing Figure 5.5 (b) with Figure 5.5 (a), we denote two different velocity maps also if they are both acquired during a shear rate step of $\dot{\gamma} = 20\,\mathrm{s}^{-1}$ for a $\phi = 10\%$ calcite with NaOH sample. Such inhomogeneous velocity maps are much less frequent and their origin is not fully understood but could be due to the presence of very large calcite aggregates. Nevertheless such velocity maps are not considered for the calculation of the velocity profiles.

By averaging over time the spatio-temporal velocity $v(r,t)$ we can obtain the velocity profile $v(r)$. Figure 5.6 shows the velocity profiles $v(r)$ for both samples (pure calcite and calcite with NaOH) obtained at four different shear rates.

White diamonds (resp. red squares) represent the velocity of pure calcite (resp. calcite with sodium hydroxide). The presented shear rates (10, 20, 50 and $100\,\mathrm{s}^{-1}$) are the ones of the second increasing ramp, corresponding to step 4). Each measurement of $v(r)$ is repeated four times for each sample. The error on the velocity $v(r)$ is estimated as the biggest standard deviation between the one calculated on the velocity average over the vertical direction and the one calculated on the velocity average over time. In our case, the first one has the highest value. Then, the velocity profiles along the gap width $v(r)$, are

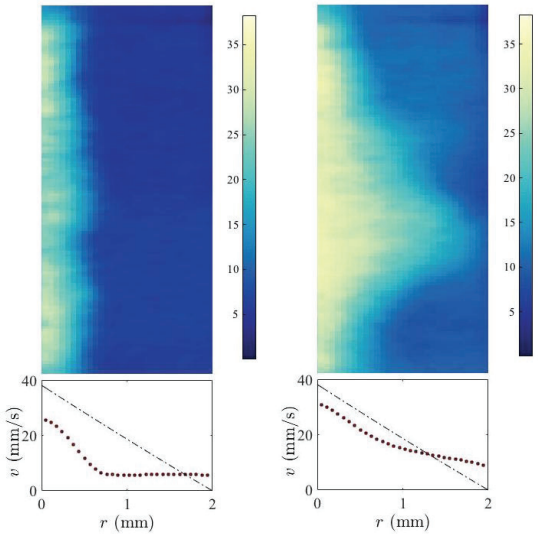

Figure 5.5 – Image (a) and (b) are composed by a time-averaged velocity map (top) and the corresponding spatio-temporal velocity profile (bottom). The color bar represents the velocity in mm/s. Both velocity profiles are acquired during a shear rate step of $\dot{\gamma} = 20\,\mathrm{s}^{-1}$ for a $\phi = 10\%$ calcite with NaOH sample. Figure 5.5 (a) is one of the steps of the second increasing shear rate ramp and Figure 5.5 (b) is one of the step of the second decreasing shear step ramp (see Section 2.2.3). The second complete shear rate ramp is: $\dot{\gamma} = 10, 20, 50, 100, 50, 20, 10\,\mathrm{s}^{-1}$.

shown with an error bar corresponding to the spatial (in)homogeneity in z. We can observe that both samples exhibit wall slip at both rotor and stator, and that slip decreases at high shear rate compared to the shear motion. Moreover the velocity profiles of pure calcite are quite homogeneous along the gap whereas the sample with NaOH displays shear banding, i.e. velocity inhomogeneities along the gap, for shear rates smaller than $\dot{\gamma} = 50\,\mathrm{s}^{-1}$. The region close to the rotor is more sheared than the one close to the stator corresponding respectively to liquid-like and solid-like zones.

To sum up, we compare two samples with exactly the same apparent macroscopic properties (i.e. same G' and $\eta(\dot{\gamma})$) but with different local behaviors. Indeed velocity profiles for the pure sample are homogeneous whereas the samples with NaOH exhibit shear bands. Both samples show wall slip, stronger for low shear rates.

5.2.3 Influence of the concentration

We also study the influence of the concentration on the velocity profiles for both samples (pure calcite and calcite with sodium hydroxide), the aim being to study the robustness of the previous results with respect to a change in concentration. So we study pure calcite paste with concentration ranging from 10 to 20 % and calcite paste with NaOH with concentration ranging from 8 to 15 %.

Figure 5.7 shows two velocity profiles at $\dot{\gamma} = 20\,\mathrm{s}^{-1}$ obtained with pure calcite samples respectively at $\phi = 10\%$ (white diamonds) and $\phi = 11\%$ (pink diamonds). The two profiles are comparable and this is also observed for all other studied shear rates $\dot{\gamma}$. Wall slip is present and no shear-banding appears.

The same conclusion can be drawn for the pure calcite sample at $\phi = 12\%$, as shown in Figure 5.8 for an increasing ramp from 10 to 100 s^{-1}. The velocity profiles display slip, especially at low $\dot{\gamma}$, but no

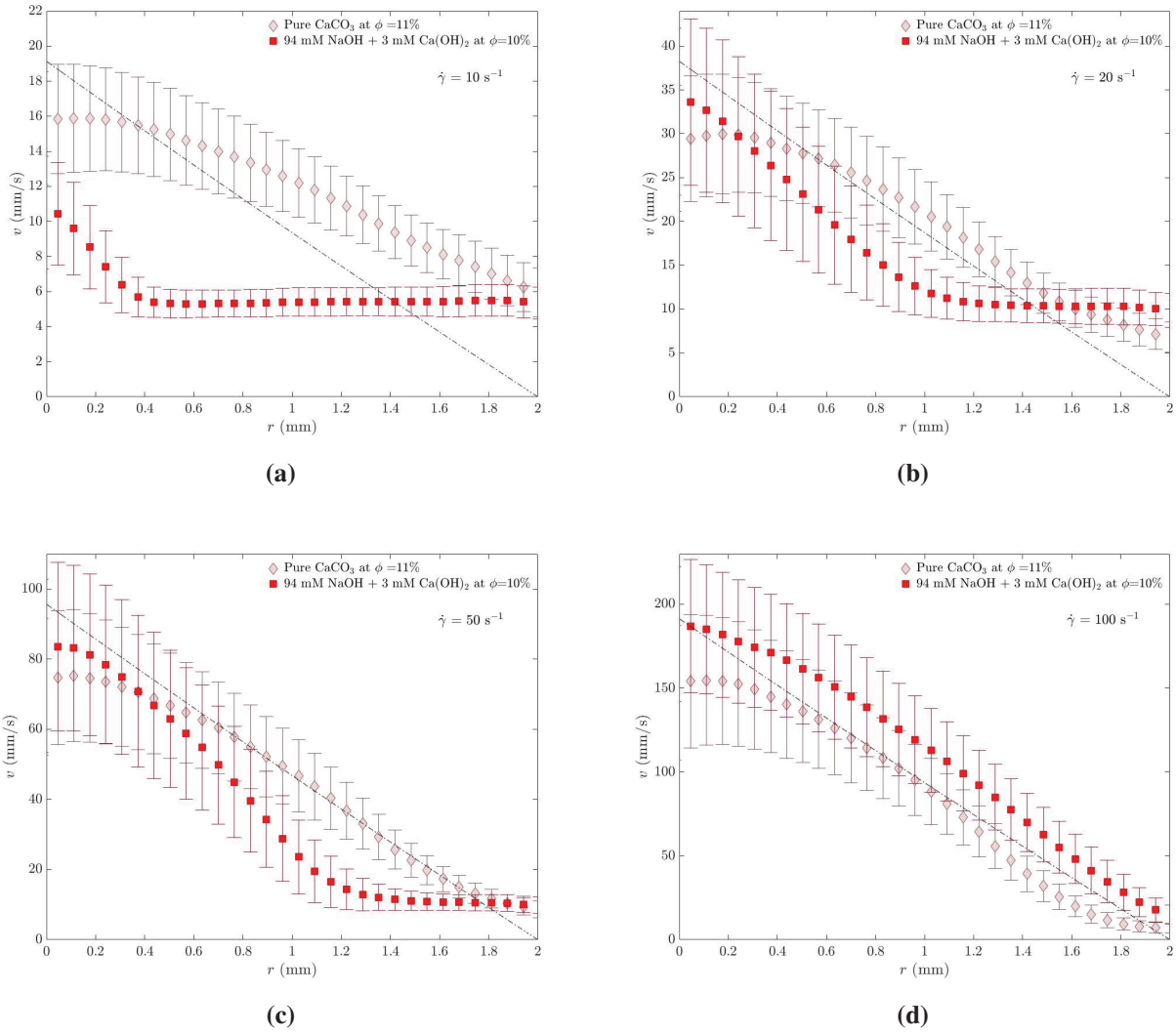

Figure 5.6 – Velocity profiles for two samples with the same rheological behavior: pure $CaCO_3$, $\phi = 11\%$ and $CaCO_3$ with NaOH, $\phi = 10\%$. The shear rates are $\dot{\gamma} = 10, 20, 50, 100\,s^{-1}$.

shear bands are detected.

For higher concentration (ϕ = 15 or 20 %), time averaged velocity maps exhibit spatial inhomogeneities along z and strong wall slip, even at high shear rates (i.e. 50 s^{-1}). These inhomogeneities make the analysis difficult. Nevertheless, we have no clear signature of shear banding, contrary to the case of NaOH for lower volume concentration ($\phi = 10\%$).

Concerning the calcite paste with NaOH, we decide to decrease the volume concentration down to 8 % to check if the shear-bands persist in the case of a more liquid paste. Figure 5.9 shows the velocity profiles for $\phi = 8\%$ and 10% measured at low shear rates ($\dot{\gamma} = 1 - 2\ s^{-1}$). Both velocity profiles do show shear banding. We also increase the concentration of NaOH at $\phi = 15\%$. We found the same problems as with concentrated pure calcite paste (spatial inhomogeneities and strong slip). Nevertheless we observe shear banding with a larger solid region.

Generally, we cannot make a reproducible study on samples at high concentration, i.e. 15-20 %, due to the strong inhomogeneities along the z direction. For this reason, we decide not to go into the details of this analysis.

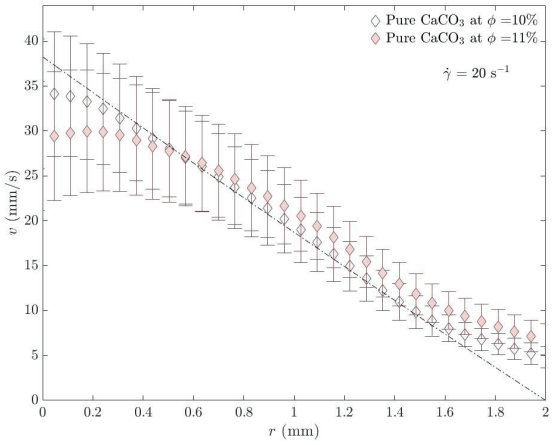

Figure 5.7 – Velocity profile for $CaCO_3$ samples at $\phi = 10$ and 11%. For both samples the shear rate is $\dot{\gamma} = 20\,\mathrm{s}^{-1}$.

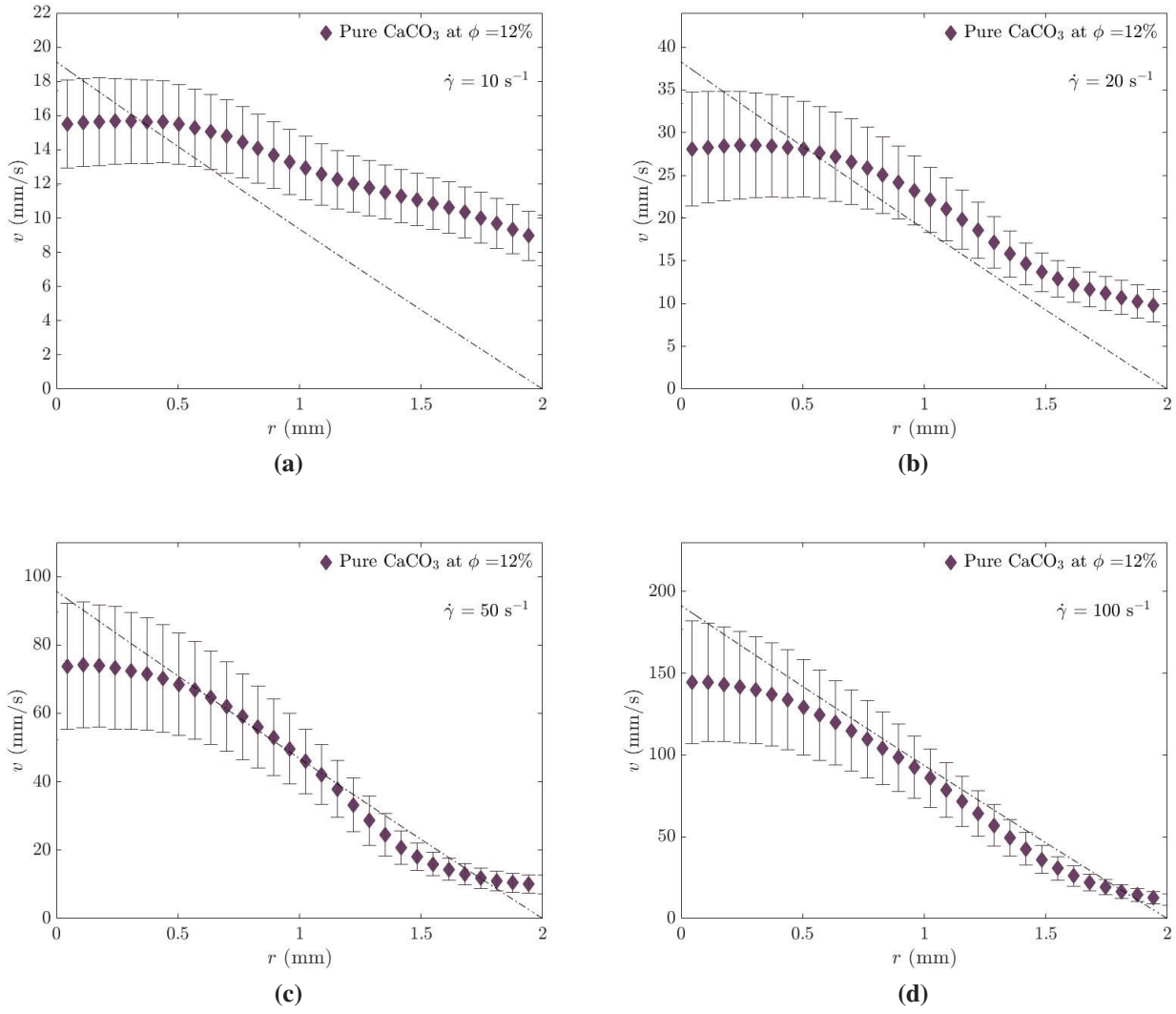

Figure 5.8 – Velocity profiles for pure $CaCO_3$, $\phi = 12\%$ at increasing shear rate.

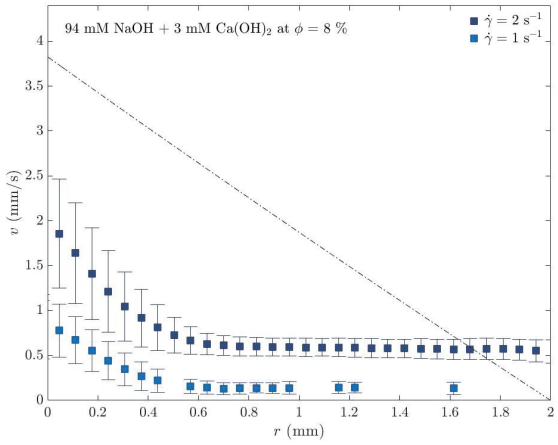

Figure 5.9 – Velocity profile for $CaCO_3$ with NaOH, $\phi = 8\%$.

5.3 Discussion

In the previous section, we studied the local rheology of two systems — pure calcite at $\phi = 11\%$ and calcite with sodium hydroxide at $\phi = 10\%$— which are characterized by identical macroscopic rheology (flow curve and storage modulus). We observed two different scenarios. At first, for pure calcite samples, the velocity profiles are homogeneous along the gap for all studied shear rates. Slip is present at both rotor and stator, especially at low shear rates whose macroscopic signature is the decrease in the flow curve of the shear stress at low shear rates. Then, for calcite with sodium hydroxide, the velocity profiles exhibit shear-bands for $\dot{\gamma} \leq 50\text{s}^{-1}$ and become homogeneous only at higher shear rates. As for the pure sample, slip is present at both rotor and stator and becomes more important at lower $\dot{\gamma}$. We also verified that the shear banding phenomenon does not depend on the volume concentration down to 8 %.

The main difference between the two systems lies in the interaction between the calcite particles at the microscopic scale. Indeed both the Zeta potential and Debye length are smaller in the paste with sodium hydroxide than for pure calcite, such that the DLVO interaction in calcite with NaOH is purely attractive (only Van der Waals attraction), whereas the colloids in pure calcite interact through a potential with a small repulsive barrier, comparable to thermal energy. Both systems are attractive but the attraction is stronger with addition of NaOH.

In our experiments, the existence of the shear-bands seems therefore to be correlated to a strong attraction between colloidal particles, allowing us to make a link between the microscopic colloidal interaction (i.e. DLVO barrier) and the macroscopic properties (i.e. velocity profiles).

This link between attraction and shear banding phenomena has been previously shown in the work of Bécu et al.(2006) [1]. This study focused on concentrated emulsions. By changing the concentration of surfactants, the authors could tune short range attractive forces. In particular, for a low surfactant concentration the resulting system is nonadhesive, for a higher quantity on the contrary, the depletion forces increase and the system becomes adhesive. For these two systems (adhesive and non adhesive), velocity profiles are recorded using USV and are shown in Figure 5.10.

Figure 5.10 (i) displays the results for a nonadhesive emulsion. For low/intermediate wall velocity v_0, (a)-(c), the profiles show a total wall slip. Increasing v_0, the velocity profiles become homogeneous (d). The adhesive emulsion in Figure 5.10 (ii) instead shows total wall slip only for very low wall velocity (a). Shear bands appear for low and intermediate values of v_0. At high wall velocity, the profiles also

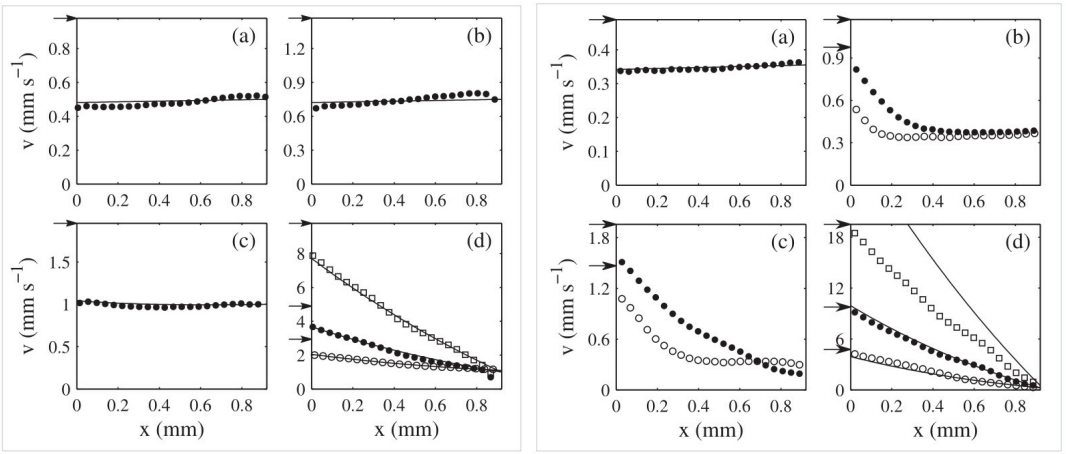

Figure 5.10 – Adapted from Bécu et al.(2006) [1]. (i) Velocity profiles in the nonadhesive emulsion for (a) $v_0 = 0.98$, (b) $v_0 = 1.47$, (c) $v_0 = 1.96$ and (d) v_0 =2.94 (○), 4.90 (●) and 9.79 mm s^{-1} (□). (ii) Velocity profiles in the adhesive emulsion for (a) $v_0 = 0.49$, (b) $v_0 = 0.98$ (○), 1.17 (●), (c) $v_0 = 1.47$ (○), 1.96 (●) and (d) v_0 =4.78 (○), 9.78 (●) and 19.5 mm s^{-1} (□). Arrows indicate the wall velocity v_0.

become homogeneous. To summarize, the nonadhesive system is homogeneous throughout the yielding transition whereas the adhesive one shows shear banding.

The common features between the Bécu et al. study and ours are that both systems - concentrated emulsions and calcite suspensions- are yield stress fluids and that shear bands occur once the attraction is increased. But it is important to point out that these two systems are intrinsically different in nature. Our calcite paste is a colloidal gel with a fractal structure while the system studied by Bécu et al. is a jammed concentrated system, i.e. a soft paste.

Following this distinction, we can find in the literature two relevant theoretical works that address the influence of attraction on velocity profiles, in jammed systems and in fractal ones. These studies are respectively the ones from Chaudhuri et al.(2012) [2] and Irani et al.(2014) [4].

In the article of Chaudhuri et al. [2], molecular dynamics simulations of soft particles jammed systems are performed to describe the flow of yield stress fluids such as foams, emulsions or polymer microgels. In this model they tune the particle interactions (from repulsive to attractive system) and study how it affects the velocity profiles.

For a non-attractive system (Figure 5.11), they find that the velocity profiles strongly fluctuate both in space and time. However these fluctuations vanish as the velocity profiles are averaged on large deformations. Shear inhomogeneities in the case of a non-attractive system are not therefore an intrinsic feature of the system, but is only a transient phenomenon.

For the attractive system the inhomogeneities of the velocity profiles are more pronounced (Figure 5.12) possibly longer than the durations of the simulations or the measurements (but not permanent). This could explain the observation of shear bands in the concentrated attractive emulsions of Bécu et al. [1], although these heterogeneities are not necessarily associated with a non-monotonic flow curve $\tau(\dot{\gamma})$, usually invoked to explain shear bands [7].

In the article of Irani et al. (2014) [4], the authors study the dynamics of assemblies of non-Brownian soft particles with a fractal structure in the vicinity of jamming. They also tuned particle interactions and measured the impact of a weak attraction on rheology.

The authors demonstrate the existence of non monotonic flow curves once attraction between parti-

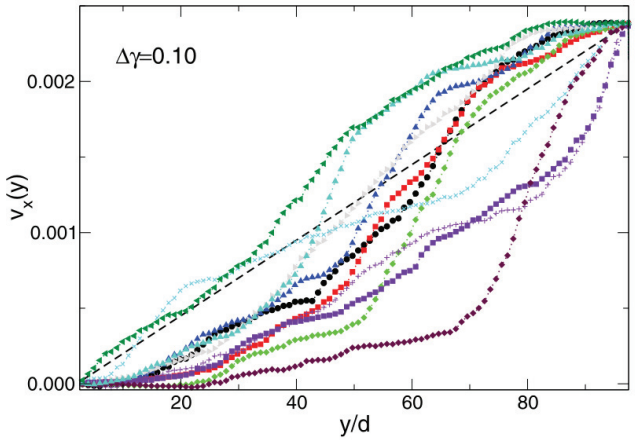

Figure 5.11 – Reproduced from Chaudhuri et al. [2]. A series of representative velocity profiles for repulsive particles, averaged during a strain window of $\Delta\gamma = 0.10$, and sampled during steady-state flow at an imposed $\dot{\gamma} = 2.5x10^{-5}s^{-1}$. These profiles reveal strong deviations from linear profiles, which strongly fluctuate both in space and time.

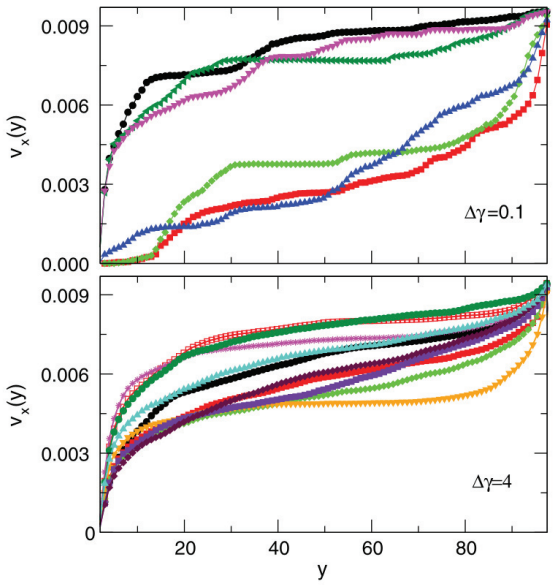

Figure 5.12 – Reproduced from Chaudhuri et al. [2]. A series of representative velocity profiles for attractive particles, averaged during a strain window of $\Delta\gamma = 0.10$ (top), and $\Delta\gamma = 4.0$ (bottom) and sampled during steady-state flow at an imposed $\dot{\gamma} = 10^{-4}s^{-1}$. These profiles reveal strong deviations from linear profiles, which strongly fluctuate both in space and time. Compared to the repulsive system, these profiles remain strongly non linear at large deformation $\Delta\gamma = 4.0$, suggesting that a linear velocity profile is not stable in the presence of strong particle adhesion.

cles is added into the system, as shown in Figure 5.13. Decreasing stress τ vs $\dot{\gamma}$ are instable and led to persistent shear banding over a range of shear rates that does not depend on the system size [7]. Irani et al. also demonstrate that these inhomogeneities are linked to the properties of the contacting network and disappear as soon as the attraction is suppressed. This theoretical study considers fractal suspensions whose microstructure and properties are similar to our fractal gel. The only difference is that our calcite particles are Brownian whereas the soft particles of Irani et al. are not. It would be interesting to study the role of thermal energy on the micro-structure and on its dynamics.

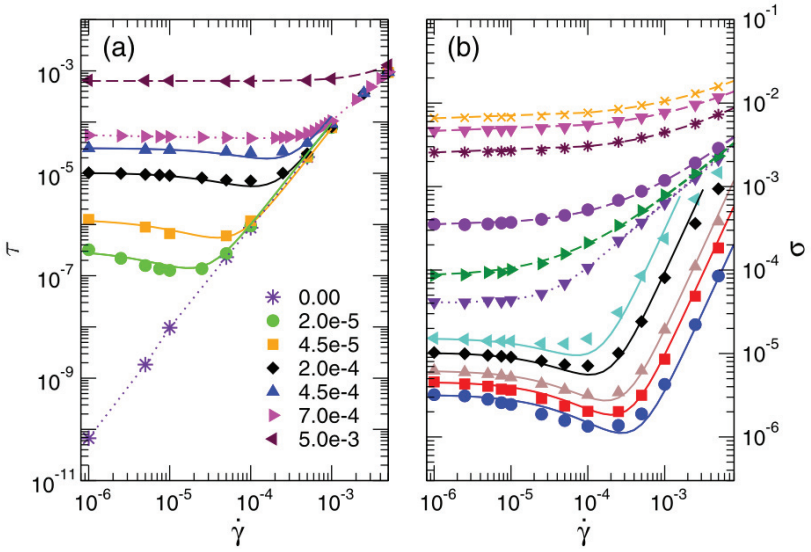

Figure 5.13 – Reproduced from Irani et al.(2014) [4]. Shear stress τ as a function of the strain rate $\dot{\gamma}$ for a system size N = 10^3: (a) for different attraction strengths u at ϕ = 0.82; (b) for different packing fractions (from the bottom to the top) ϕ = 0.75, 0.78, 0.80, 0.82, 0.83, 0.84, 0.843, 0.85, 0.9, 0.95, 1.0 for the attraction strength u = 2x10^{-4}.

Finally, one perspective of our work would be to verify if the shear bands observed in the attractive system (pure calcite with NaOH) are stationary (i.e. permanent in time). To do so it is necessary to monitor the velocity profiles on much longer times. One difficulty encountered is that the mechanical properties of the calcite paste (with NaOH) start to change with large deformations. For example the storage modulus is multiplied by a factor 3 if sheared at $\dot{\gamma} = 400\text{s}^{-1}$ instead of $\dot{\gamma} = 100\text{s}^{-1}$, even for a few seconds. It is then difficult to separate the impact of interactions forces from that of flow history on the mechanical properties and the velocity profiles.

5.4 Other investigated systems

As mentioned at the beginning of this chapter, we have studied the effects of other additives on the local rheology of calcite paste. As specified in Table 5.1, we also add to calcite paste 100 mM of hydrochloric acid (HCl), or calcium hydroxide ($Ca(OH)_2$) at two concentrations: 30 and 50 mM. These two systems present a strong evolution of their mechanical properties with time, as already shown for the calcium hydroxide in the previous chapter. The study of the temporal evolution of the elastic modulus for the sample containing HCl is described in the Annex B. In this section we show the preliminary results on flow for these two complex systems.

Concerning the calcite paste with HCl, Figure 5.14 displays the time averaged velocity map together with the velocity profiles for a sample at $\phi = 10\%$. Both profiles are acquired at $\dot{\gamma} = 20\ \text{s}^{-1}$: Figure 5.14 (a) during the increasing ramp and Figure 5.14 (b) in the decreasing ramp. The complete shear rate ramp imposed to this sample is $\dot{\gamma} = 10, 20, 50, 100, 200, 400, 200, 100, 50, 20, 10\ \text{s}^{-1}$. Figure 5.14 (a) shows a homogeneous behavior, Figure 5.14 (b) instead displays shear banding with a high wall slip at the rotor ($r = 0$). The evolution between the two profiles is very strong, even if they are acquired only 45 min apart. In this interval of time, the storage modulus strongly evolves too by almost one order of

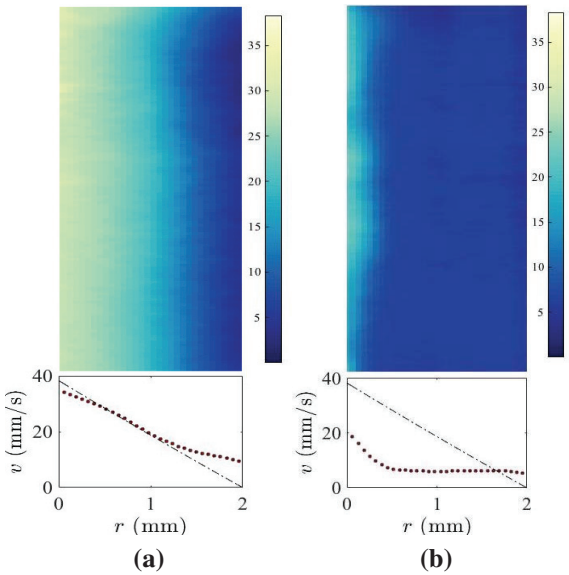

Figure 5.14 – Time-averaged velocity maps and the corresponding velocity profile (averaged over z) for a sample with 100 mM of HCl at $\phi = 10\%$. The color bar represents the velocity in mm/s. Comparison between the ascending (a) and descending (b) shear rate ramps for $\dot{\gamma} = 20\ \mathrm{s}^{-1}$.

magnitude, i.e. from 3000 to 20000 Pa. Such a strong evolution was not observed for the pure calcite paste or the calcite paste with NaOH. The mechanical evolution of the sample is certainly due to the effects of chemical reactions, i.e. calcite dissolution and precipitation, as also shown in Annex B for the elasticity measurements.

Concerning calcite paste with calcium hydroxide, Figure 5.15 compares the flow curve of pure calcite and calcite with 30 or 50 mM of $Ca(OH)_2$ for $\phi = 10\%$.

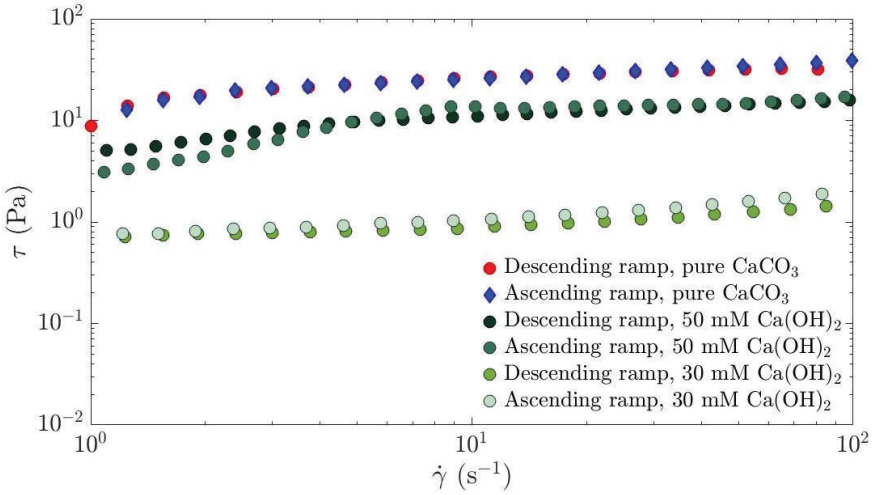

Figure 5.15 – Flow curve comparison for pure $CaCO_3$, calcite with 30 and 50 mM of $Ca(OH)_2$. All samples are at $\phi = 10\%$.

All these flow curves are obtained on fresh pastes tested after the first pre-shear step (2 min). We can notice that, as for the viscoelastic properties, calcium hydroxide makes the samples more fluid (i.e. decreasing both the storage modulus and the viscosity). Moreover also here as in Chapter 4, the

30 mM of calcium hydroxide gives a stronger effect compared to the 50 mM for a $\phi = 10\%$ sample, confirming the DLVO calculation. Figure 5.16 shows the time evolution of the flow curves and of the elastic modulus of a calcite sample containing 30 mM of calcium hydroxide at $\phi = 10\%$. The protocol used in this specific case is composed by two steps: flow measurements with a descending/ascending ramps from $\dot{\gamma} = 400 - 0.4$ s^{-1} (≈ 20 min) and a measure of the storage modulus during 30 min. This two steps are repeated several times for ≈ 7 h. Figure 5.16 (a) shows the flow curves $\tau(\dot{\gamma})$ at different instant while Figure 5.16 (b) shows the storage modulus as a function of time. Due to the evolution of the storage modulus during the 30 min of testing, we plot G' at the end of this step as G'_{end}, so once a plateau value is reached. Both quantities, i.e. τ and G'_{end}, show a strong increase as a function of time, especially in the first hours.

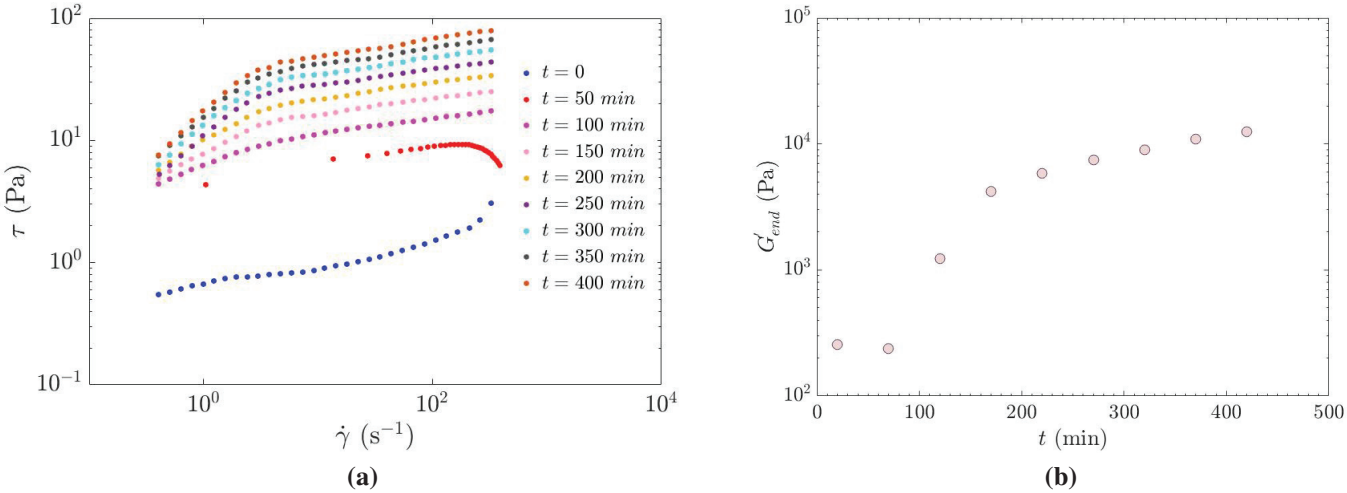

Figure 5.16 – (a) Evolution of flow curves in time for a calcite sample with 30 mM of $Ca(OH)_2$ and $\phi = 10\%$. Between two flow curves, the storage modulus is recorded during 30 min. The value at the end of this step versus time, is displayed in (b).

Moreover, Figure 5.17 shows the time averaged velocity maps and the corresponding velocity profiles for a calcite sample with 30 mM of calcium hydroxide ($\phi = 10\%$). The complete shear ramp is displayed (from (a) to (g)) as: $\dot{\gamma} = 10, 50, 100, 400, 100, 50, 10$ s^{-1}. During all the increasing ramp, i.e. 10 to 400 s^{-1}, the suspension acts as a Newtonian liquid. The behavior in the decreasing ramp, i.e. 100 to 10 s^{-1}, evolves strongly. The image (g), in fact, shows shear banding and is recorded only 40 min after the first velocity profile.

All the tests made for samples containing calcium hydroxide (both 30 and 50 mM) evidence a strong temporal evolution. This is certainly due to the reactivity of the systems in particular in presence of carbon dioxide, as already discussed in Chapter 4. Nevertheless, the limited quantities of carbon dioxide available in this geometry (Couette with a top lid) also suggests an evolution due to the imposed shear.

The complexity of these systems, more precisely the temporal evolution of their mechanical properties, prompted us to only analyze the stable ones: pure calcite and calcite with NaOH, presented above. An other perspective of this work would be to study more systematically these more complex system, in order to distinguish the contribution of the reactivity or aging from the contribution of the imposed shear. This could be done by testing a sample after 10-20 h in the geometry without any shear.

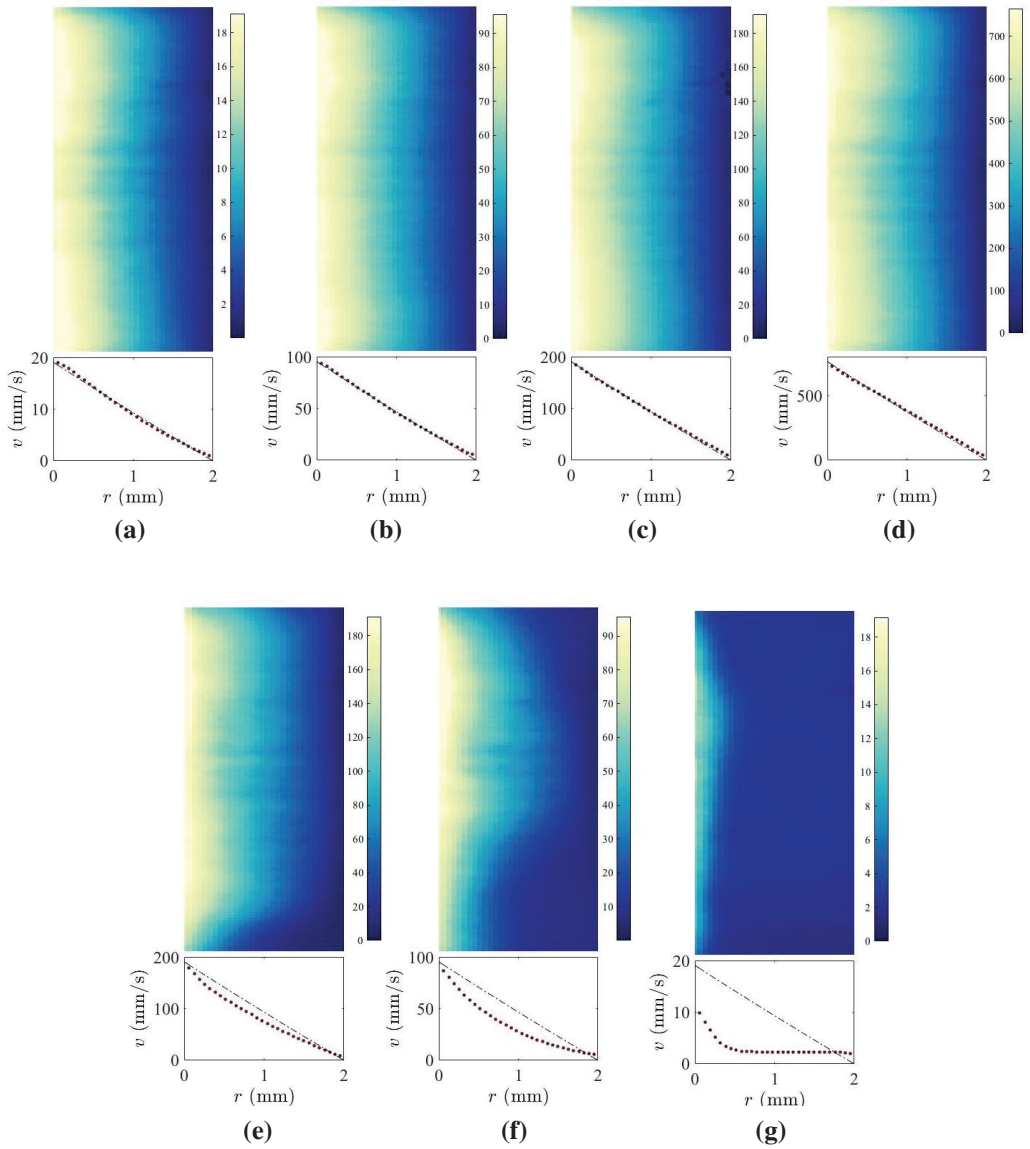

Figure 5.17 – Time-averaged velocity maps and the correspondent spatio-temporal velocity profile for a $\phi = 10\%$ calcite sample with 30 mM of $Ca(OH)_2$. The color bar represents the velocity in mm/s. (a)-(g) Complete shear rate ramp as $\dot{\gamma} = 10, 50, 100, 400, 100, 50, 10\ s^{-1}$.

5.5 Conclusion

In this chapter, we have made a link between the flow behavior at the macroscopic scale and the particle interactions at the colloidal scale, interactions that have been changed by adding simple ionic species to the calcite paste. We mostly focus our study on two suspensions: pure calcite and calcite with sodium hydroxide, NaOH, whose mechanical properties weakly evolve with time (low reactivity). We compare the local rheology of two systems characterized by identical macroscopic rheological behavior but different microscopic interactions. The pure calcite is a weakly attractive system whereas calcite with NaOH is a strongly attractive one. Velocity profiles show the signature of the attraction by displaying shear banding for the more attractive system. The correlation between attraction and shear banding is known for jammed system (e.g. emulsion and microgel) [1, 9, 5] . In particular the authors studied

first repulsive jammed systems exhibiting homogeneous flows. Then they changed the local interaction by making the system attractive (via depletion forces or hydrophobic interaction) and they showed the existence of shear banding though velocity profiles measurements. For diluted systems such as colloidal gels, there are several works [8, 3, 6] in which attractive systems exhibit shear banding without any evidence of homogeneous flow for the equivalent systems without attraction. So the transition shown by our calcite paste from a (weak) repulsive systems (pure calcite) with an homogeneous flow to an attractive system (calcite with NaOH) showing shear bands, has never been observed so far for colloidal gels.

The first perspective of this study, inspired by the theoretical work by Chaudhuri et al. [2], is to evaluate the stationarity of our shear bands by studying how the velocity profiles for the strong attractive system evolve in time.

Bibliography

[1] L. Bécu, S. Manneville, and A. Colin. Yielding and flow in adhesive and nonadhesive concentrated emulsions. *Physical review letters*, 96(13):138302, 2006.

[2] P. Chaudhuri, L. Berthier, and L. Bocquet. Inhomogeneous shear flows in soft jammed materials with tunable attractive forces. *Physical Review E*, 85(2):021503, 2012.

[3] P. Coussot, J. Raynaud, F. Bertrand, P. Moucheront, J. Guilbaud, H. Huynh, S. Jarny, and D. Lesueur. Coexistence of liquid and solid phases in flowing soft-glassy materials. *Physical review letters*, 88(21):218301, 2002.

[4] E. Irani, P. Chaudhuri, and C. Heussinger. Impact of attractive interactions on the rheology of dense athermal particles. *Physical review letters*, 112(18):188303, 2014.

[5] M. Mattiello. *Structure and dynamics of dense suspensions of soft colloids with tunable short-range attraction*. PhD thesis, Université Paris Sciences et Lettres, 2018.

[6] P. Møller, S. Rodts, M. Michels, and D. Bonn. Shear banding and yield stress in soft glassy materials. *Physical Review E*, 77(4):041507, 2008.

[7] G. Ovarlez, S. Rodts, X. Chateau, and P. Coussot. Phenomenology and physical origin of shear localization and shear banding in complex fluids. *Rheologica acta*, 48(8):831–844, 2009.

[8] F. Pignon, A. Magnin, and J.-M. Piau. Thixotropic colloidal suspensions and flow curves with minimum: Identification of flow regimes and rheometric consequences. *Journal of rheology*, 40(4):573–587, 1996.

[9] A. Ragouilliaux, G. Ovarlez, N. Shahidzadeh-Bonn, B. Herzhaft, T. Palermo, and P. Coussot. Transition from a simple yield-stress fluid to a thixotropic material. *Physical Review E*, 76(5):051408, 2007.

Chapter 6

Conclusions and perspectives

This PhD work has been devoted to the rheology of calcite paste and its relation with the microscopic interaction between nanometric colloids. It has been motivated both by the numerous applications involving calcium carbonate and by fundamental questions in the physics of colloidal gels.

Main results

The first part of the thesis deals with the viscoelastic properties of pure calcite paste in order to built a reference system before the addition of other species. We first focused on the elastic regime. We extracted two quantities of interest: the linear storage modulus G'_{lin} and the deformation at the end of linearity γ_{cr}. Both are measured in a wide range of volume concentrations. DWS (Diffusion Wave Spectroscopy), an optical technique based on multiple light scattering, is used to ascertain the absence of measurement artifacts such as wall slip effects or heterogeneous deformation fields.

Upon increasing the solid volume fraction ϕ from 5 to 30 %, the trends of G'_{lin} and γ_{cr} evidence two different scaling laws: G'_{lin} shows a change in exponent while γ_{cr} goes through a minimum for the same range of solid content. This non monotonic trend of the deformation can be interpreted in the framework of the fractal elasticity model of colloidal suspensions proposed by Shih et al. [5]. This model assumes a transition from a strong-link to a weak-link regime as the solid concentration is increased. At low volume concentration (strong-link regime) both rigidity and deformation of the paste are dominated by the properties of fractal floc. The flocs become smaller and stiffer as the solid concentration increases, so that at high volume concentration (weak-link regime) the links between the flocs prevail. In the literature many others systems were analysed with this fractal model. In our case, calcite paste is the first system for which the transition from the strong-link to the weak-link regime is observed without any external perturbation. A major prediction of colloidal gel theory, never verified so far. Thanks to this interpretation, we also were able to characterize a floc size and a fractal dimension for the two regimes. In particular the fractal dimension increases with the solid fraction, pointing to a change of the aggregation with concentration.

The second part of the thesis deals with the influence of additives on the macroscopic rheology of calcite paste and on microscopic interaction between colloidal particles. In that aim a wide range of ionic strengths, pH and ionic species are analyzed, adding calcium hydroxide ($Ca(OH)_2$), calcium chloride ($CaCl_2$), hydrochloric acid (HCl) and sodium hydroxide (NaOH). These broad ranges of inorganic

additives are tested to obtain strong variations of elasticity and yielding of the paste, in comparison with the mechanical properties of pure calcite suspension. We decided to select two main additives: calcium and sodium hydroxide as they give the most spectacular effects on rheological properties. Then to link macroscopical properties with microscopic interactions, the ionic composition of the solution is determined through a complete chemical speciation, and the surface charge is characterized by Zeta potential measurements ζ [4]. Knowing the ionic strength and ζ, we calculated DLVO interactions for each sample and compared them to the macroscopic mechanical response.

Immediately after preparation, increasing the initial calcium hydroxide concentration results in a higher paste workability (i.e. decreasing in both elastic modulus and viscosity). This initial effect is due to the dissolution of $Ca(OH)_2$, which increases the amount of calcium (Ca^{2+}) ions in the solution. At the same time, ζ rises due to the adsorption of calcium ions on the calcite surface. We observed that the elastic modulus of this weak gel increases strongly with time due to the precipitation of calcium carbonate upon reaction with atmospheric CO_2. The final properties (after $\approx 10\,h$) of the pastes with $Ca(OH)_2$, realign with the pure one. To sum up, looking at the DLVO calculation, pure calcite is a weakly attractive system. Once inserted high quantities of calcium hydroxide, the repulsion between $CaCO_3$ particles increases, resulting in a more workable paste, which recovers elasticity upon carbonation.

The addition of sodium hydroxide instead results in a strong attractive system without any repulsive contribution (pure van der Waals interaction). The sample containing NaOH has the higher values of G'_{lin} and γ_{cr} and evolve slowly with time. The most interesting result with this strong attractive system is highlighted in flow measurements. Ultrasonic velocimetry device coupled to rheology allows to follow the local dynamics of the sheared samples. We compared the two more stable systems: pure calcite and calcite with sodium hydroxide, tuning the volume concentration to have exactly the same apparent macroscopic rheological behavior. The comparison of velocity profiles recorded by the ultrasonic technique shows a clear signature of attraction in the presence of NaOH, by the occurrence of shear bands. This correlation was already observed in jammed emulsions but never verified so far for colloidal gels.

More generally, concerning the link between the macroscopic rheology and the microscopic interaction, we show that the elastic modulus of all studied samples varies inversely with the energy barrier of DLVO potential.

Perspectives

Regarding the elastic properties of colloidal pastes, we found that the non spherical geometry of the particles should play a key role in the interaction forces, estimated from DLVO calculations, hence on the gel network structure and its elastic properties. Quantifying the role of the anisotropy of the particles on the gel structure and its elastic response remains an open question. In this direction, we recently started a collaboration with Juan Olarte Plata and Prof. Fernando Bresme (Imperial College London) to investigate this question through numerical simulations of molecular dynamics. Understanding the link between local forces, particle geometry, gel network structure, elastic and flow properties is a first step toward the control of paste mechanical properties through the incorporation of organic additives.

Another open question is the role of the timescale of solicitation which can be comparable to the timescale of particle re-aggregation, as pointed by Koumakis and Petekidis [3]. This could be explored by quantifying the frequency response of our system.

Regarding the flow properties of calcite paste, we have highlighted the existence of shear bands, as in other attractive systems including soft-jammed suspensions as emulsions. However, theoretical models [1, 2] have underlined the very different nature of shear inhomogeneities —transient or persistent/permanent— depending on the jammed or gel-like structure. Evaluating the persistence of shear bands in our calcite samples is thus necessary to obtain a complete picture of the mechanisms at the origin of this flow inhomogeneities.

Bibliography

[1] P. Chaudhuri, L. Berthier, and L. Bocquet. Inhomogeneous shear flows in soft jammed materials with tunable attractive forces. *Physical Review E*, 85(2):021503, 2012.

[2] E. Irani, P. Chaudhuri, and C. Heussinger. Impact of attractive interactions on the rheology of dense athermal particles. *Physical review letters*, 112(18):188303, 2014.

[3] N. Koumakis and G. Petekidis. Two step yielding in attractive colloids: transition from gels to attractive glasses. *Soft Matter*, 7(6):2456–2470, 2011.

[4] S. Pourchet, I. Pochard, F. Brunel, and D. Perrey. Chemistry of the calcite/water interface: Influence of sulfate ions and consequences in terms of cohesion forces. *Cement and Concrete Research*, 52:22–30, 2013.

[5] W. Y. Shih, W.-H. Shih, and I. A. Aksay. Elastic and yield behavior of strongly flocculated colloids. *Journal of the American Ceramic Society*, 82(3):616–624, 1999.

Appendices

Appendix A

Zeta potential on dilute suspensions

Zeta potential ζ measurements on diluted suspension of calcite are carried out with the ZetaSizer (Malvern) described in Section 2.3.2 at the Fennec équipe (Institut Lumière Matière, Université Claude Bernard Lyon 1) under the supervision of Matteo Martini.

In particular these measurements are made on the supernatant of calcite diluted suspensions. The paste at $\phi = 20\,\%$ is diluted to obtain a suspension at $\phi = 0.2\,\%$. The diluted solution ($\phi = 0.2\,\%$) is placed in an open batch in contact with the atmosphere waiting for the calcite particles sedimentation and then the supernatant is collected. To dilute the calcite paste, several solutions were tested such as deionized water, calcite saturated solution and calcite saturated solution adding 3 mM of calcium hydroxide. As already mention in Section 2.1, this quantity of $CaOH_2$ is added to the deionized water to reach a pH$\approx$ 8 and avoid calcite dissolution. The results of the Zeta potential titration (i.e. ζ measurements as a function of pH) of calcite samples with these three solutions are collected in Figure A.1. The pH is changed by the ZetaSizer by adding two solutions: 0.1 M of HCl or 0.1 M of NaOH.

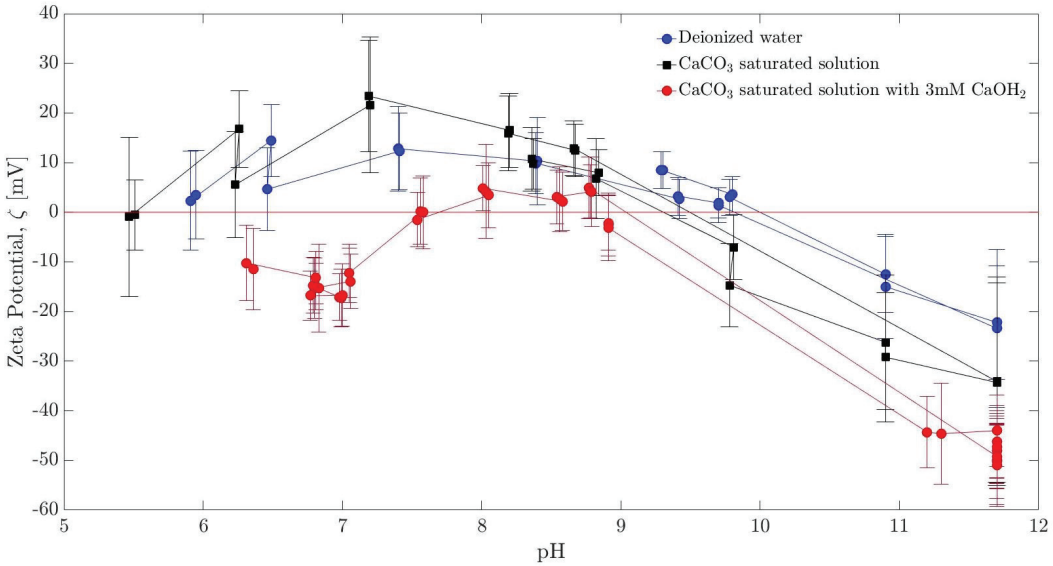

Figure A.1 – Zeta potential titration of calcite diluted suspensions with several solutions such as: deionized water, calcite saturated solution and calcite saturated solution with 3 mM of calcium hydroxide. Tests are made on the supernatant of the $\phi = 0.2\,\%$ suspensions, pH is changed by adding two solutions: 0.1 M of HCl or 0.1 M of NaOH.

Moreover individual Zeta potential measurements are made on dilute systems as listed in Table A.1.

Samples	**pH**	ζ **(mV)**
Pure	8.5	11.47
3 mM **Ca(OH)**$_2$	8.9	-6.4
15 mM **Ca(OH)**$_2$	9.0	-2.4
30 mM **Ca(OH)**$_2$	9.2	1.7
50 mM **Ca(OH)**$_2$	9.3	2.5
100 mM **Ca(OH)**$_2$	10.1	18.4
47 mM **CaCl**$_2$ + 3 mM Ca(OH)$_2$	8.7	16.8
97 mM **CaCl**$_2$ + 3 mM Ca(OH)$_2$	8.9	18.3

Table A.1 – Zeta potential ζ measurements for diluted calcite suspensions. The tests are made on the supernatant of $\phi = 0.2\,\%$ suspensions, diluted with a $CaCO_3$ saturated solution.

The non monotonic trend of the Zeta potential with the addition of calcium hydroxide is still obscure. In fact, looking at the results obtained by ζ measurements on dense calcite pastes shown in Chapter 4, we cannot explain the initial negative value of Zeta potentials for both 3 and 15 mM of $Ca(OH)_2$. Similar results are obtained by Pierre et al. [11] without any explanation.

The main conclusion of these measurements is that ζ strongly depends on pH but also on the volume fraction ϕ. In fact the values obtained with diluted and concentrated ($\phi = 10\,\%$) suspensions are very different.

Moreover, from the same machine by Diffusion Light Scattering (DLS) we obtained a particles size of of $\approx 2\,\mu$m for the pure dilute calcite suspension. This value is in agreement with the floc size calculated by fractal analysis at low volume calcite concentration (Section 3.1).

Appendix B

Inorganic additives: role on elasticity and yielding

In order to control the mechanical properties of calcite paste, it is necessary to understand the role of the interaction forces that occur between $CaCO_3$ particles. In Chapter 4, we already presented the results for calcium hydroxide and sodium hydroxide addition, linking macroscopic rheological values with microscopic particle interactions. In this appendix are presented the preliminary results of the others systems listed in Table 2.1 on elasticity and yielding of $\phi = 20\,\%$ suspensions, in which calcium cloride $CaCl_2$ and hydrochloric acid HCl have been added. They are compared with the data obtained with 3 mM of calcium hydroxide.

B.1 Materials and Methods

B.1.1 Sample preparation and pH measurement

The protocol for the sample preparation is presented in Section 2.1. Socal 31 calcite powder is homogeneously suspended in aqueous solutions. The initial calcite volume concentration is fixed to $\phi = 20\,\%$. The solutions are prepared by dissolving $Ca(OH)_2$, $CaCl_2$ and HCl (from Sigma-Aldrich) in deionized water, at the concentrations presented in Table B.1. In particular, as already mentioned, we found that the addition of 3 mM of $Ca(OH)_2$ to deionized water increases the pH of the initial solution up to 8, avoiding an initial calcite dissolution. For this reason, we added this quantity to all samples tested.

For all the samples, the pH values are measured with a pH-meter HANNA edge, with an uncertainty range ± 0.2.

B.2 Rheological Measurements

In order to characterize the elastic regime of the calcite pastes in presence of additives and compare these results with the pure system, the same protocol described in Section 2.2.1 is used. We briefly recall it below.

We impose an oscillatory deformation applied by a stress-controlled rotational rheometer (Anton Paar MCR 301). The measurements are performed in a plate-plate (PP) geometry at room temperature.

The chosen gap width of 4 mm has been shown to avoid slippage at the walls. All the measurements have been performed with plates covered with sand paper (roughness 46 μm). The measured viscoelastic response of the paste is characterized by the storage G' and loss G'' moduli [8].

The measurements are preceded by a preparation consisting of two steps: the pre-shear —1 minute at imposed shear rate of $\dot{\gamma} = 10\ s^{-1}$— and the time structuration —5 minutes resting step at imposed deformation $\gamma = 0.01\ \%$ and frequency $f = 1$ Hz. The amplitude sweep phase, from which the viscoelastic moduli can be computed, consists in an oscillatory deformation at imposed frequency ($f = 1$ Hz, $\gamma = 0.001 - 10\ \%$).

B.2.1 Data analysis

As introduced in Section 2.2.1, we analyze the amplitude sweep results, i.e. the elastic modulus G' as a function of the deformation γ. We extract two quantities of interest: the values of the storage modulus in the linear regime (constant G') called G'_{lin} and at the deformation at the end of the linearity or critical strain γ_{cr} [9], characterizing the transition from the elastic to the viscous regime. Based on the pH measurements and the molar compositions of each paste, a full description of the ionic composition is calculated with the speciation freeware Visual MINTEQ [1], as detailed in Section 2.4.

B.3 Results

In this section, we first detail the pH variations with the corresponding chemical analysis and then the effects of each species on the elastic properties of calcite paste.

B.3.1 Variation of pH and chemistry of the pastes

In Table B.1 are listed the tested samples with the corresponding values of pH and calcium ions calculated by Visual MINTEQ ($\phi = 20\ \%$). Figure B.1 shows the measured pH as a function of the molar equilibrium calcium concentration [Ca^{2+}]. Each color corresponds to the main additive used.

Samples	**pH**$_{meas}$	**[Ca^{2+}] (mM)**
Pure ○	8.8	0.24
3 mM **$Ca(OH)_2$** ●	10.2	0.15
1 mM **HCl** + 3 mM $Ca(OH)_2$ ■	9.6	0.55
5 mM **HCl** + 3 mM $Ca(OH)_2$ ■	9.1	2.5
50 mM **HCl** + 3 mM $Ca(OH)_2$ ■	6.9	24.6
100 mM **HCl** + 3 mM $Ca(OH)_2$ ■	6.5	47.3
47 mM **$CaCl_2$** + 3 mM $Ca(OH)_2$ ■	9.4	43.6
97 mM **$CaCl_2$** + 3 mM $Ca(OH)_2$ ■	11.2	85.9

Table B.1 – List of all the tested samples with a calcite concentration of $\phi = 20\ \%$. The concentration of calcium ions are calculated with MINTEQ at the measured pH.

Taking as a reference point the 3 mM of $Ca(OH)_2$ (●), we can look at the effect of HCl and $CaCl_2$.

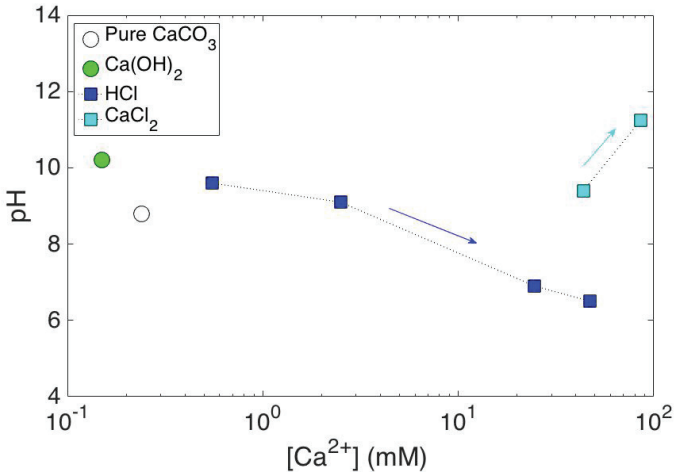

Figure B.1 – Analysis of pH for all the tested samples. The x-axis, in a logarithmic scale, represents the molar concentration of Ca^{2+} calculated by Visual MINTEQ. Following the colored arrows the amount of each additive increases. All the samples are at $\phi = 20\,\%$.

For hydrochloric acid (■), we can notice that this addition results in a pH decreasing, as expected. Under pH = 8, we observe an increase in calcium ionic concentration, due to significant calcite dissolution, as reported in the literature [6].

We now turn to the role of calcium chloride (■), which has been added directly at rather large concentrations. For an addition of ≈ 50 mM of $CaCl_2$, the calcium concentration increases and the pH is quite stable.

Adding $CaCl_2$ up to ≈ 100 mM results in an increase of $[Ca^{2+}]$ but also of pH. The difference of pH between the two samples is surprising because pH values calculated for the equilibrium with and without atmosphere (resp. 7.4 and 11.4) depend little on the concentration of calcium chloride. This suggests that the carbonation dynamics is different in the two samples.

B.3.2 Elasticity and yielding results

In this section, the effects of additives addition on the elasticity and yielding of calcite paste is examined. The values of G'_{lin} and γ_{cr} as a function of calcium ions concentration are displayed in Figures B.2 and B.3.

Influence of HCl (■)

The addition of hydrochloric acid decreases the pH and dissolves calcite. This calcite dissolution does not affect too much the volume concentration of the paste, which decreases by less than 1 %. However, it increases the quantity of Ca^{2+}, Cl^- and $CaCl^+$ ions in the suspension. Starting from the sample containing only 3 mM of $Ca(OH)_2$(●) and follow the blue arrow on figures B.2 and B.3, we find that the addition of HCl results in a progressively decrease of G'_{lin}; The γ_{cr} increases at the beginning and after is stable.

For the sample with 100 mM of HCl and 3 mM of $Ca(OH)_2$ we also look at its evolution in time, such as in Chapter 4 for calcium and sodium hydroxide samples. In particular, we follow the storage modulus in time, as result of the time structuration step in protocol β (10 h at $\gamma = 0.01\,\%$ and $f = 1$ Hz),

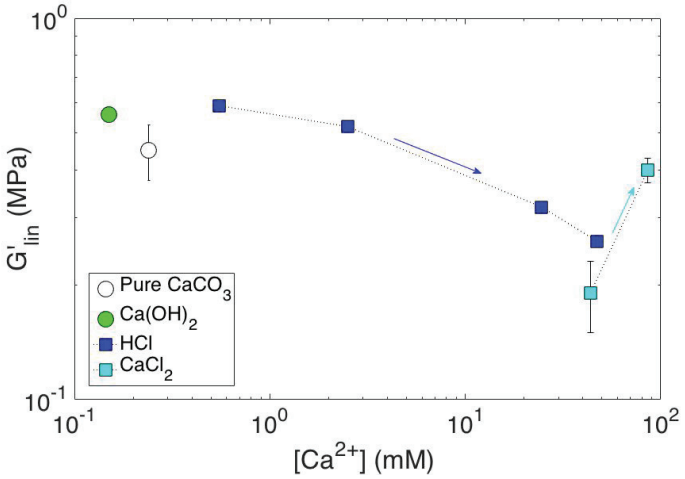

Figure B.2 – Linear storage modulus, G'_{lin}, as a function of the Ca^{2+} ions concentration. Following the colored arrows, the amount of each additive increases. All the samples are at $\phi = 20\,\%$.

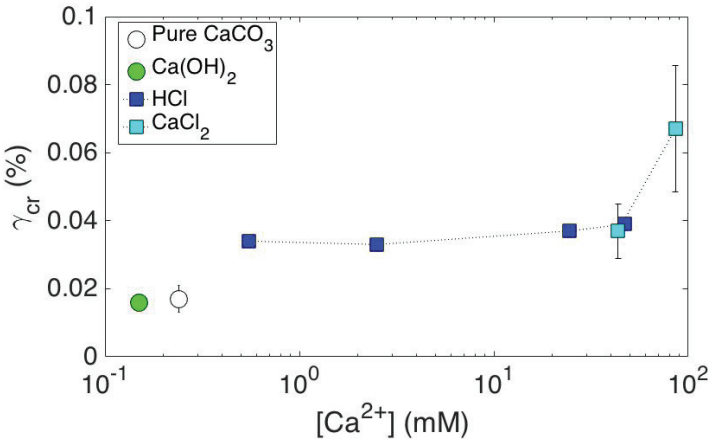

Figure B.3 – Values of the critical deformation, γ_{cr}, as a function of the Ca^{2+} ion concentration. Following the colored arrows, the amount of each additive increases.

as shown in Figure B.4.

The sample with HCl is compared with the pure one. The initial elastic modulus is lower for the sample with HCl. This is surprising because the DLVO calculation predicts a strong attraction for this system. This is due to the high ionic strength $I = 143$ mM (screening) although the measured Zeta potential is ζ = 15.6 mV. We attribute this effect to the presence of CO_2 bubbles due to the initial calcite dissolution, as shown in reaction (3):

(3) $CaCO_3 + 2HCl \longrightarrow CaCl_2 + CO_2 + H_2O$

The elastic modulus of a yield stress fluid has been shown to decrease in the presence of CO_2 bubbles with the gas volume fraction [5].

Second we find a strong evolution of the linear storage modulus in the first 15 min. This is probably due to the ejection of CO_2 bubbles from the sample. This temporal evolution however remains to be fully understood and has also been observed in flow measurements (Section 5.4).

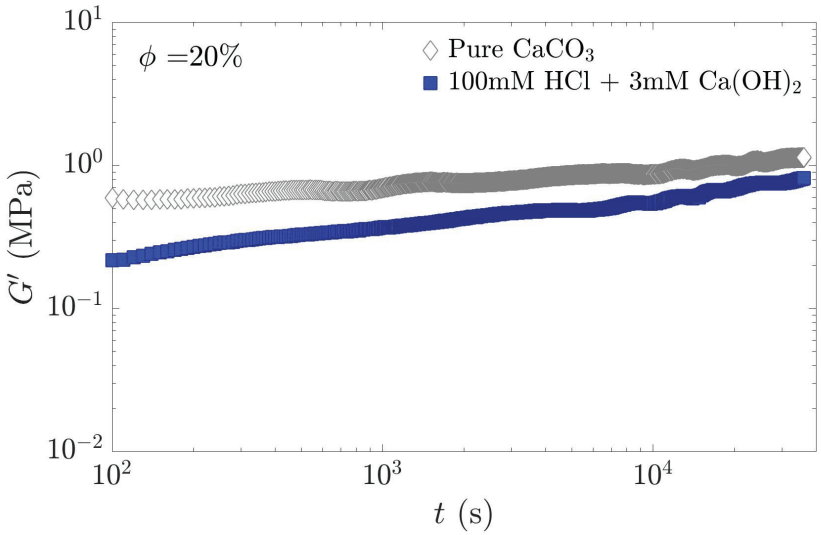

Figure B.4 – Time evolution of the storage modulus of calcite suspensions at $\phi = 20\,\%$ for the pure system and the one with 100 mM of HCl and 3 mM of $Ca(OH)_2$.

Influence of $CaCl_2$ (■)

Figures B.3 shows that the yield strain increases upon calcium chloride addition. This is in good agreement with the effect observed adding calcium hydroxide (Section 4.2.5). The effect on the elastic modulus (figure B.2) is less clear: it first decreases then increases. For both 47 and 97 mM of $CaCl_2$ the high ionic strength (resp. 134 and 270 mM) screen completely the electrostatic repulsion. We do not understand this behavior.

Appendix C

Organic additives: role of dicarboxylic acids

C.1 Rheological results

In this appendix, the role of small organic molecules i.e. dicarboxylic acids on elasticity and yielding of calcite paste is detailed.

Dicarboxylic acids are organic compounds containing two carboxyl functional groups -COOH, varying the number of carbons nC in the structure between them. We tested small dicarboxylic acids, from oxalic acid— nC=2 ($C_2H_2O_4$)— to adipic acid —nC=6 ($C_6H_{10}O_4$)— and a wide range of molar concentration —from 5×10^{-4} to 0.1M. The initial calcite paste volume concentration is $\phi = 20\,\%$. The sample preparation and the rheological measurements are performed following the usual protocol also detailed in Section B.2.

The results obtained with the addition of dicarboxylic acids without any pH or ionic strength control are presented in Figure C.1 and Figure C.2.

Both figures show the values of G'_{lin} and γ_{cr}, normalized by the values of the pure calcite paste $G'_{\text{lin}}(0)$ and $\gamma_{\text{cr}}(0)$ and plotted versus the number of carbons nC present in the dicarboxylic acid structure.

As we can see most of the values lie between the two dashed lines, representing the dispersion range of the pure calcite values (orange solid line). We can notice an increase of γ_{cr} for the two extremes nC-values. However this effect is not monotonic with the molar concentration. Further studies need to be made to link these points with values of pH and ionic strength, and to clarify the influence of chemical and physical parameters as we did for the ionic species presented in Chapter 4.

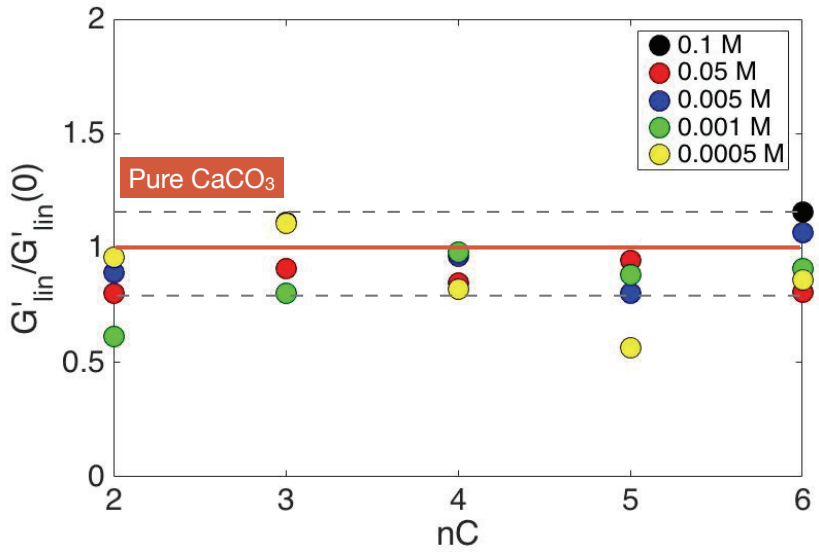

Figure C.1 – Normalized linear storage modulus, $G'_{\text{lin}}/G'_{\text{lin}}(0)$, as a function of the number of carbons in the dicarboxylic acid structure. Dashed lines represent the error-bar of the pure calcite $G'_{\text{lin}}(0)$ value (orange solid line). All the samples are at $\phi = 20\,\%$.

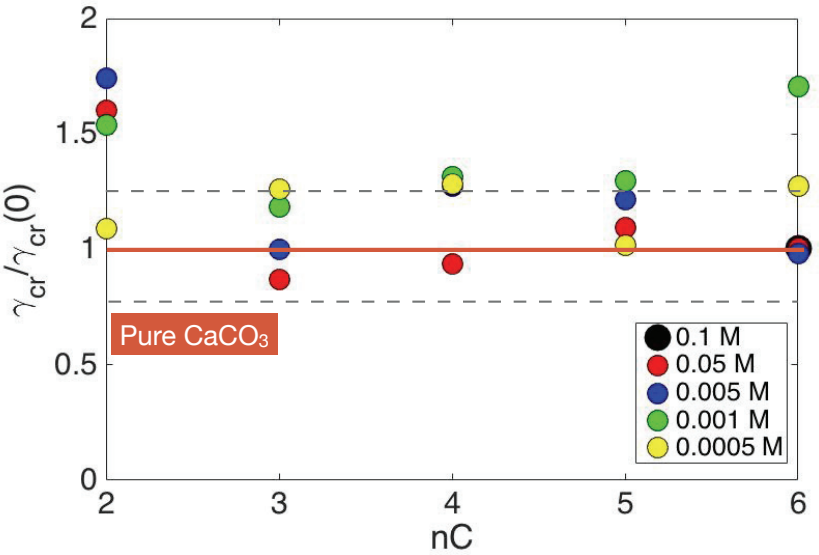

Figure C.2 – Normalized values of the critical deformation, $\gamma_{\text{cr}}/\gamma_{\text{cr}}(0)$, as a function of the number of carbons in the dicarboxylic acid structure. Dashed lines represent the error-bar of the pure calcite $\gamma_{\text{cr}}(0)$ value (orange solid line). All the samples are at $\phi = 20\,\%$.

Appendix D

Solid calcite

D.1 Interest of solid calcite

In this side study we investigated the mechanical properties of a calcite-based cement. This study on solid calcite demonstrates the difficulties in producing a cement starting from rhomboedrical nanocalcite particles. This subject was developed mainly during the internship of Benjamin Thominet, who also designed the molds described in the following sections.

D.2 Introduction

Cement is well known as a very complex material mainly due to its multi-components nature and to the several mechanisms that occur during the cohesion process (i.e. hydration, coagulation and setting) [10]. As production process we use an adapted version of the protocol proposed by Baglioni et al. [2] in which the main goal is to produce an autogenous lime-based grouts for restoration purpose. In particular, they add to the grout several ammonium based carbonates to have an autogenic production of CO_2. These compounds are soluble in water in which they slowly release CO_2. The interest in the addition of autogenic additives is to furnish a higher quantity of CO_2 in the suspension making faster and more homogeneous the setting process (transformation of lime in calcium carbonate). This procedure can reduce the presence of voids between distinct layers.

Moreover, others studies on solid $CaCO_3$ are carried out using amorphous calcium carbonate (ACC) or vaterite. Vaterite is a spherical crystalline form of calcium carbonate ($CaCO_3$) thermodynamically unstable which dissolves in aqueous solution and then crystallizes in calcite i.e. the rhomboedral crystalline form of $CaCO_3$ thermodynamically stable [12, 7].

In particular, a study by Combes et al. [4] demonstrates the feasibility of calcite based cement obtained by mixing amorphous calcium carbonate (highly reactive) with vaterite (crystalline) and a small amount of water to induce a reaction that end in 100 % of calcite (crystalline) [7, 13].

Moreover, Bouville at al. [3] focus on nanovaterite based cement with a setting process in which the key-role of pressure and particle size is explored. Inspired by biomineralization, a "cold sintering process" is set up to obtain, at room temperature and under pressure, a dense and strong ceramic from nanovaterite. Here a dissolution-precipitation mechanism and then a plastic deformation occur between adjacent spherical vaterite agglomerates composed by nanoparticles. Both processes are activated by

water and the following densification mechanism is enhanced by decreasing the particles size and increasing the externally applied stress. The uniaxial pressure on a cylindrical mold is in the range of $10-800$ MPa. As shown in Figure D.1, increasing the applied stress the spherical agglomerates deform until disappearing, displaying only a residual porosity.

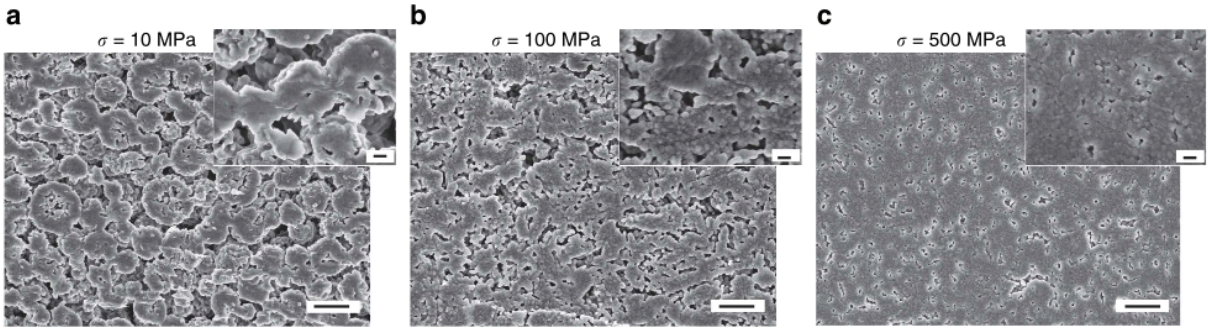

Figure D.1 – Adapted from Bouville at al. [3]. Densification behavior of nanovaterite compacts and comparison with model geological calcite. (a-c) Scanning electron micrographs of vaterite compacts subjected to different external stresses. Scale bar, 1 μm (a-c), inset: 200 nm

Bouville et al. [3] found that the final strength and elastic modulus of their sample have the same order of magnitude as stone, concrete or wood.

D.3 Materials and methods

Our study is focused on rhomboedral calcite, one of the main constituents used in the elaboration of cement, the main goal is to obtain a solid sample to test the flexure and hardness properties.We adopted a simplified version of the procedure proposed by Baglioni et al. [2] to facilitate the setting and have a more homogeneous structure all along the mold. We choose the simpler additive proposed, the ammonium bicarbonate NH_4HCO_3, which dissolves in water:

$$NH_4HCO_{3(aq)} \longrightarrow NH_{3(g)}+CO_{2(g)}+H_2O_{(l)}$$

Providing CO_2 in the suspension, the consequent reaction in a lime-based grout is:

$$Ca(OH)_{2(s)}+CO_{2(g)} \longrightarrow CaCO_{3(s)}+H_2O_{(l)}$$

The principle is to trigger the precipitation of calcium carbonate - from lime and ammonium carbonate- that will stick the grains of our suspension together. So we added different amounts of $Ca(OH)_2$ to promote the precipitation of $CaCO_3$ and so increase its cohesiveness and reduce the porosity of our samples. As a first step a rectangular mold for flexure test is used without any applied pressure. Second micro-indentation tests are made on calcite solid samples produced under pressure in a cylindrical mold.

To produce our suspensions, several amounts of 70 nm calcium carbonate powder (Socal 31, SOLVAY) are dispersed in distilled water. A 5 % in weight (respect to the total solid amount) of additives is always inserted in a proportion 1:1 of calcium hydroxide ($Ca(OH)_2$) and ammonium bicarbonate (NH_4HCO_3) [2]. The choice of the additive amount (5 %) has been arbitrary.

We built two stainless steel molds as shown in Figure D.2, one rectangular for flexure test with a dimension of 20x20x120 mm^3 and a cylindrical one with a diameter of 14 mm. In the inner cylinder a paste volume of $1-1.5$ mL is inserted to obtain a final sample with a thickness around 5 mm. For the first mold we tested several liquid to solid ratio (g_{liquid}/g_{powder}), in a range of $L/S = 0.9-1.5$ corresponding to $\phi \simeq 30-20\,\%$. The molds, once filled with the paste, are placed in a oven. We tried different protocols varying both temperature between 60 and 110° C and heating time from 3 to 6 h.

In the cylindrical mold instead we used a liquid to solid ratio L/S in a range of $0.15-0.50$ ($\phi \simeq 70-40\,\%$) and an applied pressure (on the cylinder mold) from 280 to 500 MPa [3].

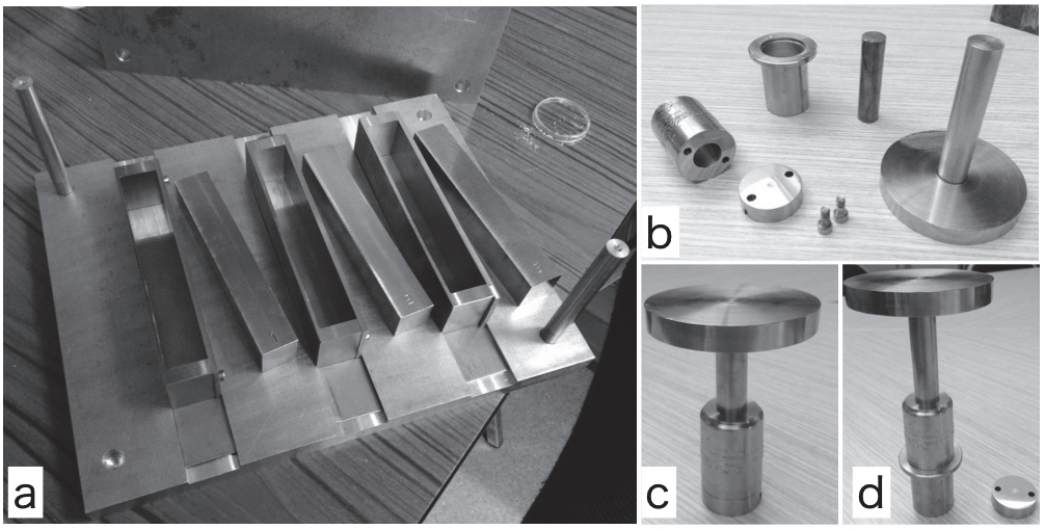

Figure D.2 – Stainless steel molds. (a) Three rectangular molds for flexure test covered by solid rectangular parts during the setting process. An upper lid is fixed on top to have a surface where to apply an external stress. (b-d) Cylindrical mold during the sample loading (c) and unloading (d). For both phases a pressure is applied on the top of the large cylinder.

D.4 Results

The results obtained with the rectangular mold are shown in Figure D.3. In the upper figure (a) are reported three samples of $CaCO_3$ with $Ca(OH)_2$ and NH_4HCO_3 for different calcite volume concentration: (I) $L/S = 1.5$, (II) $L/S = 1.1$ and (III) $L/S = 0.9$. In the other two pictures (b) and (c) are shown further details for (I) and (III). This three samples are the result of 48 h of setting at room temperature, only imposing an initial hand pressure to distribute the paste homogeneously in the molds. We obtained similar results with all the others protocols varying both temperature and heating time. The pressure is not varied here because of the mold geometry, in fact applying a high pressure, the sample partially squeezes out creating voids and inhomogeneities on the upper surface. All the samples prepared with this technique give very fragile samples for which we could not perform flexural tests.

Figure D.4 instead shows some samples obtained with the cylindrical mold. A detailed description of these samples is reported in Table D.1 varying the L/S ratio, the time under pressure t_{up}, the external applied stress σ_{ext}, the samples volume V_c and the values obtained by micro-indentation tests expressed by HV500, Vickers Hardness test with mass load of 500g.

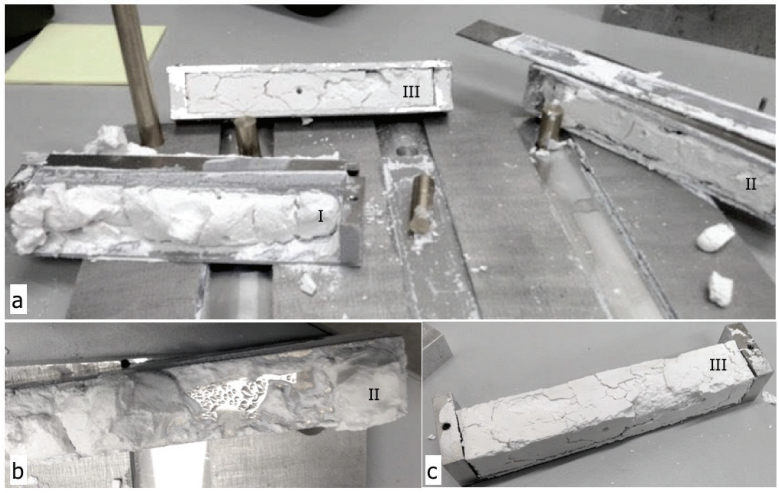

Figure D.3 – Solid samples obtained with the rectangular mold.

Figure D.4 – Examples of solid samples obtained with the cylindrical mold.

In Figure D.5 are compared the values of indentation hardness in the whole range of measurable L/S ratios for $\sigma_{ext} = 280\,\text{MPa}$, $t_{up} = 60\,\text{min}$ and $V_c = 1\,\text{mL}$.

D.5 Discussion

D.5.1 Rectangular mold

As shown in Figure D.3 solid samples obtained with the rectangular mold are unusable for flexure tests due to the multiples fractures already presents after the setting process. Trying to make a general analysis, we noticed that increasing the volume concentration, the sample seems more compact (Figure D.3(c)) without showing residual humidity as in lower concentration (Figure D.3(b)). We can also affirm that the heating process reduces drastically the setting time but increase the fragility of the system with more cracks all along the sample. We cannot evaluate the effect of the pressure for a design problem as already mentioned. The improvements that we can propose are essentially two: as first try to increase the volume concentration with a more efficient mixing apparatus to avoid the residual humidity and densify the system, as second design a different cover to have a more efficient sample compaction. These two points are linked: a higher L/S ratio can support a higher external stress without flowing out of the mold. This non-optimized protocol makes impossible any quantitative evaluation.

Table D.1 – Indentation hardness results for different protocol conditions for samples obtained with the cylindrical mold. Legend: XX = totally broken or X = partially broken during the unloading phase, OV = overnight and (OV) = overnight in the loading phase without pressure.

L/S	t_{up} (min)	σ_{ext} (MPa)	V_c (mL)	HV500
0.50	10	280	1.5	XX
0.50	45	280	1.5	XX
0.50	45	390	1.5	XX
0.25	45	280	1.0	X
0.25	60	280	1.0	187 ± 5
0.25	60	280	1.0	206 ± 12
0.25	90	280	1.0	X
0.20	60	280	1.0	282 ± 22
0.20	90	280	1.0	X
0.20	90	500	1.0	X
0.20	OV	280	1.0	X
0.15	60	280	1.0	332 ± 12
0.15	60	280	1.0	237 ± 12
0.15	60	280	1,0	302 ± 14
0.15	120	280	1.0	277 ± 20
0.15	60	390	1.0	294 ± 18
0.10	60	280	1.0	285 ± 16
0.10	60 (OV)	280	1.0	489 ± 41

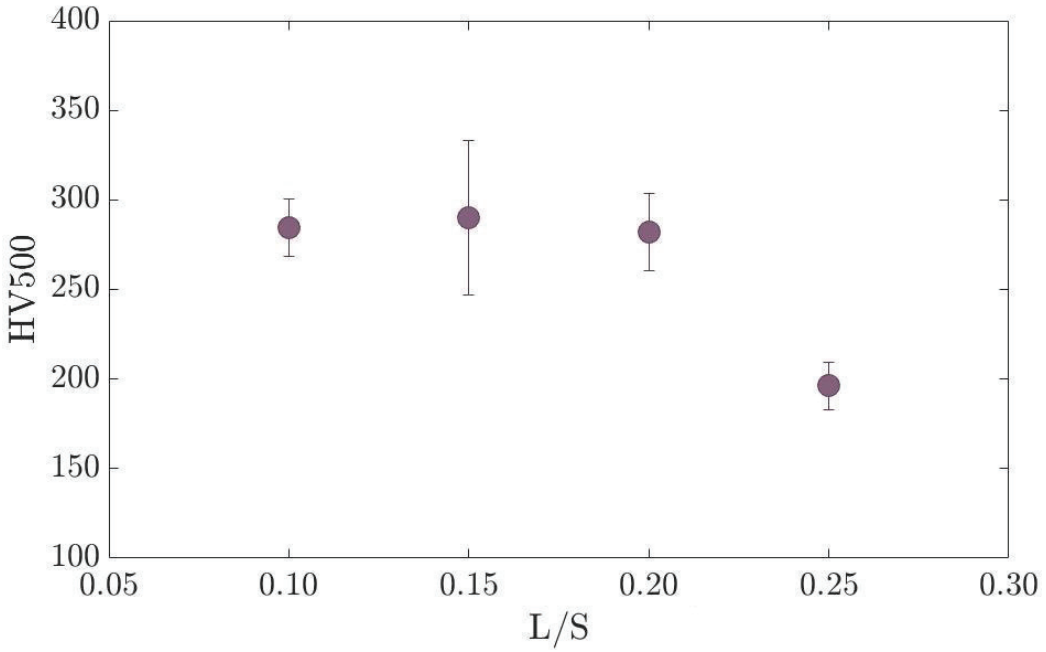

Figure D.5 – Indentation hardness (HV500) as function of the L/S ratio for $\sigma_{ext} = 280$ MPa, $t_{up} = 60$ min and $V_c = 1$ mL

D.5.2 Cylindrical mold

Indentation hardness tests are made on solid calcite produced with a cylindrical mold. As shown in Figure D.4 several samples are damaged after the unload phase (XX in Table D.1). Some others present

a smooth surface but are partially fractured (X in Table D.1). All the samples are collected in Table D.1 for different protocol conditions. For high L/S ratio, the samples were completely or partially damaged, making impossible the hardness measurement. Reducing L/S down to 0.2 (value suggested by Bouville et al. [3]) we finally obtained measurable samples. Figure D.5 shows the data of HV500 (Vickers Hardness test with mass load of 500 g), for the same protocol conditions. We observe a plateau with a hardness around $250-300$ MPa for low L/S ratio, then a decrease for $L/S \geq 0.2$. Even if the data are scarce, it seems that increasing pressure above 280 MPa or the holding time more than 1 h has no significative effect on the final hardness properties. The only sample that shows larger HV500 is the last one which is tested after one night in contact with the atmosphere, but its reproducibility has not been tested.

Although we obtained measurable hardness values, the solid calcite is still very fragile, without any relevant usage.

D.6 Conclusion

To summarize, we tried to obtain a solid calcite sample with an initial addition of calcium hydroxide and ammonium bicarbonate to our suspension, playing the role of cement between the calcite grains. We used two different molds: a rectangular one for flexure strength measurements and a cylindrical one for indentation hardness tests. The obtained samples are always very brittle. After several protocol variations we obtained indentation hardness measurements in a range HV500$\simeq 250-300$ MPa with $L/S = 0.1-0.2$, $\sigma_{\text{ext}} = 280$ MPa, $t_{\text{up}} = 60$ min and $V_{\text{c}} = 1$ mL.

As shown by the literature, good cements are obtained mixing vaterite and amorphous calcium carbonate or making vaterite under pressure. In both cases, a recrystallization process occurs to obtain at the end a cohesive material. We have shown here that this use of metastable components is necessary and that the tests we have carried out with a thermodynamically stable phase never lead to sufficient cohesive materials.

Bibliography

[1] Visual minteq version 3.1, https://vminteq.lwr.kth.se.

[2] P. Baglioni, L. Dei, F. Piqué, G. Sarti, and E. Ferroni. New autogenous lime-based grouts used in the conservation of lime-based wall paintings. *Studies in Conservation*, 42(1):43–54, 1997.

[3] F. Bouville and A. R. Studart. Geologically-inspired strong bulk ceramics made with water at room temperature. *Nature communications*, 8:14655, 2017.

[4] C. Combes, B. Miao, R. Bareille, and C. Rey. Preparation, physical–chemical characterisation and cytocompatibility of calcium carbonate cements. *Biomaterials*, 27(9):1945–1954, 2006.

[5] L. Ducloué, O. Pitois, J. Goyon, X. Chateau, and G. Ovarlez. Coupling of elasticity to capillarity in soft aerated materials. *Soft matter*, 10(28):5093–5098, 2014.

[6] C. Geffroy, A. Foissy, J. Persello, and B. Cabane. Surface complexation of calcite by carboxylates in water. *Journal of Colloid and Interface science*, 211(1):45–53, 1999.

[7] K. Hosoi, T. Hashida, H. Takahashi, N. Yamasaki, and T. Korenaga. Low temperature solidification of calcium carbonate through vaterite-calcite wet transformation. *Journal of materials science letters*, 15(9):812–814, 1996.

[8] R. G. Larson. The structure and rheology of complex fluids. 150, 1999.

[9] T. Liberto, M. Le Merrer, C. Barentin, M. Bellotto, and J. Colombani. Elasticity and yielding of a calcite paste: scaling laws in a dense colloidal suspension. *Soft matter*, 13(10):2014–2023, 2017.

[10] R. J.-M. Pellenq and H. Van Damme. Why does concrete set?: The nature of cohesion forces in hardened cement-based materials. *Mrs Bulletin*, 29(5):319–323, 2004.

[11] A. Pierre, J. Lamarche, R. Mercier, A. Foissy, and J. Persello. Calcium as potential determining ion in aqueous calcite suspensions. *Journal of dispersion science and technology*, 11(6):611–635, 1990.

[12] Q. Shen, H. Wei, Y. Zhou, Y. Huang, H. Yang, D. Wang, and D. Xu. Properties of amorphous calcium carbonate and the template action of vaterite spheres. *The Journal of Physical Chemistry B*, 110(7):2994–3000, 2006.

[13] G.-T. Zhou, Q.-Z. Yao, S.-Q. Fu, and Y.-B. Guan. Controlled crystallization of unstable vaterite with distinct morphologies and their polymorphic transition to stable calcite. *European Journal of Mineralogy*, 22(2):259–269, 2010.